# The Synthesis, Characterisation and Application of Transparent Conducting Thin Films

This thesis is submitted in partial fulfillment of the requirements for the Degree of Doctor of Engineering (Chemistry).

**Mathew Robert Waugh**

University College London

2011

I, Mathew Robert Waugh, confirm that the work presented in this thesis is my own. Where information has been derived from other sources, I confirm that this has been indicated in the thesis.

*This thesis is dedicated to 'the Champ'.*

# Abstract

Transparent conducting thin films of metal oxides, doped metal oxides, and carbon nanotubes (CNTs), have been produced using various deposition techniques, including: Aerosol Assisted Chemical Vapour Deposition (AACVD), Atmospheric Pressure Chemical Vapour Deposition (APCVD), and Spray Coating. The resultant thin films were tested for their performance in a number of applications, including: Low emissivity ('Low-E') glazing, photovoltaic electrode materials, gas sensing and photocatalysis.

AACVD was shown as a viable, and attractive, deposition technique for the synthesis of tin oxide, and doped tin oxide thin films, which allows for controllable doping levels, crystallinity, and surface structure. The tailoring of these physical attributes allows for enhanced performance of the functional properties of the films, whereby, a lower growth temperature produced highly transparent, highly conductive coatings with a low haze value for 'Low-E' applications, whereas, higher growth temperatures produced the high electrical conductivity, transparency, and light scattering properties required for high performance electrodes in thin film photovoltaics. In addition, a dual coating methodology was developed using both AACVD, and APCVD, to grow tin oxide thin films in a rapid timescale, but with modified surface structures showing changes to the short range waviness, kurtosis, and the surface area.

Growth of carbon nanotubes, using CVD, was investigated over a range of metal catalysts, with varying Pauling electronegativity values, and over a range of temperature, methane, and hydrogen conditions. A growth mechanism has been postulated, whereby, the electronegativity of the metal catalyst, and the solubility and diffusion of the carbon through that catalyst, affects the type and properties of the carbon structure produced. To the authors knowledge, this is the first reported growth of MWCNTs using a chromium solo-metal catalyst, and the first reported growth of the unique 'carbon nanofibres' which were produced using gold and silver metal catalysts.

Functionalisation of SWCNTs using a microwave reflux process was shown to yield sulphonate and sulphone modified nanotubes, which are highly soluble in water and able to undergo spray coating to produce carbon nanotube, nanonet transparent conducting thin films. The functionalisation process was shown to be reversible upon heating of the modified nanotubes.

AACVD has been deemed unable to produced doped zinc oxide transparent conducting films. However, undoped zinc oxide films were produced. They displayed a high photocatalytic action in the degredation of stearic acid, and a UV light induced superhydrophilicity.

The modification and deposition techniques, established throughout this work, were utilised to form transparent, hybrid, metal oxide-CNT coatings, for gas sensing. The hybrid materials displayed enhanced response times to combustible target gases, which has been attributed to the catalytic effects of the exposed carbon nanotube surfaces; and to the spillover of adsorbed oxygen from the active nanotubes to the metal oxide surface.

# Acknowledgements

*……"Learn from yesterday, live for today, hope for tomorrow. The important thing is not to stop questioning."* Albert Einstein.

*…… "Stupid is as stupid does."* Forest Gump.

## List of Analytical Techniques:

- **Atomic Force Microscopy** analysis was performed using a Veeco Dimension 3100 in intermittent contact mode using a cantilever and tip under resonant frequency. Analysis was done using Gwyddion 2.14 freeware.

- **Crystallite Size** was determined from the XRD patterns using the Scherrer equation[1, 2]. The full width at half maximum standard used was a 25 $cm^2$ alumina flat plate obtained from the National Institute of Standards and Technology (NIST), with peak intensities given by NIST and peak positions by the ICDD.

- **Diffuse Transmittance** measurements were done on a JASCO V-570 UV/VIS/NIR spectrophotometer by deducting direct transmittance spectra from the total transmittance spectra (using direct transmittance and optical integrating sphere modes to capture the two spectra respectively) to yield a % diffuse transmittance spectra.

- **Hall effect measurements** were carried out using the Van Der Pauw method[3], to determine the sheet resistance, free carrier concentration (N) and mobility ($\mu$). A square array of ohmic contacts arranged on a 1 $cm^2$ sample with a calibrated magnetic field was used.

- **Haze Measurements** were performed using a BYK Gardner haze-gard plus, operating over the CIE luminosity function y visible spectral range.

- **Infrared Spectroscopy** was performed using a Perkin Elmer FT-IR spectrum RXI spectrometer over a wavenumber range of 500 $cm^{-1}$ to 4000 $cm^{-1}$.

- **Raman Spectroscopy** was performed using a Renishaw invia Raman microscope at 514.5 nm and 785 nm (green and red lasers respectively). The operating power was set between 1 and 5 % to avoid radiative degradation of the samples.

- **Scanning Electron Microscopy and Energy Dispersive Elemental Analysis** SEM was performed using a JEOL JSM-6301F Field Emission SEM at an accelerating voltage of 5 keV. EDXA was performed using an attached Oxford Instruments INCA Energy EDXA system.

- **Sheet Resistance** measurements were recorded using an 'in house set-up' linear four point probe.

- **Thermo-Gravimetric Analysis** was done on a NETZSCH STA–449C Jupiter balance under helium flow, up to a temperature of 1500˚C.

- **Transmission Electron Microscopy (High Resolution)** Transmission Electron Microscopy (TEM) was completed using a JEOL JEM-4000EX HRTEM at 100 kv.

- **Transmission Electron Microscopy and Electron Diffraction** were performed using a JEOL JEM-100CX 2 microscope at an accelerating voltage of 100 kv.

- **UV/Visible Absorption Spectroscopy** was performed using a Perkin Elmer Lambda 25 spectrometer over 250 – 900 nm.

- **UV/Visible/Near IR** spectra were taken using a Perkin Elmer Fourier transform Lambda 950 UV/Vis spectrometer over a wavelength range of 300 nm to 2500 nm in both transmission and reflection modes.

- **Wavelength Dispersive X-ray** was used to quantify thin film atomic ratios using a Phillips XL30 E-SEM and Oxford instruments INCA Energy detector.

- **X-ray Diffraction** measurements, to analyze crystallinity and orientation of the samples, were completed using a Bruker D8 X-ray diffractometer with CuK$\alpha$1 and CuK$\alpha$2 radiation of wavelengths 0.154056 nm and 0.154439 nm respectively, emitted with an intensity ratio of 2:1, a voltage of 40 kV and current of 40 mA were used. The diffraction pattern was taken over 10-70º 2$\theta$.

# Contents

# 1 Introduction

*The following work presents the results obtained from an investigation into the use of metal oxide and carbon nanotube visibly transparent and electrically conductive thin films, in opto-electronic and gas sensing applications. Chemical vapour deposition (CVD) and spray pyrolysis were used to synthesize carbon nanotubes and to deposit transparent conducting thin films of the following materials: doped-$SnO_2$, single-walled carbon nanotubes (SWCNT), multi-walled carbon nanotubes (MWCNT), ZnO and CNT-MO(carbon nanotube-metal oxide) hybrid materials.*

*The thin film materials produced were then assessed in their performance for a multitude of applications, which included: 'low-E' heat mirror glazing, transparent electrode materials for thin film photovoltaics, photocatalytic degredation of organic materials, and gas sensing.*

## 1.1 Thesis Overview

The following content of this introductory chapter gives a definition of transparent conducting materials. It covers the basis of chemical vapour deposition and spray pyrolysis for the growth of transparent conducting thin films, followed by a description of metal oxide and carbon nanotube electronic structure, outlining the basic model of conductivity within solids, and the interaction of free charge carriers with light. Finally, this introductory chapter covers the basic theory and desired characteristics of materials required for 'Low-E' heat mirror glazing, electrode materials for thin film photovoltaics, photocatalysis, and gas sensing.

Chapter 2 describes the deposition of doped tin oxide thin films by atmospheric pressure CVD (APCVD) and aerosol assisted CVD (AACVD). It describes the relative performance of each of these methods for producing transparent conducting coatings for 'Low-E' glazing and transparent electrodes for solar cells. We demonstrate that our novel deposition method, Collison-AACVD, produces films with favorable characteristics, outperforming those of current commercial products.

Chapter 3 reports the combination of Collison-AACVD and APCVD in a novel dual approach to tin oxide thin film deposition, which allows control over the light scattering properties of the resultant thin films.

Chapter 4 details the growth and characterisation of carbon nanotubes (CNT) and carbon nanofibres (CNF) using a CVD process. We review a range of transition metal catalysts and assess their performance in the synthesis of CNT and CNF species.

Chapter 5 describes the functionalisation of CNTs to render them water soluble, and the subsequent spray deposition of CNTs to form nanonet thin films for use in transparent conducting applications.

Chapter 6 describes the AACVD of ZnO thin films and their function as photocatalysts in the UV light induced degradation of stearic acid, with a view to assessing the properties of ZnO as a self-cleaning, glazing material.

Chapter 7 presents the results obtained from gas sensing experiments performed using CNT, ZnO, $SnO_2$ and CNT-MO hybrid materials, in the detection of ethanol and nitrogen dioxide.

Chapter 8 reviews the results presented in this thesis and draws conclusions from the novel materials and techniques.

## 1.2 Transparent Conducting Materials

Transparent conducting thin films are a class of material which achieve large values of electrical conductivity, whilst maintaining a high transmission in the visible range of the electromagnetic spectrum[4]. Since the realisation of this type of material, vast amounts of research and development have gone into commercialising these thin film coatings. The current commercial products are based on n-doped metal oxide thin films, so-called transparent conducting oxides (TCO's). These films have a far reaching range of applications from heat-mirror window-coatings, which control the transmission of infrared energy into and out-of buildings[5], to their use as the transparent electrode materials in photovoltaic cells, touch-screen technology and flat panel displays: including, liquid crystal displays (LCD), organic light emitting displays (OLED) and plasma screen displays[6].

The first TCO material was reported in 1907 when K.Badeker sputter coated a thin film of cadmium and heat treated the sample in air[7]. The heating step led to the incomplete oxidation of the cadmium to non-stoichiometric cadmium oxide, leaving oxygen vacancies in its structure. The oxygen vacancies led to penta-valent cadmium ions, which generated occupied defect energy levels from which electronic promotion into the cadmium oxide conduction band could easily occur. Though, this was the first demonstration of an n-type transparent conducting material, the films still showed a relatively high electrical resistance compared to metals and was unstable over time - as full oxidation occurred.

Current TCO materials include tin-doped indium oxide $In_2O_3$:Sn (ITO), fluorine doped tin oxide $SnO_2$:F (FTO) and aluminium doped zinc oxide ZnO:Al (AZO). These materials, instead of relying on intrinsic vacancies within the metal oxide structure, use the defect energy levels created by the extrinsic dopant species to generate n-type conduction. Discovered in 1954 by Rupperecht[8], ITO was the first of the modern TCO materials, however this system suffers from some significant drawbacks due to the rarity and high cost of indium and degradation of the films at the high temperatures required for certain device processing. These drawbacks have led to the development of

fluorine-doped tin oxide, antimony-doped tin oxide, and more recently doped zinc oxide systems, as low cost, high performance, and durable alternatives.

The prevalence of transparent conducting thin films in a vast amount of current technology creates a large driving force for the constant search to find new and improved transparent conducting thin film materials. A leading candidate for this new generation of transparent conducting layers, are carbon nanotube (CNT) nanonet thin films. Carbon nanotubes are a relatively new class of material which can display metallic-like conductivity and excellent mechanical strength. CNT-nanonet thin films are based on the principle of a randomly assembled layer of CNTs, just a few tubes in thickness, where overlap of the tubes creates a network of possible electronically conductive channels, thus allowing the electrons to seek low energy pathways across the film[9].

The purpose of the following doctoral work was to review a range of transparent conducting thin film materials, including the TCOs and CNT nano-nets, and to investigate both traditional and novel techniques for deposition, and performance in both traditional and novel applications.

## 1.3 Thin Film Deposition Techniques

Deposition of high quality, uniform thin films, is an intensive area of research which has yielded many varied deposition techniques[10, 11,12]. Each technique falls into one of three broad categories: wet chemical deposition; physical vapour deposition and chemical vapour deposition. Careful selection of the appropriate deposition technique is essential for control over the properties of the resultant films. Different techniques can affect growth rates, crystallinity (epitaxial/single-crystal, polycrystalline or amorphous[13]), substrate interaction (adhesion, line-of sight/non-line of sight coating) and morphology.

Each of the categories and a range of common individual techniques are described as follows:

### 1.3.1 Wet Chemical

Including, amongst others, chemical bath techniques and Sol–Gel techniques, which are a wet chemical process that involve the use of a chemical precursor solution which reacts to produce a colloidal solution (sol), this then forms a continuous solid (gel) upon evaporation of the solvent:

- Dip Coating[14] - immersion of the substrate into a precursor chemical solution followed by evaporation and annealing to yield the metal oxide layer.
- Spin Coating[15] - The precursor is dropped onto the centre of a spinning substrate which then spreads out quickly and evaporates the solvent.

### 1.3.2 Physical Vapour deposition

Physical Vapour deposition techniques are the range of techniques used to deposit thin films onto a substrate using purely physical processes, involving the condensation of a vaporised form of the material[16, 17]:

- Evaporative deposition - resistive heating is used to vaporise the material which is then allowed to deposit onto a substrate.
- Electron beam vapour deposition[18] - a high energy beam of electrons bombards the sample material causing vaporisation.
- Sputter coating - involves the use a plasma discharge to vaporise the material
- Pulsed laser deposition[19] - a high energy laser pulse causes evaporation of the material.

### 1.3.3 Chemical Vapour Deposition

Chemical Vapour Deposition (CVD) is the most widely used technique to form thin film TCO materials, it involves deposition of the metal oxide film from the reaction of gas phase precursors on the substrate surface[20]. The most common form involves the use of metal-organic precursor species and is thus named MOCVD (Metal-Organic CVD). The advantages of CVD, are that it can be performed as a continuous process

5

which uses a relatively low consumption of energy, therefore can be achieved on an industrial scale. CVD is a non-line of sight process, so is able to coat complex shapes and surfaces and gives uniform conformal coatings which are usually chemically bonded to the substrate, giving high adhesion. CVD has the ability to control crystal structure, morphology and orientation by selection of process parameters. Highly dense and pure materials can be produced with control over the deposition rate and a high number of possible precursors can be used[21]. Common types of CVD are as follows:

- APCVD - Atmospheric Pressure CVD[21] uses heating of the precursor to generate a vapour pressure which is transported using a carrier gas flow to a heated substrate for reaction(done at atmospheric pressure).

- LPCVD [22]- Low Pressure CVD uses the vapour pressure of the precursors under low pressure conditions, to aid transport to the reaction chamber.

- PECVD [23] - Plasma Enhanced CVD uses APCVD conditions with a plasma generated in the reaction chamber, to enhance reaction of the precursors.

- FACVD[21] - Flame Assisted CVD uses an aerosol of the precursor solution which is injected into a flame to activate and accelerate precursors at the target substrate.

- AACVD[24, 25] - Aerosol Assisted CVD is a modification of vapor deposition which uses a solution of the precursor in solvent, that is then transported to the substrate in an aerosol form using an inert carrier gas. The solvent then evaporates above the heated substrate allowing reaction of the precursors.

- Spray Pyrolysis[20] – Spray pyrolysis is considered a modification of vapour deposition, again using a fine spray of precursor solution (generated by a spray nozzle using compressed gas) which delivers the precursor metal organic molecules to the substrate surface for thermal reaction and film formation.

Chemical vapour deposition does have certain drawbacks, which include the possibility of carbon contamination from metallorganic precursors in the films, adhesion problems under certain conditions, limitations on temperature not compatible with the substrate, the shelf-life of the precursors, and possible side reactions.

## 1.3.4 The CVD Process

The CVD process can be split into two major sub-processes:

1) Supply and transport of precursor.

2) Film deposition reaction.

The work in this thesis is mainly concerned with APCVD, AACVD and spray pyrolysis, thus, the key stages in each of these techniques will be addressed.

### *1.3.4.1 APCVD Mass Transport Kinetics*

APCVD uses metal-organic precursors which are heated within a bubbler (see fig.1-1) to supply the reaction. The rate of supply is governed by the thermal heating of the precursor to alter the vapour pressure, and the rate at which the inert carrier gas is introduced into the bubbler to transport the gaseous precursor (the overall pressure is always atmospheric pressure in this system). Precursors are required to have a relatively high vapour pressure at achievable temperatures. Liquid precursors generally give a better supply of gaseous vapour though design modifications will allow certain solid precursors to be used.
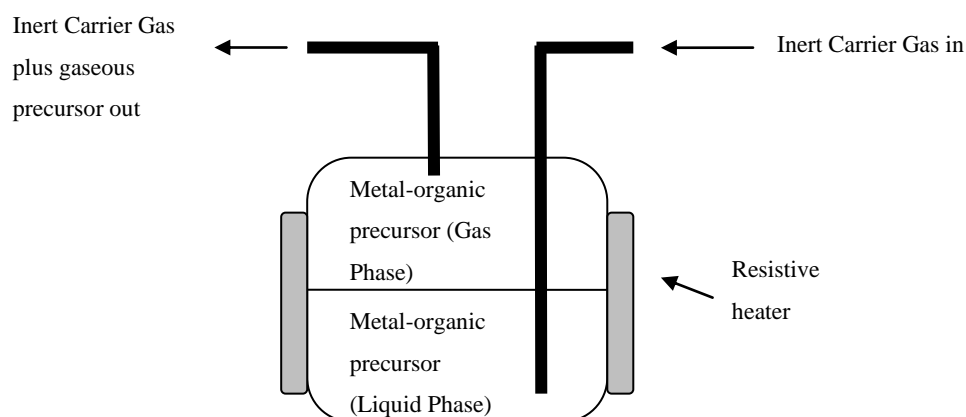


**Figure 1-1** Schematic diagram of a bubbler used to thermally generate the correct vapour pressure for transport of the metal-organic precursor using an inert carrier gas during Atmospheric Pressure Chemical Vapour Deposition.

Assuming an ideal mixing of ideal gases in the bubbler, then a thermodynamic equilibrium is established. This means:

**Equation 1-1**

$$\frac{N_p}{N_c} = \frac{P_p}{P_c}$$

Where $N_p$ and $N_c$ are the number of moles of precursor and carrier gas respectively. $P_p$ and $P_c$ are the partial pressures of the precursor gas and carrier gas respectively.

In a system with only the carrier gas and the precursor gas:

**Equation 1-2**

$$P_c = \left(P_{total} - P_p\right)$$

Operating under atmospheric pressure (760 torr) we can substitute 760 torr for $P_{total}$, and substitute formula 1-2 into formula 1-1, rearranging to give:

**Equation 1-3**

$$N_p = \frac{N_c \times P_p}{\left(760 - P_p\right)}$$

Given that at room temperature and atmospheric pressure 1 mole of gas occupies 22.4 litres. Dividing $N_c$ by 22.4, allows use of flow rates of carrier gas ($f_c$ in $Ls^{-1}$) to calculate flow rate of precursor ($F_p$) in $moles.s^{-1}$. Giving the final equation to calculate the molar flow rate of precursor based on vapour pressure and carrier gas flow rate as:

**Equation 1-4**

$$F_p = \frac{f_c \times P_p}{22.4\left(760 - P_p\right)}$$

Equation 1-4 allows calculation of the molar flow of precursors from the bubbler, based on known vapour pressure values for the precursor over the desired temperature range.

### 1.3.4.2 AACVD/Spray Pyrolysis Mass Transport

AACVD and Spray Pyrolysis use a solution of precursor (solid or liquid) dissolved in a particular solvent to supply the reaction. An aerosol or spray is generated from the solution for transport to the substrate surface. Dissolved precursor species give advantage over APCVD, in that non-volatile precursors can be used. However, the precursors must be soluble in an appropriate solvent.

The mass transport in these techniques is controlled by the concentration of the precursor species in the solution and the rate of supply of that solution. Supply of solution is usually governed by mechanised syringe drivers in spray pyrolysis techniques, which can accurately measure the volume dispensed. AACVD relies on either ultrasonic or Collison (physical buffeting with a compressed gas) to generate the aerosol, these techniques can usually be tailored to modify the rate at which the aerosol is supplied.

### 1.3.3.1.3 Film Formation Reaction

The following section outlines the basic film formation process, common to all MOCVD methodologies, that results in a surface reaction of the precursors on the heated substrate. Other film formation processes such as gas phase reactions, plasma or flame activation and precursor pre-reaction are complimentary or alternative routes to film formation, but are considered beyond the scope of this introductory chapter.

Fig.1-2 illustrates the MOCVD film formation process which can be summarised as follows[26]:

1) Mass transport from the reactor inlet into the deposition zone.

2) Thermal decomposition of the precursor metal-organic species to form the film constituents and waste organics.

3) Adsorption of the atomic film constituents to the heated substrate surface and expulsion of the waste organic species to the exhaust.

4) Surface diffusion and migration of the film constituents to nucleation and growth sites.

5) Incorporation of the constituents into the growing film.
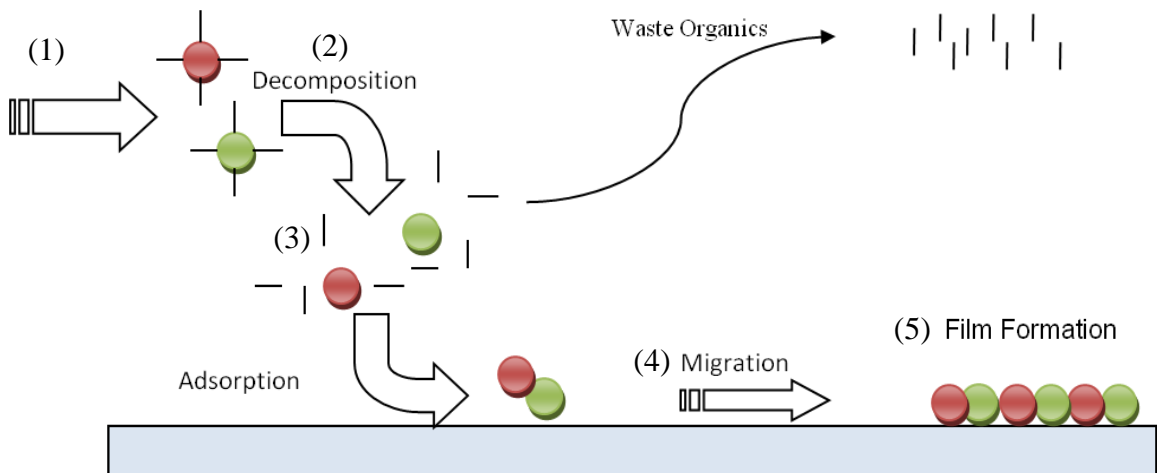


**Figure 1-2** Schematic diagram of the idealised film formation process during MOCVD. Coloured balls represent the desired film atoms for the forming thin film. Sticks represent the organic groups attached to the precursor before reaction and film formation.

Fig.1-2 represents a general case for MOCVD. Variations on the MOCVD technique are abundant and beyond the scope of this introduction: further reading is available through many established text books[10, 20, 26, 27], outlining the variations in reactor design, gas handling systems, growth characteristics, reaction rates, reaction mechanisms and kinetics, transport phenomenon and computational modeling.

## 1.4 Metal Oxide Electronic Structure

The stability and conductivity of modern TCO materials, including doped tin oxide and doped zinc oxide, relies on the doping of the transparent metal oxides to yield a highly conductive thin film. The basis for selection of an appropriate dopant species relies on knowledge of the band structure for the metal oxide host. The relative energy levels associated with the valence electrons, the unoccupied conductance energy levels, and the energy levels created by dopant atoms in the host matrix, must be considered.

The structures and properties of metals are characterised by their delocalized valance electrons which give such materials high electrical conductivity. Whereas, in ionic and covalent structures the electrons are usually localised on particular ions or atoms.

A mathematical description which can be applied to ionic solid state materials to describe the behavior of the electrons is known as band theory. To illustrate how the introduction of dopant species into an ionic insulating metal oxide can result in n-type and p-type conduction modes, a brief description of this solid state bonding model will follow.

Band theory is concerned solely with the valance electrons: assuming that the inner core electrons are localised on discrete atoms and therefore non-interacting. The Feynman model then assumes that valence orbitals overlap with neighbouring valence orbitals[28]. The symmetry of the overlaps are described by the wave number k, which must satisfy the Bloch function equation, so that the allowed electronic wavefunctions within the solid are corresponding to periodic arrangements of the atomic orbitals in the

structure[29]. These wavefunctions are then stationary solutions to the Schrodinger equation of a periodic potential for an electron thus resulting in no scattering in the infinite crystal when the Bloch function is satisfied[30]. Scattering mechanisms are thus caused by defects, phonons, other electrons, and boundaries.

The periodicity in atomic spacing results in both bonding (low energy) and antibonding (high energy) interactions between orbitals. This leads to an overall splitting pattern of valence orbitals for the bulk material where the energy difference between concentric energy levels is minimal, so the entire set of valance orbitals can be considered a continuum or band[31]. This is illustrated in fig.1-3.
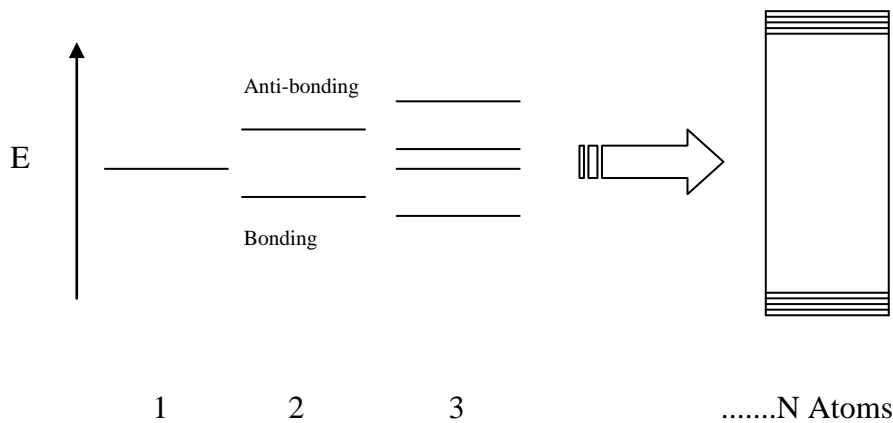


**Figure 1-3** Orbital energy splitting with increasing addition of atomic orbitals leading to an effective energy continuum (Numbers show the quantity of interacting atoms – each with 1 interacting orbital).

This splitting leads to electronic bands for each of the different orbital angular momentum valence shell orbitals (s, p, d...) that have different fundamental energies associated with them. The relative size, and therefore the relative energy minima and maxima, of the orbital bands will determine whether there is energetic overlap between bands of differing angular dependence[32].

Metallic conductivity is assumed if one of the bands is partially filled; ie the Fermi level (highest occupied energy level) falls within a band. This allows low energy pathways for the electrons to flow through the material which is referred to as de-

localisation. If the valence band (highest energy occupied band) is full, the unoccupied empty band closest in energy becomes the conduction band, due to the fact that promotion of electrons to this energy level will result in de-localised conductance. The magnitude of the energy gap between the valence and conduction band determines whether the material is an insulator (large energy difference effectively prevents thermal electronic promotion), or a semiconductor (smaller energy difference allowing some electronic promotion which is temperature dependent).
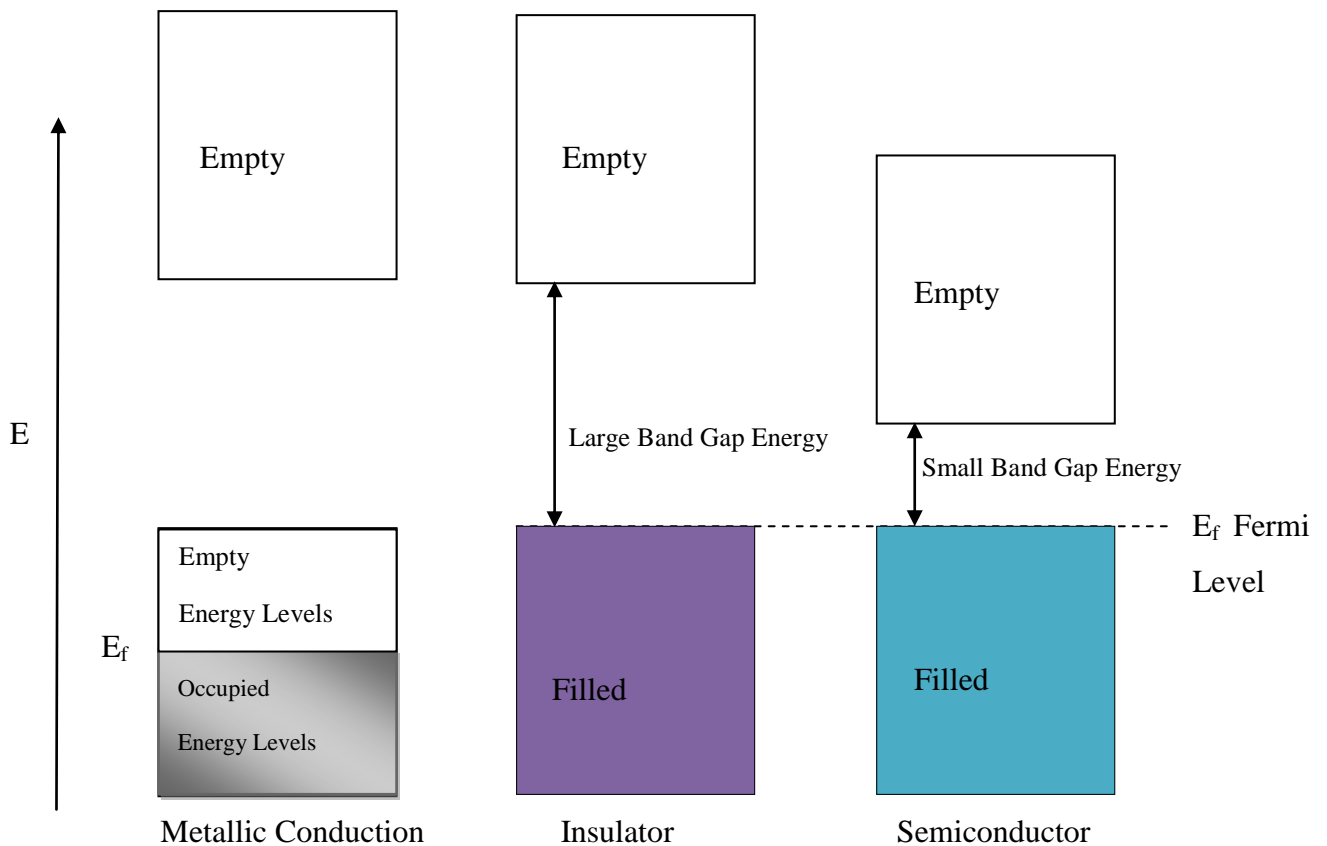


**Figure 1-4** Diagram representing the occupied energy levels and band gap energies in a metal, insulator and semiconductor material. $E_f$ is the Fermi level (the highest electronically occupied energy level).

### 1.4.1 Metal Oxide Doping

Doping in both n and p type metal oxide materials is the result of the addition of a dopant species to a bulk semiconducting or insulating lattice structure. In an n-type doping; the dopant atom sits in place of one of the constituent atoms in the bulk, resulting in a non-bonding electron which creates an donar energy level close to that of the conduction band. This allows facile promotion from the donar energy level, and delocalised conductivity in the now partially filled conduction band. In a p-type doping; the dopant atom causes an electronic deficiency in the ionic bonding, thus creating an empty acceptor energy level just above the valence band, which can accept an electron from that valence band, and leaves behind a positive 'hole'. This allows conduction via what can be thought of as movement of a 'positive hole' through the material[32].
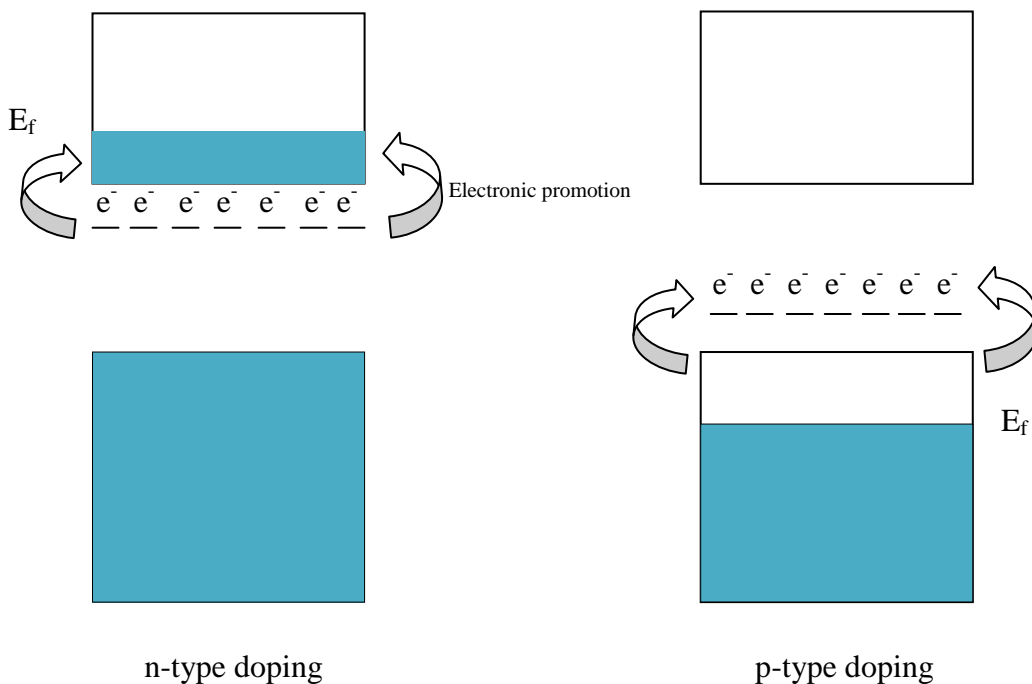


**Figure 1-5** Band structure diagrams of n-type and p-type doped semiconductor materials: showing promotion of the electrons over a small defect ionisation energy level. $E_f$ is the Fermi level (the highest electronically occupied energy level).

## 1.5 Metal Oxide Selection for TCO materials

The combination of high electrical conductivity and high optical transparency (in the visible region of the spectrum) are two traits which are not easily reconciled. Optical transparency requires a band gap larger than 3.2 eV to prevent absorption in the visible region of the electromagnetic spectrum, and this makes doping of the metal oxide very difficult[33].

Extensive work has gone into modeling the properties required to develop new TCO materials. Assuming that a suitable bandgap in the host material electronic band structure, and a suitable relative donor energy level for an n-type dopant species have been calculated for the n-type TCO material, there still must be consideration taken to account for the ability of the host material to accept the dopant species. The three major reasons for failure to dope metal oxide frameworks must be considered. They are as follows[34]:

1. Insoluble dopants: The dopant atom cannot be introduced into the appropriate host lattice site because of limited solubility. This includes cases of competing compound phase formation, impurity segregation or precipitation (eg large impurity atoms) and substitution in the wrong sites.

2. Deep level donors: where the energy level of the dopant species is too deep for ionisation to occur at normal temperatures, thus no electronic promotion occurs.

3. Compensated dopants: where both solubility and the donor energy level is suitable, however, upon promotion of free charge carrier species, spontaneously generated oppositely charged defects occur effectively negating the doping effect - so called 'Killer defects'. This is due to reduction in the formation energy of these defects as doping increases and the Fermi energy level altered[34].

Problems 1 and 2 can be overcome by careful selection of dopant atom size and electronegativity, however if the 3$^{rd}$ failure to dope problem is encountered, this places a limit on the type of doping and extent of doping which the material can endure.

As such, a set of empirical rules has been established which quantify the properties needed from a metal oxide for TCO application[28, 35,8]. In order to achieve n-type conductivity in a wide band gap (>3.2 eV) metal oxide, the material should exhibit a large electron affinity and a relatively low conduction band minimum, this enables the material to be easily n-doped and to maintain its free charge carriers. A large range of energy states within the conduction band is desirable, in order to reduce scattering caused by a high carrier density due to the lack of available energetic pathways. Another important consideration is the stability of the structural frame work with respect to increased levels of doping. Increasing the number of defect atoms with differing size to the host lattice atoms, in substitutional positions, can lead to phase separation. Deformation in the structure of the framework material can also cause 'killer defects' [34].

Other considerations to note concern the morphology of the metal oxide film; clearly from a practical point of view production of an amorphous uniform film with no grain boundaries and a higher level of flexibility would be favourable, this however often degrades the transparency and the conductivity in traditional semiconductors[36]. Therefore highly crystalline films with minimal crystal defects and large crystallites (in polycrystalline films) are favourable.

The research presented in this thesis will look at the deposition of doped tin oxide and doped zinc oxide thin films using novel deposition techniques. Theoretical calculations and experimental evidence demonstrate that both of these metal oxide systems display the appropriate physical and optical properties for use as transparent conducting oxides, alongside an ability to accommodate certain n-type dopants which should result in a high electrical conductivity.

## 1.6 Carbon Nanotube Electronic Structure

The following section outlines the physical description and electronic structure of SWCNT, this is done by using the underlying structure of graphene as a starting point. It demonstrates the importance of understanding the diameter and chirality of carbon nanotube species in relation to their electrical behavior. We shall then examine this electrical behavior in terms of using this material as a transparent conducting thin film.

The possible existence of carbon nanotubes (CNT) stemmed from the discovery of fullerenes by Kroto et al.[37] in 1985. The first reported characterisation of Carbon Nanotubes came in 1991 when Iijima et al[38] observed Multi walled nanotubes as the side product from a fullerene experiment. Iijima went on to produce and characterise both multi-walled and single-walled nanotubes at the NEC research laboratory in Japan. This discovery sparked a whole new field of research into these unique nanostructures, in the last 15 years both the theory and experimentation into this new and exciting field has developed at an unprecedented pace.

SWCNT can be thought of as the extension of fullerenes in one spatial dimension. SWCNTs range in diameter from 0.4 nm which is the lower limit determined by strain on the tube (strain is proportional to 1/diameter), the upper limit being 3 nm where any larger and the structure collapses.

Carbon nanotubes can be considered a rolled up graphene sheet, which can be described in terms of the chiral vector $C_h$[39]:

**Equation 1-5**                                      $C_h = na_1 + ma_2$

Where:

$a_1$ and $a_2$ are unit vectors on the graphene lattice

$n$ and $m$ are integer values

$C_h$ is the chiral vector (forming the circumference of the rolled up tube)

This chiral vector, $C_h$, connects crystallographically equivalent sites on a 2D graphene sheet and so forms the circumference of the rolled up nanotube. This gives 3 distinct types of symmetry: Zigzag, Armchair and Chiral ($0 < \theta < 30$) as shown in fig.1-6[40].
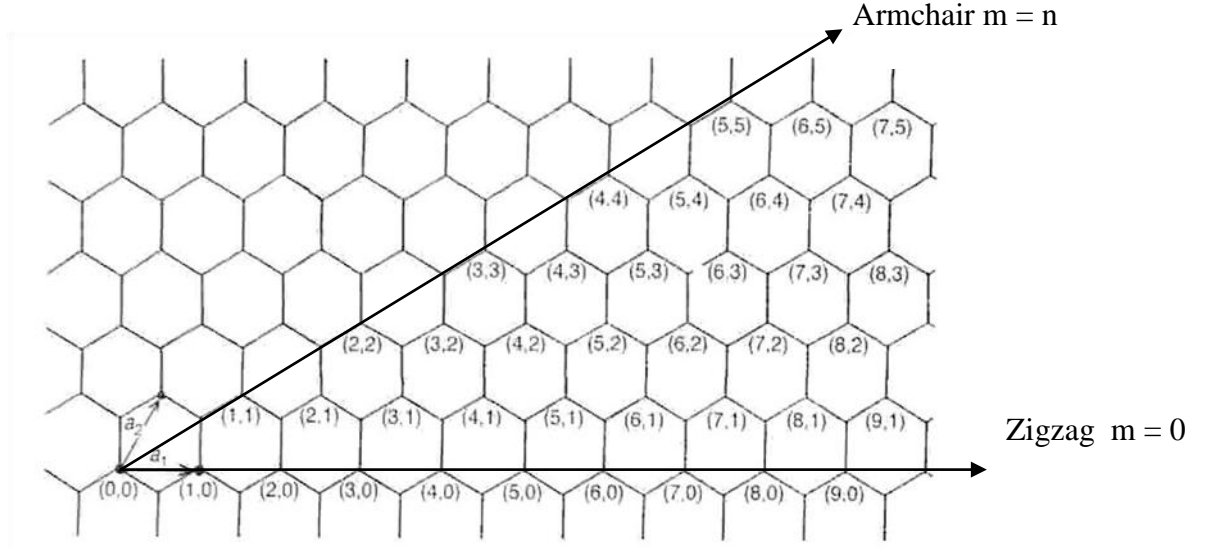


**Figure 1-6** Graphical representation of the graphene structure with symmetry vectors of various CNT orientations shown.

This description allows for a simple relation between the vector and the diameter of the tube.

**Equation 1-6**

$$D=|C|/\pi=\frac{a(n^2+nm+m^2)^{1/2}}{\pi}$$

Where $|C|$ is the length of $C_h$ vector and a is the length of the integer unit used to describe $C_h$. The Chiral angle is given by;

**Equation 1-7**

$$\theta = \tan^{-1}\left[\sqrt{3n}\,/(2m+n)\right]$$

Both armchair and zigag tubes are achiral and, as such, have mirror planes associated with them. All other angles result in chiral symmetry nanotubes. The unique electronic characteristics of CNTs stem from the electron confinement in the graphene sheet thickness and electronic quantum confinement around the circumference of the tube, which sets up periodic boundary conditions.

Single walled carbon nanotube (SWCNT) chirality is determined - as we have seen - by the tube axis orientation with respect to the hexagonal lattice. The physical derivation of a SWCNT from graphene means that we can also derive the electronic structure from that of graphene.

The hexagonal lattice of graphene is not a direct Bravais lattice, due to the fact that atoms A and B (shown in fig.1-7a) do not have the same orientation (using the unit vectors $a_1$ and $a_2$ described earlier). Therefore the 2 dimensional, 2-atom, primitive unit cell is used (shown in fig.1-7a), to create a 2D oblique Bravais lattice. This can then be translated into reciprocal space where each point (hk) in the reciprocal lattice represents a set of lattice planes (hk) in the real space lattice, thus allowing the Bloch equations for propagation of an electron in a periodic structure to be solved using just one Brillouin zone. [40, 41]
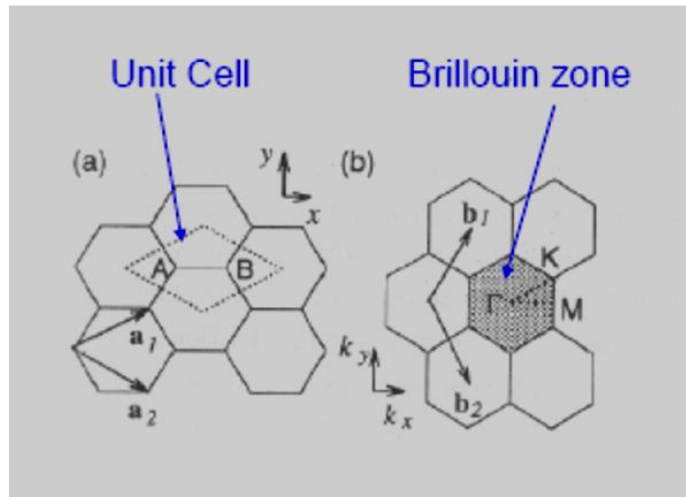


**Figure 1-7** a) Real lattice of graphene. Dotted box shows the 2 atom primitive unit cell. $a_1$ and $a_2$ are the real lattice vectors. b) Reciprocal graphene lattice showing first Brillouin zone and reciprocal lattice vectors. Exert from[42].

19

Application of the tight binding model to calculate the electronic band structure for a single graphene sheet along the dotted triangular co-ordinates shown in fig.1-7b yields a band structure as shown in fig.1-8[43].
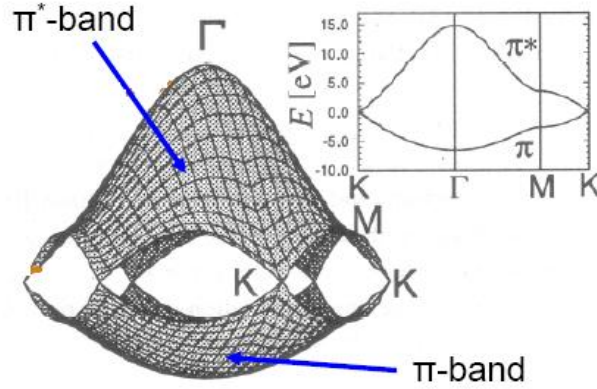


Figure 5: Graphene Energy Dispersion Relations [4]

**Figure 1-8** Shows the graphene energy dispersion relations calculated using the tight binding energy model.[42].

The energy diagram shown in fig.1-8 displays the low energy $\pi$ band (bonding p-orbital combinations) and the higher energy $\pi*$ band (anti-bonding orbital combinations). At zero Kelvin the $\pi$ band is completely filled and the $\pi*$ band is completely empty, however the 2 bands are degenerate at K points, thus making 2-D graphene a zero-energy bandgap semiconductor (as the density of states at the Fermi level is still actually 0 therefore not a metal). Layering of graphene into graphite leads to interactions between the layers in the third dimension causing a partial filling of the electronic bands, and as-such graphite is a metallic conductor at 0 K.[41, 43]

Taking the structure of graphene, it is possible to roll it up into a particular chirality nanotube, thus creating a 1 dimensional material. Electronic propagation is confined in the tube thickness and quantized around the circumference of the tube due to the enforced periodic boundary conditions. This results in allowed 1 dimensional vectors in the reciprocal lattice as shown in fig.1-9 (for a SWCNT with real unit vectors (4,2)), which correspond to only certain allowed electronic states in the valence and conduction bands of graphene.
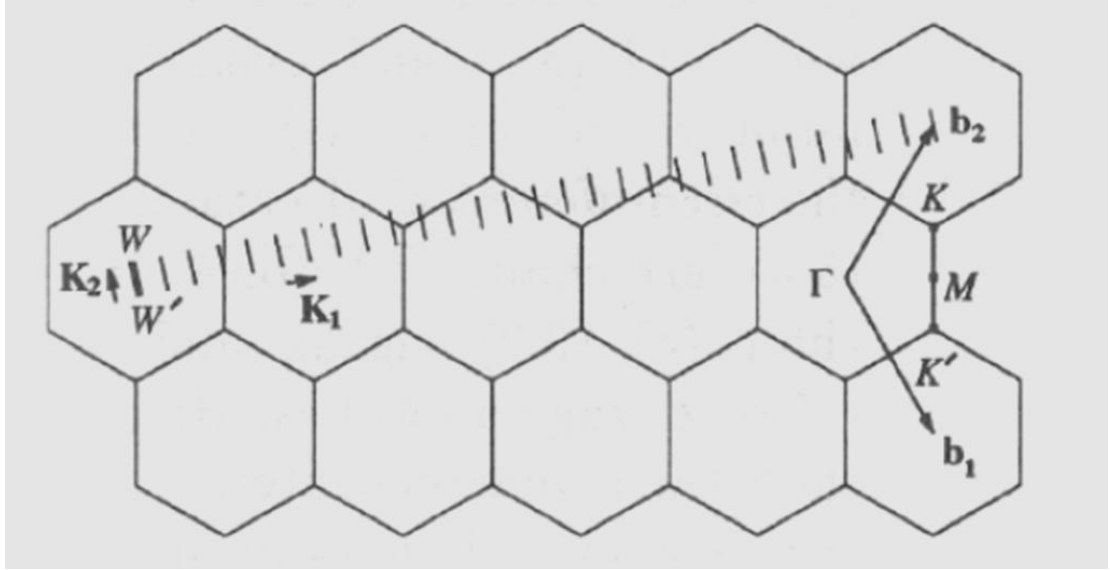
**Figure 1-9** Reciprical lattice graphene with the allowed reciprocal lattice vectors ($K_1$ and $K_2$) shown for a (4,2) chiral single walled carbon nanotube. Exert from[42]

Fig.1-9 shows the reciprocal lattice of the (4,2) SWCNT. $K_2$ represents the reciprocal lattice vector corresponding to the real space vector of the tube axis. $K_1$ represents the reciprocal lattice vector corresponding to the circumferential real space vector of the tube. The allowed reciprocal space vectors after quantization of the graphene by rolling it into a (4,2) SWCNT, are shown dissecting the reciprocal graphene lattice. WW' represents the first Brillouin zone.

The allowed vectors in the $K_2$ direction show a continuum, due to the assumed infinite length of the carbon nanotube along its axis. The allowed vectors in the $K_2$ direction arise from the quantization around the circumference of the tube. The chirality and diameter of the SWCNT will change the orientation and spacing of these allowed reciprocal vectors. This causes N allowed cuts in the energy dispersion bands of graphene.

Because the K points in the reciprocal lattice represent a zero-energy bandgap, when the allowed vectors from a specific tube cross these K points it results in a metallic conductivity with a possible near-ballistic transport of electrons up to one micrometer[44]. However if no allowed vectors cross the K points then the tube will be semiconducting. This leads to the prediction that metallic tubes must posses a chirality

where (n-m) is a multiple of 3: leading to the conclusion that approximately 1/3 of SWCNT tubes are metallic and 2/3 are semiconducting, and that the diameter is inversely proportional to the bandgap.
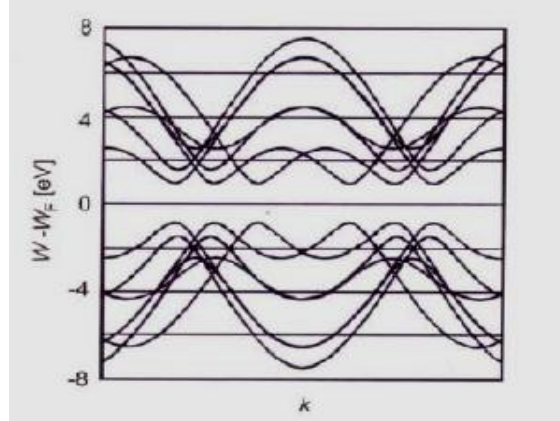


**Figure 1-10** Energy bands of a (4,2) CNT. Each band corresponds to one of the N cross sections of the graphene dispersion relations folded into the first Brillouin zone. The (4,2) SWCNT is semiconducting since the N cross-sections do not pass through the K points[41].

In addition to this unique electronic behavior which is controlled by the physical manifestation of the carbon nanotubes, they also exhibit exceptional mechanical properties. The mechanical behaviour of CNTs shows a large resilience to strain, due to the small dimensions of the tubes which prevents micro cracks or dislocation failure piles forming. This means the tubes can be reversibly distorted without atomic rearrangement. They also show a very high stiffness towards an axial load, again dependent on the helicity of the tube structure[45].

## 1.6.1 Carbon Nanonet Thin Films

Based on the principle of an interconnected network of conducting tubes, CNT-nanonet transparent conducting thin films have been receiving significant attention. They offer the possibility of not only a low cost, carbon based transparent conducting material with exceptional electrical properties, but also, an added flexibility over their TCO counterparts. This raises the possibility of use in many applications such as flexible displays, touch screens, and electronics. Initial research into fabrication of these

22

thin films has been met with some success. Sheet resistance values as low as 30Ω/□ have been reported[46,47] with a vast range of deposition techniques that have been used to achieve film deposition. These techniques range from printing[48], filtration[46], dip-coating[47], and spraying[49]. Though promising, the properties of the films made to date will need to be improved if this type if thin film is to compete with the existing TCO thin films for electronic application. The research in chapters three and four will look at the growth of various carbon nanotube species, characterisation of their physical and electrical properties, and their application as transparent conducting thin film materials, drawing comparisons to other TCO materials.

## 1.7 Electrical conductivity

Band theory provides a framework for modeling the electronic state within an idealised metal oxide or carbon nanotube material. However, after assuming the presence of mobile conducting electrons or holes within a material, the mechanism of conductance must also be addressed in order to appreciate the influence of scattering interactions on the overall conductance in a real thin film. The following derivation acts as a basis for further discussion (throughout this thesis) which will address the electronic conductance mechanisms within the produced thin films, and the electrical response to an optical field.

### 1.7.1 Conductivity and Ohms Law: The effect of an electric field

The following is a short derivation of the required modeling parameters of conductivity within a solid state material containing free charge carriers. The equations, hereby defined, act to illustrate the desired properties that govern the performance of a successful transparent conducting material[50].

A very simple model, based on the Drude model of conduction[51, 52] can be assumed as follows:

- The electron is assumed to be a particle.
- There is a corresponding number of positivly charged nuclei in a cubic lattice symmetry to electrons to give overall neutrality.
- Collisions occur between the electrons and ionic nuclei only (ignoring electron-electron interactions, defects, surfaces and impurities).
- Collisions are instantaneous, and result in a change in velocity, whereby the collisions occur with probability per unit time ($t^{-1}$ the relaxation-time approximation).
- The electrons are modelled as a Boltzman Temperature dependent gas with thermal velocity ($v_{th}$)     ($1/2 m v_{th}^{2} = 3/2 KT$).

We represent the electric field as E = U/L where U is the potential difference applied between a solid of length L. Where E is present at each point in the solid causing acceleration of the electrons (a)

**Equation 1-8**

$$a = E(e/m)$$

e  = charge on an electron

m = mass of an electron

So every electron in the solid has thermal velocity in every direction which cancels out to 0, plus an induced acceleration in the direction of the field which is totally lost after every collision with the lattice. This has introduced a frictional dampening term[30].

If we define t as the average time between collisions (mean free relaxation time) then the drift velocity of electrons $V_d$ is given by $V_d = a.t$ So combining this with eq.1-8

**Equation 1-9**

$$V_d = E \; \frac{e}{m} t$$

This gives a current density flux    $J = N_e. V_d.e$

$N_e$ = electron density

**Equation 1-10**

$$J = \frac{N_e e^2 t}{m} E$$

This is a version of Ohms law

**Equation 1-11**

$$J = \sigma E$$

Where conductivity;

**Equation 1-12**

$$\sigma = \left( t \frac{e}{m} \right)(N_e e)$$

And the electron mobility $\mu_e$;

**Equation 1-13**

$$\mu_e = t \frac{e}{m}$$

This expression for the conductivity shows that contrary to popular belief conductivity is not constant but actually changes with the applied electric field due to the variation of t with E .

However because t is related to the length between collisions by;

**Equation 1-14**

$$L = t(V_{th} + V_d)$$

Which, from eq.1-9 shows that it is $V_d$ that varies with E. If $V_{th} \gg V_d$ then ohms law will not be violated. Metals are well described by ohms law as they have low mobility electrons but many of them, to provide conduction. However the relationship can breakdown with semiconductors if they rely on few electrons with very high mobilities of conduction, causing a large $V_d$ term.

Eq.1-12 models the behavior of the conductivity in an ideal solid, where the electron is truly free to move within the ionized lattice, and its movement dampened only by the collisions with that lattice. This is a simplified approximation which discounts other scattering mechanisms and quantum mechanical effects taking place in real materials. A modified version of this equation can be used, where the mass of the electron is replaced with the effective mass ($m_e$), this implied value can approximate for the forces acting to retard the electron's mobility (such as defects, surfaces, impurities and other electrons).

The Drude model clearly shows the relation between the conductivity of a material and the charge carrier density and mobility. A high conductivity can be achieved by a large charge carrier density, or by a large drift velocity, which in turn is afforded by large charge carrier mobility. Due to the effect of mobility taking into account all forces acting on the electron through the effective mass, it is the number and mobility of the free carriers which can be taken as the characteristic parameters determining the charge transport in a material containing free charge carriers such as a TCO.

The Drude model provides a simplistic kinetic model for the electronic behaviour of free electrons, which gives very good explanation of AC and DC conductivity in metals, it also shows the electronic relationships governing Ohms law. It must be stated however, that the Drude model can underestimate electronic velocities, it fails to calculate electronic heat capacity, and fails to predict the dependence of the Hall

effect on a magnetic field. To move to a more complete, quantum mechanical description of free electrons in a material, the Somerfield model should be reviewed[30].

However, for discussion in the following chapters, the Drude model of conduction will suffice to demonstrate the relationship between electrical and optical properties of the thin film materials.

## 1.7.2 Interaction of free carriers and an applied optical field

As already stated in the opening section, transparent materials must have a band gap energy which is greater than the energy of visible light. This prevents electronic excitation from the conductance to the valance band, and therefore maintains visible transparency in the material. Semiconducting TCO materials will absorb in the ultraviolet region (or higher energy) of the spectrum. However, they also display another optical feature, which is exploited in their application as heat-mirror window coatings that control the transmission of IR radiation across the glazing. Depending on the charge carrier mobility and the charge carrier density of the thin film, the material will display a reflection beginning somewhere in the IR, and reflecting all longer wavelengths. This reflection is caused by the free electronic plasma, and as such, the starting wavelength of the reflection is called the plasma edge. The following section will cover the exploitation of this plasma edge in insulating glazing materials, and the basis of this phenomenon[27, 53].

Using the Drude model of conduction for free electrons in metals we can derive a set of equations explaining the behavior of electromagnetic radiation with our transparent conducting materials. Depending on the wavelength of the incoming radiation we shall see that the interaction of free charge carriers with the electromagnetic field can lead to polarization of the field within the material, thus influencing the relative permittivity of the field.

Below is a short derivation showing the interaction of an applied optical field with free carriers within a bulk solid.

Free carriers will interact with the optical field through polarisation. Where the model assumes:

- The charge carriers are weakly bound within the lattice
- The restoring force acting on the charge carriers, $k_f$, can be modeled using a harmonic oscillator approximation.
- The relaxation time is independent of the frequency of light.

This means that the response of the free carriers is dependent upon the frequency of the incoming light and the effective mass of the charge carrier. At a high frequency where the inertial mass for such a rapid acceleration prevents motion, no absorption will occur. Whereas, at a lower frequency, for an equivalent mass charge carrier, the resistance to change in motion is smaller and allows the carrier to freely respond and oscillate with the field, resulting in a resonance loss. This resonance can be modeled as follows;

The charge carriers are displaced an average distance, x, resulting in an induced polarisation, P;

**Equation 1-15**

$$P = N_e ex$$

Where:

$N_e$ is the free carrier density

e is the charge on each free carrier

So the field induced by this polarisation is defined as P/ε, where ε is the dielectric constant of the material. This field acts as a negative restoring force to the charge carrier, where the force is defined as the charge multiplied by the field:

**Equation 1-16**

$$\frac{md^2x}{dt^2} = \frac{-P}{\varepsilon}e = \frac{-N_e ex}{\varepsilon} \cdot e$$

This equation of motion can be solved in an oscillatory fashion giving the following solution which can then be shown to link the plasma frequency to the conductivity[53];

**Equation 1-17**

$$x = A\exp i \left\{ \left( N_e e^2 \Big/ m_e \varepsilon \right) t \right\} = A\exp i \left( \omega_p{}^2 t \right)$$

Where:

$m_e$ is the effective mass of an electron and

**Equation 1-19**          $\omega_p = (N_e e^2 / m_e \varepsilon)^{1/2}$

and from the previously derived equation for conductivity (σ) from Drude's model, using the effective mass of an electron the account for additional retarding forces;

**Equation 1-20**

$$\sigma = \left( \frac{e}{m_e} t \right) (N_e e)$$

Therefore:

**Equation 1-21**

$$\omega_p{}^2 = \frac{\sigma}{\varepsilon t} = \frac{N_e e \mu_e}{\varepsilon t}$$

Where:

$\mu_e$ is the charge carrier mobility

This set of equations form the basis of a mathematical description of the plasma resonance frequency, $\omega_p$, and its relation to the conductivity of the material. The plasma resonance frequency, is the frequency of electromagnetic radiation which can induce resonance of the free carriers within the material, and thus result in light reflection.

It can be seen from equation 1-19 that the plasma frequency, and therefore the starting frequency of the plasma edge, is directly dependent upon the charge carrier density ($N_e$), and indirectly dependent on the charge carrier mobility through the effective mass relationship: $\mu_e = \dfrac{e}{m_e} t.$

The above equations can then be combined with the equations for the relative permittivity of a material (as given in Drude's model), and Maxwell's equations for the propagation of light, to show that the amount of absorption and reflection taking place at each wavelength depends on the dielectric constant of the medium and the conductivity of the material.

The maximum achievable reflectivity at wavelengths longer than the plasma resonance frequency is determined directly by both the charge carrier density and the charge carrier mobility[27].

Since increasing the charge carrier density or increasing the charge carrier mobility shifts the plasma edge towards the visible, there is a fundamental limit on the electrical conductivity of transparent conducting thin film materials. Whereby, exceeding the limit will result in a visibly reflective film.

## 1.8 Applications of TCO materials

The following section outlines the applications investigated for the transparent conducting materials produced. The applications fall into two categories:

1) The application of transparent conducting thin films in 'heat mirror' glazing and transparent electrode materials for photovoltaics, which rely on the use of highly conductive and highly transparent forms of the materials.

2) The application of the materials studied for photocatalysis and gas sensing, which rely on the semiconducting nature of the materials, where population of the conduction band with free electrons is not a requirement.

### 1.8.1 Heat Mirror Glazing

Section 1.5.2 showed how materials with free charge carriers can interact with an applied optical field, leading to the reflection of light above a certain wavelength (above the plasma resonance frequency). This frequency depends on the charge carrier density and the charge carrier mobility of the material. TCO materials exhibit this reflective ability in the far IR, so whilst maintaining their visible transparency they can be used to control the transfer of thermal IR radiation across a coated substrate.

Whilst the application of double or triple glazing in a window prevents *conductive* and *convective* heat loss from a room, the application of an additional transparent conducting oxide coating allows for a significant reduction in the *radiative* heat loss from a room in cold climates. This process is governed by allowing the near IR portion of the sun's heat into the room, whilst reflecting re-emitted longer wavelength radiation (the blackbody portion of the spectrum) back into the building[54]. This has been utilised in a wide range of commercial products including Pilkington K-glass. The process relies on careful control of the TCO electrical properties to control the onset wavelength and reflectivity of the plasma edge[55].

Fig.1-11 shows a spectrum of the suns energy as it hits the earth's surface, it can be seen that nearly half of that energy occurs in the near infrared region of the spectrum from 800 nm to 2500 nm. The near IR energy of the sun is mainly responsible for heating. Fig.1-11 also show the radiation given out as blackbody radiation which occurs between 3 and 50 μm. Blackbody radiation is emitted from any hot object, including radiators and people within a building and facilitates radiative transfer of heat.
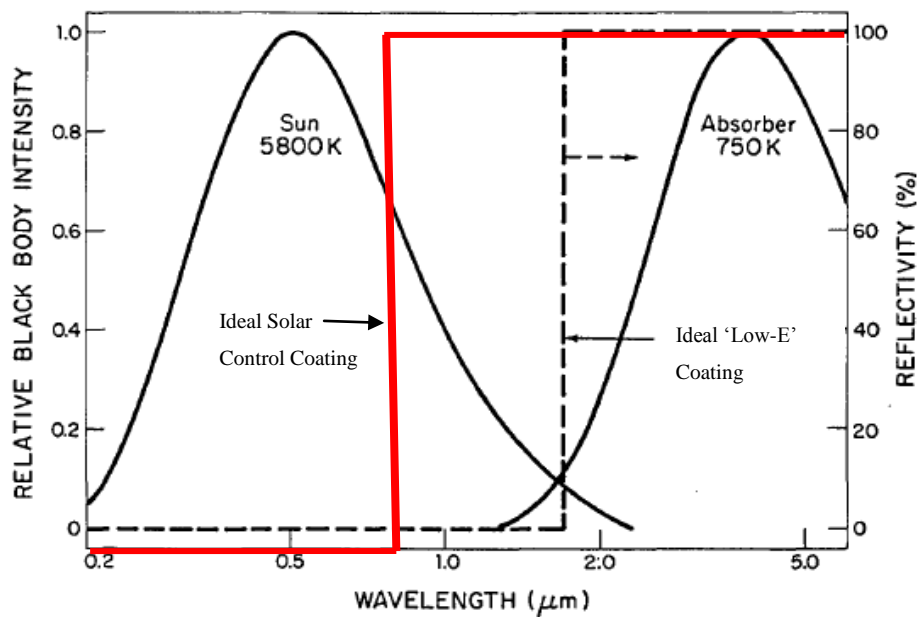


**Figure 1-11** Spectra showing the solar spectrum irradiance at the earth's surface and typical blackbody radiation from an object at 750 K, alongside idealised low emissivity heat mirror and solar control coating transmittance spectra.[56]

Fig.1-11 shows the idealised transmittance spectra for two types of 'heat mirror' coatings for windows. The solid red line represents a 'solar control coating' which is typically made from a thin film of sputtered metal. This film maintains a relatively high transmittance in the visible because the film is so thin that substantial reflection cannot occur at the permittivity values for visible light. However, as the wavelength increases the permittivity decreases, and larger levels of reflection occur, so that the near IR heat energy from the sun is reflected and prevented from entering the building. This coating is used in 'hot climates'.

The second type of coating, shown by the dashed line, which is of interest for TCO materials, is called a 'low-Emissivity' coating. Careful control of the TCO electrical properties creates a resonance frequency of light with the electronic plasma which begins at approximately 2.5 μm and extends out into the blackbody. This coating allows visible light and near IR radiative heat energy through the window into the building, but reflects the blackbody radiative heat energy generated within the building back inside. It therefore maintains maximum solar gain and maximum radiative insulation for buildings in cold climates[57].

Clearly the goal for this type of technology is to maximise reflection in the correct area of the electromagnetic spectrum and maintain high transmission across the visible part. This requires control of the charge carrier density, charge carrier mobility, film thickness and morphology.

The essential properties of the TCO for low-E glazing, includes chemical and mechanical stability of the coatings, a high reflective value for the far IR radiation (>2500 nm) and a rapid onset of the plasma edge which separates the transparent and reflective regime across the wavelength range [54, 58, 59].

European legislation requires that all new windows in 'cold' climates incorporate a TCO low-Emissivity coating, allowing for the reduction in energy losses from homes by up to 15%[60].

## 1.8.2 Transparent Electrodes for Photovoltaics

Transparent Conducting Oxide materials underpin the photovoltaic industry by providing the transparent electrodes for thin film solar cells, amorphous silicon solar cells, dye sensitized solar cells (DSSC) and polymer based solar cells[61, 62].

Traditional crystalline silicon solar cells have very high electron mobilities within the core layer, owing to the large crystal grains and relatively few imperfections in the silicon. This high mobility means that traditionally a grid of thin metal wires have been utilized as the top electrode of solar cells. Where the metal grid functions to collect

the current, but it covers a low enough surface area to still let in the light. However, with the next generation of thin film materials which are based on polycrystalline or amorphous materials, the electron mobility is much lower[63]. This reduced mobility means that lateral resistance across the surface of the solar cell is too high to use metal grids. As-such, third generation thin film solar cells use highly conductive, transparent conducting thin films as the top layer contact electrode on solar cells, where they prevent lateral resistive losses across the top electrode surface whilst maintaining high transmittance of the light into the absorbing layer of the solar cell stack[64].

In addition to a high durability, high adhesion and resilience to high temperature processing, thin film materials for solar cell applications are required to achieve an electrical sheet resistance of less than 10 $\Omega/\square$, a high electronic mobility, and a combined transparency with the glass substrate of greater than 80% (at 550 nm)[59]. They should also couple light into the cell via refractive index matching reduction of reflective losses, and light trapping using scattering sites at the thin film interface[59,65]. This equates to an ideal morphology which consists of flat pyramidal structures and a film haze value of 8-15%[54, 59, 66]. Light emitting polymer and polymer solar cell devices require an equal level of optical transparency and conductivity to window coatings, but also demand tailored work-function values which allow for energy level matching between device components[58, 67].

## 1.8.3 Photocatalysis

Transparent semiconducting thin films have the ability to generate reactive species upon irradiation with light, this leads to a wealth of photo-chemistry and a range of novel applications. Semiconducting thin films are used in the production of self-cleaning, anti-fogging glazing and antimicrobial coatings for hard surfaces. The following section outlines the mechanism of this catalytic behavior and the requirements of a high performance photocatalytic material.

We saw in section 1.2 that the electronic structure of a semiconducting material is composed of filled and unfilled electronic bands, formed from the overlap of possible

electronic orbital combinations. The valence band (VB) is completely filled, and the conduction band (CB) is completely empty, the energy separating the two bands is known as the band gap ($\Delta E$). Promotion of an electron from the VB to the CB can occur when a photon with an energy greater than the $\Delta E$ (hv > $\Delta E$) strikes the semiconducting material. This creates a free electron in the CB and leaves a positive 'hole' behind in the VB, collectively referred to, as an electron-hole pair ($e^-$ $h^+$)[68].

In the majority of materials, and aided by lattice defects, the electron and hole pair, generated by optical promotion, will recombine to produce heat energy. However, in certain metal oxides the electron and hole remain separated long enough to migrate to the surface of the material, at which point they can facilitate reduction or oxidation of surface species, respectively. This typically results in the formation of hydroxyl radicals (see fig. 1-12) from the oxidation of surface hydroxyl groups by the $h^+$. The promoted electron can also reduce oxygen to superoxide in the surrounding air, which in turn leads to the formation of hydrogen peroxide, and other hydroxyl radical species[69].

$$O_2^{\cdot-} \longrightarrow [HO_2^{\cdot}, HO_2^{-}, H_2O_2, OH^{\cdot}]$$

$$\downarrow$$

$$H_2O$$

hv

e- →

ΔE

$O_2$

Surface-OH

h+

$CO_2$ / Dead Microbes

Surface-OH$^{\cdot+}$

Organic dirt / Microbes
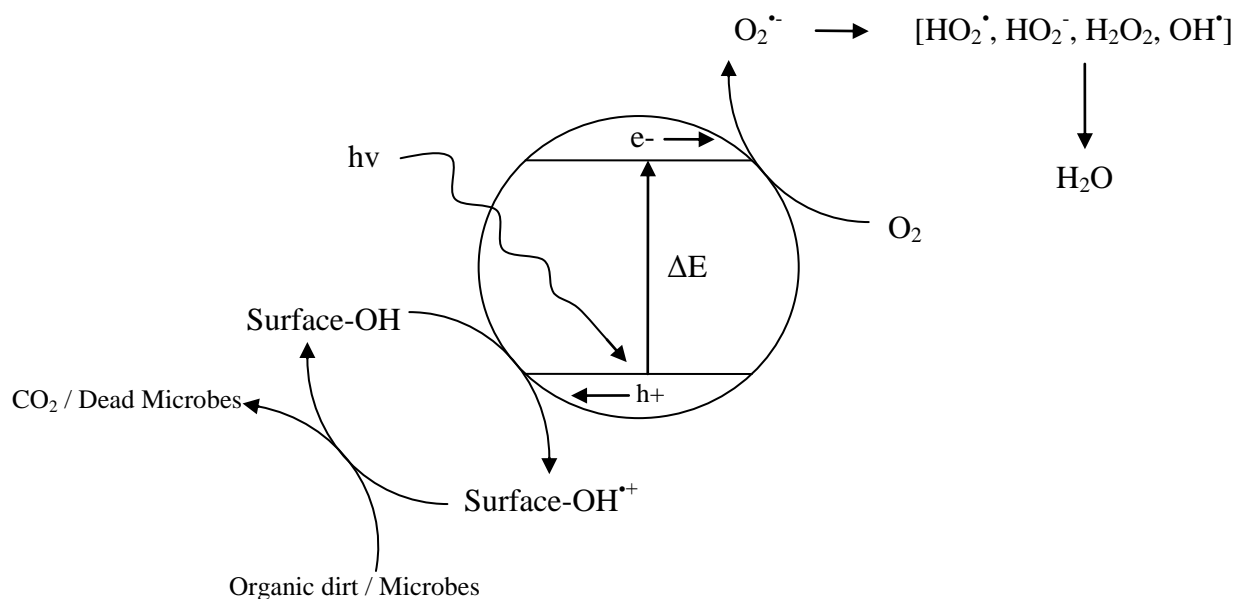
**Figure 1-12** The photo-generation of an electron-hole pair within a semiconducting material, leading to the reduction of oxygen to superoxide (which causes hydroxyl based free radical generation near the surface), and the oxidation of hydroxyl, surface bound groups, to hydroxyl radicals.

In addition to the generation of hydroxyl radicals, the surface is also modified by the formation of hydroxyl surface groups (see fig. 1-13) from bridging $O^{2-}$ sites. The oxidation of surface $O^{2-}$ groups to $O_2$ by the $h^+$, and the subsequent dissociative adsorption of water onto the empty sites, results in hydroxylation of the surface. This in turn modifies the surface from hydrophobic to hydrophilic.
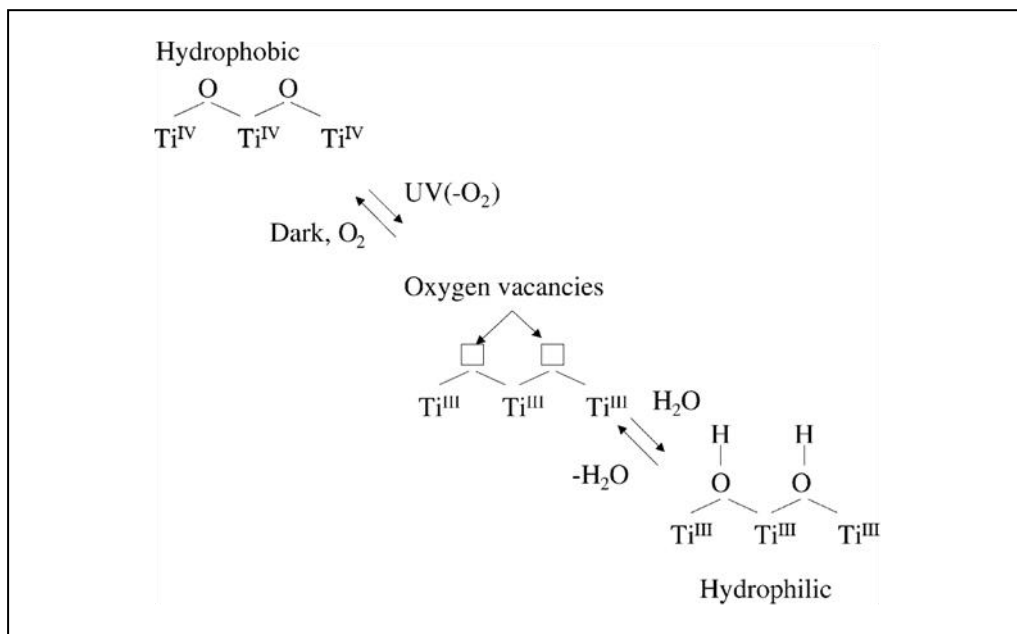
**Figure 1-13** The Ultraviolet induced modification of the TiO$_2$ surface chemistry from bridging O$^{2-}$ species to bridging hydroxyl groups, resulting in a change from a hydrophobic to a super-hydrophillic titania surface. Reproduced from work by Mills et al.[70]

The photogeneration of a hydrophilic surface, hydroxyl radicals and superoxide species leads to the activated material, which is exploited in self-cleaning anti-fogging coatings. The process is two-fold, firstly the now hydrophilic wettable surface creates a film of water which can wash away dirt when it rains, it also stops misting of the glazing by preventing droplets with a contact angle of over 20° from forming. Secondly, should any organic debris or grease remain on the window, the reactive hydroxyl species and superoxide will photomineralize the offending organics, thus loosing the dirt and grease. In a similar fashion the antimicrobial action uses the reactive hydroxyl radicals and superoxide to destroy the microbial agents[71] (See fig. 1-12).

Requirements for an effective photocatalytic material include:

- An ability to generate electron-hole pairs, and prevent re-combination long enough for the electrons and holes to reach the surface of the thin film.
- Activation by sunlight.
- Cheap and easy to produce.
- Chemically inert.
- Physically adherent and durable.

Research into photo-catalytically active materials is mostly focused on titania based films and powders, due to the fact that titania is the only material found to exhibit all but one of the above properties. The only area in which it falls down is that it only absorbs UV light which accounts for only 5 % of the sunlight energy at the Earth's surface[72]. In Chapter 6 we shall look at the photocatalytic degredation of an organic species by ZnO thin films formed by AACVD, and a comparison of its efficiency compared to the titania standards.

### 1.8.4 Semiconductor Chemical Gas Sensing

A chemical gas sensor can be described as a device which responds to chemical stimulus and transmits a resulting impulse. The function of an electrical semiconducting gas sensor relies on the change in electrical conductivity, which semiconducting materials experience when exposed to a gaseous atmosphere of different compositions. This response is measured using an electrical circuit, and the resulting change in resistance is used as the output signal for the device. The first generation of commercial electrical-based gas sensors were prepared in the 1960's by Taguchi in Japan, and were based on thick films of compressed metal oxide powders. Since their initial inception much research has been dedicated into improving the three critical operational characteristics of these gas sensors, namely: sensitivity, selectivity and stability, in

addition to cost, size, power consumption and operating temperature. First generation sensors produced using thick film technology proved to be highly irreproducible, owing to the films resistance being mainly dominated by electronic propagation across grain boundaries. Therefore a second generation of gas sensors came to be based on thin film deposition techniques such as CVD, sol-gel, and physical evaporation, which proved far more consistent, though at a cost of a lower surface area due to a lower porosity, and therefore a lower response[73].

The resistance across the semiconducting component of gas sensors, which generates a response to different gases, is governed by two dominant processes. The first is the charge transfer process which takes place when gaseous species adsorb or desorb from the surface, resulting in a transfer of electrons between the gaseous species and the semiconducting surface, and therefore a change in the number of charge carriers in the material. The second is the transport mechanisms which takes place between the electrodes and through the semiconducting material.

Let us first examine the charge transfer process. The first stage is the approach of the gaseous species to the surface of the semiconductor which leads to a Lennard-Jones physisorption, followed by a chemisorption, chemically attaching the gas to the surface. If this bonding is followed by a charge transfer of one or more electrons resulting in ionization of the gaseous species, it is known as ionosorption. Following this charge transfer process, the surface of the semiconductor and a region which extends into the bulk becomes non-neutral (ie it has a non-zero electric field), this is called the surface space charge region (SCR). Depending on the type of semiconductor (is it intrinsically n- or p-type) and the direction of electronic transfer between the gas and the surface, this may result in the SCR becoming more or less resistive. Either way the change in resistance is picked up by the electronic circuit and registers a particular response. The level of increase or decrease in resistance indicates the reducing or oxidizing nature of the adsorbed gas, and can be calibrated to indicate the concentration of that gas. Because most sensors operate in an oxygen environment, the surface will be covered in adsorbed oxygen which means that either the gaseous species can adsorb directly to the surface and alter the charge carrier concentration, or it can react with the

oxygen and remove it from the surface, thus changing the charge carrier concentration indirectly. The following equations demonstrate each case for electronegative ('reducing') $NO_2$ and for combustible ('oxidising') ethanol[74]:

$$NO_{2(gas)} \leftrightarrow NO_{2(ads.)}$$

$$NO_{2(ads.)} + e^- \leftrightarrow NO_{2(ads.)}^-$$
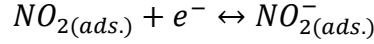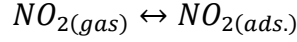
**Equation 1-22** Chemical equilibrium equations governing the adsorption of $NO_2$ gaseous species to the surface of a semiconducting material, and the subsequent charge transfer, resulting in removal of electrons from the semiconductor.

$$O_{2(gas)} \leftrightarrow O_{2(ads.)}$$

$$O_{2(ads.)} + e^- \leftrightarrow O_{2(ads.)}^-$$

$$O_{2(ads.)} + 2e^- \leftrightarrow 2O_{(ads.)}^-$$
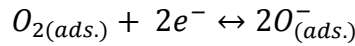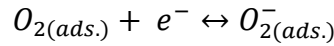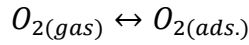
**Equation 1-23** Chemical equilibrium equations governing the adsorption and charge transfer between oxygen and the semiconductor surface. The $O_2^-$ species dominates up to 500 K. The $O^-$ species dominates over 500 K, resulting in the removal of electrons from the semiconductor.

$$H_5C_2OH_{(gas)} \leftrightarrow H_5C_2OH_{(ads.)}$$

$$H_5C_2OH_{(ads.)} + 6O_{(ads.)}^- \leftrightarrow 2CO_{2(gas)} + 3H_2O_{(gas)} + 6e^-$$
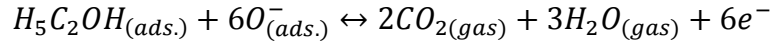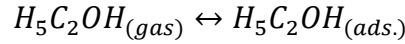
**Equation 1-24** Chemical equilibrium equations governing the adsorption mediated combustion of ethanol with surface adsorbed oxygen (above 500 K), resulting in the injection of electrons back into the semiconductor.

The above chemical equations provide a basis for the charge transfer process which takes place between the surface, and oxidative or reducing gases. However, the mechanisms of transport through the semiconducting material must also be considered. Assuming operation in an oxygenated atmosphere, an electronic depletion layer will be present in the surface space charge region of the material. If the migration of oxygen vacancies in a metal oxide semiconductor are slow enough, such that the vacancies in

the bulk are constant, then the SCR is the part of the structure which controls the transport of charge and so controls the response.

Fig.1-14 shows four scenarios illustrating the effect of morphology on the transport between the SCR of separate grains of material. Fig.1-14a shows large grains where the SCR region does not reach the core so the resistance of the core is unaffected by the gas. This means the electronic depletion is largest at the grain boundaries, which then dominate the conductivity, meaning only a smaller surface area triggers a response. Fig 1-14b shows smaller grains where the SCR layer reaches the core of the grain so that no free charge carriers remain, only thermally activated electrons control conductivity. If the Debye length is greater than half the length of the grain this leads to a flat band edge and renders the full surface of the grain responsive to the adsorbate[75]. Thus experiments performed by Yamazoe et al. demonstrate reducing the grain size in a material significantly increases the response[76].
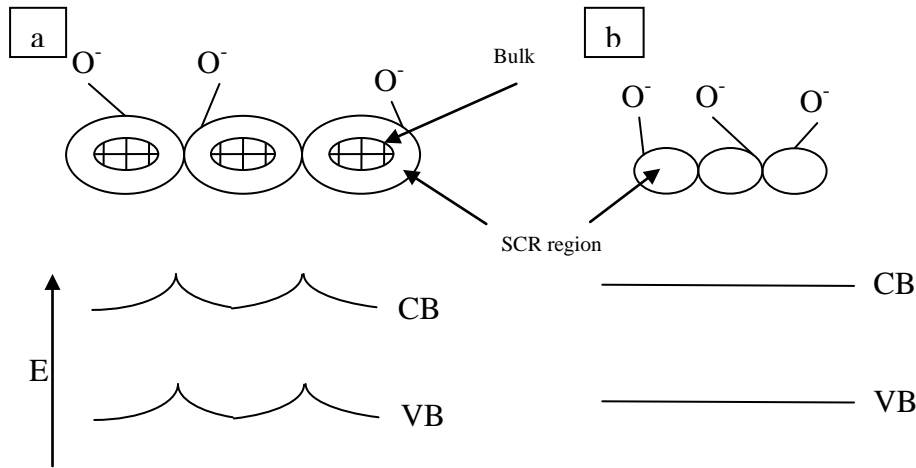


**Figure 1-14** Diagram showing a) the depletion layer and bulk region of a large grain semiconductor material, the grain boundaries have the highest depletion of electrons so the band bending leads to a large barrier which must be overcome by propogating electrons (in an n-type material) b) Small grains give a complete SCR, and if $L_{debye}$> $L_{grain}$/2 then the depletion approximation is not valid and the bands are completely flat.

The importance of selecting the appropriate semiconductor material is critical for gas sensor device performance. The conductivity should show large changes when the appropriate gas species are adsorbed, and it needs to be able to operate under atmospheric conditions, showing a selective, sensitive and stable response. In addition to the material selection, the appropriate morphology control is also critical in governing the level of response and sensitivity. Well researched, and high performance metal oxides for gas sensing include n-type ZnO, $SnO_2$, $TiO_2$ and p-type $In_2O_3$, $WO_3$ and $MoO_3$[77]. Chapter 7 of this thesis will present the results obtained from gas sensor experiments for the detection of ethanol and $NO_2$, using ZnO, $SnO_2$, CNT nanonet thin films and CNT-ZnO hybrid materials.

## 1.9 Summary

This introductory chapter has outlined the basic materials, processes and applications in the area of semiconducting thin films, and in particular transparent conducting materials. The basic chemistry and physics behind the functioning of these materials has been given, and the relationships between the rudimentary structural composition, morphology and the electrical properties have been shown. Outlines of the deposition techniques have been illustrated, with focused discussion on chemical vapour deposition as an efficient versatile industrially scalable process.

The importance of this type of material as a fundamental component in modern electronics, anti-static coatings, solar cells, solid-state lighting and glazing, exemplifies the driving force which is pushing this technology to its limits. With the added impetus towards energy saving technology and the integral part played in solar cell renewable energy technology, the pace at which this field is advancing shows no sign of deceleration.

# 2 Doped Tin Oxide

## 2.1 Doped Tin Oxide Thin Films by AACVD and APCVD

*The following chapter describes the use of Aerosol Assisted Chemical Vapour Deposition (AACVD), and Atmospheric Pressure Chemical Vapour Deposition (APCVD), for the growth of doped tin oxide thin films. Dopants including: fluorine, antimony and bismuth, were incorporated into the host tin oxide matrix. The resultant films were analysed with a view to assessing their performance as transparent conducting oxides (TCOs), for application in energy saving glazing and as the transparent electrode in thin-film solar cells. It was found that the use of an aerosol delivery system enabled fluorine-doped tin oxide films to be formed with enhanced functional properties in terms of electrical resistance and surface morphology, compared to commercial standards.*

## 2.2 Introduction

Chapter one illustrated the pivotal role which transparent conducting oxides (TCOs) play in both energy capture and conservation. TCO materials display the combined properties of high optical transparency with a high electrical conductivity[78, 79], and as such can function as the transparent electrode in thin-film photovoltaics and as the blackbody reflector in low-E coatings. It was also shown that the electrical properties endowed upon these materials are critical to their performance in the aforementioned applications, and that due to band gap limitations and doping

bottlenecks, there is only a very narrow subsection of materials can function as TCO thin films. Two such commercially realised materials are tin-doped indium oxide (ITO) and fluorine-doped tin oxide (F:SnO$_2$), which have been incorporated into photovoltaic devices and low-$\varepsilon$-window glazings[54, 80] amongst many other transparent conductor applications.

The commercial demand for TCO materials has led to a large body of research into optimising the properties, and minimising the production cost of fluorine-doped tin oxide and ITO. The U.S. production, in 2006, of fluorine doped tin oxide films on glass was 29 million m$^2$, showing a 20% increase from 2005 (before this the growth was typically 6% or less year to year[81]). This rapid increase in production is a result of the rapid expansion of the thin film photovoltaic industry, where the use of fluorine doped tin oxide for photovoltaic applications has risen from an almost zero market share in the year 2000, to a 50% share in 2009. This industry is steering the move away from sputtering deposition techniques, and towards CVD and nanoparticle printing methodologies[82].

Due to the increasing scarcity of indium and the low resilience of ITO to the high temperatures required in photovoltaic manufacture, the cost benefits and properties of F:SnO$_2$ as an alternative TCO are becoming evident[83]. However, optimisation of the optical and electronic properties of TCOs to allow for tailoring to specific applications, are a key commercial challenge[84, 85].

The following chapter describes the experiments performed in order to investigate the use of Aerosol Assisted Chemical Vapour Deposition of doped tin oxide thin films as a low cost, scalable alternative to traditional commercial deposition techniques such as APCVD, dc/rf sputtering, sol-gel and spray pyrolysis [21, 81, 86, 87]. The current commercial production of F:SnO$_2$ thin films is heavily reliant on the use of APCVD, or spray pyrolysis, for large scale manufacture. APCVD gives a high performance product with exceptional electrical properties ($< 10$ Ω/□ sheet resistance), however controlling the morphology of the thin films for light scattering remains a key challenge. Spray pyrolysis is a highly cost effective technique: however, it is a technique which produces films of a lower electrical performance.

The following chapter demonstrates that AACVD is a route which produces thin films with the exceptional electrical characteristics of APCVD, the ease of spray pyrolysis, and a high level of control over film morphology and light scattering. This chapter shall also highlight the crucial role which droplet sizes plays in the AACVD deposition process, in order to control morphology and the physical characteristics of the resultant films. This is a significant finding, which can be applied to the AACVD process in more general terms[88-91], allowing for increased levels of manipulation during the growth process, resulting in further refined end products to meet the ever increasing demands of novel technologies.

## 2.3 Experimental

### 2.3.1 AACVD

Aerosol Assisted Chemical Vapour Deposition (AACVD) was accomplished using a horizontal-bed, quartz, cold-walled tubular carbon reactor with a laminar gas flow for the deposition of the precursor onto the substrate. The horizontal tubular reactor with a cross sectional area of 10 cm$^2$ was fitted with a top plate above the substrate to limit the longitudinal roll convection and provide a laminar gas/aerosol flow. A schematic of the reactor is shown in fig.2-1.
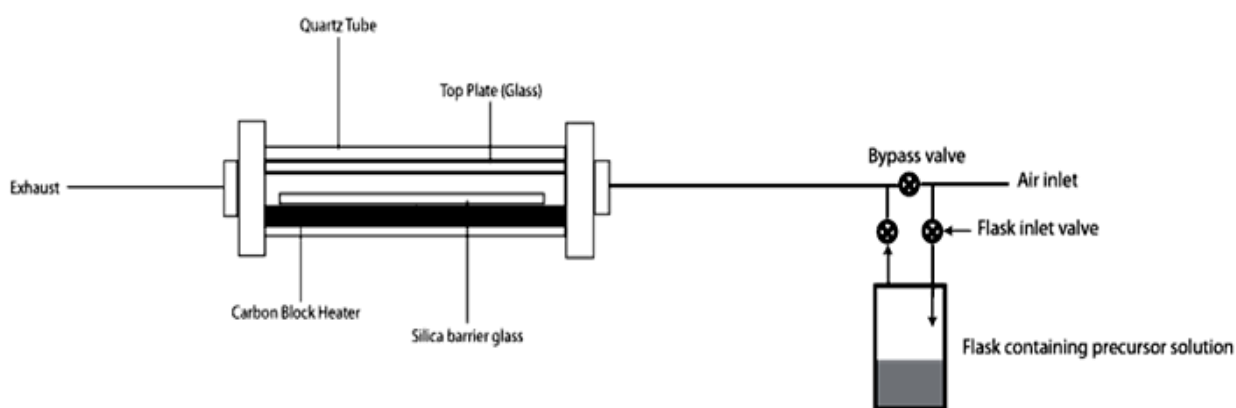


**Figure 2-1** Schematic of Aerosol Assisted Chemical Vapour Deposition rig used for the deposition of fluorine doped tin oxide. The aerosol source was changed to give either smaller (0.3 µm) or larger (45 µm) droplets of precursor.

The aerosol which was fed over the heated substrate in the reaction chamber was produced using two distinct techniques: collision type and ultrasonic generation. These two methods for aerosol droplet generation produce varying sizes of droplet and resulted in very different film characteristics.

### *Ultrasonic Aerosol Generation:*

The application of high frequency sound waves, known as ultrasonic generation, produces droplets where the size is related to the density and surface tension of the solvent as well as the operating frequency of the piezoelectric, and are related Lang's equation (eq.2-1) [92]:

**Equation 2-1**

$$D = 0.34(8\pi\sigma/\rho f^2)^{1/3}$$

Where: $\sigma$ is the surface tension, $\rho$ is the density, f is the operating frequency and d is the droplet diameter (m).

The droplet size produced using a standard humidifier (20 kHz) and methanol as the solvent, is 45 μm. The aerosol is then carried towards the reaction chamber using a plain flow of nitrogen gas (1 Lmin$^{-1}$). This technique, which produced relatively large aerosol droplets, shall be referred to from here on in, as ultrasonic-AACVD (u-AACVD).

### *Collison Aerosol Generation:*

In contrast to the ultrasonic technique, a Collison type atomizer was also used to generate an aerosol but of smaller droplet diameter. The precursor solution was delivered as an aerosol which was created using a TSI 3076 constant output Collison (name), collision (mode of operation) type atomizer, using compressed air as the carrier gas. This type of aerosol generator produces a constant droplet concentration of $10^7$/cm$^3$ and a mean droplet diameter of 0.3 μm [93]. These relatively small droplets have a higher surface area to volume ratio. This technique will be referred to as collision-AACVD (c-AACVD).

***Conditions:***

The aerosol solution used in both techniques was prepared using mono-butyl tin chloride (MBTC 10g) in methanol (200 ml). Addition of varying amounts of trifluoroacetic acid (TFA) served as the fluorine dopant source (0.0135 g, 0.03375 g, 0.0675g, 0.135g, 0.405 g, 0.675 g, gives 1:100, 2.5:100, 5:100, 10:100, 30:100 and 50:100 atomic ratio of fluorine : tin respectively) . Additional experiments were carried out using alternative dopants at 30:100 atomic ratio. The alternative cation dopants which were assessed included: antimony and bismuth. The antimony-fluorine co-doped system was also studied.

Pilkington barrier glass (25 nm layer of crystalline $SiO_2$ coated onto float glass) was used as the substrate material to prevent leaching of ionic impurities from the glass. These were cleaned using isopropyl alcohol (IPA) and acetone.

The substrate temperature was varied from 350-550°C along with the molar ratio of F/Sn from 0-50 at. % in the precursor solution. The deposition time was kept constant at 30 minutes. The substrate temperature and fluorine content were varied in order to optimise the process and form the highest quality films. Both ultrasonic and Collison type aerosol generation were tested under the different growth conditions.

## 2.3.2 APCVD

Atmospheric Pressure Chemical Vapour Deposition (APCVD) was also used as a deposition technique for $F:SnO_2$ thin films, in order to allow for comparison with the same precursor set: Monobutyl tin trichloride was used as the tin precursor, delivered by a heated bubbler (160°C). Aqueous tri-fluoroacetic acid was used as the fluorine source, delivered by a syringe driver through a heated evaporator (10 vol % acid, 200°C) with a plain flow of nitrogen carrier gas. A gas flow of ethyl acetate was used as the oxygen source (60°C). The deposition was performed in a similar carbon reactor as mention previously (2.3.1), with a barrier glass substrate, and over 350- 550°C. The flow rates and syringe driver speed were varied to optimize the deposition. A schematic of the rig is shown in fig.2-2.

Nitrogen In                              Nitrogen In     Nitrogen In

Syringe Driver
10vol.% TFA in
Water

Evaporator

Bubbler  1
(MBTC)

Bubbler 2 (ethyl
acetate)

Exhaust Line

Quartz Tube

Top Plate (Glass)

Exhaust

Mixing Chamber

Carbon Block Heater

Silica barrier glass
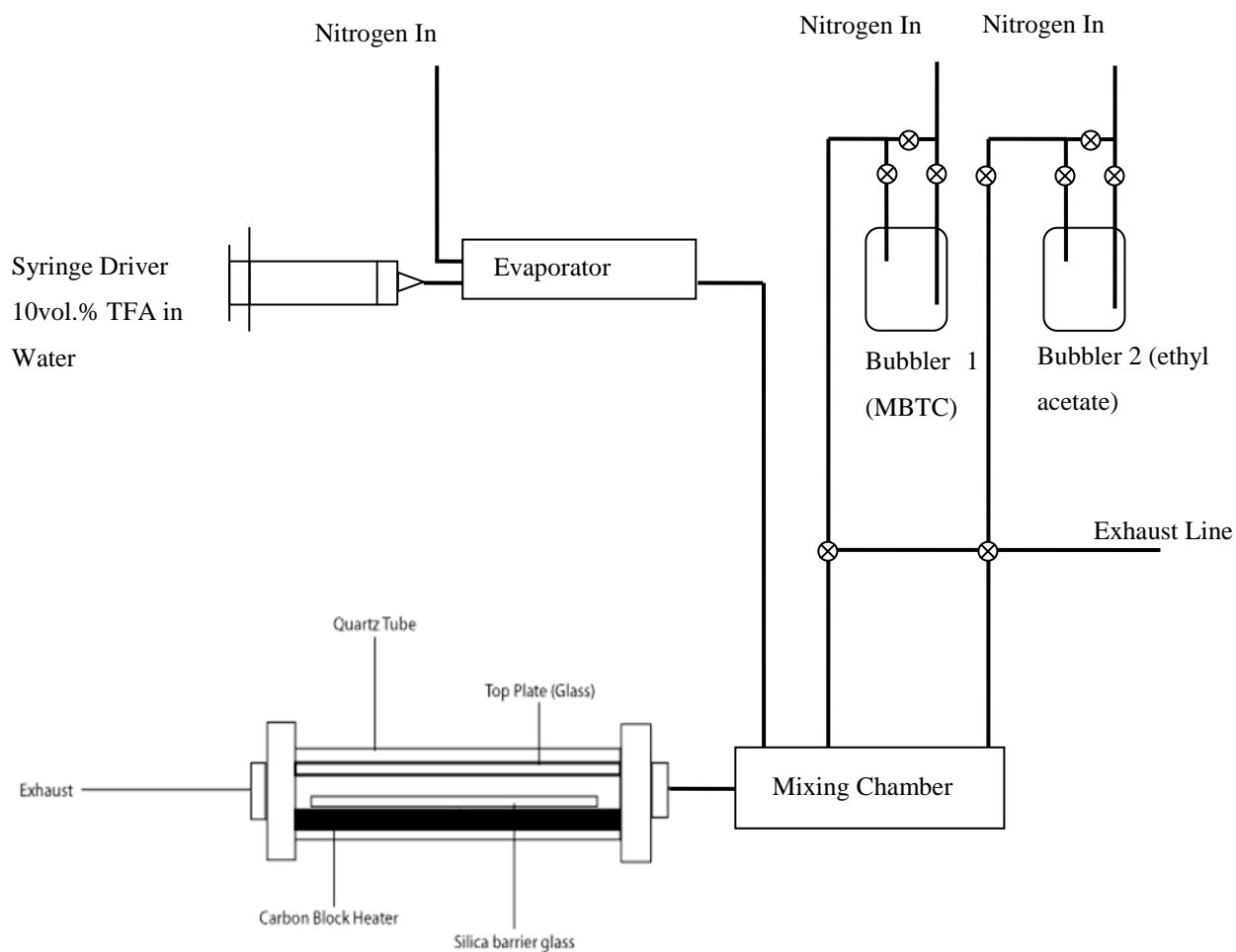
**Figure 2-2** Schematic diagram of the Atmospheric Pressure Chemical Vapour Deposition rig used for the
deposition of doped tin oxide thin films
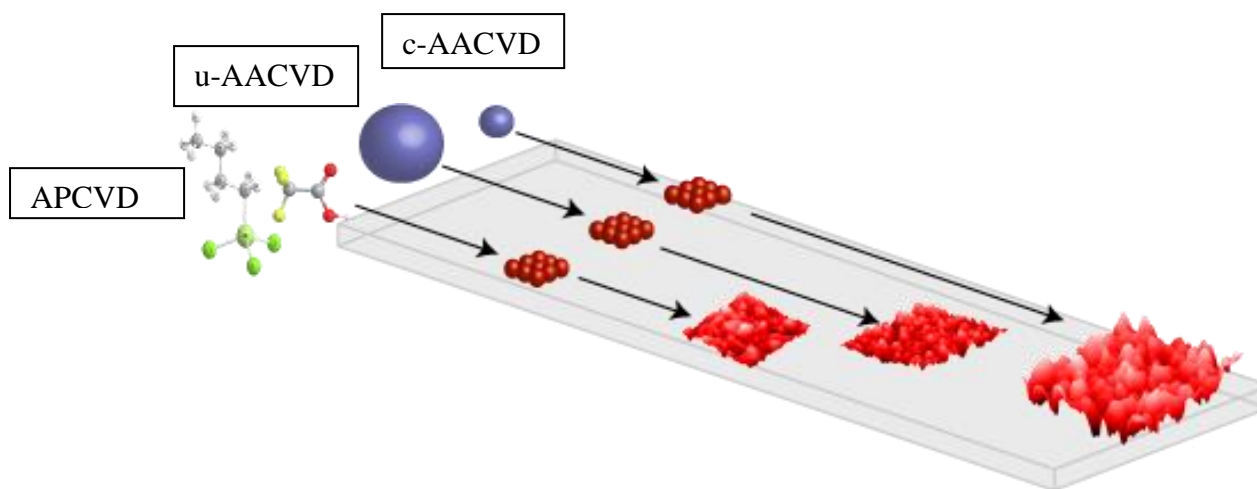
**Figure 2-3** Schematic of the different deposition processes, ranging from APCVD (left) which delivers the reagent to the heated substrate via a molecular gas, u-AACVD (middle) which delivers the reagent via a large aerosol droplet (~45 μm) and c-AACVD (right) which delivers the reagent species to the heated substrate for reaction via a small aerosol droplet (~0.3 μm). These varying delivery routes affect the growth modes and end properties of the resultant thin films.

## 2.4 Results and Discussion

### *Fluorine Doped Tin Oxide:*

F:SnO$_2$ films were produced over a range of deposition temperatures and concentrations of fluorine in the precursor solution, by using both a Collison type and an ultrasonic type AACVD system, from monobutyl tin trichloride and tri-fluoro acetic acid in methanol. Films were also produced using an APCVD thermal delivery method. These three techniques were chosen to highlight the changes in functional properties afforded by changing the state of the incoming precursor. APCVD uses a stream of molecular gas species reacting on the surface of the substrate for film formation. Whereas, AACVD utilises an incoming solution-based liquid droplet as the reacting species. We demonstrate that by controlling the aerosol, we can produce superior films to APCVD or sputter methods, by using a small droplet size (0.3 μm), generated by a Collison-type atomiser. As such the following work will focus on the high quality films produced by c-AACVD (small droplet 0.3 μm), and compare the results to the F:SnO$_2$

49

counterparts grown by u-AACVD (large droplet 45 μm), plus APCVD films deposited in our lab, and data recorded from leading APCVD commercial products.

### *Cation and Co-Doped Tin Oxide:*

The final section of this chapter will focus on the role of chlorine incorporation from the MBTC precursor and the incorporation of cation dopants into the tin oxide matrix. The alternative cation dopants assessed, included: antimony, bismuth, and the antimony-fluorine co-doped system.

## 2.4.1 AACVD of fluorine-doped tin oxide thin films

A range of $F:SnO_2$ films were produced, all showing high optical transparency and film growth rates were between 5-15 nm/min. The films were completely free from pin-hole defects, indicating that the deposition process did not produce powdery deposits caused by large scale gas-phase nucleation. The films showed good adhesion to the glass substrate passing both the Scotch tape test and steel scalpel scratch test: this is somewhat unusual for AACVD derived films which can tend to be particulate in nature from extensive gas phase reaction [21, 94]. Further, it indicates that the films are likely to be growing from finely attached nucleation points at the surface. Solubility testing of the films was carried out in organic solvent (ethanol and toluene) and under basic conditions (2M NaOH) and acidic conditions (2M HCl). The presence of the film, on the substrate surface, was monitored using electrical resistance measurements, which showed the films suspended in the organic solvents, acid and base showed no change after a period of three months. The films were indefinitely stable in air for over six months, showing no change in optical or electrical properties. Film thickness measurements by side-on scanning electron microscopy gave a depth range of 200 nm up to 500 nm depending on the deposition conditions. Both c-AACVD and u-AACVD gave transparent conducting thin films of $F:SnO_2$ which produced repeatable properties, including electrical resistance measurements. Collison-AACVD produced films with a repeatable sheet resistance of 7-8 Ω/□, whilst the ultrasonic-AACVD process gave films with repeatable values of 90 Ω/□.

## 2.4.2 XRD Analysis

### *Collison-AACVD XRD analysis:*

X-ray diffraction patterns of the Collison-AACVD, as-deposited, $F:SnO_2$ films at substrate temperatures ranging from 400-550°C are presented in fig.2-4. The films obtained, were mostly amorphous when deposited at 350°C, and polycrystalline in nature at higher deposition temperatures. Furthermore, they showed increasing crystallinity with respect to deposition temperature. The diffraction patterns all correspond to the cassiterite structure of tin oxide ($SnO_2$).

**Lattice Parameters:**

The lattice parameters were computed by implementing a Le Bail refinement, using GSAS. The lattice parameters *a* and *c* varied from 4.74-4.75 Å and 3.17-3.21 Å, depending on deposition conditions (see table 2-1). These lattice parameters are in good agreement with those of stoichiometric tin oxide powder which has a tetragonal rutile structure and crystallises in the space group, $P4_2/mnm$ [79]. The lattice parameters are *a* = *b* = 4.74 Å and *c* = 3.19 Å.

Fluorine doped tin oxide is known to have fluorine incorporated by substitution of oxygen because of the similarities of the ionic radii ($F^-$: 1.17 Å, $O^{2-}$: 1.22 Å), this results in free electrons which populate the conduction band. However, as previously reported using laboratory XRD equipment, no constriction of the lattice parameters due to incorporation of fluorine into the unit cell is observed because of the low concentration in the films.

51
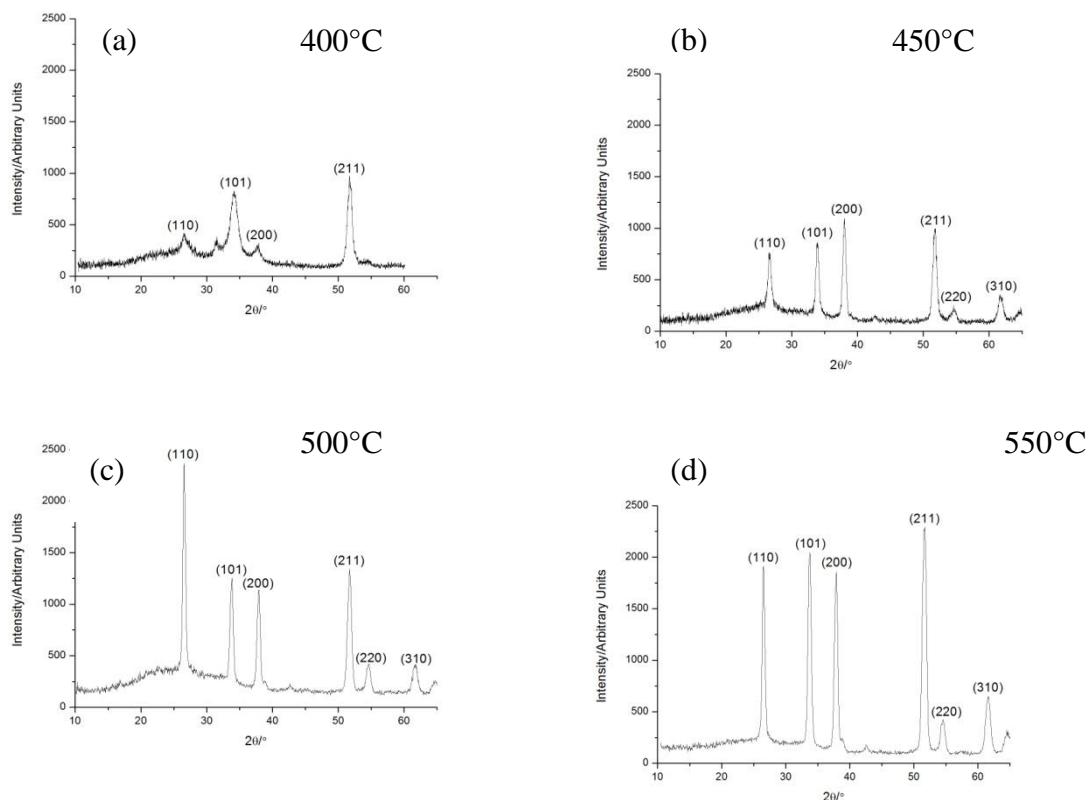
**Figure 2-4** XRD patterns of F:SnO$_2$ (Precursor solution: 30:100 atomic ratio F:Sn. In a solution of monobutyl tin trichloride in methanol solvent) deposited at substrate temperatures (a) 400°C, (b) 450°C, (c) 500°C and (d) 550°C using c-AACVD.

| T (°C) | a (Å) | c (Å) | Unit cell volume (Å$^3$) |
|--------|-------|-------|--------------------------|
| **400** | 4.75 | 3.17 | 71.4 |
| **450** | 4.74 | 3.19 | 71.4 |
| **500** | 4.74 | 3.2 | 71.8 |
| **550** | 4.74 | 3.21 | 72.1 |

**Table 2-1** Variation in crystallite diameter and unit cell parameters of the F:SnO$_2$ with changing deposition temperature deposited by c-AACVD (aerosol droplet size of 0.3 µm), determined by XRD analysis using the Scherrer equation and Le Bail refinement[95].

**Crystallite Size:**

The crystallite size was determined using the Scherrer equation:

**Equation 2-2**

$$t = \frac{0.9\lambda}{\sqrt{B_M^2 - B_S^2}\ \cos\theta}$$

Where: t is the crystallite thickness, $\lambda$ the X-ray wavelength, $\theta$ the Bragg angle (half the measured diffraction angle) and $B_M$ and $B_S$ are the width in radians of the diffraction peaks of the sample and a standard at half height. The standard sample used was a 25 cm$^2$ alumina flat plate obtained from the National Institute of Standards and Technology (NIST) with peak intensities given by NIST and peak positions by the ICDD.

It was seen that the crystallite size increased with deposition temperature. This is attributed to the greater mobility of incoming reactants and surface diffusion which results in larger crystallites.

| T (°C) | Crystallite Diameter (nm) | a (Å) | c (Å) | Unit cell volume (Å$^3$) |
|--------|---------------------------|-------|-------|--------------------------|
| **400** | 10 | 4.75 | 3.17 | 71.4 |
| **450** | 24 | 4.74 | 3.19 | 71.4 |
| **500** | 28 | 4.74 | 3.20 | 71.8 |
| **550** | 26 | 4.74 | 3.21 | 72.1 |

**Table 2-2** Variation in crystallite diameter and unit cell parameters of the F:SnO$_2$ with deposition changing deposition temperature, determined by XRD analysis using the Scherrer equation and Le Bail refinement[95].

**Preferred Crystal Plane Orientation:**

The degree of preferred orientation of the Bragg crystal plane with respect to the substrate surface was determined using the texture coefficient. This analysis is important in transparent conducting thin film materials because it is the dominant crystal plane (as seen in the XRD spectra) which is responsible for the conduction of electrons across the film surface.

The reflections analysed were the (110), (101), (200) and (211). The degree of preferred orientation was determined from the texture coefficient (TC) from the following equation [96]:

**Equation 2-3**

$$TC(hkl) = \frac{I(hkl)/I_0(hkl)}{\frac{1}{N}\sum_N I(hkl)/I_0(hkl)}$$

Where: TC is the texture coefficient of a given (hkl) plane, I is the measured relative intensity, $I_0$ is the standard relative intensity of the corresponding powder pattern [97] and N is the number of reflections. A deviation from unity correlates to a higher degree of preferred orientation of the film.

| Collison-AACVD F:SnO$_2$ Film Deposited at 400°C | | | | | |
|---|---|---|---|---|---|
| **hkl** | Bragg Angle $2\theta/°$ | I | $I_0$ | $I/I_0$ | TC (hkl) |
| **110** | 26.7 | 16.7 | 100 | 0.17 | 0.22 |
| **101** | 34.1 | 69.2 | 79.8 | 0.87 | 1.12 |
| **200** | 37.6 | 11.6 | 22.6 | 0.51 | 0.66 |
| **211** | 51.7 | 100 | 64.9 | 1.54 | 2.00 |

**Table 2-3** Bragg crystal planes and corresponding XRD reflection angles for tin oxide, where: I indicates the experimental reflection intensity of our thin films deposited at different temperatures. $I_0$ indicates standard intensities from powder diffraction. TC is the texture co-efficient describing preferred orientation.

| **Collison-AACVD F:SnO$_2$ Film Deposited at 450°C** |
|---|---|---|---|---|---|
| **hkl** | Bragg Angle 2θ/° | I | I$_0$ | I/I$_0$ | TC (hkl) |
| **110** | 26.6 | 52.5 | 100 | 0.52 | 0.29 |
| **101** | 33.9 | 75.4 | 79.82 | 0.94 | 0.52 |
| **200** | 38.0 | 100 | 22.62 | 4.42 | 2.41 |
| **211** | 51.6 | 93.7 | 64.91 | 1.44 | 0.79 |

| **Collison-AACVD F:SnO$_2$ Film Deposited at 500°C** |
|---|---|---|---|---|---|
| **hkl** | Bragg Angle 2θ/° | I | I$_0$ | I/I$_0$ | TC (hkl) |
| **110** | 26.6 | 100 | 100 | 1 | 0.88 |
| **101** | 33.8 | 47.8 | 79.8 | 0.60 | 0.53 |
| **200** | 37.9 | 46.3 | 22.6 | 2.05 | 1.80 |
| **211** | 51.7 | 58.2 | 64.9 | 0.90 | 0.79 |

| **Collison-AACVD F:SnO$_2$ Film Deposited at 550°C** |
|---|---|---|---|---|---|
| **hkl** | Bragg Angle 2θ/° | I | I$_0$ | I/I$_0$ | TC (hkl) |
| **110** | 26.5 | 74.8 | 100 | 0.75 | 0.45 |
| **101** | 33.7 | 84.1 | 79.8 | 1.05 | 0.63 |
| **200** | 37.9 | 74.8 | 22.6 | 3.31 | 1.99 |
| **211** | 51.6 | 100 | 64.9 | 1.54 | 0.93 |

**Tables 2-3 cont.** Bragg crystal planes and corresponding XRD reflection angles for tin oxide, where: I indicates the experimental reflection intensity of our thin films deposited at different temperatures. I$_0$ indicates standard intensities from powder diffraction. TC is the texture co-efficient describing preferred orientation.
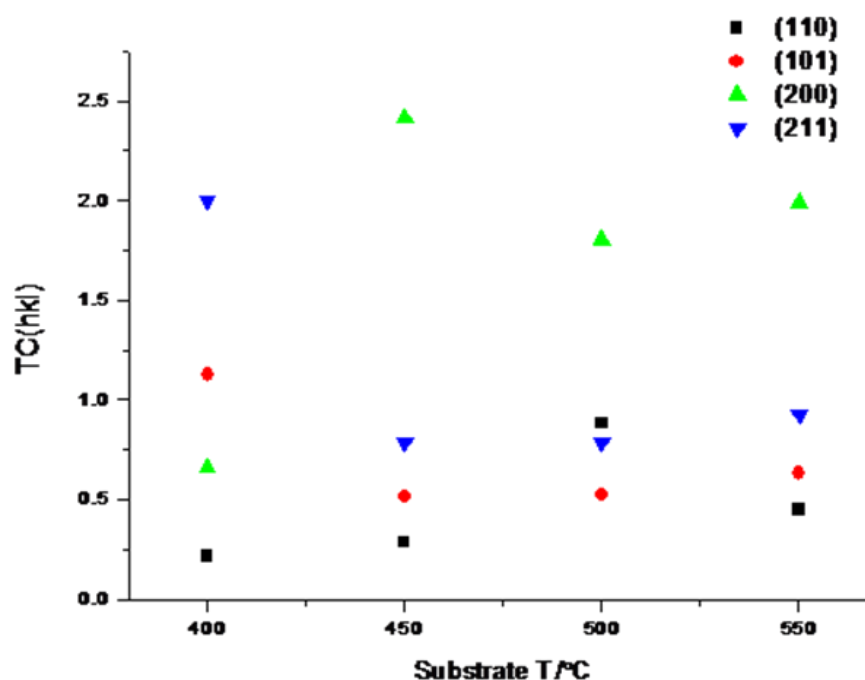
**Figure 2-5** Variation of the Texture Coefficient (TC) with different temperatures of F:SnO$_2$ deposition using c-AACVD (30:100 molar ratio F:Sn content in the precursor solution).

The preferred orientation planes in doped tin oxide films have been reported to correspond to the (121), (112), (110), (200) or (301) depending on the substrate temperature, film thickness and dopant concentration [98]. Afify et al. and Agashe et al. reported that the (200) plane is particularly sensitive to substrate temperature which controls the growth of the films [99, 100]. Belanger et al. prepared FTO films by CVD and observed that, in films with a thickness of c.a. 0.4 μm, the dominant planes were found to be the (200), (400), (301) and (211)[101]. Belanger et al. also found that deep trap levels of grain boundaries surfaces are mostly associated with the (110), (211) and (301) orientations and not with the (200) plane [101].

The diffraction patterns show that at lower temperature there is an initial broad feature in the diffraction pattern at low 2θ, this is attributed to the glass substrate. The (211) plane was found to be the most intense reflection at a substrate temperature of 400°C, with a calculated TC (211) of 2.00, showing that the crystallites are preferentially oriented with respect to this plane at the lower temperature. The TC (200) calculated at a substrate temperature of 400°C was found to be 0.66, more closely related to that of the randomly oriented powder pattern. As the substrate temperature increases the TC (211) decreases to near unity and represents that of the bulk powder. From the above results it can be seen that the films produced by c-AACVD above 400°C exhibited (200) as the preferred crystal plane orientation. This agrees with the results of Afify et al.[99] and Agashe et al.[100] who demonstrated a similar temperature sensitivity of the crystal planes. The 200 orientation, demonstrated to be prevalent at the higher temperatures, is predicted to have no deep lying trap levels at grain boundary surfaces correlating to a higher degree of conductivity across the substrate plane [101].

### *Ultrasonic-AACVD XRD analysis:*

XRD analysis was also performed on the ultrasonic-AACVD F:SnO$_2$ thin films. The lattice parameter analysis and reflection pattern again indicated the presence of the cassiterite structure of tin oxide (SnO$_2$) in the space group P42/*mnm* 2.

Comparison of the XRD from the Collison-AACVD with the results given for the ultrasonic-AACVD (Fig.2-5 and Table 2-4), using the texture co-efficient, shows an even greater preferred orientation of the (200) crystal plane. This could indicate the level of surface diffusion compared to gas phase nucleation varies between the two techniques. The collision-type AACVD produces smaller aerosol droplets, with a greater surface area to volume ratio. This larger ratio will increase the curvature of the surface, thus reducing the nearest neighbor interactions between solvent molecules and proportionally exposing more solvent molecules to the gas phase, facilitating the ease of vaporisation. Increased solvent vaporisation means more thermally induced reaction before the droplets reach the surface; thus introducing more random orientation into the

forming film. Whereas, the ultrasonic-AACVD droplets contain a larger bulk core which delivers more precursor onto the substrate surface without pre-reaction; thus increasing the amount of surface diffusion taking place, which is responsible for the preferred orientation of the film with respect the substrate.
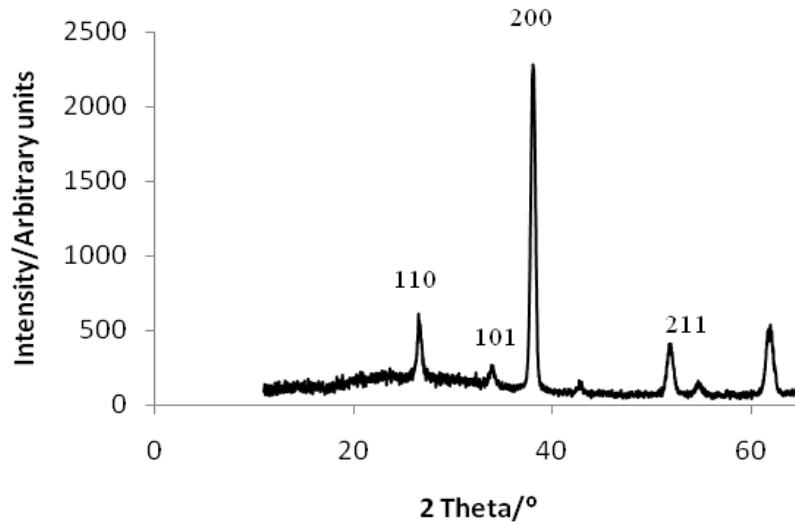


**Figure 2-5** XRD pattern of F:SnO$_2$ (Precursor solution: 30:100 atomic ratio F:Sn. In a solution of monobutyl tin trichloride in methanol solvent) deposited at substrate temperature of 500°C using u-AACVD.

| Ultrasonic-AACVD F:SnO$_2$ Film Deposited at 500°C | | | | | |
|---|---|---|---|---|---|
| **hkl** | Bragg Angle 2θ/° | I | I$_0$ | I/I$_0$ | TC (hkl) |
| **110** | 26.5 | 25.9 | 100 | 0.26 | 0.19 |
| **101** | 33.7 | 11.1 | 79.8 | 0.14 | 0.1 |
| **200** | 37.9 | 100 | 22.6 | 4.44 | 3.22 |
| **211** | 51.6 | 43.3 | 64.9 | 0.67 | 0.49 |

**Table 2-4** Bragg crystal planes and corresponding XRD reflection angles for tin oxide, where: I indicates the experimental reflection intensity of our thin films deposited at different temperatures. I$_0$ indicates standard intensities from powder diffraction. TC is the texture co-efficient describing preferred orientation.

## 2.4.3 Film Morphology

Scanning Electron Microscopy (SEM) was used to study the surface morphology of the F:SnO$_2$ thin films deposited by c-AACVD and u-AACVD.

### Collison-AACVD Morphology:

Films deposited at 350°C by collision-AACVD showed no surface structure due to the low crystallinity of the tin oxide matrix which was evident in the XRD pattern data[102]. Fig.2-6 shows the films deposited by c-AACVD, between 400°C - 550°C (30:100 atomic ratio of F to Sn in the precursor solution), demonstrate a surface structure composed of octahedral particles. The octahedral particles increase in size with the deposition temperature from ca. 100 nm, to 300 nm in diameter. This size increase follows the trend given by the crystallite size from the XRD patterns, however, the particles seen are much larger agglomerations of the crystallites. The film grown at 550°C shows formation of discrete octahedral particles.
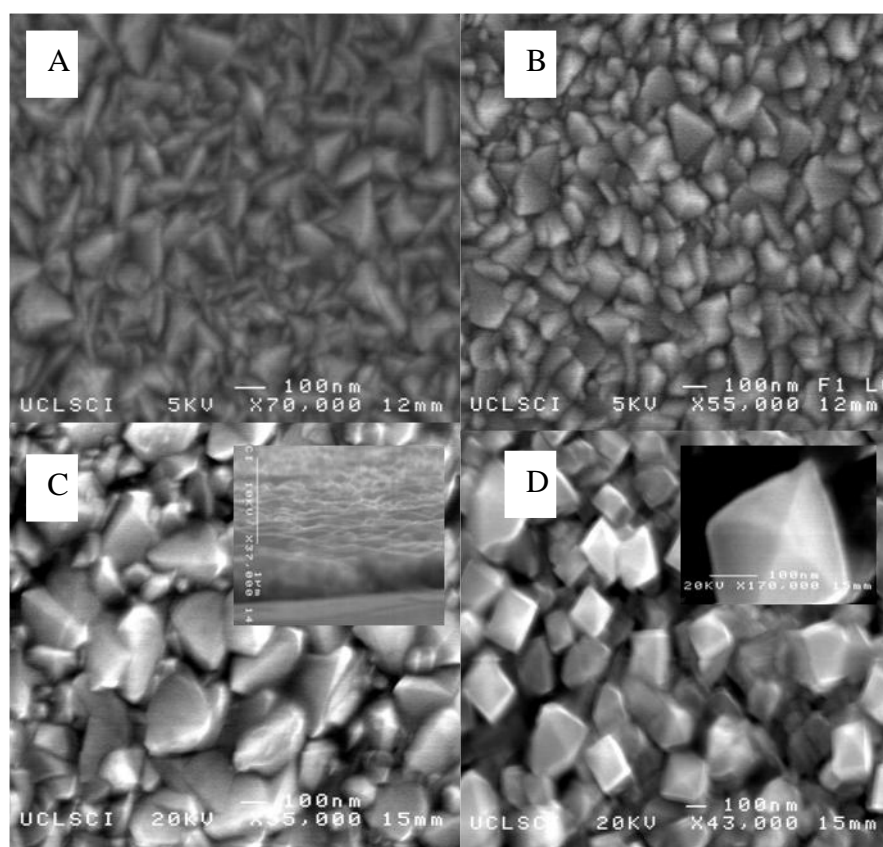


**Figure 2-6** SEM images of F:SnO$_2$ deposited by c-AACVD using a Collison type atomiser ( 0.3 µm droplet size) and a precursor solution containing 30:100 atomic ratio F:Sn, in a monobutyl tin trichloride methanoic solution at (a) 400°C, (b) 450°C (inset shows side on image) (c) 500°C and (d) 550°C (inset shows close up particle).

### *Ultrasonic-AACVD Morphology Analysis:*

Fig.2-7 shows SEM images of F:SnO$_2$ films deposited using u-AACVD (employing an ultrasonic humidifier to generate the aerosol). The film morphologies show a marked difference compared to those shown for the Collison-AACVD method (Collison atomizer). The particle shape, coverage, and roughness all vary in comparison to the Collison aerosol method. The ultrasonic aerosol generates a surface structure with more rounded particles that, for each comparable temperature, have a smaller diameter than those produced by the Collison method. Films formed at 500°C via u-AACVD have a diameter of ~ 100 nm, rather than ~ 200 nm of those formed by c-AACVD. The images shown in fig.2-7 (deposited at 500°C) would suggest a looser packed structure than that seen for comparable films produced by c-AACVD. This would suggest the rate of incoming flux of precursor or aerosol droplet size between the two methods is causing a change in the type of growth seen in the film.

The growth type of the forming film is controlled by the surface diffusion and nucleation processes taking place during the reaction. These processes are, in turn, controlled by the temperature, pressure, and aerosol/gas phase composition[26]. Comparison of the two methods at 500°C and at atmospheric pressure, allows the identification of the cause of changing growth characteristics. It can be attributed to the composition of the incoming precursor, which varies according to aerosol droplet size. Both films seem to display a Volmer-Weber type island growth, where small clusters of tin oxide are nucleated onto the glass surface. These clusters then grow into islands, which coalesce into a continuous film. This growth mode demonstrates that the constituent atoms of the film are more strongly bound to each other than they are to the substrate, it is also noted as a feature of AACVD caused by partial pre-reaction of the precursor in the gas phase. The larger aerosol droplets used in the u-AACVD experiments showed a higher crystal orientation with respect to the substrate (XRD data), this suggests an increased level of surface diffusion allowing the crystal planes to reach the lower energy configuration. However, as the incoming droplets are approximately 150x larger than those of c-AACVD, the extent of nucleation on the surface is more localized (to where the droplets land), leading to a looser packing of the

growth islands. The film formed in the c-AACVD has a higher degree of gas phase nucleation and a lower preferred orientation. However, the smaller particles allow a more dispersed nucleation of the surface leading to a more tightly packed film.
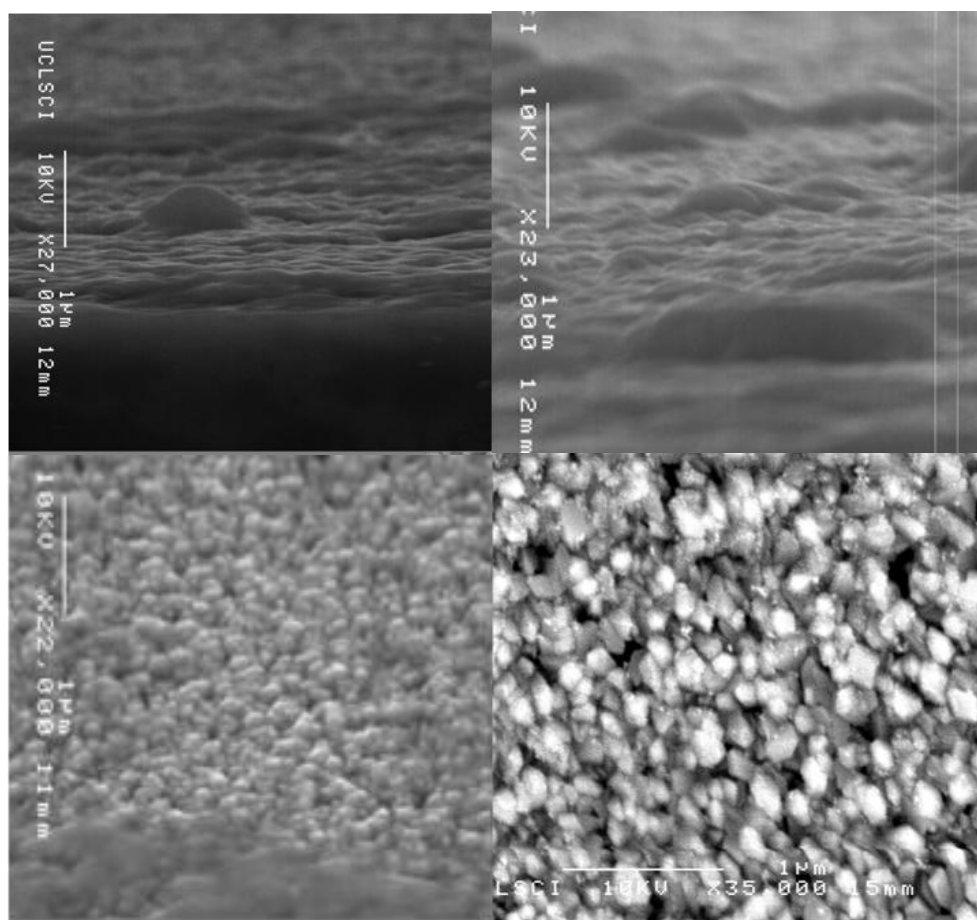


**Figure 2-7** SEM images of F:SnO$_2$ from a precursor solution containing 30:100 atomic ratio F to Sn, in a monobutyl tin trichloride methanoic solution deposited by u-AACVD (ultrasonic piezoelectric generator 45 µm droplet size) at 500°C (a) side on image and (b) side on-image. (c) tilt image 30° (d) Top down image

## 2.4.4 APCVD of fluorine-doped tin oxide thin films

A range of F:SnO$_2$ thin films were produced using thermal APCVD. The films showed high optical transparency and film growth rates were between 1-2 μm.min$^{-1}$. The films showed good adhesion to the glass substrate passing both the Scotch tape test and steel scalpel scratch test. Solubility testing of the films was carried out in organic solvent (ethanol and toluene), under basic conditions (2M NaOH), and under acidic conditions (2M HCl), where the presence of the film on the substrate surface was monitored using electrical resistance measurements. The testing showed the films suspended in the organic solvents, acid, and base did not change after a period of three months. The films were indefinitely stable in air for over six months, showing no change in optical or electrical properties.

Monobutyl tin trichloride, ethyl acetate and trifluoroacetic acid (5-10 vol% in water) were used as the precursors, the set-up is shown in fig.2-2. Flow rates, temperatures and syringe injection speeds were varied to produce the optimum films, the variable conditions are shown in Table 2-5, where the nitrogen flow through the evaporator for the syringe injector was kept constant at 1 Lmin$^{-1}$ nitrogen.

| Substrate Temperature °C | Deposition Time Seconds | Nitrogen flow through MBTC bubbler Lmin$^{-1}$ (temperature of bubbler °C) | Nitrogen flow through ethyl acetate bubbler Lmin$^{-1}$ (temperature of bubbler °C) | Syringe injection speed of TFA ml.min$^{-1}$ (vol.% of TFA in water) | Minimum Sheet Resistance of F:SnO$_2$ film Ω/□ . |
|---|---|---|---|---|---|
| 500°C | 60 | 0.5 (165°C) | 3 (50°C) | 5 (5vol.%) | 250 |
| 500°C | 60 | 1(165°C) | 3 (50°C) | 4 (10 vol.%) | 40 |
| 500°C | 60 | 1(165°C) | 3 (50°C) | 5 (5 vol.%) | 250 |
| 500°C | 60 | 1(165°C) | 3 (50°C) | none | 300 |
| 500°C | 60 | 1(165°C) | 3 (130°C) | none | 1000 |
| 500°C | 60 | 1(165°C) | 3 (70°C) | 2 (10vol.%) | 450 |
| 500°C | 60 | 0.5(165°C) | 3 (70°C) | 0.5(10vol.%) | 10 |
| 500°C | 30 | 0.5(165°C) | 3 (70°C) | 0.5(10vol.%) | 10 |
| 500°C | 10 | 0.5(165°C) | 3 (70°C) | 0.5 (10vol.%) | 10 |

**Table 2-5** Table of conditions used in the APCVD of fluorine doped tin oxide thin films. MBTC refers to Monobutyle tin trichloride, TFA refers to tri-fluoro acetic acid. The set-up of the rig used can be seen in figure 2-2.

The resultant films were appraised according to the sheet resistance of the surface. It was found that longer runs resulted in delamination of the films as they became very thick, so the deposition time was reduced. Resistance values showed no discernable trends and indicated the process was very inconsistent in terms of the electrical conductivity of the films produced.

The following conditions were selected as optimum and taken forward for further analysis: 500°C, 10 second deposition time, 0.5 Lmin$^{-1}$ nitrogen through the MBTC bubbler at 165°C, 3 Lmin$^{-1}$ nitrogen through the ethyl acetate bubbler at 70°C, 0.5 ml.min$^{-1}$ syringe injection of TFA solution (10 vol.%) with 1 Lmin$^{-1}$ nitrogen through the evaporator.

The molar flow can therefore be calculated for each bubbler using the following equation[103]:

**Equation 2-4**

$$F_p = \frac{f_c \times P_p}{22.4(760 - P_p)}$$

Where: $F_p$ is the precursor molar flow (moles min⁻¹), $f_c$ is the carrier gas flow rate (L.min⁻¹), $P_p$ is the vapour pressure of the precursor at a specific temperature (mmHg (Torr)) . The equation assumes atmospheric pressure operation (760 Torr) and a room temperature carrier gas flow through the flow meter (where 1 mole occupies 22.4 litres). It also assumes an ideal mixture of ideal gases, such that $\frac{N_p}{N_c} = \frac{P_p}{P_c}$ where N is the number of moles.

| Precursor | Molar Flow Rate (mmol.min⁻¹) | Precursor ratio | Atomic ratio of Sn, O and F |
|---|---|---|---|
| **Monobutyl tin trichloride** | 4.2 | 6.5 | 2.15 |
| **Ethyl acetate** | 149 | 229 | 76 |
| **Tri-fluoro acetic acid** | 0.65 | 1 | 1 |

**Table 2-5** Calculated molar flow rates and ratio's of reactants under optimised reaction conditions for the APCVD of fluorine doped tin oxide thin films using Monobutyl tin trichloride bubbler (165°C, 0.5 Lmin⁻¹). Aqueous trifluoroacetic acid via a syringe driver (0.5 ml.min⁻¹, 10 vol %), ethyl acetate bubbler (70°C, 3 Lmin⁻¹) and a plain flow of nitrogen carrier gas at 1 L.min⁻¹. Ethyle acetate is assume to relinquish only 1 oxygen atom per molecule (oxygen is in excess).

The optimised conditions for film deposition were taken forward and multiple repeats (10 repeats) were done to assess the repeatability of the electrical conductivity. Although the physical properties of the tin oxide showed a good repeatability in terms of transparency, adhesion, and rate of deposition, the electrical properties gave a large variance. The measurements showed sheet resistance values from 10 $\Omega/\square$ up to 250 $\Omega/\square$ using exactly the same APCVD conditions. As such, XRD and morphology analysis were performed on our samples, but, the electrical and optical comparisons of AACVD and APCVD shown later in the chapter were done using Pilkington-NSG TEC glasses (Commercial fluorine-doped tin oxide thin films on glass substrates deposited by APCVD), so that the novel AACVD films could be compared with a leading industry product.

## 2.4.5 XRD Analysis

Fig.2-8 shows an example X-ray diffraction pattern of the as-deposited APCVD F:SnO$_2$ films at a substrate temperature of 500°C. The resultant films showed diffraction patterns corresponding to the cassiterite structure of tin oxide (SnO$_2$) which has a tetragonal rutile structure and crystallises in the space group, P4$_2$/*mnm* [79].
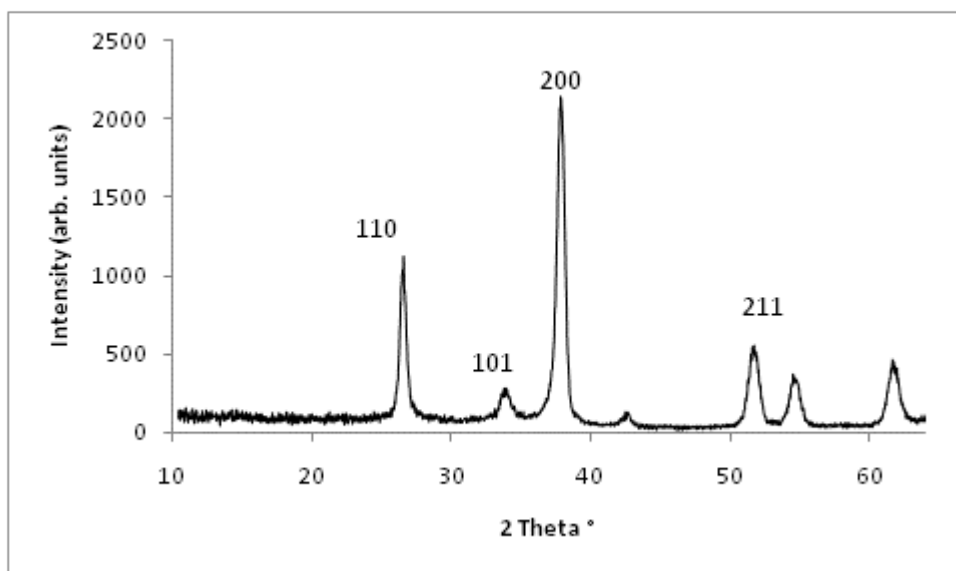


**Figure 2-8** XRD pattern of F:SnO$_2$ thin film (Precursor set: MBTC, ethyl acetate and TFA aqueous solution) deposited at substrate temperature of 500°C using thermal APCVD.

| APCVD F:SnO$_2$ Film Deposited at 500°C | | | | | |
|---|---|---|---|---|---|
| **hkl** | Bragg Angle 2θ/° | I | I$_0$ | I/I$_0$ | TC (hkl) |
| **110** | 26.5 | 52.6 | 100 | 0.53 | 0.38 |
| **101** | 33.7 | 13.3 | 79.8 | 0.17 | 0.12 |
| **200** | 37.9 | 100 | 22.6 | 4.42 | 3.21 |
| **211** | 51.6 | 25.6 | 64.9 | 0.39 | 0.29 |

**Table 2-6** Bragg crystal planes and corresponding XRD reflection angles for tin oxide. Where: I indicates the experimental reflection intensity of our thin films deposited at different temperatures. I$_0$ indicates standard intensities from powder diffraction. TC is the texture co-efficient describing preferred orientation.

The XRD results demonstrate c-AACVD, u-AACVD and APCVD, under the conditions outlined, produce Casserite structured SnO$_2$. However, the level of preferred crystal plane orientation with each of the methods was shown to be variable. Each technique shows that at the higher temperatures it is the [200] plane which dominates, however the APCVD and u-AACVD routes seem to result in a higher degree of surface diffusion at 500°C, which results in texture co-efficient values of 3.21 and 3.22 respectively, this is in contrast to the 1.80 value shown for c-AACVD at 500°C.

The crystallite size was also calculated for both the APCVD and ultrasonic-AACVD films produced at 500°C using the Scherrer equation, this gave values of 34 nm and 44 nm respectively. Both these values show a larger crystallite sizes to that of the 28 nm given by the Collison-AACVD film at 500°C, again this indicates a greater level of surface reaction leading to larger crystal regions in the polycrystalline films.

## 2.4.6 Film Morphology

Fig.2-9 shows SEM images of $F:SnO_2$ films deposited using APCVD. The film morphologies show a marked difference compared to those shown for the Collison-AACVD method (Collison atomizer) and u-AACVD (ultrasonic aerosol). The particle shape, coverage and roughness all vary in comparison to both aerosol methods. Collison-AACVD produced octahedral particles, u-AACVD produced rounded particles, where-as APCVD is shown (fig.2-9) to produce more randomly shaped particles with a size of approximately 100-200 nm. The images given in fig.2-9, deposited at 500°C, show a densely packed structure.

APCVD utilizes a gas phase flux of incoming precursor as opposed to the aerosol droplet of the other techniques. This difference presumably results in a high degree of nucleation of the substrate surface, which could explain the smaller crystallite sizes seen compared to the more sparsely nucleated u-AACVD. The gas phase precursor also clearly results in a very tightly packed and dense film structure.
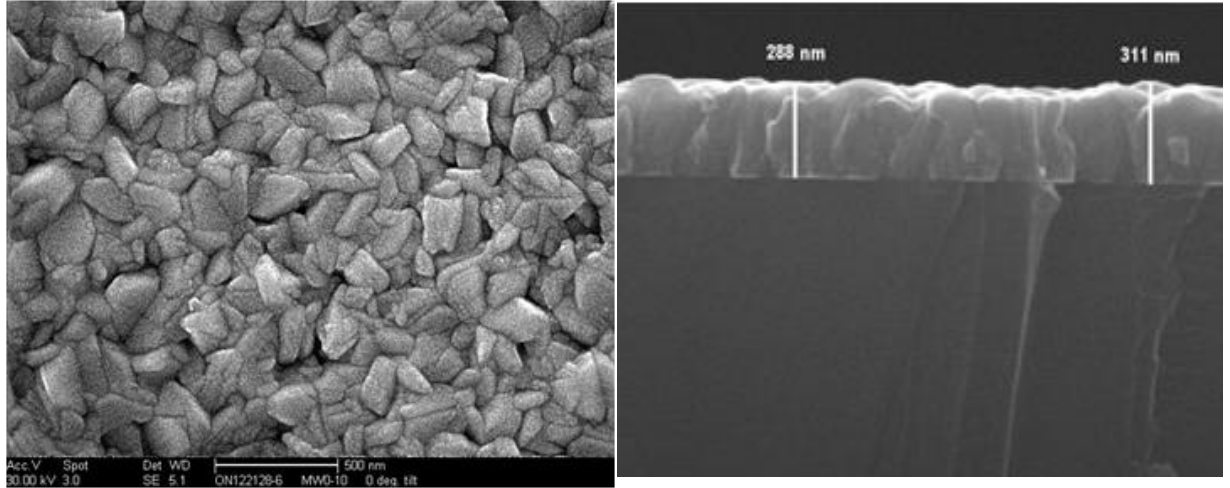


**Figure 2-9** SEM image of $F:SnO_2$ thin film (Precursor set: MBTC, ethyl acetate and TFA aqueous solution) deposited at substrate temperature of 500°C using thermal APCVD. Left) Top-Down.    Right) Side-on

## 2.4.7 Electrical Properties

Electrical testing was done to assess the electrical performance of the best films produced from each deposition technique. Sheet resistance measurements were recorded using a linear four point probe. Hall Effect measurements were done using the Van der Pauw technique in order to determine the dominant charge carrier type, charge carrier mobility and charge carrier concentration.

Each technique produced fluorine-doped tin oxide thin films which exhibited n-type conductivity as determined using the Van der Pauw technique. The ultrasonic aerosol gave a minimum sheet resistance of 90 $\Omega/\square$ and the APCVD gave a minimum sheet resistance of 10 $\Omega/\square$. The c-AACVD process gave a minimum stable sheet resistance of 7 $\Omega/\square$. Directly after deposition by c-AACVD the films displayed a sheet resistance as low as 2-3 $\Omega/\square$, however over a 72 hour time period the resistance increased to 7 $\Omega/\square$ and remained at this level indefinitely. This change has been attributed to the filling of intrinsic oxygen vacancies present in the as-deposited film[104].

The incorporation of fluorine is well known to enhance the conductivity of $SnO_2$. Extrinsic doping of fluorine in $SnO_2$ causes net-oxygen substoichiometry, whereby the fluorine atoms replace oxygen atoms, in the oxygen sites of the tin oxide structure. This doping causes the formation of $F^{1-}$ sites in the place of $O^{2-}$ sites leading to charge compensation, which forces the formation of Sn(II) from Sn(IV)[104]. This leads to filled donar states near the conduction band of $SnO_2$, resulting in an n-type conductor material that maintains a band gap with a greater energy than visible light. However, it should be noted that studies have shown that excessive fluorine incorporation can decrease conductivity: work done by Ramaiah et al. reported that the conductivity of heavily doped samples, where (F/Sn atomic ratio > 0.15) led to a decrease in film conductivity[105].

The effect of deposition temperature on the carrier density, mobility and resistivity is very significant. It has been reported that the resistivity decreases with increasing temperature of deposition up to a minimum resistivity value. Further increasing the deposition temperature past this point, results in an increase in resistivity.

The initial decrease is related to the increase in crystallite size, which improves the charge carrier mobility.[79]

The conduction mechanisms of F:SnO$_2$ are highly dependent on the carrier concentration. When the charge-carrier concentration is relatively low, of the order of $10^{18}$ cm$^{-3}$, the conduction is governed by grain boundary effects. Grain boundaries act to limit the mobility of the electrons by charge trapping at lattice defect sites; or segregation of the dopant atoms from the lattice, reducing charge carrier density[106]. When the carrier concentration is between $10^{18}$ and $10^{19}$ cm$^{-3}$, the conduction mechanism is determined by grain boundaries and bulk properties. When the free charge carrier concentration is relatively high, in excess of $10^{19}$ cm$^{-3}$, the conduction mechanism is attributed to the bulk properties which screen the grain boundary effects, this is due to a high Fermi level in the material (Fermi level is proportional to $N^{2/3}$) whereby free electrons have a higher energy to cross the depleted boundary region[106]. In addition, to a first approximation, grain boundary conduction mechanisms can be largely ignored if the grain size is much larger than the electron mean free path [79, 107].

### 2.4.8 Electrical Properties of c-AACVD Thin Films

Table 2-7 and fig.2-10 show the behavior of electrical properties of F:SnO$_2$ thin films produced by c-AACVD.
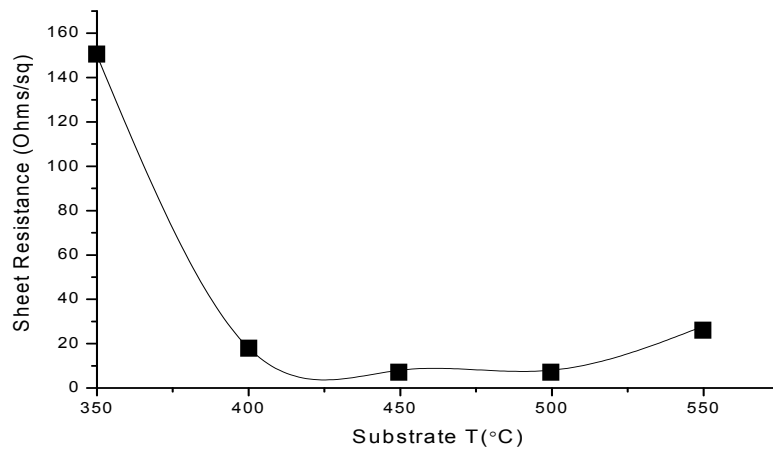


**Figure 2-10** Variation in sheet resistance with deposition temperature of F:SnO$_2$ thin films produced by c-AACVD (30:100 atomic ratio F:Sn in precursor solution).
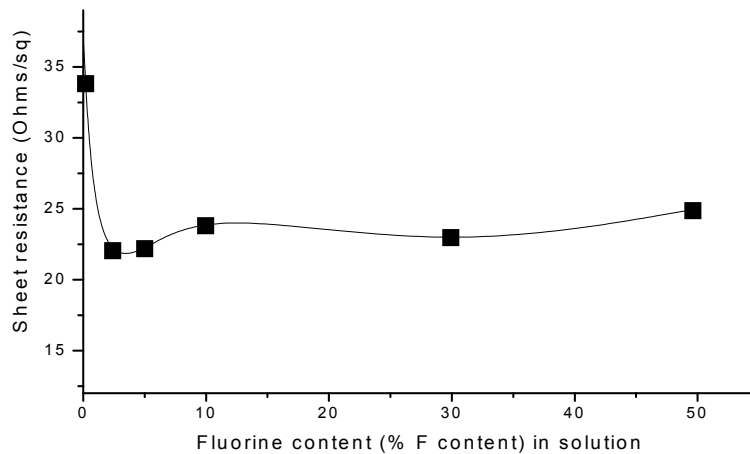
**Figure 2-10 cont.** Sheet resistance of the resultant film versus variation in the atomic ratio of fluorine to tin content of the starting solution (at a constant substrate deposition temperature of 400°C) during F:SnO$_2$ thin film deposition by c-AACVD.

It can be seen from the data, that the sheet resistance is reduced with increasing deposition temperature as predicted by previous work[107]. The minimum sheet resistance occurs between a deposition temperature of 450°C and 500°C. Increasing the temperature of deposition beyond 500°C is shown to be detrimental to the conductivity of the material, this is attributed to the formation of a more stoichiometric tin oxide film, with less dopant incorporation. This is verified by table 2-7 and fig.2-11 which show the average charge carrier density for each of the temperatures. The density of free charge carriers (N) in the material drops by a factor of 10 between 500 °C and 550 °C.

| Deposition Temperature (°C) | Film thickness (nm) | N (cm$^{-3}$) | μ (cm$^2$/Vs) | R$_{SH}$ (Ω/sq) |
|---|---|---|---|---|
| 450 | 680 | $5.7 \times 10^{20}$ | 25 | 8 |
| 500 | 720 | $6.4 \times 10^{20}$ | 12 | 7 |
| 550 | 700 | $8.2 \times 10^{19}$ | 9.4 | 28 |

**Table 2-7** Film thickness, Charge carrier density (N), Hall mobility (μ) and sheet resistance (R$_{SH}$) of F:SnO$_2$ thin films as a function of deposition temperature keeping the fluorine to tin content in the precursor solution constant at 30:100 atomic ratio F:Sn Deposited by c-AACVD .
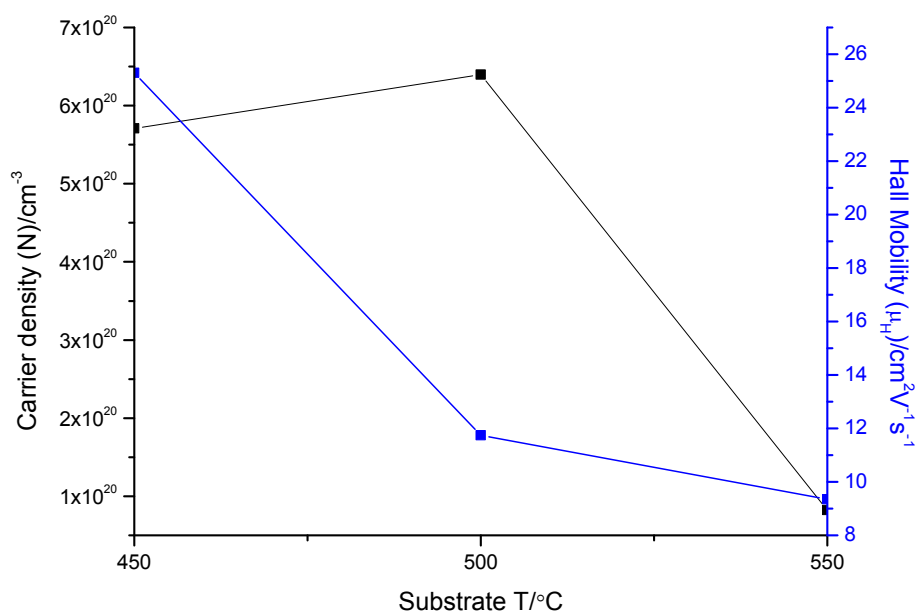


**Figure 2-11** Charge carrier density (N) and Hall mobility (μ) of F:SnO$_2$ thin films as a function of deposition temperature keeping the fluorine to tin content in the precursor solution constant at 30 atomic ratio of F:Sn. Deposited by c-AACVD.

71

Conductivity in metal oxide semiconductors is controlled by scattering of the electrons as they drift though the lattice under the influence of an external electric field. This scattering may be caused by the following scattering mechanisms: 1) Lattice impurities (ionized or neutral) 2) Thermal vibrations of the lattice 3) Structural defects (dislocations, vacancies and surface scattering) 4) Grain boundaries in polycrystalline films[108]. In order to assess the likely mechanisms taking place in the films, analysis of the Hall mobility and charge carrier density was performed to ascertain the dominating cause of electronic scattering during conduction.

The electron mean free path length of the c-AACVD films were estimated from the charge carrier density and Hall mobility measurements using the following formula[109]:

**Equation 2-5**

$$L = \mu \frac{h}{2e} \left( \frac{3N}{\pi} \right)^{\frac{1}{3}}$$

where L is the electron mean free path length, h is Planck's constant, N is the Charge carrier density and e is the charge on an electron.

This analysis indicates that the electronic path lengths ranged from 0.8 nm- 4.7 nm. The crystallite size of the films deposited between 450°C and 550°C by c-AACVD, as-calculated by XRD analysis, are suitably larger than the electronic path-length to negate any grain boundary dominance over the conduction mechanisms, as stated in earlier discussion. The charge carrier density is well above $10^{19}$ again overriding any grain boundary scattering effects.

Lattice vibration effects can be ignored when using comparative analysis, as each of the films were measured at room temperature. This leaves the possibility of impurity scattering and structural defect scattering. To assess the contribution of ionized impurity scattering, the Brooks-Herring[110] adaptation of the Conwell and Weiskopf[111] equation was used to calculate the predicted mobility of the electrons in our films based on the experimentally measured charge carrier density, this assumes solely an ionized impurity scattering mechanism. This can then be compared with the actual mobility data.

72

Brooks-Herring formula for the mean free relaxation time[110]:

**Equation 2-6**

$$T = \frac{(2m*)^{1/2}\varepsilon^2 E_f^{3/2}}{\pi N e^4 f(x)}$$

Where:

**Equation 2-7**

$$E_f = \left(\frac{h^2}{8m*}\right)\left(\frac{3N}{\pi}\right)^{2/3}$$

**Equation 2-8**

$$f(x) = \ln(1 + x) - \frac{x}{1 + x}$$

**Equation 2-9**

$$x = \frac{8m* E_f R_s^2}{h^2}$$

**Equation 2-10**

$$R_s = \frac{h}{2e}\left(\frac{\varepsilon}{m*}\right)^{1/2}\left(\frac{\pi}{3N}\right)^{1/6}$$

If

**Equation 2-11**

$$\mu = \frac{eT}{m*}$$

Therefore:

**Equation 2-12**

$$\mu_{calc} = \left(\frac{2}{m^*}\right)^{1/2} \frac{\varepsilon^2 E_f^{3/2}}{\pi e^3 f(x) N}$$

Where: $E_f$ is the Fermi energy, h is Planck's constant, N is the charge carrier density (assuming the number of ionized impurities in the lattice is equivalent to the number of free charge carriers), m* is the reduced effective mass (taken as 0.3m) where m is the resting electronic mass[108], e is the charge on an electron, $\varepsilon$ is the permeativitty of free space and T is the relaxation time.

Table 2-8 shows the calculated values based on the Brooks-Herring formula were of the order of the actual charge carrier mobilities measured experimentally. This suggests that indeed the ionized impurity scattering mechanism may well be a dominant process in the c-AACVD thin films. However, looking at the trend based upon the Brooks-Herring calculations, with the decrease in charge carrier concentration seen at 550°C, a substantial rise in the charge carrier mobility should occur. This effect would be assumed to further increase by taking into consideration the larger crystallite sizes and higher degree of crystallinity shown for the higher temperature films (see XRD data). In fact, the opposite effect occurs: with the highest temperature film (with the least free charge carriers) having the lowest mobility. The Hall effect measurements showed that in fact the electron mobility steadily decreases with increasing deposition temperature. This is contrary to what was expected in terms of the analysis.

However, further analysis of the SEM imaging shows that the increasing particle size (particles made up of crystallite agglomerations) occurs with increasing deposition temperature, leading to more discrete particulate formation. The increasing resistance to electronic movement between such particles seems to override the greater mobility within and between the individual crystallites. This exemplifies the need for precise control over crystal structure not only at the atomic and macro level, but also in the nano-scale range.

| Deposition Temperature (°C) | Film thickness (nm) | N (cm$^{-3}$) | Actual Mobility μ (cm$^2$/Vs) | Calculated Mobility μ (cm$^2$/Vs) |
|---|---|---|---|---|
| 450 | 680 | 5.7x10$^{20}$ | 25 | 2.21 |
| 500 | 720 | 6.4x10$^{20}$ | 12 | 2.04 |
| 550 | 700 | 8.2x10$^{19}$ | 9.4 | 8.03 |

**Table 2-8** Showing the calculated mobility data, based on the Brooks Herring formula, for electronic behavior based upon ionized impurity scattering in doped semiconductor materials

Variation in sheet resistance, with respect to the fluorine content in the precursor solution, showed no dependency on the atomic ratio of F:Sn at a 450°C deposition temperature (see fig.2-10b). Only the film deposited without the addition of fluorine showed a significantly higher resistance. Wavelength dispersive X-ray analysis showed that the 1:100 atomic ratio F:Sn precursor solution gave the same ratio of fluorine to tin in the deposited film. However, above this level of fluorine doping less percentage incorporation was seen (see table 2-9). This doping limitation has been found in previous work[112]. Though the percent incorporation went down, the level of fluorine doping went up in actual terms however did not correlate with a change in the conductivity. This can again be attributed to the overriding particle boundary effect.

| Deposition Temperature (°C) | Atomic ratio of F:Sn in the aerosol solution (%) | Atomic ratio of F:Sn in the deposited film (X : 100) | Percentage fluorine incorporation(%) |
|---|---|---|---|
| 450 | 1 | 1 | 100 |
| 450 | 10 | 1.6 | 15% |
| 450 | 50 | 2.2 | 4.4% |

**Table 2-9** Table showing the atomic ratio of F:Sn in the precursor aerosol solution and the atomic ratio of F:Sn in the as-deposited films. Deposited by Collison AACVD at 450°C

It is therefore assumed that, it is a combination of structural properties (the aforementioned particle separation) and charge carrier density which dominates the control of film conductivity. Detrimental effects through ionized impurity scattering seem to be outweighed by the conductivity gains from the addition of more free charge carriers, at the levels of fluorine doping we have seen, and the self-limiting percentage of fluorine incorporation prevents ionized impurity scattering reducing the mobility too far. This explains the increase in sheet resistance at 550°C and the decreasing mobility of the films with increasing temperature.

## 2.4.9 Electrical comparison

The ultrasonic-AACVD deposition resulted in thin films of $F:SnO_2$ with a sheet resistance too high (>90 $\Omega/\square$) for accurate Hall effect measurements, this level of resistance is also too high for any infrared reflectivity. The films produced using thermal APCVD were deemed too variable to take forward for electrical analysis. In place of the APCVD $F:SnO_2$ thin films produced in the lab, leading commercial products were tested, to allow for electrical and optical comparison. Table 2-10 shows the electrical properties of Pilkington NSG TEC 8 and TEC 15, fluorine doped tin oxide thin films on glass (deposited by APCVD), both of which are used in commercial products for Low-E glazing and transparent conducting electrodes.

| Deposition Temperature (°C) | Film thickness (nm) | $N$ (cm$^{-3}$) | $\mu$ (cm$^2$/Vs) | $R_{SH}$ ($\Omega$/sq) |
|:---:|:---:|:---:|:---:|:---:|
| TEC 8 | 650 | $5.34 \times 10^{20}$ | **27.9** | 8 |
| TEC 15 | 350 | $5.64 \times 10^{20}$ | **20.9** | 15 |

**Table 2-10** Film thickness, Charge carrier density (N), Hall mobility ($\mu$) and sheet resistance ($R_{SH}$) of leading commercial $F:SnO_2$ thin film products. Pilkington NSG TEC8 and TEC15.

Comparison of the electrical properties shown by these leading products with the films we have produced by c-AACVD at 450 °C and 500 °C, shows very similar levels of carrier concentration and electron mobility. The c-AACVD films demonstrate a marginally higher charge carrier density (5.7 x $10^{20}$ cm$^{-3}$ and 6.4 x $10^{20}$ cm$^{-3}$ for 450 °C and 500 °C respectively), but a marginally lower charge carrier mobility (25 cm$^2$/Vs and 12 cm$^2$/Vs for 450 °C and 500 °C respectively). In terms of the lower mobility this reflects the smaller crystallite size, but also more importantly the resistance between nano-sized particles which plays a key role in governing the mobility of the c-AACVD films. The APCVD films have a very tightly packed structure resulting in a higher mobility. The increased charge carrier concentration in the c-AACVD films is presumably caused by a higher level of fluorine doping. However, WDX analysis of the films did not prove accurate enough (due to beam penetration difficulties with WDX thin film analysis) to verify whether this was the root-cause.

## 2.4.10 Optical Measurments

The room temperature transmission and reflection characteristics of our F:SnO$_2$ films, produced by c-AACVD, were compared to the optical properties of Pilkington TEC8 and TEC15 products using visible/near IR spectrometry. The spectra obtained from each coating were assessed in terms of their transparency across the visible and their reflectivity in the infrared, for application in Low-E glazing.

The spectra shown in fig.2-12 and 2-13 were taken using an air background and indicate a high transparency across the visible (~80% transmission at 550 nm in air, which includes the substrate absorbance) and a high reflectivity in the far infrared (> 65% reflection at 2500 nm in air). This indicates their ability to function as Low-E glazing products.

Pilkington TEC 8 and TEC 15 coatings on glass were used as the reference coatings (sheet resistances of 8 Ω/□ and 15 Ω/□ respectively), this allows for comparison of optical properties between our c-AACVD films (deposited at 400°C (18 Ω/□) / deposited at 450°C (8 Ω/□)) and with commercial films of a similar electrical

conductivity. It has already been seen that the Hall-effect measurements displayed a small difference in charge carrier density and electron mobility between the film deposited at 450°C and the commercial counterparts. Optical measurements allow the determination of the effect of these differences in terms of function as a Low-E coating.

Chapter 1 outlined that the onset of the far infrared reflection (the reflection which is desired in Low-E applications) occurs at the plasma resonance frequency where the electromagnetic radiation incident on the film can induce resonance of the free carriers, within the metal oxide matrix. It can be shown that the plasma frequency is dependent upon the conductivity, the di-electric constant, and the mean free relaxation time of the material. This means that increasing the charge carrier density, and decreasing the charge carrier effective mass (reducing retarding forces on the free electrons such as scattering defects) will increase the plasma resonance frequency of the TCO, thus shifting the resonance reflection effect to a shorter wavelength.

Where the plasma resonance frequency $(\omega_p{}^2)$ is defined by the following equation:

$$\omega_p{}^2 = \frac{\sigma}{\varepsilon t} = \frac{N_e e \mu_e}{\varepsilon t}$$

$N_e$ is the free carrier density

e is the charge on each free carrier

$\mu_e$ is the free carrier mobility

$\varepsilon$ is the dielectric constant of the material

t is the mean free relaxation time

$\sigma$ s the conductivity

This means that the onset of the reflective edge in the IR should be directly related to the conductivity of the material. This is the reason that comparison of films with like-for-like sheet resistance values have been done (between the c-AACVD thin films and Pilkington NSG products).

The optical comparisons are shown in fig.2-12 and fig.2-13. The films produced by c-AACVD display prominent interference effects. These interference fringes are caused by the multiple reflections at the three interfaces of the air/thin film/transparent substrate bi-layer. The interference fringes are absent in the commercial products due to a mitigating 'colour suppression' layer.

The c-AACVD F:SnO$_2$ films show a rapid onset of the IR reflection and a reflectivity at 2500 nm which is 10-15 % higher than the commercial products. It should however be noted that a 2-5% drop in transmission (ignoring the interference pattern) over the visible accompanies the high IR reflectivity, however, the commercial coating has a built in anti-reflective 'colour suppression' layer that improves transmission. Essential properties for low-E glazing coatings include a high reflective value for far IR radiation (>2000 nm) and a rapid onset of the plasma edge which separates the transparent and reflective regime across the wavelength range [54, 113]. Both of these attributes are present in the films formed in this work, and both exceed commercial performance in the F:SnO$_2$ films deposited by c-AACVD at 400°C and 450°C.
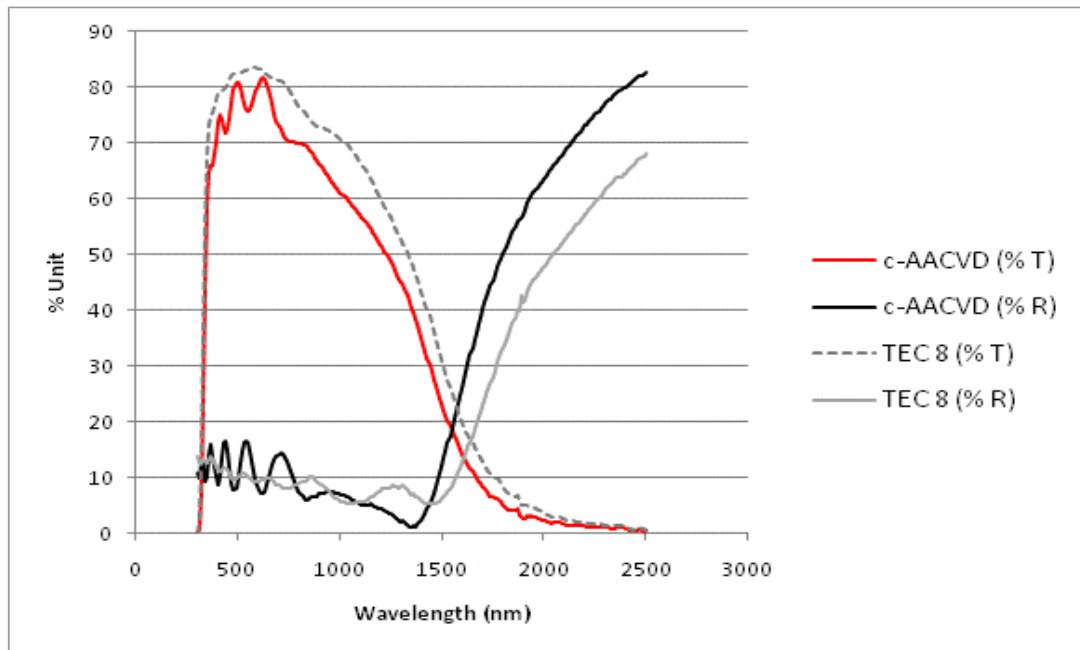


**Figure 2-12** Optical transmittance and reflectance taken with an air background comparing c-AACVD grown F:SnO$_2$ (450°C deposition temperature and 30:100 atomic ratio F:Sn content in the monobutyl tin trichloride/trifluoroacetic acid methanoic precursor solution (8 $\Omega/\square$)) and commercial F:SnO$_2$ (8$\Omega/\square$ Pilkington TEC 8).
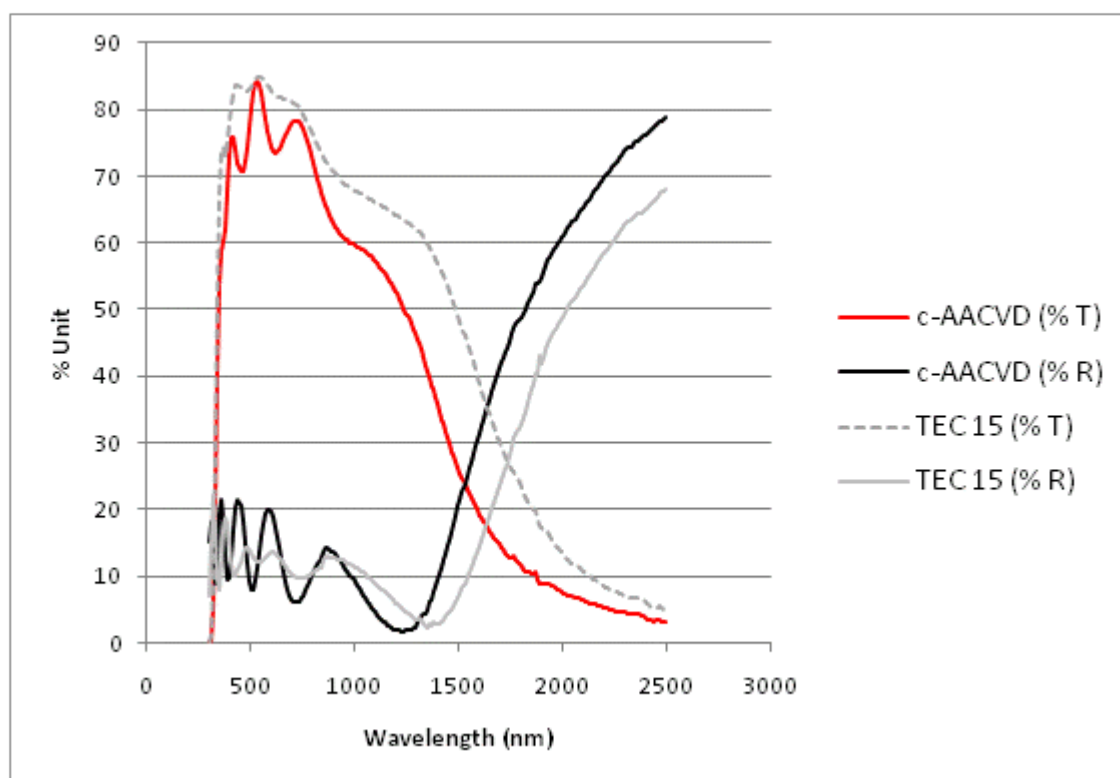
**Figure 2-13** Optical transmittance and reflectance spectra taken with an air background comparing c-AACVD grown F:SnO$_2$ (400°C deposition temperature and 30:100 atomic ratio F:Sn content in the monobutyl tin trichloride/trifluoroacic acid methanoic precursor solution (18 Ω/□)) and commercial F:SnO$_2$ (15Ω/□ Pilkingtion TEC 15).

The high level of reflection in the IR is also accompanied by a ~200 nm blue shifting of the plasma edge in our c-AACVD films produced at 450°C, compared to the Pilkington TEC 8 product. This would suggest a higher conductivity in the c-AACVD thin films, however, sheet resistance measurements and calculated conductivities of the materials shown in Table 2-11 demonstrate that it is the TEC 8 with a marginally higher conductivity. Clearly, additional factors must be playing a part in the onset frequency of the plasma edge, that are not accounted for in the conductivity measurements.

| Material | Thickness | Sheet Resistance $(\Omega/\square)$ | Conductivity based on $R_{SH.}$ $(S.m^{-1})$ | Conductivity based on Hall effect measurements $(S.m^{-1})$ |
|---|---|---|---|---|
| TEC 8 | 650 | 8 | $1.92 \times 10^5$ | $2.38 \times 10^5$ |
| c-AACVD(450°C) | 680 | 8 | $1.84 \times 10^5$ | $2.2 \times 10^5$ |

**Table 2-11** Comparison of resistance and conductivity values of TEC8 and c-AACVD(450°C) found using different methods.

In chapter one, it was shown that it is not just Low-E applications in which the optical performance of $F:SnO_2$ is critical. Utilising transparent conducting materials as the transparent electrode in thin film photovoltaics also requires precise control over the optical properties.

TCO materials for photovoltaics require a high optical transparency and high electrical conductivity, to maximize the efficiency of solar energy capture and the power out. They also require the ability to scatter the incoming light and trap it within the thin film absorbing layer. Theoretical calculations have shown this light trapping ability translates to a measured haze value of 8-15 % ($T_{diff}/T_{tot}$), and a pyramidal surface structure.

Haze measurements were performed on the c-AACVD thin films (shown in table 2-12). The c-AACVD 450°C film shows a very low haze value: optimum for Low-E coatings to ensure a clear window. Higher temperature films display haze values which correlate with the optimum values for use in thin film photovoltaics. This is in conjunction with an average light transmission across the visible of 80%, a high electrical conductivity and the desired surface morphology demonstrated in the SEM imaging (2-14), making films produced via Collison-AACVD an attractive prospect for photovoltaic application.

| Sample Number | Average visible light transmission (%) | Haze Value ($T_{diff}/T_{tot}$) |
|---|---|---|
| 3 (450°C) | 79.4 | 1.74 |
| 4 (500°C) | 79.1 | 7.84 |
| 5 (550°C) | 80.1 | 11.42 |

**Table 2-12** Transmission and Haze values for $F:SnO_2$ films from a precursor solution containing 30:100 atomic ratio F to Sn in a monobutyl tin trichloride methanoic solution deposited at varying temperatures by c-AACVD using a Collison type atomiser.
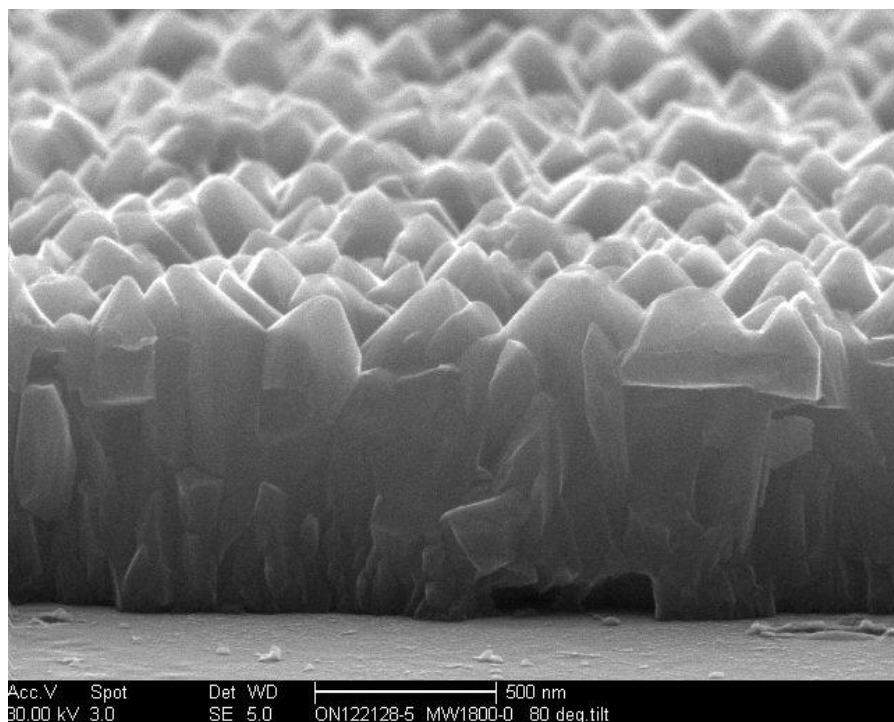


**Figure 2-14** SEM side on image of a $F:SnO_2$ thin film deposited at a substrate temperature of 500°C using c-AACVD of MBTC and TFA in methanol. Showing pyramidal surface morphology of the doped tin oxide for light scattering.

## 2.4.11 Cation and co-doped tin oxide

Thus far, the focus has been on the doping of tin oxide with anionic fluorine, this system is the most researched and best performing in terms of transparent conducting applications. However, there remains the possibility of doping the tin oxide host matrix by replacing the cationic sites usually occupied by tin ions. Much work has been done looking into a host of possible cationic dopants including: antimony, arsenic[114], molybdenum[115] and phosphorous[116].

The following results illustrate the effect of cationic doping and cationic/anionic co-doping of tin oxide using Collison-AACVD. The aerosol solution was prepared using mono-butyl tin chloride (MBTC 10 g) in methanol (200 ml), with the addition of the following dopant precursors shown in table 2-13:

| Dopant precursor | Constituent atomic ratio of dopant atom 1 : tin. | Constituent atomic ratio of dopant atom 2 : tin. | Temperature of deposition(°C) |
|---|---|---|---|
| SbCL$_3$ | Sb (30:100) | - | 450 |
| BiF$_3$ | Bi(30:100) | F (90:100) | 450 |
| SbF$_3$ | Sb(10:100) | F (30:100) | 450 |

**Table 2-13** Experimental conditions used for the cationic/anionic co-doping of tin oxide by c-AACVD at 450°C.

Chlorine has not been included in the above table as an anionic dopant. The presence of chlorine in both the above systems, as-well as the fluorine doped tin oxide system described earlier, was noted from the EDX analyses carried out on the resultant thin films. Chlorine is present in all precursor solutions from the use of MBTC (mono-butyl tin trichloride) as the tin containing species. As such, incorporation of chlorine into the forming films is likely from the incomplete decomposition of MBTC. The presence of chlorine atoms and oxygen vacancies have been shown to play a role in increasing the conductivity[117, 118], Shanti et al.[119] found films with a conductivity of 1.4

$x10^4$ Sm$^{-1}$ owing to these effects. However, as chlorine is consistently present in all techniques it can be considered a baseline effect.

## 2.4.12 Electrical Analysis

Table 2-14 shows the electrical properties of the thin films deposited by c-AACVD using a variety of cationic/anionic dopant precursors. Addition of antimony resulted in a reduced sheet resistance compared to the un-doped films, demonstrating the ability of antimony to donate an electron into energy levels near the conduction band, this is a well known result for spray pyrolysis and CVD routes[120]. Addition of antimony and fluorine gave an even lower level of sheet resistance: presumably functioning as co-dopants. However, neither of these films showed a sheet resistance as low as the 8 Ω/□ seen with solely fluorine doping at 450°C.

Hall effect measurements revealed antimony doped films had a free charge carrier density with a ten-fold increase over the best singly doped F:SnO$_2$ film produced by c-AACVD, or produced commercially. However, the mobility in the antimony containing films was comparably very low, this accounts for the inferior sheet resistance (Table 2-14). The high carrier concentration can be attributed to a higher level of antimony doping (2-2.7 : 100 atomic ratio Sb:Sn) compared to fluorine (< 2.2 : 100 atomic ratio Sb:Sn) and higher % of electronic donation of those antimony atom into defect energy levels. The low mobility can be explained by high levels of ionized impurity scattering by the larger antimony ionic radii.[119]

| Dopant precursor | Temperature of deposition(°C) | R$_{SH}$ (Ω/□) | N (cm$^{-3}$) | μ (cm$^2$/Vs) | Atomic ratio of dopant atom 1 :Sn (in film) | Atomic ratio of dopant atom 2 :Sn (in film) |
|---|---|---|---|---|---|---|
| None | 450 | 36 | - | - | - | - |
| SbCl$_3$ | 450 | 26 | 7.9 x10$^{21}$ | 0.22 | 2.1(Sb):100 | - |
| BiF$_3$ | 450 | 1700 | - | - | 6.2(Bi):100 | 4.4(F):100 |
| SbF$_3$ | 450 | 19 | - | - | 2.7(Sb):100 | 2.5(F):100 |

**Table 2-14** Electrical comparisons for each type of dopant atom used for the deposition of fluorine doped tin oxide thin films. N is charge carrier density and μ is charge carrier mobility. The final columns show the atomic ratio of the various dopants with respect to tin atoms in the films measured using WDX.

Films produced using bismuth as a dopant source yielded sheet resistance values far higher than films with no dopant additive. It was thought this change could be due to phase segregation of bismuth oxide and tin oxide, due to the high level of bismuth detected by WDX in the films (see table 2-14), leading to a reduced conductivity. However, looking at fig. 2-15 shows only the diffraction pattern of tin oxide for the bismuth doped tin oxide thin films. There is however, a severely reduced crystallinity shown in the XRD. It is this reduced crystallinity, presumably caused by the large ionic radius of bismuth and its relatively high doping level disrupting the tin oxide structure, which has led to a low crystallinity and very poor conductivity.
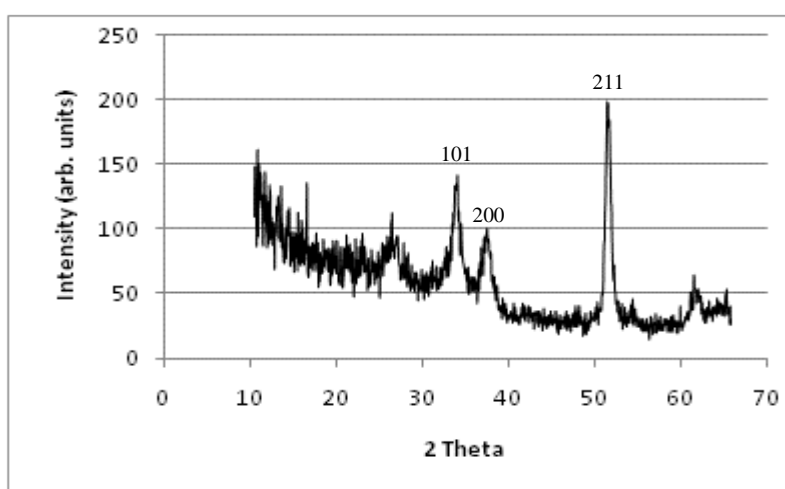


**Figure 2-15** XRD pattern of Bi:F:SnO2 (Precursor solution: 90:100 atomic ratio of F:Sn and 30:100 atomic ratio of Bi:Sn. In a solution of monobutyl tin trichloride in methanol solvent) deposited at substrate temperature of 450°C using c-AACVD.

## 2.4.13 Optical analysis

Transmission and reflection optical analysis was performed on the cation doped films, revealing both the $SbCl_3$ and $SbF_3$ doped films to show some reflectivity in the infrared. However, the % reflectance was 15-20% lower than comparable c-AACVD films produced using solely fluorine doping, and in addition the onset of the reflectance edge was far slower. The transmission properties of the $SbCl_3$ and $SbF_3$ films showed a much lower transmission across the visible. Solely doping with the antimony, from $SbCl_3$, gave a blue films. This blue colouration has been attributed to the antimony producing an almost free-electron impurity energy level which behaves like a partially

filled metallic band, this sits at ~1.5 eV below the conduction band of the tin oxide lattice, resulting in an absorption which produces a blue colouration[120, 121]. Co-doping Fluorine and antimony from $SbF_3$ gave black colouration in the resultant films, presumably caused by multiple defect energy levels causing absorption across the visible. This colouration change is shown in the profile of the transmission across the visible in the spectra shown in fig.2-16 and fig.2-17.
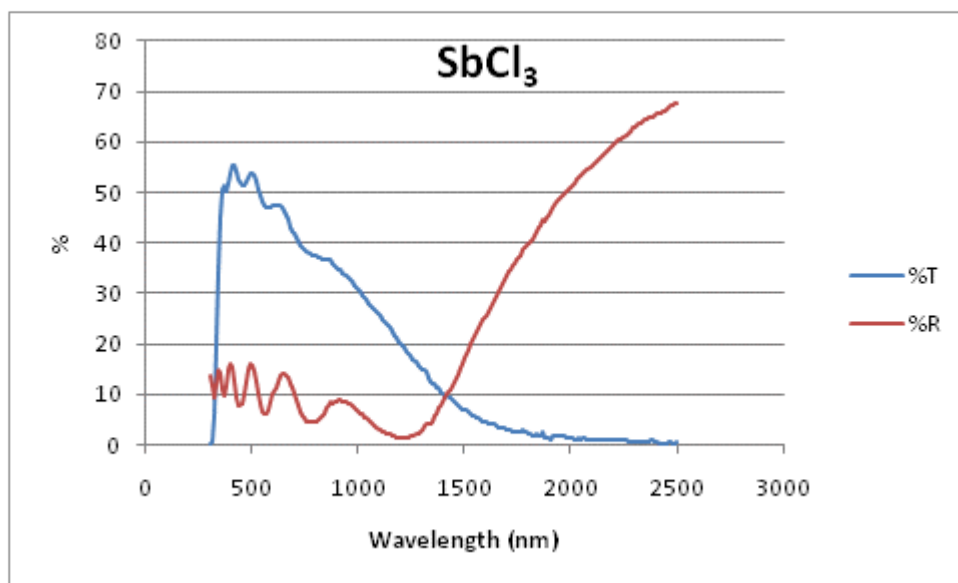


**Figure 2-16** Optical transmittance and reflectance taken with an air background. c-AACVD grown F:$SnO_2$ : 450°C deposition temperature, $SbCl_3$ dopant precursor with 30:100 atomic ratio of Sb:Sn in the monobutyl tin trichloride methanoic precursor solution.
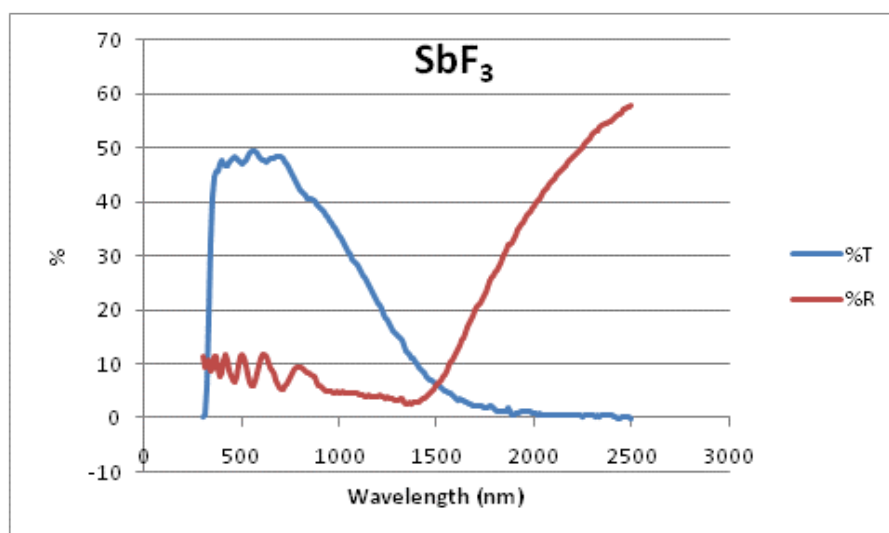
**Figure 2-17** Optical transmittance and reflectance taken with an air background. c-AACVD grown F:SnO$_2$ : 450°C deposition temperature, SbF$_3$ dopant precursor with 10:100 Sb:Sn atomic ratio and 30:100 atomic ratio of F:Sn in the monobutyl tin trichloride methanoic precursor solution.

Co-doping with bismuth and fluorine from BiF$_3$ resulted in films with a brown colouration. The low conductivity of these films meant that no reflectance edge was present in the IR. An absorption mechanism was noted to take place moving into the infrared.
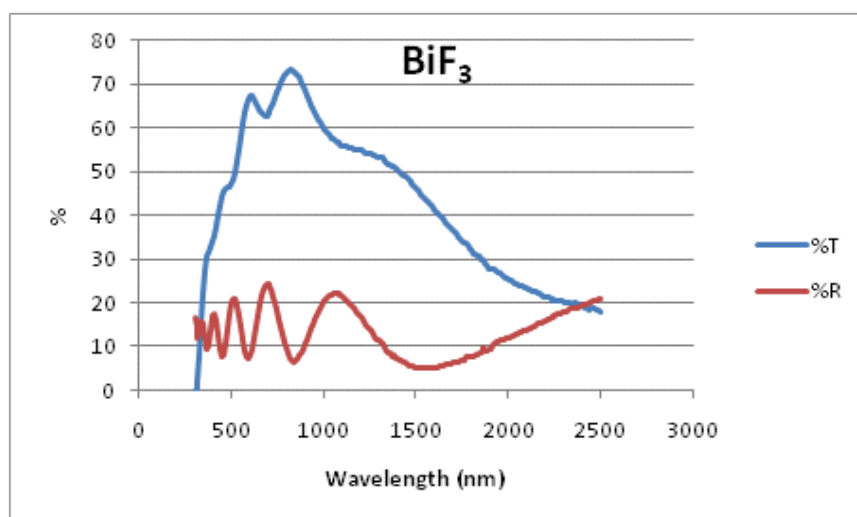


**Figure 2-18** Optical transmittance and reflectance taken with an air background. c-AACVD grown F:SnO$_2$ : 450°C deposition temperature, BiF$_3$ dopant precursor with 30:100 Bi:Sn atomic ratio and 90:100 F:Sn atomic ratio in the monobutyl tin trichloride methanoic precursor solution.

87

## 2.5 Research Comparisons

Much research has been done into doped tin oxide as a transparent conducting material. The following overview provides a comparison of some of the leading published results in the field.

The fluorine doped tin oxide thin films were produced by c-AACVD with a thickness of ~700 nm, a sheet resistance of 7 $\Omega/\square$, a resistivity of 5 x $10^{-4}$ $\Omega$cm, charge carrier density of 6.4 x $10^{20}$ $cm^{-3}$, a mobility of 25 $cm^2$/Vs. The films showed a visible transparency of 90 % and a haze value which could be tailored for light scattering or optical clarity.

| Material | Process | Sheet Resistance $R_s(\Omega/\square)$ | Transmission at 550nm T (%) | Mobility $\mu(cm^2V^{-1}sec^{-1})$ | Carrier Concentration $(cm^{-3})$ |
|---|---|---|---|---|---|
| F:SnO$_2$ | Spray | 10.6 | 86 | - | - |
| Sb:SnO$_2$ | Spray | 90 | 90 | - | - |
| Sb:SnO$_2$ | Spray | 84 | 84 | 12 | $8 \times 10^{26}$ |
| Sb:SnO$_2$ | CVD | 72 | 87 | - | - |

**Table 2-15** Table of results of previous studies into transparent conducting materials taken from a review by Dawar and Joshi[122]

| Material | Process | Deposition Temp (°C) | Growth Rate $(ms^{-1})$ | Resistivity $(\Omega.cm)$ | Transmission at 550nm T(%) | Remarks |
|---|---|---|---|---|---|---|
| Sb:SnO$_2$ | Spray | 346-446 | 4.1-7.5 x $10^{-10}$ | 8 x $10^{-4}$ | 80 | |
| Sb:SnO$_2$ | Spray | 600 | - | 65 $\Omega/\square$ | 90 | |
| Sb:SnO$_2$ | Spray | 680 | - | 7.5 x $10^{-3}$ | 90 | |
| Sb:SnO$_2$ | Spray | 500-700 | - | 10 x $10^{-3}$ | 80 | |
| F:SnO$_2$ | CVD | 570 | 60 x $10^{-10}$ | 3.3 x $10^{-4}$ | 90 | |
| F:SnO$_2$ | Spray | 400 | - | 4.6 x $10^{-4}$ | 85 | F/Sn 0.5at.% |
| F:SnO$_2$ | Spray | 400 | - | 5.4 x $10^{-4}$ | 90 | |
| F:SnO$_2$ | Spray | 400-500 | - | 9 x $10^{-3}$ | 91 | |
| F:SnO$_2$ | Spray | 450 | 3.3 x $10^{-10}$ | 4.3 x $10^{-4}$ | 90 | 10% F |
| F:SnO$_2$ | Spray | 450 | 4.1 x $10^{-10}$ | 9 x $10^{-4}$ | 90 | F/Sn 10wt.% |

**Table 2-16** Table of results of previous studies into transparent conducting materials taken from a review by Hartnagel et al.[79]

Table 2-15 and table 2-16 show the results obtained from previous experimental investigations into TCO materials using various experimental techniques. These results show similar electrical characteristics to our films, which have been deposited by c-AACVD, however in addition to the excellent electrical performance, our films show an increased % reflectance in the IR and a surface morphology which can be tailored using the temperature of deposition to suite different applications. We have also shown the onset of the plasma edge has been shifted using c-AACVD as a deposition technique.

## 2.6 Conclusion

This chapter presented the deposition of doped tin oxide thin films using three distinct methods: Collison-AACVD, ultrasonic-AACVD and thermal-APCVD. Using the same precursor set, but different deposition techniques, has produced functional transparent conducting thin films of $F:SnO_2$ which show varying electronic, crystal, and surface texture properties.

The novel method of Collison-AACVD proved to be a fast, simple and cost-effective method for the deposition of highly functional doped tin oxide thin films. It demonstrated control over the deposition conditions using c-AACVD, which in turn, affords control over the properties of the TCO material in terms of charge carrier mobility, charge carrier density, IR reflectance, crystallinity, and the surface morphology. Films can be tailored either for Low-E or Photovoltaic application, with a combination of properties which can out-perform the leading commercial products.

A c-AACVD deposition temperature of 450°C was found to be optimum for the production of $F:SnO_2$ thin films for use as low-emissivity coatings, having a low visible light haze value (1.74), a high charge carrier mobility (25 $cm^2/VS$), and a high charge carrier density (5.7 x $10^{20}$ /$cm^{-3}$) resulting in a high transmittance across the visible (~80%) and a high reflectance in the far IR (80% at 2500nm). A deposition temperature of 500°C was found to be optimum for the production of $F:SnO_2$ thin films for use as top electrodes in thin film photovoltaics, giving a low sheet resistance (8Ω/□) and a surface texturing on the micrometer scale with a haze value of 8 % for light scattering and trapping within thin film photovoltaic devices.

Comparison of c-AACVD with APCVD and u-AACVD, afforded an insight into the likely mechanisms by which the tin oxide films form, in terms of surface diffusion, nucleation, and gas phase pre-reaction. This insight should help develop further control over deposition conditions in order to tailor film properties to meet commercial demand.

# 4 CVD of Carbon Nanotubes

## 4.1 CVD synthesis of carbon nanotubes and novel carbon nanofibres

*The following chapter describes the use of chemical vapour deposition in the synthesis of carbon nano-structures grown by the thermally induced decomposition of methane over a range of transition metal catalysts. The experimental landscape was mapped over the following conditions: temperatures 800-1100°C, transition metal catalysts Zr, V, Mn, Co, Ni, Fe, Cr, Ag, Au; and varying methane to hydrogen ratios. Both single wall carbon nanotubes and multi-wall carbon nanotubes of varying shell numbers were grown using selected catalysts. Deposition and structural purity were shown to be highly dependent upon the experimental conditions. Novel carbon nano-fibre structures have been produced using gold and silver catalysts. The as-grown samples have been analysed using transmission and scanning electron microscopy, Raman spectroscopy, and Vis/IR spectroscopy.*

## 4.2 Introduction

Chapters 2 and 3 presented the results obtained from the deposition of doped-tin oxide thin films. Tin oxide as a transparent conducting oxide thin film, plays a role in much of our current technology, and is a well established field of research. This chapter and the following chapter shall make a move away from the established metal oxide technologies, and will present the results obtained from the synthesis of carbon nanotubes by CVD, followed by the results obtained for the deposition of carbon nanotube nanonet transparent conducting thin-films in the following chapter.

Since the landmark paper on carbon nanotubes (CNTs) by Iijima in 1991[38], the study of these carbon structures has led to vast quantities of research both experimentally and theoretically[132-134]. Due to CNTs unique physical and electronic properties, which were alluded to in the introductory chapter, they have been at the forefront of nanotechnology development and research. Realisation of practical applications within the commercial sector have already begun, however, the full industrial potential of nanotubes has yet to be seen. Under laboratory conditions the scope for potential uses of CNTs is seemingly endless. Whilst the reality within industry is that the large-scale production of such materials is relatively limited. Furthermore, sufficient control over type and purity required to enable direct integration into high-end technologies has proven problematic[135].

Methods used in the production of CNTs, such as carbon arc deposition or laser ablation, are relatively small-scale techniques which yield only relatively low quantities of the material. As such they have limited scale-up potential. However, recently chemical vapour deposition (CVD) of carbon containing precursors has proved to be a viable route towards large-scale production of carbon nanotubes, now available industrially on the multi-tonne scale. The CVD technique uses a nano-sized metal catalyst to allow tubular carbon growth from a carbon feedstock, requiring less challenging conditions than that of the arc synthesis approach[136]. The challenge facing CVD is the ability to further enhance the selectivity and purity of the end product, allowing for its use in fields requiring precise control over wall number, tube diameter and chirality[133].

The following work is intended as a review of the growth conditions, and as an investigation into the selectivity and purity afforded by established and novel metal catalysts used in the CVD of CNT. The outcome of this investigation is intended to be used as a basis to establish possible growth conditions for different types of CNT, with a view towards the specific integration into transparent conducting nanonet thin films.

Much work has been done into the individual effects of temperature[137], hydrogen content[138, 139] and the catalyst type[140, 141]. However there is limited analysis which reviews all three variables, in addition most research concentrates on the use of only cobalt, iron, and nickel catalysts[142-144]. Comparison of these parameters between different papers and different research groups has limited validity because this type of synthesis is very sensitive to the experimental set-up, and the individual methods used. The following results map the experimental landscape, of the above three parameters, using the same equipment, method, and the same operator to allow for a valid comparison between all experimental variables, in order to elucidate possible trends and the interplay of those variables.

In the following results, a wide experimental landscape has been mapped, including temperature conditions and hydrogen/methane ratio conditions, over not only the three traditionally used catalysts (Co, Fe, Ni) but also zirconium, vanadium, manganese, chromium, silver and gold, all of which were supported on powdered magnesium oxide substrate. A similar size distribution of catalyst was used to minimise size induced effects on growth type. A long synthesis time was used to allow for growth in catalyst metals where carbon diffusion is a slower process.

Assuming that the ease of electronic transfer between the metal and the adsorbed gases plays a role in the catalysis of carbon species formation, the aforementioned catalysts were selected in order to give a wide range of Pauling electronegativity values between the various metals. It was anticipated that this electronegativity trend would provide insight, on a relatively simplistic and empirical level, into metal-catalyst electron transfer effects on CNT formation.

## 4.3 Experimental

### 4.3.1 Catalyst preparation

The following transition metal containing compounds were used as the precursors for the deposition of the respective metals onto a magnesium oxide substrate with a 5 wt.% loading of the catalytic metal atoms; zirconium chloride [$ZrCl_4$] (0.064 g), vanadium acetylacetonate [$V(C_5H_8O_2)_3$] (0.17 g), manganese chloride [$MnCl_2.4H_2O$] (0.09 g), cobalt nitrate [$Co(NO_3)_2.6H_2O$] (0.123 g), nickel acetate [$Ni(CH_3COO)_2.4H_2O$] (0.106 g), iron oxide nanoparticles ($Fe_2O_3$) (0.036 g), chromium chloride [$CrCl_3.6H_2O$] (0.128 g), silver chloride (AgCl) (0.033 g) and auric acid [$HAuCl_4$] (0.043 g). Each transition metal containing compound was dissolved in ethanol (40 ml) and bath sonicated for 15 min, powdered MgO (0.5 g) was added and the solutions were sonicated for a further 60 minutes and left over night at 100°C to remove the solvent, a similar preparation method is outlined by Li et al.[142]

### 4.3.2 Chemical Vapour Deposition

Fig.4-1 shows a schematic of the rig used for the reduction of the metal catalyst and the subsequent carbon deposition. Argon is used as an inert gas to force oxygen from the sealed system, hydrogen and methane can then be introduced as a mixed feed, with individually controllable flow rates. The hydrogen abatement system uses solenoid valves to ensure regulation of the inert gas feeds, in order to prevent hydrogen build up in the furnace, and maintain a pilot flame at the exhaust to safely react any excess combustible gases.

Flow Meters                                              Tube Furnace          Exhaust

H$_2$

Me

H$_2$ Abatement System and Flow Controllers

Metal Catalyst          Pilot Flame

N$_2$          Ar
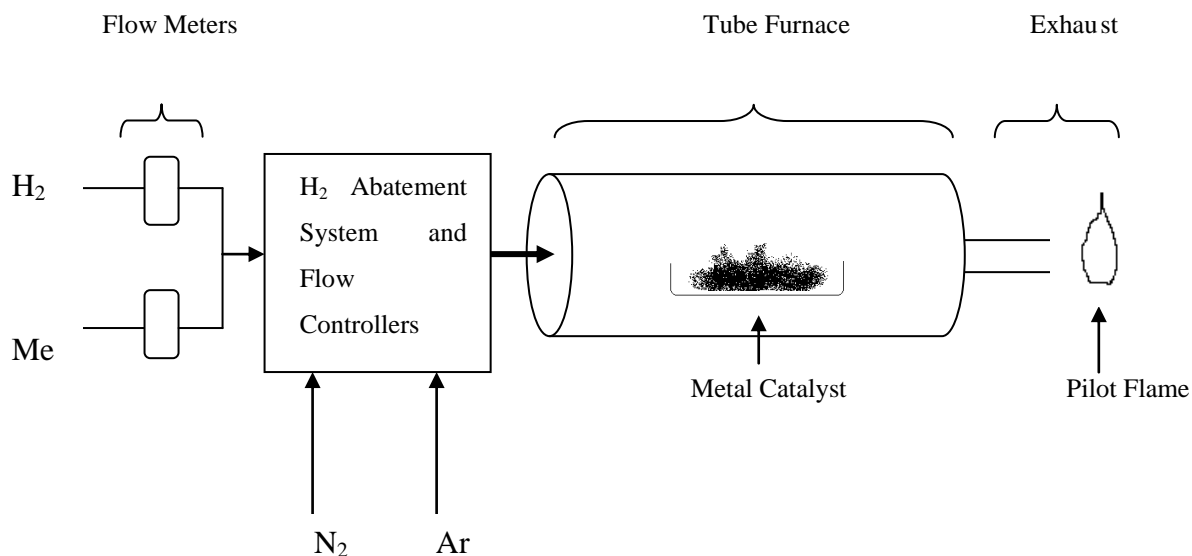
**Figure 4-1** Diagram of the Chemical Vapour Deposition rig used for the reduction of the metal catalyst on a powdered MgO substrate and the subsequent thermal decomposition of carbon feedstock (Methane) for CNT synthesis.

Powdered samples of the catalyst (containing the metal species adsorbed onto MgO (0.025 g)) were loaded into open-ended alumina boats and inserted into the centre of the tube furnace. The furnace was then sealed, air tight apart from the exhaust, and heated to 1000°C under a steady 3 Lmin$^{-1}$ flow of argon. Upon reaching 1000°C, a flow of hydrogen (0.5 Lmin$^{-1}$) was introduced and maintained for 1 hour in order to ensure the metal compounds were fully reduced to their constituent metals on the surface of the MgO.

After reduction of the metal catalysts for 1 hour, the methane carbon feedstock was introduced under the appropriate experimental conditions, as outlined in table 4-1. The furnace was then allowed to cool under an inert gas flow to prevent oxidation of any carbon deposits. The experimental conditions were repeated for each of the metal catalysts outlined earlier, using the same equipment, operator, and methodology.

127

| Temperature of Deposition (°C) | Experiment | Flow Rate $CH_4$ ($Lmin^{-1}$) | Flow Rate $H_2$ ($Lmin^{-1}$) |
|---|---|---|---|
| 810 | I | 0.2 | 0 |
| 910 | II | 0.2 | 0 |
| 1010 | III | 0.2 | 0 |
| 1010 | IV | 0.2 | 0.1 |
| 1010 | V | 0.2 | 0.2 |
| 1010 | VI | 0.2 | 0.3 |
| 1010 | VII | 0.2 | 0.6 |

**Table 4-1** Table of experimental parameters used for the decomposition of methane over a range of transition metal catalysts (Zr, V, Mn, Co, Ni, Fe, Cr, Ag, Au), on a powdered MgO support (5 wt % metal loading).

## 4.3.3 Analysis

Characterisation of the as-grown carbonaceous materials was performed without further treatment. This was done to assess purity and yield before removal of the catalytic material and metal oxide support.

Optical band gap measurements were taken from samples containing SWCNT as identified by Raman analysis. The samples were prepared using a technique outlined by O'Connell et al.[145] whereby a small amount of the as grown SWCNT were suspended in 10 ml of a 0.1wt.% solution containing sodium dodecyl sulphonate (SDS), in either distilled water or deuterated water ($D_2O$). The suspension was then dispersed using a high energy tip sonicator at 20 W for 20 min, followed by centrifugation at 50,000 g for 3 hours. The supernatant containing suspended SWCNT was decanted off and sonicated for a further 20 min. The Vis/IR (300-1800 nm) absorbance spectrum was recorded immediately after sonication, using a Perkin Elmer Fourier transform Lambda 950 spectrometer.

## 4.4 Results

### 4.4.1 Overview

The reduction and carbon deposition procedure outlined in the experimental section was followed using both empty alumina boats, and using magnesium oxide powder in the alumina boat, without the loading of a metal catalyst. These experiments were performed as a blank run to check the underlying substrate gave no structured carbon formation and remained as the metal oxide[146]. TEM and Raman analysis of the end products indeed showed no evidence of CNTs or any other ordered carbon structures.

Blank catalyst experiments were performed using 5 wt% metal loaded MgO (of each metal compound outlined in the experimental section), following the outlined procedure for the reduction of the metal species at 1000°C under a 0.5 Lmin$^{-1}$ flow of hydrogen. The samples were taken out before the carbon feedstock decomposition step, in order to analyse the distribution of the metals on the MgO substrate. TEM analysis revealed no major differences between the distribution of the different metals on the nano-crystalline MgO surface. The low metal wt.% used (5 wt.%) seems to prevent the sintering of larger metal nanoparticles, a size distribution below 10 nm was found. The iron oxide nanoparticles showed a more uniform metallic iron distribution (reduction of iron oxide to metallic iron occurs above 770 K in hydrogen[147, 148]), with a size range of around 10 nm. It is known that the size distribution of the metal nano-particulate catalyst plays a major role in the type, and diameter, of the CNTs synthesised[149]. TEM analysis performed on the catalysts after reduction to their constituent metals, shows similar size distribution between all the samples (apart from the preformed iron oxide nanoparticles). This therefore minimises the effect of particulate size and allows for comparison between the actual metal species type and integral properties of the metal nanoparticles; such as: melting point, vapour pressure, carbon solubility, and electronegativity.

The formation of carbon structures was investigated from the CVD of methane and methane/hydrogen mixtures over various metal catalysts which were supported on magnesium oxide, and performed at elevated temperatures (see table 4-2). Under the experimental conditions outlined in table 4-2 it was found that cobalt was the most effective catalyst for the formation of SWCNTs, and that the structural purity was enhanced by the addition of hydrogen during the reaction. Iron and nickel supported on MgO also proved effective in the production of SWCNTs. It should, however, be noted that although the presence of SWCNTs were observed by Raman, optical spectroscopy and TEM imaging in the cobalt, iron, and nickel samples, the TEM also showed the presence of double wall carbon nanotubes (DWCNTs) to a lesser extent, and possibly also multi-walled carbon nanotubes (MWCNTs).

No other catalysts gave a definitive, positive-result for SWCNT formation, however, the production of multi-walled carbon nanotubes with high yields was seen for manganese and chromium supported on MgO. The manganese catalyst produced large diameter tubes with high wall numbers, and the chromium catalyst gave smaller diameter tubes with a lower number of concentric walls. To the author's knowledge, this is the first time chromium as a solo catalyst has shown to be effective in the production of MWCNTs, there is also very little literature on the use of manganese as a solo metal catalyst for MWCNT formation[150].

Gold and silver showed a limited ability in the production of CNTs, however did produce high yields of novel carbon nano-fibre (CNF) structures. Apart from the three well studied catalysts (iron, cobalt and nickel) all other metals required the presence of hydrogen during the reaction in order to form any ordered carbon species.

| Metal Catalyst (Electronegativity in Pauling Units) | Experiment Denotation, Conditions: Temperature and Methane : Hydrogen flow ratio. | | | | | | |
|---|---|---|---|---|---|---|---|
| | I 810°C No $H_2$ | II 910°C No $H_2$ | III 1010°C No $H_2$ | IV 1010°C 2:1 | V 1010°C 2:2 | VI 1010°C 2:3 | VII 1010°C 2:6 |
| Zirconium (1.33) | - | - | - | - | - | - | - |
| Manganese (1.55) | - | - | - | - | MWCNT (High Wall No.) | MWCNT (High Wall No.) | - |
| Vanadium (1.63) | - | - | - | - | - | - | - |
| Chromium (1.66) | - | - | - | MWCNT (Low Wall No.) | MWCNT (Low Wall No.) | - | - |
| Iron (1.83) | SWCNT | - | SWCNT | SWCNT | SWCNT | SWCNT | - |
| Cobalt (1.88) | SWCNT | SWCNT | - | SWCNT | SWCNT | SWCNT | SWCNT |
| Nickel (1.91) | SWCNT | - | SWCNT | SWCNT | - | SWCNT | SWCNT |
| Silver (1.93) | - | - | - | - | - | CNT/ CNF | - |
| Gold (2.54) | - | - | - | CNT/ CNF | CNF | CNF | - |

**Table 4-2** Comparative table showing the carbon structures synthesised using each catalyst, over every experimental condition of the chemical vapour deposition process, using a 5 wt% metal catalyst loading on a powdered MgO substrate. (Blank boxes indicate only amorphous carbon formation).

## 4.4.2 Single Wall Carbon Nanotubes

Solo-catalysts: cobalt, iron and nickel (loaded onto a powdered magnesium oxide substrate) proved to be effective in the production of SWCNT. The cobalt catalyst showed the highest purity of nanotubes and produced SWCNT over the greatest range of conditions (as shown in table 4-2). Iron and nickel proved to be less effective in flexibility of conditions and in the yield obtained, however, still gave positive results for SWCNT.

## 4.4.3 Cobalt

The following section presents the results obtained from the CVD synthesis of SWCNT and DWCNT using cobalt as the solo-metal catalyst.

### 4.4.3.1 Imaging:

The images in fig. 4-2 show SWCNT, DWCNT, and triple-walled CNT, they illustrate the majority growth of bundled nanotubes and the presence of amorphous carbon which coats the tube exterior prior to any purification steps. The images show tubes 1-3 nm in diameter, with lengths extending into the micrometer range.
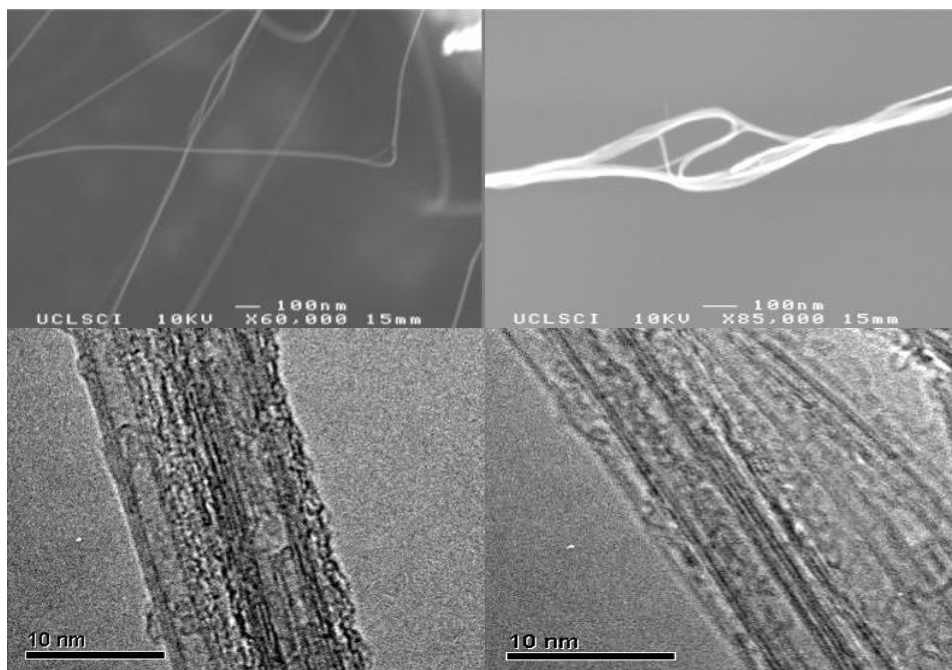


**Figure 4-2** SEM and TEM images of as grown SWCNT. Top left) SEM Cobalt (Conditions VI, 1010°C, 2:3 Me:$H_2$).Top right) SEM Cobalt (Conditions V, 1010°C, 2:2 Me:$H_2$)   Bottom left) TEM Cobalt (Conditions IV, 1010°C, 2:1 Me:$H_2$)   Bottom right) TEM Cobalt (Conditions IV, 810°C, No $H_2$).

### 4.4.3.2 Raman:

Raman spectra of the as-grown products were taken over two laser excitation energies and multiple sampling spots on the powdered products.
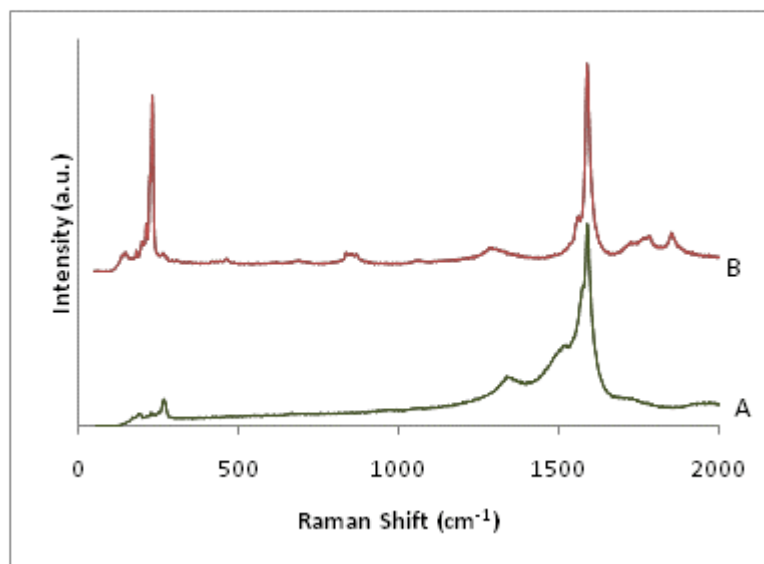


**Figure 4-3** Raman spectra of SWCNT synthesized using CVD and a cobalt catalyst. Cobalt (Conditions I, 810°C, No $H_2$) . A) 514.5 nm laser excitation. B) 785 nm laser excitation.
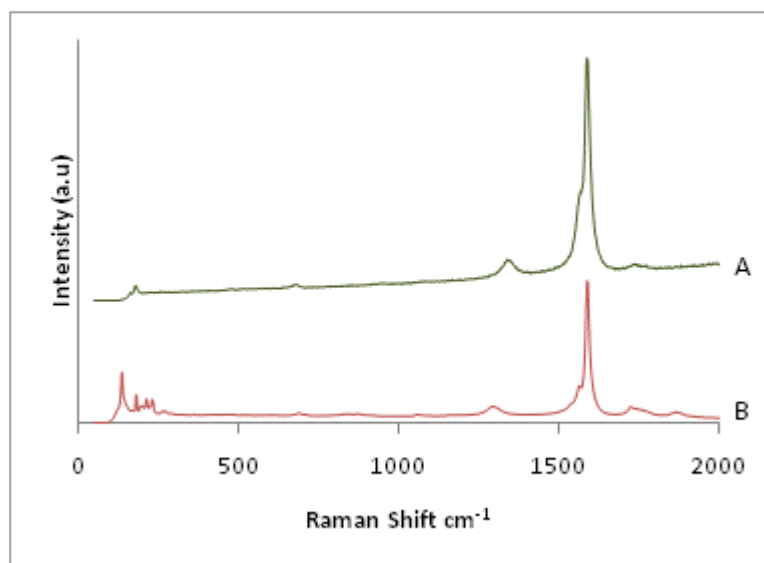


**Figure 4-4** Raman spectra of SWCNT synthesized using CVD and a cobalt catalyst. Cobalt (Conditions VII, 1010°C, 2:6 Me:$H_2$) . A) 514.5 nm laser excitation (plot scaled by a factor of 10 for clarity) B) 785 nm laser excitation.

133

Fig.4-3 and fig.4-4 show representative Raman spectra taken from the cobalt catalyst at a temperature of 810°C with no hydrogen flow, and a temperature of 1010°C with a 2:6 Me:$H_2$ ratio, respectively (Conditions I and VII from table 4-2). High intensity radial breathing modes at the low frequency end of the spectra can be seen at 150-350 cm$^{-1}$, these peaks are unique to single wall carbon nanotubes and are caused by the radial expansion of the tube walls. The high frequency end of the Raman spectrum shows the G-band at 1590 cm$^{-1}$: caused by the optical phonon mode between two dissimilar carbon atoms in the unit cell which is present in all graphitic structures[42].

Splitting of the G band is noted in the two spectra. This is caused by symmetry breaking effects from the curvature of the graphitic lattice when in its tube form, leading to phonon confinement in the circumferential direction. The main peak (G+) at 1590 cm$^{-1}$ corresponds to vibrations along the axis of the tube, the minor peak (G-) at 1570 cm$^{-1}$ is due to vibrations in the circumferential direction and is unique to SWCNT[151]. The D-band, seen at 1300 cm$^{-1}$, corresponds to the disordered mode, which relies on scattering caused by defects in the structure of the carbon lattice, nanotube caps, bending of the tube axis, or amorphous carbon. This band is present in all carbon allotropes. The D-band can be used to assess the quality of the sample by finding the ratio of the D and G+ peaks. The spectra shown in fig.4-3 and fig.4-4 have a D/G ratio of 5 % and 6% respectively which indicates an extremely high structural quality in the carbon lattice of the nanotubes even with the presence of amorphous carbon in the sample[39].
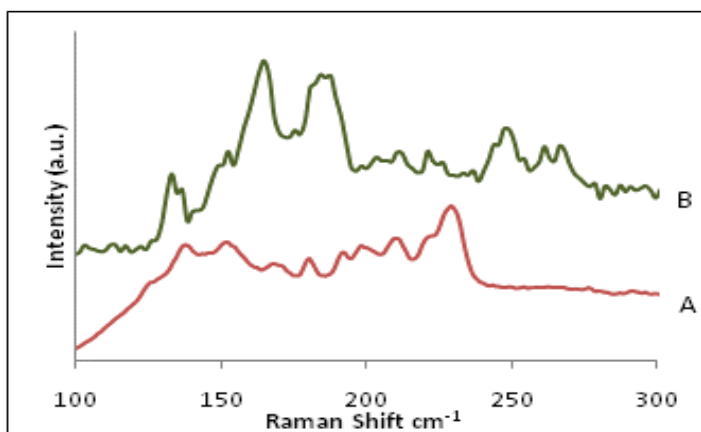
**Figure 4-5** Raman spectra of the low frequency SWCNT radial breathing mode. Cobalt (Conditions VI, 1010°C, 3:2 Me:$H_2$).  A) 785 nm laser excitation B) 514.5 nm laser excitation.

Fig.4-5 shows the Raman spectra of the low frequency SWCNT radial breathing modes from the cobalt catalyst under conditions VI. The two spectra were taken using Raman laser excitation energies of 715 nm and 514.5 nm. Variations in the two spectra arise from the resonant Raman effect: whereby the excitation laser energy is close to that of an optical absorption caused by the band gaps, or so-called van–Hove singularities, present in the semiconducting SWCNT, these cause Raman intensity to become enhanced because more light can be absorbed by those particular tubes in resonance with the laser energy. This photonic-phononic coupling results in a different spread of radial breathing modes becoming enhanced with each laser, because differing diameter and chirality tubes have different energy band-gaps. Increasing the laser frequency should preferentially enhance higher frequency modes, this can be seen in fig.4-5, where the 514.5 nm laser gives a RBM signal at higher Raman shift energies[42].

The frequency of the radial breathing modes show a strong dependence on the diameter of the excited nanotubes, thus allowing for diameter distribution to be approximated from the spectra. Using the relationship $d(nm) = 248/\nu$ (where $\nu$ is the frequency of the RBM $(cm^{-1})$), it is possible to calculate the diameter range, excited by the red laser, at 1.1-1.8 nm distribution, and by the green laser a 0.9-1.9 nm full diameter range of tubes in the cobalt catalyst conditions VI sample[152]. This analysis was repeated for each of the cobalt catalyst conditions which produced SWCNT, the results are presented in fig.4-6. The diameter distributions are consistent across the experimental conditions, showing no obvious trend in diameter distribution with conditions.
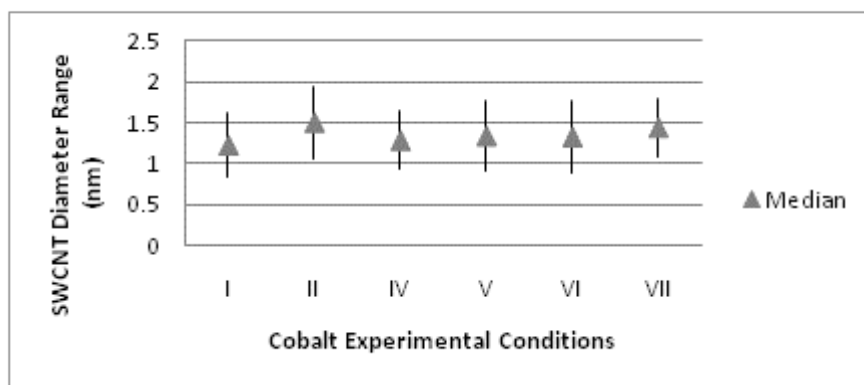


**Figure 4-6** Plot showing the diameter distribution range and the median diameter value of SWCNTs synthesized using a cobalt catalyst over a range of temperature and methane:hydrogen conditions (see table 4-2). Values calculated from the high and low values of the radial breathing modes, as-seen in the Raman spectra using red and green excitation lasers.

### *Vis/Near IR absorption*

The optical absorptions in the visible and near infrared were recorded for the as-grown SWCNT using a technique outlined by O'Connell et al.[145] which is detailed in the experimental section 4-3. The technique relies on the suspension of individually isolated SWCNT in solution, using surfactant molecules to stabilise and prevent bundling of nanotubes into ropes. Bundling must be avoided to limit quenching of the electronic transitions taking place during the photonic absorption process. Fig.4-7 shows typical spectra taken over 600–1300 nm optical wavelengths.
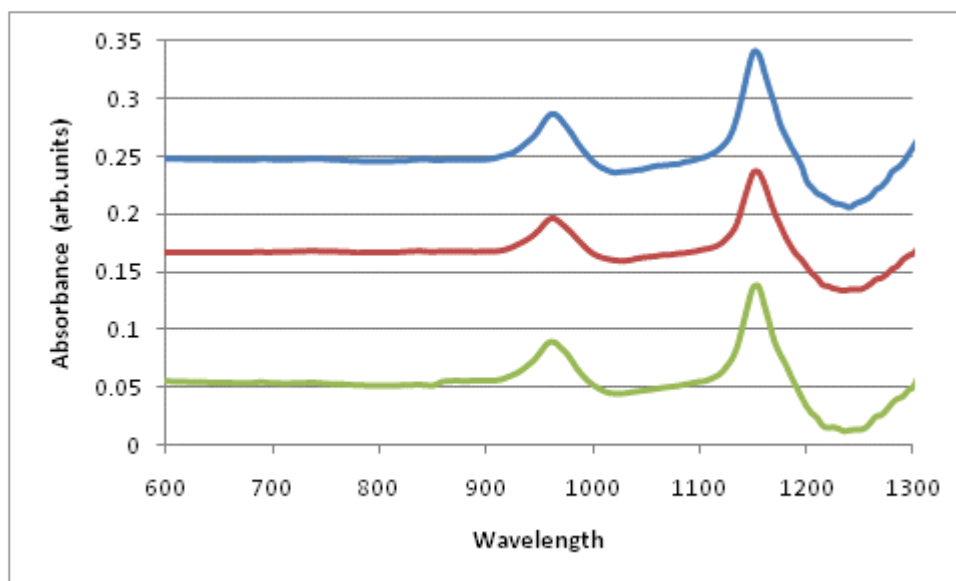
**Figure 4-7** Vis/near IR spectrum of the optical band gap measurements from the as-grown SWCNT suspended in water. *Blue)* Cobalt (Conditions I, NoH$_2$ 810°C) *Red)* Cobalt Conditions IV, 2:1 Me:H$_2$ 1010°C, *Green)* Cobalt (Conditions VI, 2:3 Me:H$_2$ 1010°C).

Major peaks can be seen at 950±25 nm and 1150±50 nm (corresponding to 1.3 ± 0.03 eV and 1.08 ± 0.05 eV respectively) for each of the SWCNT samples, this demonstrates a similar spread of optical band gaps in each sample, and hence similar diameter and chirality distributions. Using the Katuara plot given in fig.4-8, over the nanotube diameter range of 0.85 − 1.9 nm present (as indicated by the Raman and TEM analysis), we can assign the two absorbance's to transitions in SWCNT density of states[153, 154]. The first peak at 950 nm can be attributed to both secondary transitions ($^SE_{22}$) of semiconducting nanotubes in the 1.2 −1.3 nm range, and the first metallic nanotube transitions ($^mE_{11}$) in the diameter range 1.7-1.9 nm, as indicated on the Katuara plot in fig.4-8. The next absorption at 1150 nm can be attributed solely to semiconducting nanotubes in the diameter range 1.5-1.7 nm absorbing across the second transition ($^SE_{22}$).

137
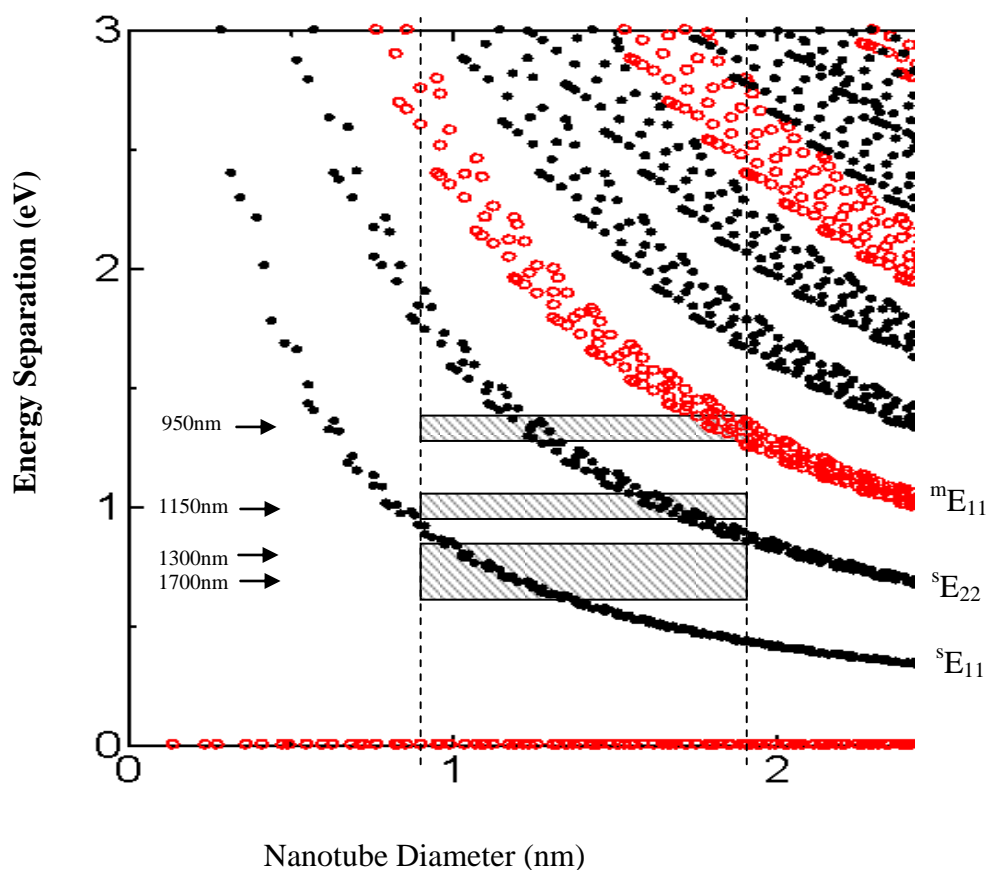
**Figure 4-8** Kataura plot showing the gap energies in the density of states for SWCNT with a distribution of diameters. Closed circles indicate semiconducting tubes, Open circles indicate metallic tubes. Labelled on the plot  are the corresponding wavelengths and boxed areas show the nanotubes (in the 0.85-1.9nm diameter range) exited by these wavelengths. Modified exert from[153].
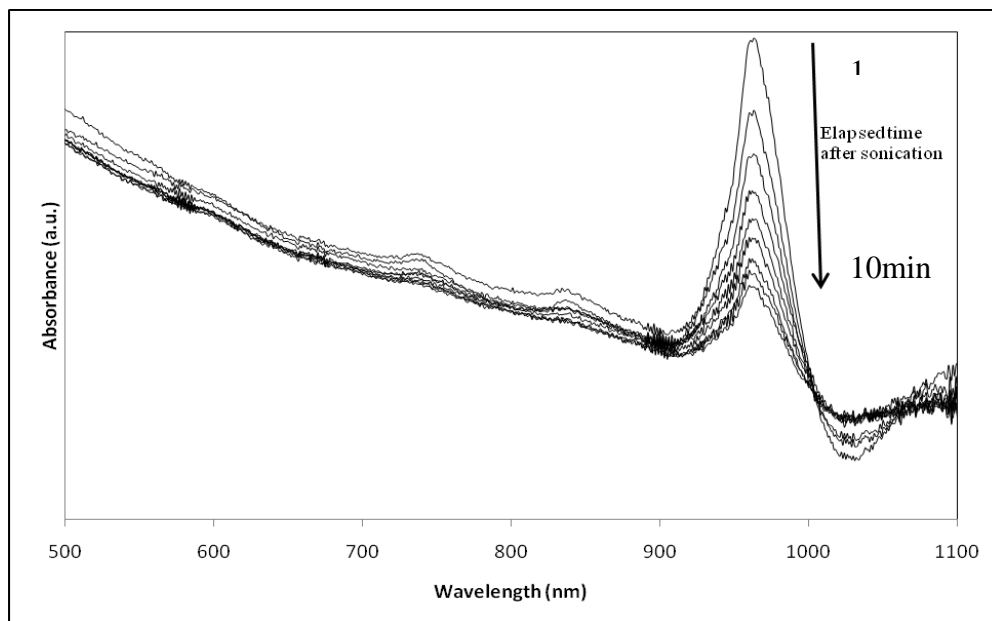
**Figure 4-9** Vis/near IR spectrum of the optical band gap measurements from the as-grown SWCNT from cobalt catalyst (Conditions VI, 1010°C, 3:2 Me:$H_2$) suspended in water. Each consecutive peak represents 1 minute of elapsed time after removal of the solution from the sonicator.

The graph depicted in fig.4-9 illustrates the time dependent rebundling of the carbon nanotubes isolated in suspension. The peak intensity for the 1.3 eV transition at 950 nm, is shown to decrease with time elapsed after removal of the solution from the sonicator. This demonstrates the electronic quenching which takes place as the nanotubes re-bundle and causes the peak intensity to drop, illustrating the importance of rapid spectral acquisition after removal of the suspension from the sonicator.

Additional optical measurements were performed using solutions prepared by a modification of the method outlined earlier: by replacing $H_2O$ with $D_2O$ a greater wavelength range could be monitored. Fig.4-10 shows the results for cobalt conditions I, cobalt conditions IV, and cobalt conditions VII, which demonstrate strong absorptions from 1600-1750 nm (0.78 eV – 0.71 eV), these absorptions can be attributed to the first transitions ($^sE_{11}$) of semiconducting nanotubes in the diameter range 1-1.3 nm, again indicated on the Katuara plot in fig.4-7.

139
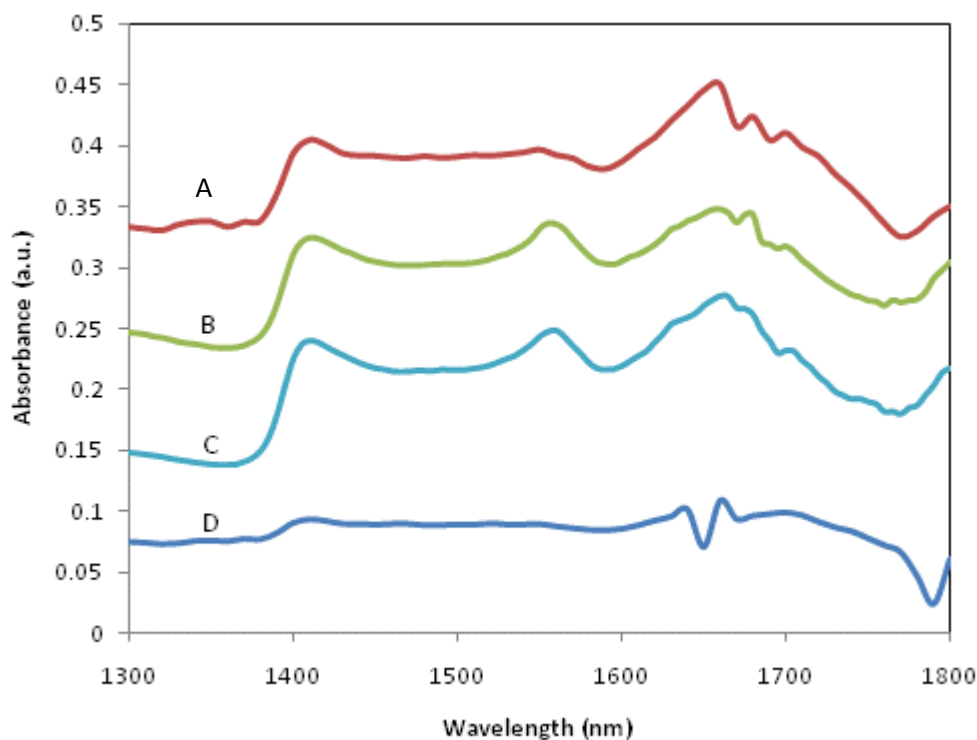
**Figure 4-10** Vis/near IR spectrum of the optical band gap measurements of as grown SWCNT suspended on $D_2O$. *A)* Cobalt (Conditions I, 800°C No $H_2$). B) Cobalt (Conditions IV, 1010°C, 2:1 Me:$H_2$). C) Cobalt (Conditions VII, 1010°C, 1:3 Me:$H_2$). D) Blank spectra of the cobalt catalyst and the MgO support after reduction in $H_2$ atmosphere at 1000°C

### 4.4.4 Iron

The following section presents the results obtained from the CVD synthesis of SWCNT and MWCNT using iron pre-formed nanoparticles as the solo-metal catalyst

#### *4.4.4.1 Imaging:*

SEM and TEM imaging (see fig. 4-11) reveals the presence of tubular structures, resulting from the CVD of methane over the iron nano-particulate catalyst supported on magnesium oxide. It was noted during the imaging that the number of tubular structures, in the as-deposited materials, were far fewer than in the cobalt samples. The CNT identified were micrometers in length and ranging from 1 nm up to larger ~20 nm diameter tubes, indicating the likely presence of both MWCNT and SWCNT.
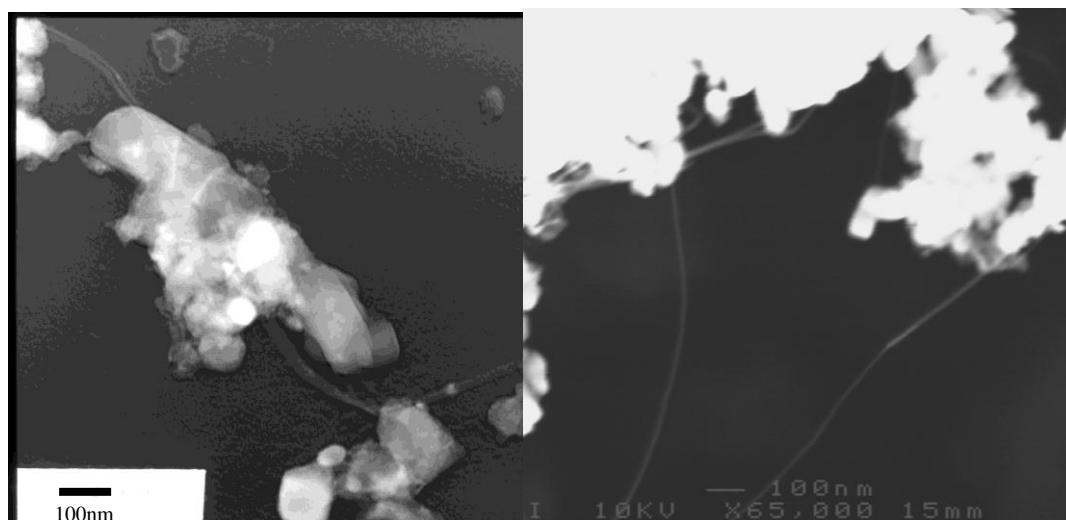
**Figure 4-11** Images of SWCNT/DWCNT from iron catalyst experiments *Left)* Iron (Conditions I) (TEM image). *Right)* Iron (Conditions V) (SEM image).

### 4.4.4.2 Raman:

The following section presents the Raman spectra obtained from the CVD SWCNT produced using preformed iron nano-particles as the solo-metal catalyst.
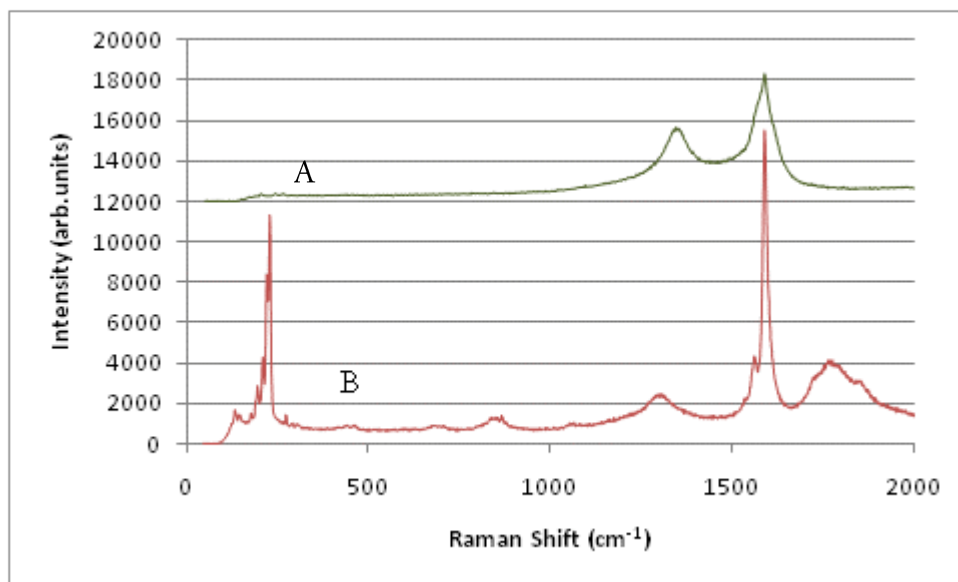


**Figure 4-12** Raman spectra of SWCNT from Iron (Conditions I, 810°C, No $H_2$). *A)* 514.5 nm laser (scaled by a factor of 10 for clarity). *B)* 785 nm laser.

141
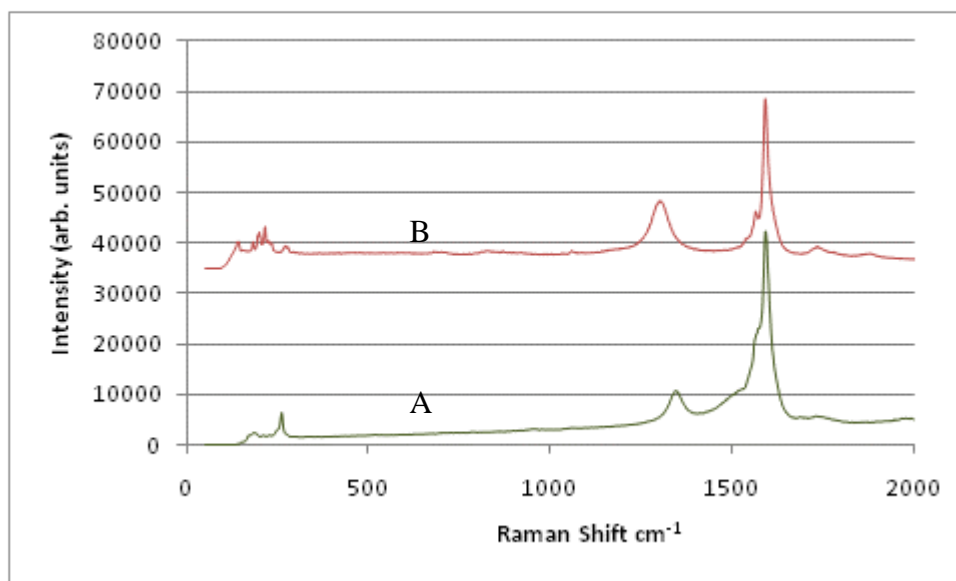
**Figure 4-13** Raman spectra of SWCNT from Iron (Conditions V, 1010°C, 2:2 Me:H$_2$). *A)* 514.5 nm laser. *B)* 785 nm laser.

Fig.4-12 and fig.4-13 show representative spectra taken from the as-deposited products. The following conditions gave a positive result for SWCNT based on the Raman profiles: iron catalyst conditions; I, III, IV, V, and VI. The spectra show the characteristic SWCNT profile including strong radial breathing modes and a splitting of the G band. However, it should be noted that all the Raman spectra taken from SWCNT synthesized using iron nano-particles, show a high D/G ratio, thus indicating larger levels of disorder than previously shown in the cobalt samples. The iron catalyst conditions I spectra show D/G ratios of 8% and 40% for the red and green laser respectively. The iron catalyst conditions V spectra show D/G ratios of 30% and 12% for the red and green laser respectively. This trend was present across all samples, thus indicating that over the experimental conditions outlined, the use of iron nanoparticles results in lower yields of CNT, more MWCNT formation, and a more disordered structure in those samples which did yield SWCNT.

## 4.4.5 Nickel

The following section presents the results obtained from the CVD synthesis of SWCNT and DWCNT using nickel as the solo-metal catalyst

### *4.4.5.1 Imaging:*

SEM imaging (see fig.4-14) reveals the presence of tubular structures in the samples from the CVD of methane over the nickel catalyst supported on magnesium oxide. The number of tubes present was lower in all samples than that of the cobalt samples. The tubes identified were micrometers in length and ranging in diameter from 1 nm upwards. However, larger diameter tubes like those found with the iron catalyst were not identified.
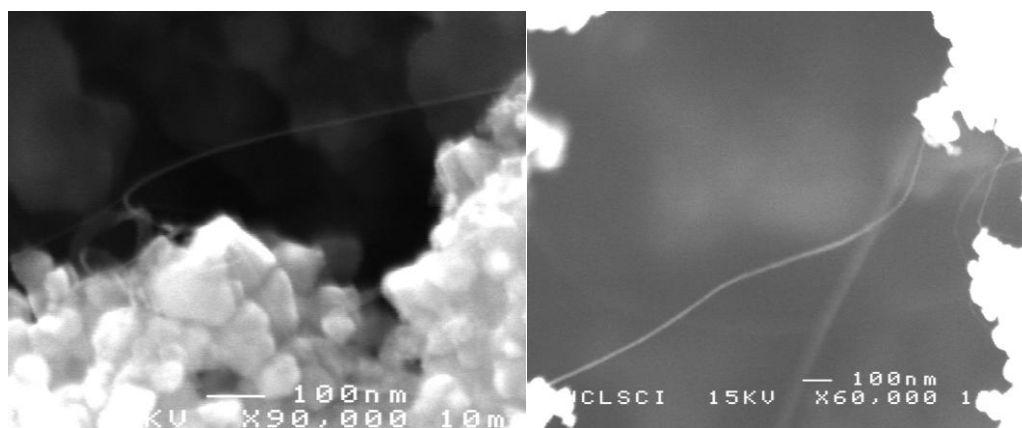


**Figure 4-14** Images of SWCNT/DWCNT from nickel catalyst experiments *Left)* Nickel (Conditions VI) (SEM image). *Right)* Nickel (Conditions VII) (SEM image).

### Raman:

The following section presents representative Raman spectra obtained from SWCNT produced using nickel as the solo-metal catalyst.
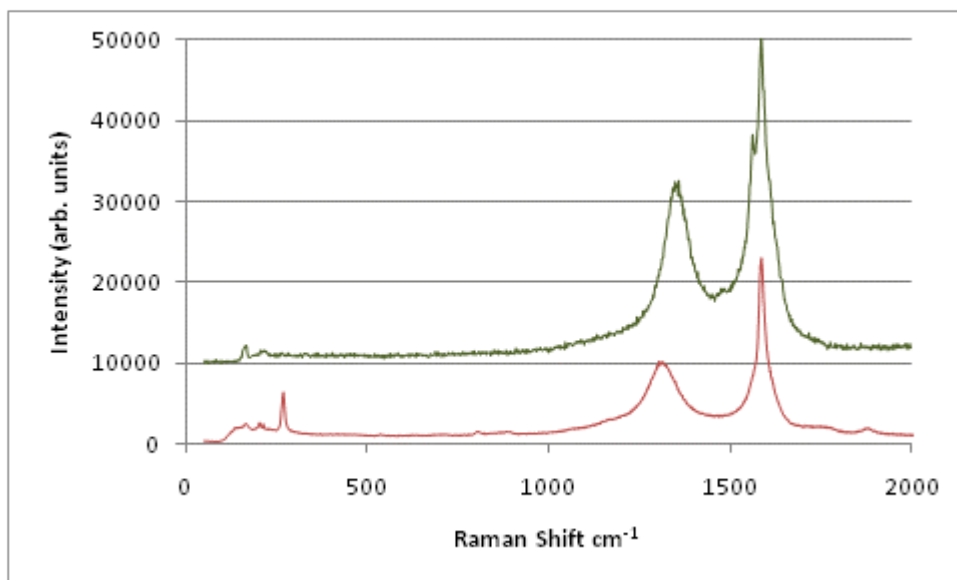


**Figure 4-15** Raman spectra of SWCNT from nickel (Conditions III, 1010°C, No $H_2$) *A)*514.5 nm laser (scaled by a factor of 10 for clarity) *B)*785 nm laser.
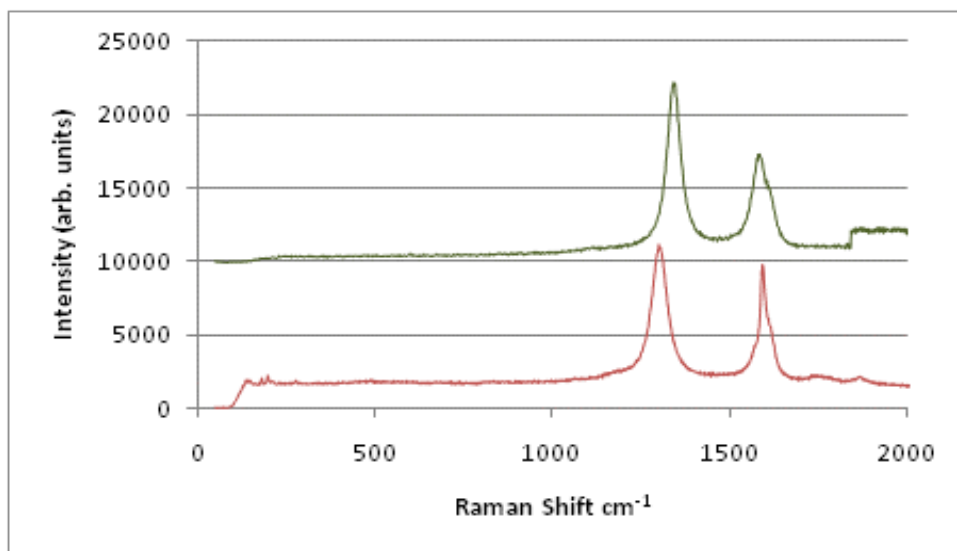


**Figure 4-16** Raman spectra of SWCNT from nickel (Conditions VI, 1010°C, 2:3 Me:$H_2$) *A)*514.5 nm laser (scaled by a factor of 10 for clarity) *B)*785 nm laser.

Fig.4-15 and fig.4-16 show representative spectra taken from the as-deposited products synthesized using a nickel catalyst. The following conditions gave a positive result for SWCNT based on the Raman profiles, nickel conditions I, III, IV, VI and VII. The spectra show the characteristic SWCNT radial breathing modes, however they are very weak. The splitting of the G band is lost in all but one of the samples due to broadening of the G+ and G- bands. This broadening is caused by a high level of defects, which in turn is indicated by the high D/G ratio. The nickel conditions III spectra show D/G ratios of 33% and 44% for the red and green laser respectively. The nickel conditions VI spectra show D/G ratios of 115% and 180% for the red and green laser respectively. The use of nickel results in lower yields of SWCNT and a more disordered structure, in those samples which did yield SWCNT, when compared to the use of cobalt.

### 4.4.6 Multi-Walled Carbon Nanotubes

Manganese and chromium metal catalysts loaded onto a powdered magnesium oxide substrate proved to be effective in the production of high yields of MWCNTs. The manganese catalyst produced large diameter MWCNTs with high wall number (approx. 100) over manganese conditions V, and manganese catalyst conditions VI. The chromium catalyst produced MWCNTs with a lower wall number (5- 20 walls) over chromium conditions IV and chromium conditions V as shown in table 4-2.

### 4.4.7 Manganese

The following section presents the results obtained from the CVD synthesis of MWCNT using manganese as the solo-metal catalyst.

### 4.4.7.1 Imaging:

Fig.4-17 shows SEM and TEM images taken from the MWCNTs grown using a manganese catalyst supported on MgO. The SEM reveals a high yield of the MWCNT material, which is growing in large aggregates on top of the magnesium oxide substrate. The TEM images reveal a large wall number: typically showing around one hundred layers per tube wall. The tubes have grown highly kinked in nature and evidence of large spherical structures can be seen inside the hollow interior of the MWCNTs.
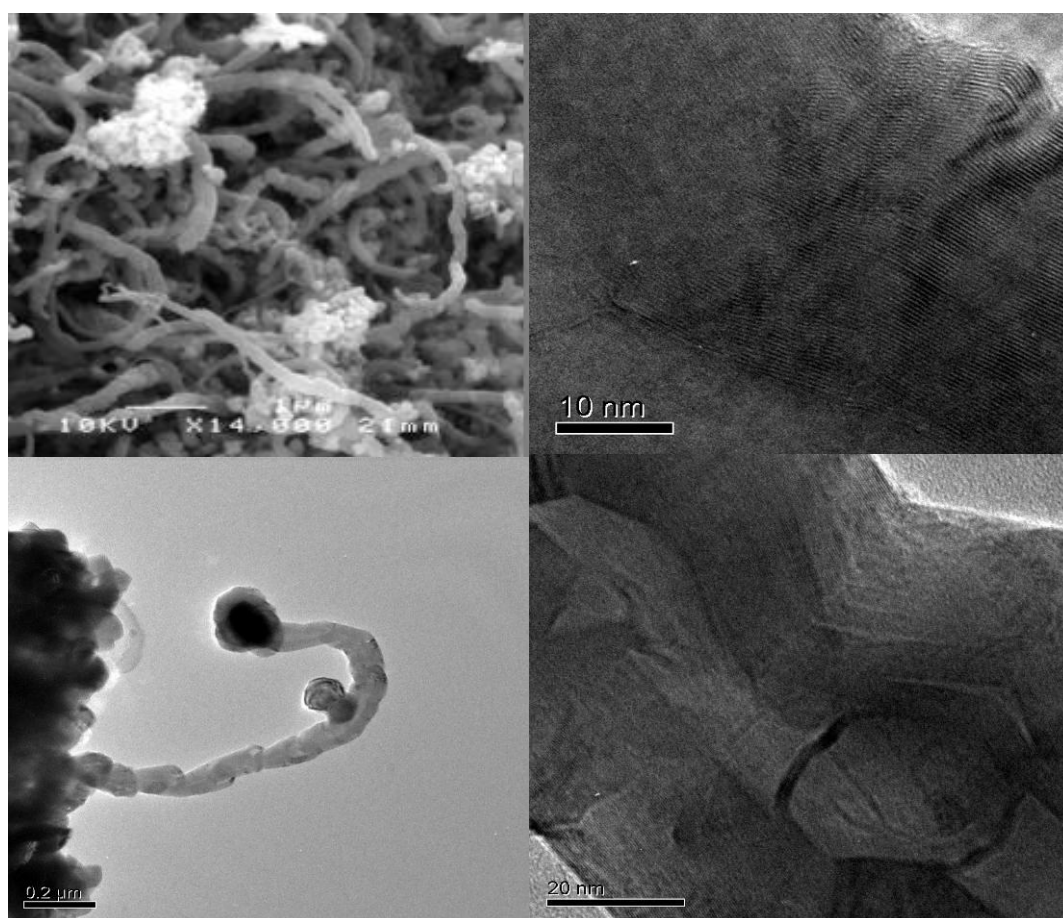


**Figure 4-17** Electron microscopy images of as-grown MWCNTs, synthesised by CVD using manganese catalyst loaded (5 wt%) MgO substrate.; Top Left) SEM manganese (Conditions VI, 1010°C, 2:1 Me:H$_2$) Top Right) TEM manganese (Conditions VI)  Bottom Left) Low-Mag TEM of kinked tube manganese (Conditions V, 1010°C, 2:3 Me:H$_2$.  Bottom Right) TEM of capped MWCNT manganese (Conditions V).

### *4.4.7.2 Raman:*

Representative Raman spectra obtained from the MWCNT produced using manganese as the solo-metal catalyst supported on MgO, are shown in fig. 4-18.
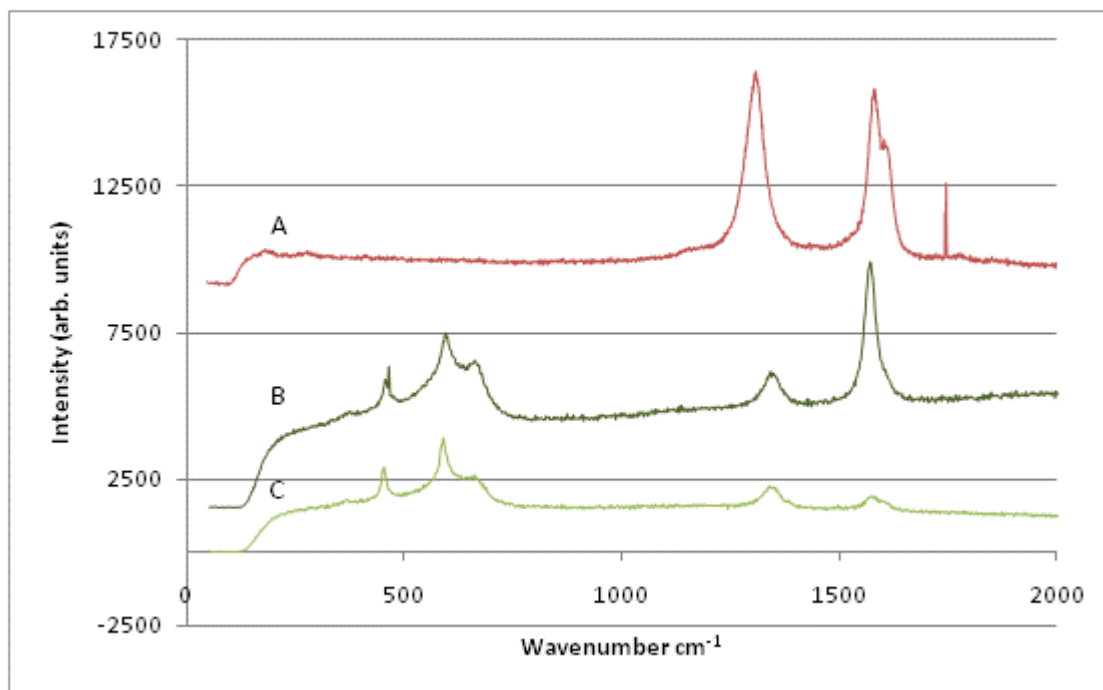


**Figure 4-18** Raman spectra of as-grown MWCNTs, synthesised by CVD using manganese metal catalyst loaded (5 wt%) MgO substrate. *A)* Manganese (Conditions VI, 1010°C , 2:3 Me:$H_2$) 785 nm laser. *B)* Manganese (Conditions VI, 1010°C, 2:3 Me:$H_2$) 514.5 laser. *C)* Manganese (Conditions V, 1010°C, 2:2 Me:$H_2$) 514.5 laser.

The spectra shown in fig.4-18 display G band and D bands which are associated with all carbon allotropes, and present over both the red and green laser energies. The disorder D-band is very high in all the spectra, indicating a large level of disorder. Radial breathing modes are not present, as these are only seen in SWCNT where the 'breathing' phononic vibrations of the small diameter tubes are unimpeded by surrounding concentric tube walls. The green laser spectra demonstrate an unusual profile around the $450 – 700$ cm$^{-1}$ range, which has similarities with the spectra of $C_{60}$ or $C_{70}$ fullerene molecules [154, 155]. Phonon modes at 465, 600 and 670 cm$^{-1}$ are too high frequency for SWCNT radial breathing modes but may be explained by the presence of fullerene molecules in the sample.

147

## 4.4.8 Chromium

The following section presents the results obtained from the CVD synthesis of MWCNT using chromium as the solo-metal catalyst.

### *4.4.8.1 Imaging:*

Electron microscopy was used to image the as-grown material; fig.4-19 shows images of the MWCNTs taken using SEM and TEM, and grown from the chromium catalyst supported on MgO. The SEM images illustrate high yield growth of MWCNTs in large aggregates, whilst the TEM imaging and analysis indicates a range of wall numbers from 5 up to 20 layers deep. Analysis of the images gives a 0.35 nm lattice spacing, which is consistent with that of graphitic interlayer spacing (0.335 nm)[156].
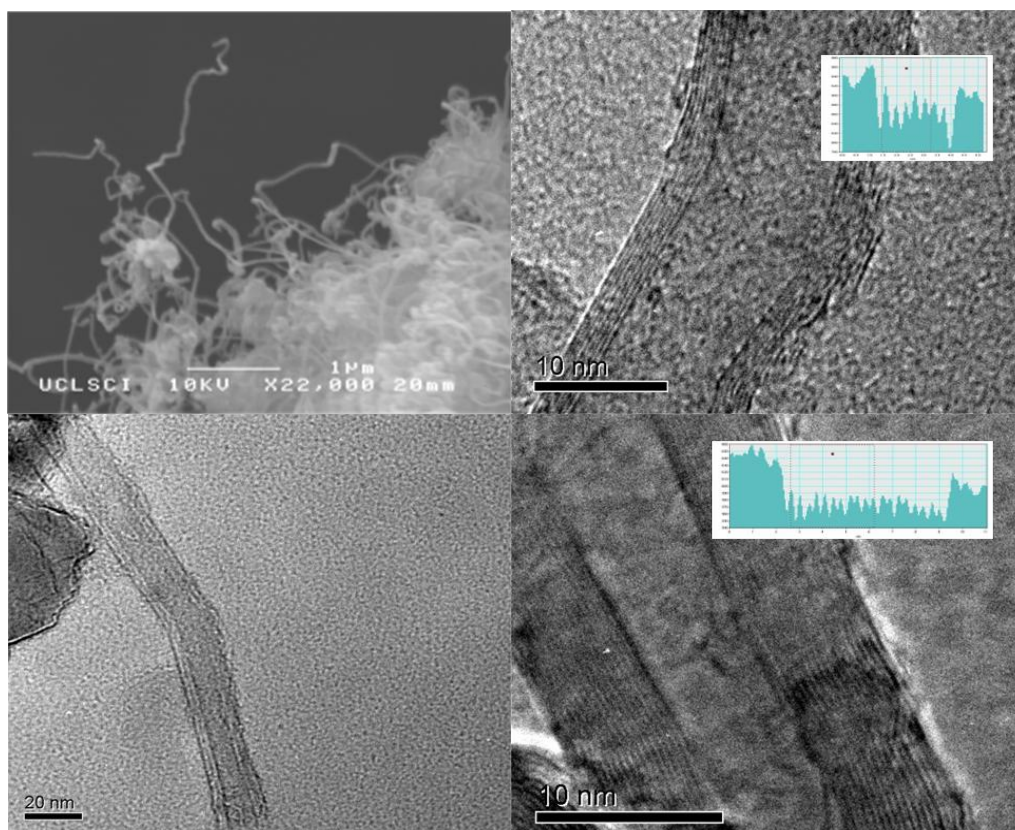


**Figure 4-19** Electron microscopy images of as-grown MWCNTs, synthesised by CVD using chromium loaded (5 wt%) MgO substrate. MWCNTs *Top Left)* SEM chromium (Conditions IV, 1010°C, 2:1 Me:H$_2$). *Top Right)* TEM chromium (Conditions IV, 1010°C, 2:1 Me:H$_2$) (Inset shows profile of multi-wall). *Bottom Left)* TEM image chromium (Conditions IV). *Bottom Right)* TEM chromium (Conditions IV) (Inset shows profile of multi-wall).

### 4.4.8.2 Raman:

A representative Raman spectrum obtained from the MWCNT produced using chromium as the solo-metal catalyst supported on MgO, are shown in fig.4-20.
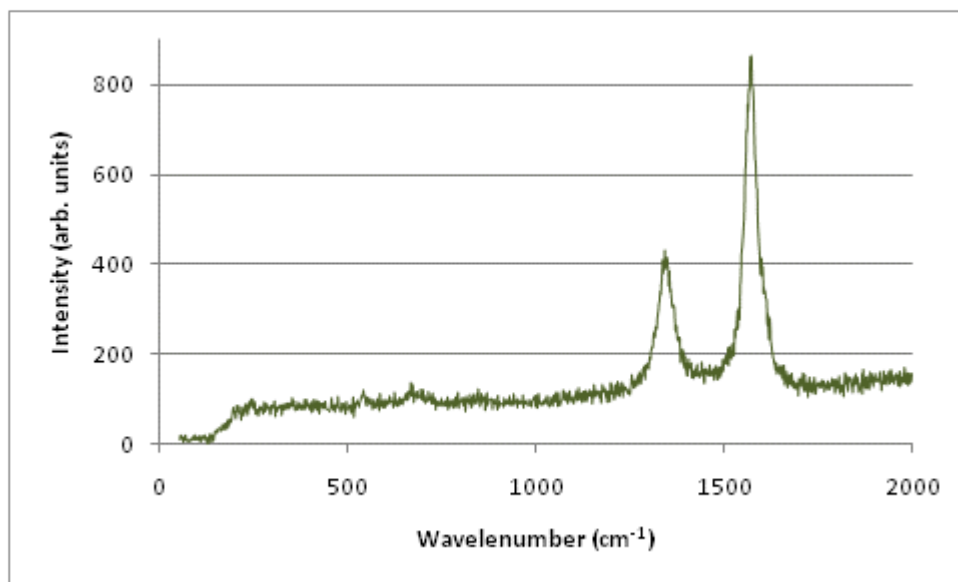


**Figure 4-20** Raman spectrum of as-grown MWCNTs, synthesised by CVD using chromium metal catalyst loaded (5 wt%) MgO substrate. Chromium (Conditions V, 1010°C , 2:2 Me:$H_2$) 514.5 nm laser.

Fig.4-20 shows an example Raman spectra taken from the powdered product of chromium catalyst conditions V. The carbon product from the reaction displays a characteristic graphitic G mode at 1573 cm$^{-1}$ caused by the optical phonon mode between two dissimilar carbon atoms in the unit cell, which is present in all graphitic structures[42]. This G-mode confirms, alongside the structural spacing analysis, that the tubular structures are graphitic. This peak is shown to be reasonably broadened compared to that of the SWCNTs seen earlier, this can be attributed to two factors: a broadening caused by the simultaneous excitation of many tubes at once leading to a merging of the G- and G+ (where G+ corresponds to vibrations along the axis of the tube and G- is due to vibrations in the circumferential direction), secondly the

broadening can be attributed to the presence of larger diameter tubes in the MWCNTs, which typically give only one large band similar to that of graphite[151].

## 4.4.9 Carbon Nano-fibres

Gold and silver metal catalysts loaded onto a powdered magnesium oxide substrate proved to be effective in the production of high yields of novel carbon nanofibres (CNFs). The growth of these structures was noted under gold conditions IV, V, VI; and silver conditions VI. The conditions required to produce these CNF structures seemed to rely on the presence of hydrogen in the case of both metals.

## 4.4.10 Gold & Silver

The following section presents the results obtained from the CVD synthesis of MWCNT using chromium as the solo-metal catalyst.

### *4.4.10.1 Imaging:*

Electron microscopy reveals the carbon structures synthesised under specific conditions using gold and silver catalysts (see fig.4-21). The SEM and TEM images reveal fibrous structures ~100 nm in diameter and a few microns long. The structure of these CNFs seem to comprise graphitic appendages projecting perpendicularly from a central core, each fibre then seems to consist of two to three of these structures bundled together. The gold catalyst gave a higher structural ordering than the silver catalyst and produced these fibres over a wider range of experimental conditions.
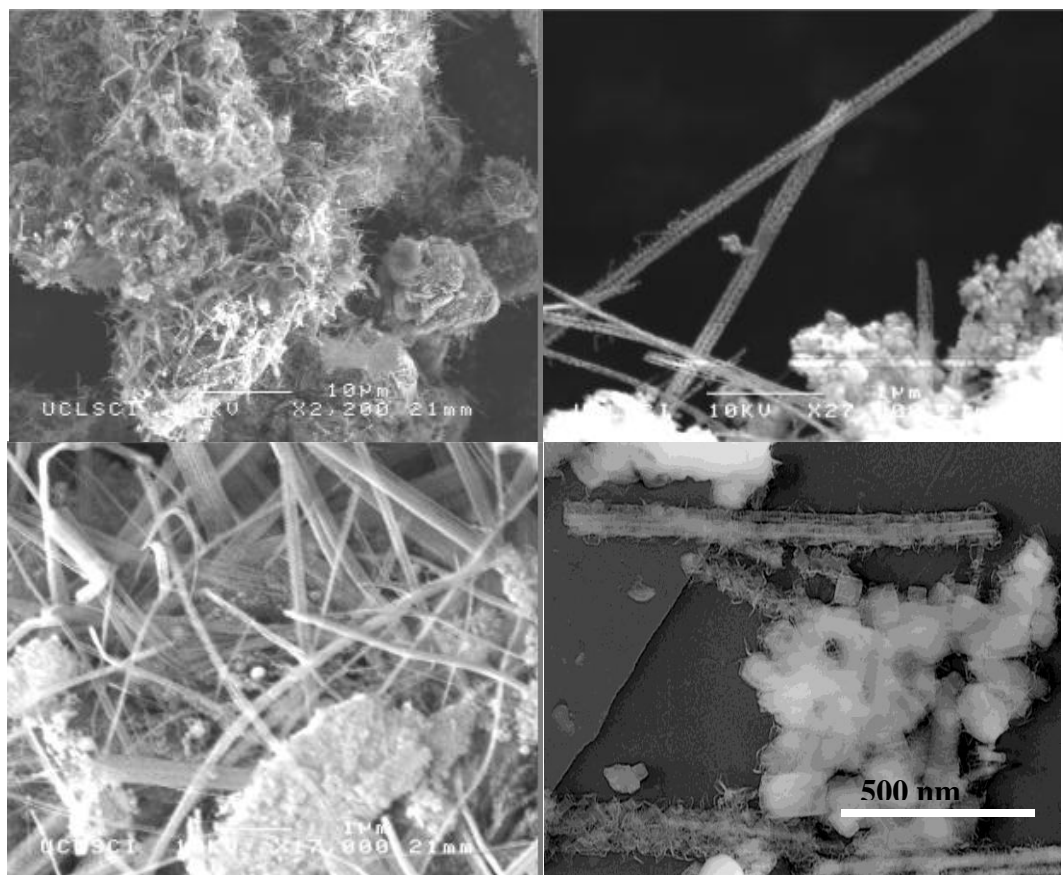
**Figure 4-21** Electron microscopy images of as-grown CNFs, synthesised by CVD using metal catalyst loaded (5 wt%) MgO substrate. *Top Left)* Silver (Conditions VI, 1010°C, 2:3 Me:H$_2$) SEM  *Top Right)* Gold (Conditions VI, 1010°C, 2:3 Me:H$_2$) SEM  *Bottom Left)* Gold (Conditions VI, 1010°C, 2:3 Me:H$_2$) SEM  *Bottom Right)* Gold (Conditions VI, 1010°C, 2:3 Me:H$_2$)TEM

The overall structure seems to be that of a hierarchically arranged collection of graphitic clusters into parallel aligned rods, which form the fibres with a segmented body. These structures were unique to the samples grown using gold and silver catalysts. Electron diffraction patterns were taken from selected beam areas in the TEM sample in order to ascertain the crystal symmetry and d-values for each component in the as-grown product. Fig.4-22 shows example diffraction patterns with the image of the sampling area used, all sampling is taken from the gold catalyst conditions VI sample (1010°C 2:3 Me:H$_2$).

151
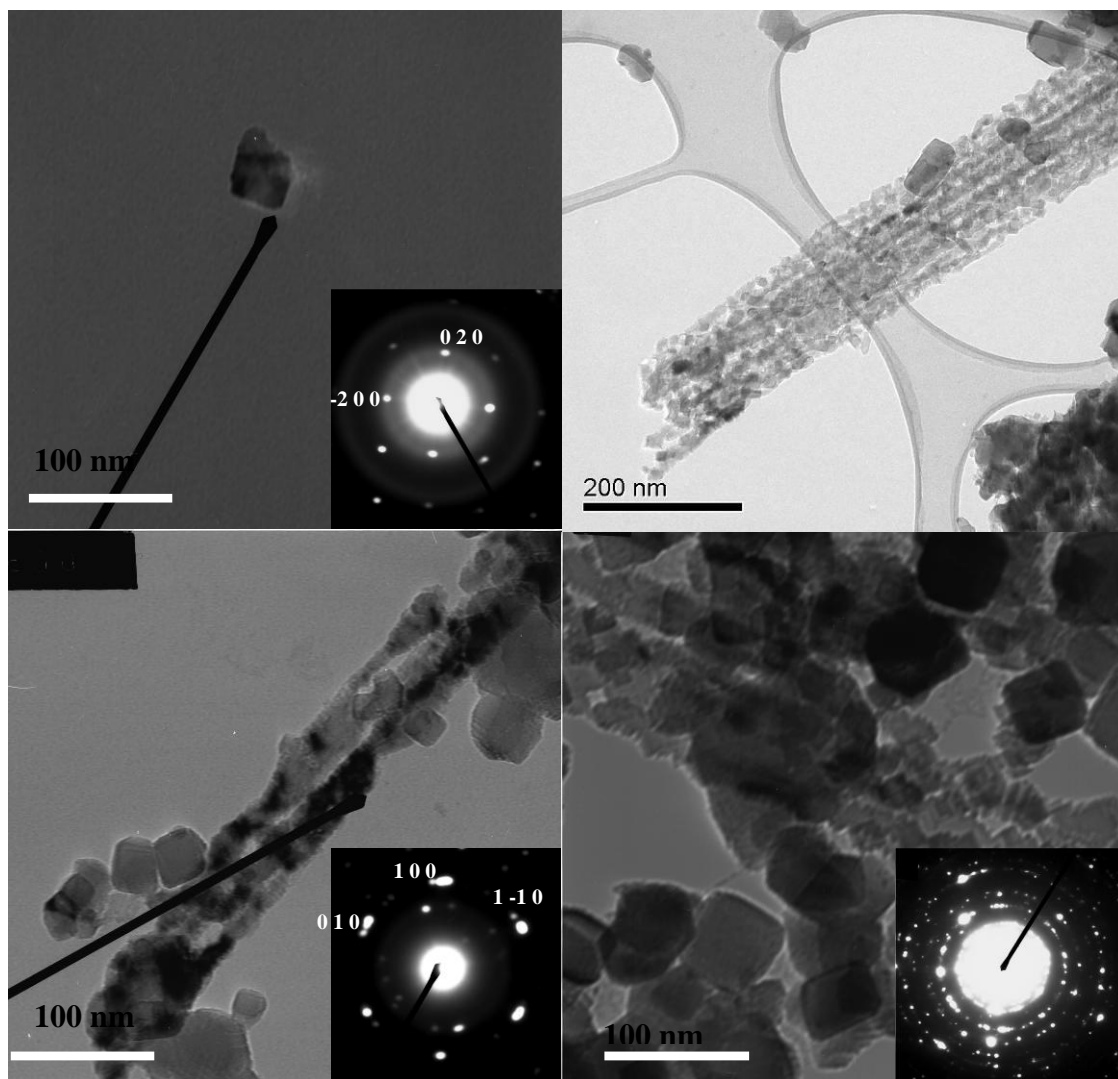
**Figure 4-22** TEM images and their respective electron diffraction patterns from the MgO substrate and the CNF structures, synthesised by CVD with Gold loaded (5 wt%) MgO powdered substrate (Gold conditions VI, 1010°C 2:3 Me:H$_2$). *Top Left)* TEM image of a MgO nanocrystal (inset shows the electron diffraction pattern). *Top Right)* HRTEM of a CNF. *Bottom Left)* TEM image of a CNF (Inset shows the electron diffraction pattern). *Bottom Right* CNF and MgO image (inset shows combined electron diffraction pattern).

The top left diffraction pattern of fig.4-22 indexes to the FM3-M face centered cubic structure of the magnesium oxide single crystal shown in the corresponding image. The calculated d spacing (1.9 ± 0.25 Å) gives lattice parameters *a, b* and *c* (where *a = b = c*) of 3.8 ± 0.5 Å. This correlates with the lattice parameter literature values of 4.214 Å for MgO[156, 157].

The bottom left diffraction pattern in fig.4-22 indexes to the P6$_3$/mmc hexagonal space group of graphite in the [001] zone axis. The calculated d spacing (1.33 ± 0.11 Å) gives lattice parameters *a* and *b* (where *a* = *b* ≠ *c*) of 2.66 ± 0.2 Å. This correlates with the C-C bond length literature value of 1.42 Å  and the literature lattice parameters *a* and *b* of 2.464 Å for graphite[158].

The bottom right diffraction pattern shows the polycrystalline concentric rings of both the cubic MgO substrate and the hexagonal graphite structure. The first visible diffraction ring can be indexed to the d spacing seen in MgO and the second diffraction ring can be indexed to the graphitic bonding d-spacing. The third visible ring with a d-spacing of 1.10 ± 0.08 Å can be indexed to the n = 3 d-spacing of the graphite interlayer planes giving a lattice parameter c of  6.6 ± 0.5 Å consistent with the literature value of 6.711 Å for graphite[158].

The above electron diffraction analysis shows that CNF structures, synthesised using gold and silver metal catalysts, are graphitic in nature and mixed in with the MgO support. There was no evidence to suggest a structural transformation in the MgO. Diffraction from the gold metal clusters was difficult to distinguish owing to the face centered cubic structure of both gold and MgO which share similar d-spacings falling within the error range of the diffraction technique used [159].

### *4.4.10.2 Raman:*

Raman analysis of these samples reveals weak radial breathing modes associated with the presence of SWCNT. The Raman display G-band modes at 1590 cm$^{-1}$ and an intense signal from the D-band seen at 1300 cm$^{-1}$ (fig.4-23). The D/G ratio reveals a high disorder in the graphitic lattice which would be assumed from the disordering of the fibres.
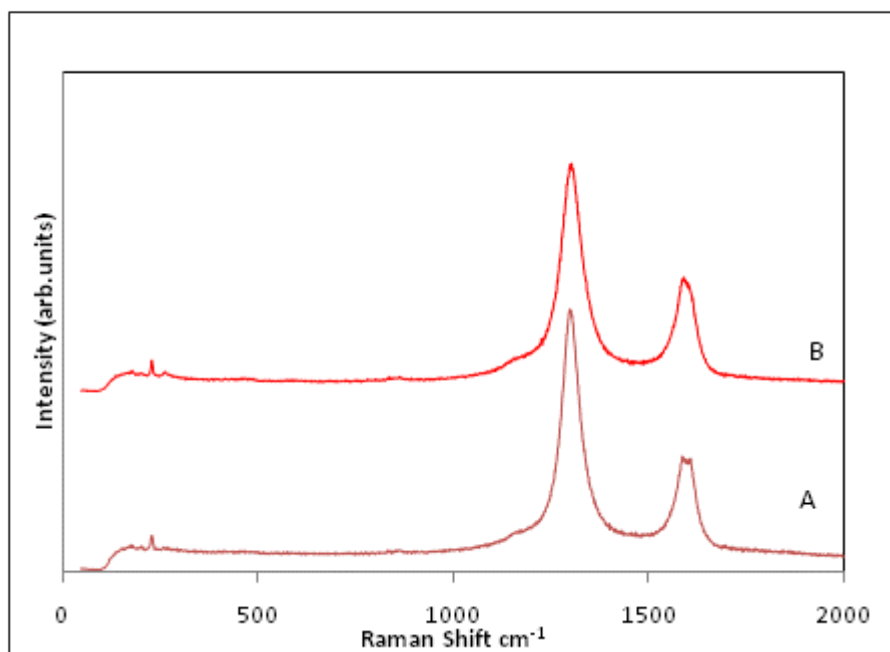


**Figure 4-23** Raman spectra of carbon species. *A)* Gold catalyst experimental conditions IV (1010°C, 2:1 Me:H$_2$) 785 nm laser.  *B)* Silver catalyst experimental conditions IV (1010°C, 2:1 Me:H$_2$) 785 nm laser.

## 4.5 Discussion

Compared to most experiments in the literature, that focus on variation of only one parameter, this study looks at variation in catalyst type, gas flow rates, and temperature. This allows empirical correlation between the integral properties of the metal catalysts with respect to the type of CNTs that have been synthesised. These properties include: melting point, vapour pressure, carbon solubility, and electronegativity.

Assuming a Vapour-Solid-Liquid (VSL) growth mechanism, as outlined originally for CNF synthesis by Baker et al.[160] then modified for CNT formation by Sinnott et al.[161], then the growth of the carbon structures should take place through six phases:

1) Decomposition of methane to carbon and hydrogen on the metal surface.

2) Desorption of $H_2$ and dissolution of carbon to form carbides with the metal.

3) Decomposition of the meta-stable carbides upon saturation of the metal nanoparticle to precipitate out graphitic carbon.

4) Expulsion of the metal from the forming graphite structure through pressure.

5) Exposure of the fresh metal surface to incoming methane.

6) Further steady state reaction either pulsed growth or smooth growth of the fibres.

Work by Deck et al.[162] and De Jong et al.[163] has shown that the ability of iron, cobalt and nickel to grow SWCNTs results from their relatively high carbon solubility at 800-900°C (2.5-5 at.%), and fast diffusion of carbon through the metal owing to the limited number of metal carbides which form[162, 163]. Their work using spray pyrolysis synthesis of CNT, suggests that vanadium, zirconium, manganese and chromium do not catalyse CNT formation under spray pyrolysis conditions. They attribute this lack of catalytic ability to the multiple intermediary carbides which these metals can form (even though the solubility of carbon is reasonably high in these metals)[162]. This increased carbide formation acts to effectively increase the concentration at which the carbon can

precipitate out of the metal catalyst particle and form fibres or CNT. The work outlined in this chapter and work by other groups [150, 164, 165], has shown that in fact a longer synthesis processes such as CVD allows these metals to catalyse CNT formation; presumably due to the higher carbon saturations which can be reached.

The results obtained from this investigation, which were obtained using similar size distributed metal catalysts, show that over the conditions V (1010°C and a 1:1 atmospheric pressure flow rate of methane and hydrogen) for each metal, different structures have been synthesized. High wall number MWCNT are produced using manganese, low wall number MWCNT are produced using chromium, SWCNT/DWCNT using cobalt and iron, followed by CNF formation using the gold catalyst. Therefore speculation of a growth mechanism which alters according to the carbon diffusion rate and the electronegativity of the metal is as follows.

The nanopaticulate gold catalyst at a temperature of 1010°C will be in a liquid state (mpt. 1063°C in the bulk and lower for gold nanoparticles) and has therefore, a relatively high carbon solubility of 4.7 at.% in this molten state, therefore saturation occurs throughout the core of the nanoparticles[166]. This core saturation results in stacked graphite layers, owing to the slow decomposition of methane on the surface of the gold. This is due to the equivalent electronegativities of carbon (2.55) and gold (2.54) causing the thermodynamically favourable graphitic growth, and so, CNF formation on the gold surface.

The cobalt and iron form SWCNTs, based on a rapid rate of methane decomposition caused by larger electronegativity differences (see table 4-2), and the high solubility and diffusion of carbon through the core of the nano particles as outlined by Deck et al. [162].

The formation of MWCNTs using manganese and chromium catalysts can be attributed to a shift in the diffusion rate of carbon within the metal causing only surface saturation of the nanoparticles whilst maintaining a carbide core (owing to the large number of carbides which may form). This may give a surface mediated growth of

156

multiple walls with a pulsed growth which results in the kinked tubes seen in the SEM and TEM imaging.

## 4.6 Conclusion

A review of structural carbon growth over a large number of conditions has shown the importance of controlling temperature, flow rates, and catalyst type in the growth of CNTs and other carbonaceous structures. The temperature and flow rates of methane and hydrogen have proved to be critical in the formation of structured carbon as shown by the limited conditions over which growth was seen (table 4-2). The exact conditions giving CNT formation varied for each catalytic metal, and the most important factor controlling the carbon species type seems to be the metal catalyst itself. To the author's knowledge this is the first time chromium has been used as a solo-catalyst in the growth of MWCNTs, which were produced in very high yield. In addition to the growth of carbon nanotubes, the novel CNF type structures were formed in high yield using a gold catalyst and the decomposition of methane under a reducing atmosphere. To the author's knowledge this is the first time the growth of these CNF structures has been recorded, the structures differ to traditional CNFs [167, 168] in their segmented nature rather than the solid fibres usually grown under decomposition conditions. These CNF structures could prove highly effective in high surface area applications such as catalytic frameworks or gas storage materials[169].

Chapter 5 shall present the research, carried out in parallel to the research in this chapter, on the deposition of transparent conducting thin films using commercially available SWCNTs. The performance of the resulting transparent conducting thin films will then be assessed based on the deposition technique and the fundamental material used in production.

# 5 Nanonet thin films

## 5.1 Covalent Functionalisation of SWCNTs and Spray Coating of Nanonet Thin films.

*The following chapter describes the use of microwave-assisted acid reflux in the covalent functionalisation of single walled carbon nanotubes. The modified SWCNTs displayed an aqueous solubility which was shown to be dependent upon the pH of the solution. Analysis of the chemically modified nanotubes displayed the presence of sulphone and sulphonate functional groups, which were identified using EDXA, TGA and IR analysis. The functionalised water soluble SWCNTs were then used for the deposition of randomly assembled nanonet thin films, and assessed for their performance as transparent electrode materials. The method outlined in the following chapter provides a fast and effective route to the formation of conductive nanotube thin-films without the need for surfactant stabilisation of the solution. Additionally, the functionalisation was shown to be a fully reversible process: sensitive to thermal treatment.*

## 5.2 Introduction

Chapter 4 outlined the results obtained from the chemical vapour thermal decomposition of methanol, over various transition metal catalysts, as a route toward tailored growth of CNTs and CNFs under different experimental conditions. The purpose of this work was to develop a technique to produce carbon nanotubes with controllable attributes for use in transparent conducting nanonet thin films. As such, experiments were run in parallel, using commercially bought single-wall carbon nanotubes, to fabricate nanonet thin films which will act as a benchmark for future experiments. The following chapter presents the results obtained from a series of experiments into a novel solublization technique for SWCNTs, and the subsequent spray deposition of these soluble species into transparent thin films on glass.

The introductory chapter detailed a number of the predominant transparent conducting materials currently available in the marketplace, which include: fluorine doped tin oxide and indium tin oxide (ITO). However, due in part to the rising cost and scarcity of indium, tight budget restraints, and the growing requirement for flexible transparent conductors on plastic, there is a drive towards the development of cheaper more accessible film materials[170].

Carbon nanotubes are becoming available on the multi-tonne scale industrially, which has led to a growing interest in the use of randomly assembled layers of carbon nanotubes (CNTs) as an alternative material for transparent thin film technologies[171, 172]. However, research into the physical and chemical manipulation of nanotubes has been hindered due to the poor solubility and weak hydrophilicity of the nanotubes in common liquid media including, organic solvents, and water[173, 174]. This poor dispersive ability of CNTs is attributed to the bundling of many individual tubes through inter-tube van-der-Waals interactions, creating large agglomerated hydrophobic particles. Solutions to this problem are an important hurdle to be overcome in this field if the full potential of these unique structures is to be harnessed.

There are some methods available to overcome this solubility problem, the solutions fall into two categories: 1) the use of non-covalently bound wrapping agents

and 2) the functionalisation of the side-walls or ends of the nanotubes with chemically bound species. Each technique has its own individual merits. The use of surfactants,[49] dyes[175] and polymers[176] to wrap the tubes and allow for debundling, falls into the first category, this achieves high-levels of solubility and stable dispersions without chemically altering the carbon nanotubes, allowing for the preservation of structural quality and electronic states. However, it also means the addition of a large amount of contamination in the final product, removal steps, and potential reactivity problems if chemical manipulation is required. The second category involves the chemical modification of the nanotube side-walls and ends; this is invariably done by oxidation of defect sites using an acid treatment. Resulting in potential carboxyl, sulphonyl and hydroxyl functional groups[177]. (Additional coupling reactions, to attach other surface bound groups such as polymers and hydrophilic or organic species, can be done sequentially[174, 178, 179].) The benefit of using covalent functionalisation is that minimal contamination of the product occurs during processing, and furthermore this route lends itself to chemical manipulation of the tubes. However, attachment of surface moieties does lead to changes in the electronic state and the structural purity of the nanotubes.

Traditional techniques used to functionalise carbon nanotubes involve sonication and refluxing in concentrated acid. They often result in only minimal functionalisation and limited solubility of the material. These thermal reflux processes also typically take from 4 – 45 hours[173, 177]. This chapter outlines a method which provides a high level of tube functionalisation, based on a microwave reflux process, which gives a water soluble product in under 5 minutes. Previous work using microwave radiation to speed up the functionalisation of nanotubes includes work published by Wang et al. [180] in 2005, and by Kakade et al.[181] and Tsukahara et al.[182] in 2008. These studies reported a high level of functionalisation, and a level of solubility comparable to the use of wrapping agents. The first goal in the work reported here is the modification of these microwave experiments in order to simplify and increase the capacity of the experimental process. This simplification was achieved by using a reflux condenser under atmospheric conditions rather than a high pressure sealed Teflon vessel. The effectiveness of the atmospheric pressure technique was assessed using comparisons of

the levels of solubility and functionality achieved in the modified single wall carbon nanotube (SWCNT) end product.

The final goal of this line of investigation was to make adhesive thin films of the water soluble functionalized-SWCNTs on glass, for use as transparent conductive coatings, and to investigate the effect of functional groups on the conductivity of the films[183].

Previous studies into the deposition of SWCNT thin films have been done via a range of techniques including solution casting [184], spray-coating,[47] self-assembly [185], Langmuir Blogett[186], airbrushing[187], and filtration methods[9]. In this work we have used a spray-coating process to form transparent conducting thin films, using both the traditional technique of surfactant stabilised solutions, and using the microwave functionalised CNT solutions as a novel process for spray-coating. This will allow comparison of the role which the electronic state of the nanotubes plays in the overall film properties, and also highlight the effects of dispersion and connectivity in the nanotube network.

The introductory chapter outlined the theory which models and predicts the conductivity within individual single walled carbon nanotubes, this can be shown to range from direct band-gap semiconducting behaviour, through to metallic like conductance[188-191]. However, specific electronic behaviour is dependent not only upon the diameter and chirality of the carbon lattice, but can also be altered through surface functionalisation and interaction with surface species[40]. Nanotubes are highly resilient and can be reversibly distorted without atomic rearrangement due to their small dimensions, they also show a very high stiffness towards axial loads[45]. These distinctive attributes provide the inherent properties and manipulative potential required for fabrication of functional thin films, with controllable transparency and conductivity, and the added benefit of the mechanical stability and malleability for low cost flexible electronics[46]. The high transparency of SWCNT films, unlike that of traditional TCO materials, is not dependent on the band gap falling outside the visible region of the electromagnetic spectrum, instead it is a result of 1) the polarization dependent optical

absorption due to the high aspect ratio and 1 dimensional nature of the tubes, and 2) the low carrier density but high mobility causing a low plasma frequency but excellent conduction[192]. Investigation into the utilisation of these properties, are detailed in the following work.

## 5.3 Experimental

### 5.3.1 Microwave Functionalisation

The carbon nanotubes were purchased from Thomas Swan (Elicarb® SW single-wall carbon nanotubes), and were produced via chemical vapour deposition using an iron catalyst. The microwave reflux set up was assembled using a Proline Micro ST22 domestic microwave: fitted with a removable reaction flask which connects to a reflux condenser through the roof of the microwave, and a variable length/flow water pipe which inserts through the side of the microwave for limiting the power during reflux (Figure 5-1.).
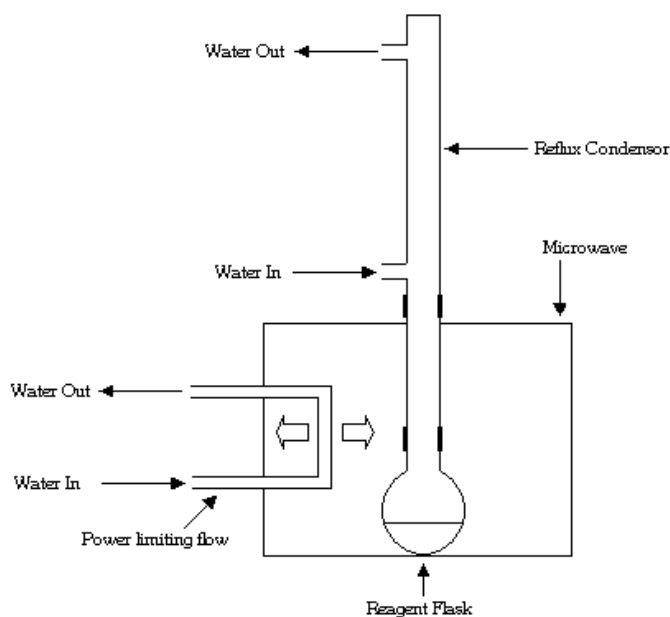


**Figure 5-1** Schematic showing the experimental apparatus used to carry out the microwave reflux of SWCNT in conc. sulphuric and nitric acids (1:1 ratio of 98% sulphuric acid : 70% nitric acid). The power limiting tubular insertion is used to optimize reflux conditions by absorbing a fraction of the microwave energy.

Initial experiments were conducted using 0.03 g of SWCNTs in 20 ml of a 1:1 solution of 70% nitric acid and 98% sulphuric acid. The reflux was done under full 750 W power with the water pipe limiter extended into the interior of the microwave and a fast water flow to prevent excessive heating of the acid solution. The reflux time was varied between 3, 6 and 9 minutes.

The solution was allowed to cool. It was then diluted with 100 ml of deionised water. The diluted solution was dialysed until a neutral pH was reached. This solution was then centrifuged at 4000 r.p.m. for 20 minutes to force precipitation of the CNT, the excess water was decanted off and the concentrated product, in the minimum volume of water, was then freeze dried overnight to yield a black powder. A scaled-up version of this experiment was run under optimised conditions using 0.4 g of CNT in 30 ml of the 1:1 70% Nitric acid and 98% Sulphuric acid solution, under 3 min of full power microwave irradiation (750 W).

### 5.3.2 Spray Coating of Carbon Nanotubes

Microwave functionalised single walled carbon nanotubes (f-CNT) were suspended in de-ionised water (0.06 g per 100 ml), this solution was taken to pH 11 using dropwise addition of NaOH (2 M) to aid deprotonation of the acidic functional groups, and maximise solubility. The suspension was then sonicated for 15 mins to encourage debundling and form a stable CNT solution.

An equivalent solution was made up from the as-bought SWCNT sample in deionised water (0.06 g per 100 ml) using dodecyl-benzene-sulphonic acid as a stabilising agent. The ratio used to form a stable solution was 5:1 SDDBS to CNT, as outlined in the work by Islam et al. [193]. This was then sonicated for 15 mins.

The two solutions were spray coated onto Pilkington barrier glass substrates, and a range of film thicknesses were produced by varying the volume of solution used (10 ml to 100 ml). The glass substrates were kept at 300°C using a graphite block heater mounted on a mechanical shuttle unit, allowing dynamic motion during spraying. The

spray head was mounted 25 cm above the moving substrate and maintained an air pressure of 30 psi. The solution was injected via PTFE transport tubing from a syringe driver at a rate of 1.5 ml min$^{-1}$.

### 5.3.3 Post Spray Treatment:

The films produced using the as-bought SWCNTs (suspended using dodecyl-benzene-sulphonic acid surfactant) were washed by submerging in de-ionised water for 30 min. to allow for removal of the surfactant molecules. This process removed much of the film haziness and allowed for comparison of electrical and optical properties.

The films produced with the water soluble f-CNT were heat treated to ensure full removal of the functional groups. This was achieved by heating to 600°C under an inert atmosphere for 2 hours which, as shown by the TGA data, was sufficient to remove the functionality and restore the pristine tube structure. Subsequent Raman and solubility testing confirmed the removal of the functional groups.

## 5.4 Results and Discussion

### 5.4.1 Solubility Testing

The functionalised carbon nanotube solid obtained from the optimised microwave reflux scale-up experiment was tested for its solubility in water, using light absorbance measurements and assuming a Beer-Lambert relation, in order to find the maximum solubility. Solutions with incrementally increasing amounts of the modified CNT (0.001 g – 0.005 g in 20 ml of deionised water) were carefully prepared, sonicated for 1 hour to aid dispersion, and the resulting solutions taken to pH 2.5 using dilute nitric acid, and to pH 11 using dilute sodium hydroxide (fig. 5-2).
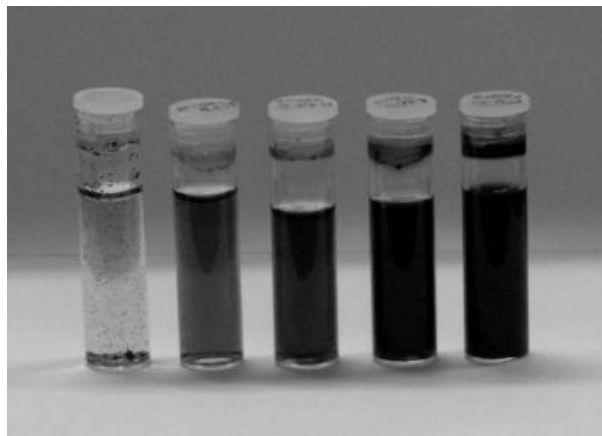
**Figure 5-2** Photograph of SWCNT solutions, far left (position 1) As-bought SWCNT in water (0.05 mg/ml). Positions 2 - 5 increasing concentration aqueous solutions of microwave functionalised SWCNT (0.05, 0.1, 0.25 and 0.74 mg/ml respectively). Sonicated for 1 hour.

Calibration curves of visible light absorbance (at 800 nm) vs. concentration ($gL^{-1}$) were plotted (see fig. 5-3 and fig. 5-4). A sonicated solution containing an excess of the CNTs, at each pH value, was then used to assess the maximum concentration assuming a Beer-Lambert relation. The maximum concentration of the CNT was found to be 0.74 mg/ml at pH 11, at pH 2.5 a lower solubility was found of 0.55 mg/ml. This dependency of solubility with pH is consistent with the results obtained in the work by Kakade et al [181], but contrary to that stated by Wang et al.[180]. The solutions were found to be highly stable, showing only minimal flocculation after 1 month. It was also found that the addition of the acid before sonication of the modified CNTs, renders them practically insoluble due to flocculation (even after prolonged sonication). This effect is presumably caused by increased protonation of the functional groups on the modified tubes. Conversely, addition of base causes an increase in the deprotonated charged state in the functional groups: leading to increased affinity to the polar solvent surroundings. Addition of the acid before dispersion by sonication prevents the initial debundling and renders the product insoluble.

Solubility testing was also attempted on the as-bought SWCNT for comparison, however, the product was found to be completely insoluble, under all pH conditions, even after prolonged sonication (fig. 5-2).
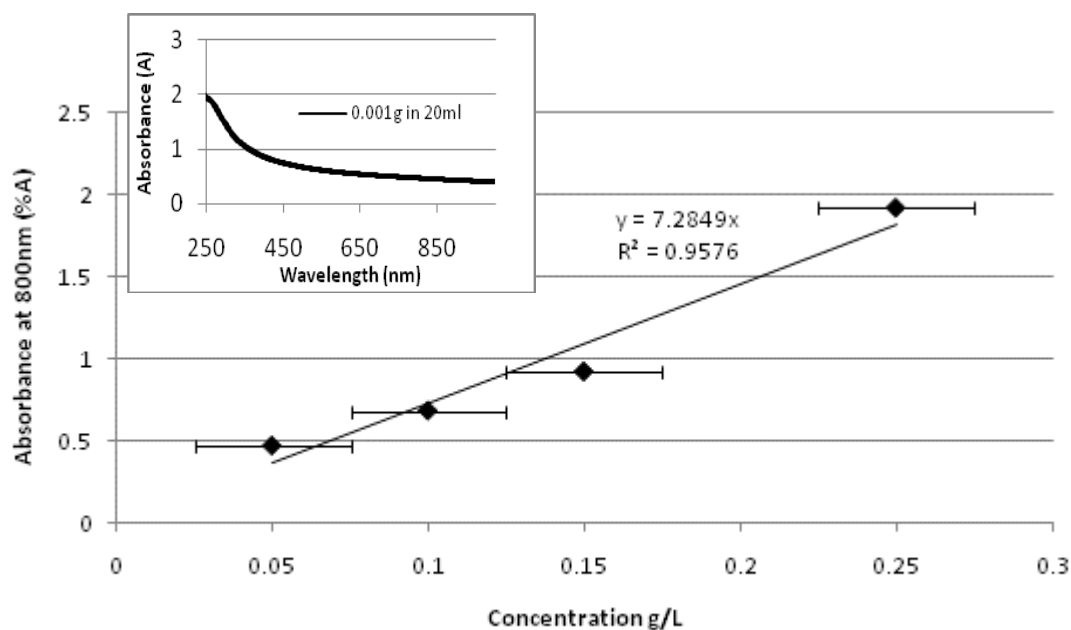
**Figure 5-3** Calibration plot of concentration vs absorbance at 800 nm, for an aqueous solution of microwave reflux functionalized-SWCNTs in water at pH 2.5. Inset shows example UV/Visible absorbance curve for 0.001g of f-CNT in 20 ml of water.
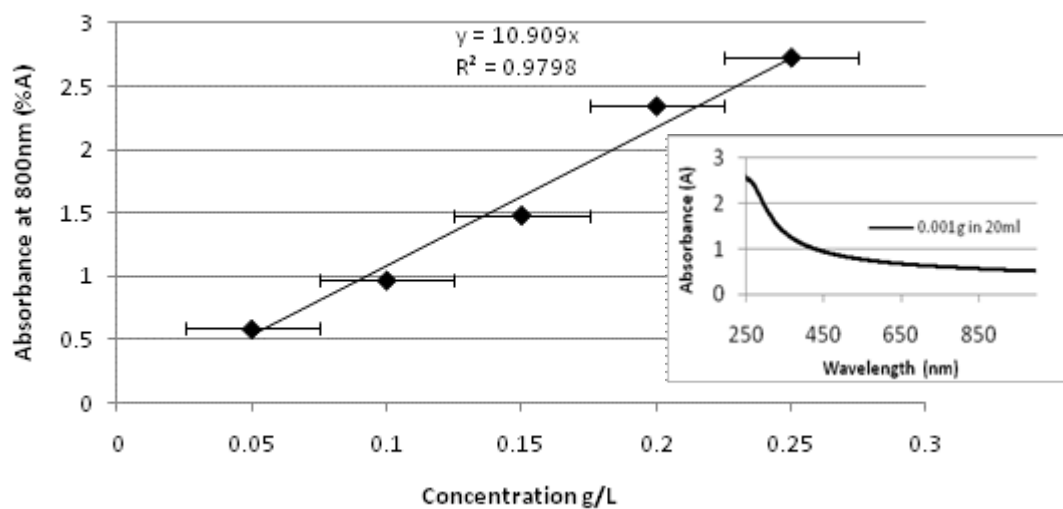


**Figure 5-4** Calibration plot of concentration vs absorbance at 800 nm for an aqueous solution of microwave reflux functionalized-SWCNTs in water at pH 11. Inset shows example UV/Visible absorbance curve for the 0.001g of f-CNT in 20 ml of water.

### 5.4.2 Raman Analysis

All Raman measurements were taken over multiple spots on the samples, and representative spectra have been used in the figures. The bottom plot on fig. 5-5 gives the Raman spectra of the as-bought CNT solid; the low frequency end of the spectrum shows peaks in the region of 120-350 $cm^{-1}$, attributed to the radial breathing modes (RBM) of the single wall carbon nanotubes. A strong RBM as seen in Figure 5 indicates a high number of single walled CNT with diameters less than 2 nm. The high frequency end of the Raman spectrum shows the splitting of the graphitic G-band[42], though the G-peak is sitting as a shoulder on the main G+ peak: this can be attributed to broadening caused by the simultaneous excitation of many tubes leading to a merging with G+, and secondly, the presence of larger diameter tubes which typically give only 1 large band similar to that of graphite[151]. The D-band at 1280 $cm^{-1}$ shown in fig. 5-5 gives a D/G ratio of 8% for the as-bought sample, which is 2 -3 % higher than the SWCNTs produced using a cobalt catalyst in the in-house CVD experiments covered in chapter 4: this indicates a marginally lower level of structural ordering in the as-bought product due to more defect sites[151].
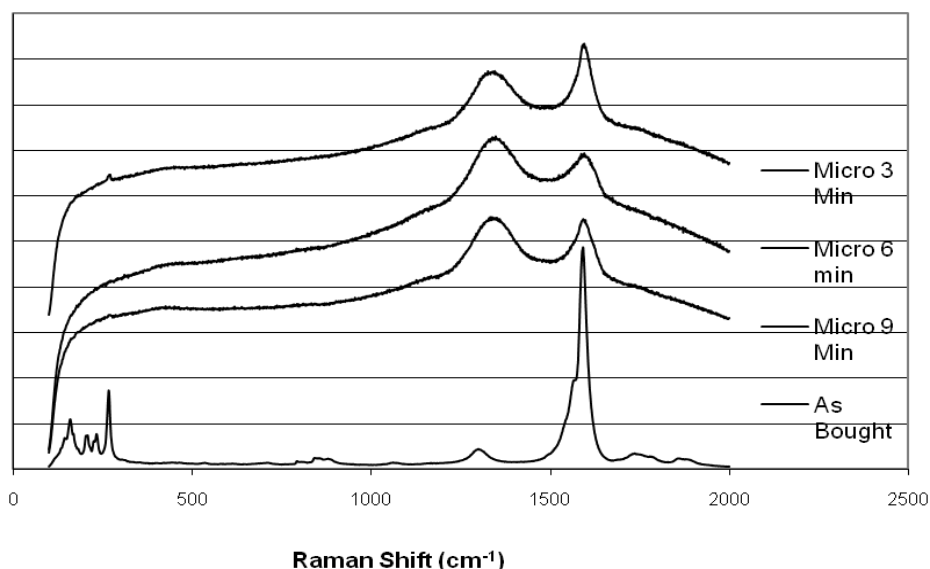


**Figure 5-5** Raman spectra of powdered f-CNT samples (microwave irradiated in a 1:1 ratio solution of conc. nitric and sulphuric acid for 3, 6 and 9 minutes) and as-bought CNT (top to bottom respectively).

In addition to the spectra for the as-bought sample, fig. 5-5 also shows the Raman spectra from the microwave functionalised single wall carbon nanotubes (f-CNT) which were irradiated for 3, 6 and 9 minutes and then extracted from solution. The spectra shown are similar to those shown by Wang et al.[180] . The radial breathing modes in the f-CNT have become obscured, and the D/G ratio increases with increasing irradiation time, suggesting added functionalisation is indeed present on the surface. Loss of the RBM intensity can be attributed to the reduction of the resonant Raman enhancement after functionalisation, because addition of an irregular arrangement of $sp^3$ bonded side groups to the SWCNTs causes a loss of symmetry in the bonded nanotube structure. This in turn causes a broadening and reduction in the van Hove singularity states, thus, reducing the resonant effects. In addition to a loss of symmetry, the covalent attachment of electron withdrawing groups such as carboxylates or sulphonates, could cause removal of electrons from the valence vHs in the DOS, again quenching the electronic transitions responsible for the Raman enhancement, and in turn causing the loss of the RBM (see *chapter 1 section 1.6* and *chapter 4 section 4.4.3* for a more detailed explanation of electronic structure).

Increased lattice disorder caused by side wall functionalisation amplifies the D-band intensity, thus increasing the D/G ratio. The loss of symmetry induced by functionalisation also causes a loss of electronic resonance in the C-C tangential mode therefore reducing the G-band intensity as seen in the spectra in fig. 5-5[39, 194, 195].

## 5.4.3 TGA and Analysis of Heat treatment

Thermogravometric analysis was performed on the as-bought SWCNTs, the functionalized-SWCNTs and for comparison on a sample of granular charcoal. The samples were heated in an inert atmosphere under a 50 mL min^{-1} flow of helium at a rate of 10 Kmin[-1], up to a maximum temperature of 1500°C.

The TGA data shows a ~10% and a ~15 % mass loss for the as-bought CNT and amorphous charcoal, respectively (fig. 5-6), with a gradual mass loss over the entire temperature regime for both profiles. The f-CNT curve shows an overall 40% mass loss up to 1500°C, with approx. 30% mass loss below 600°C in two defined steps.
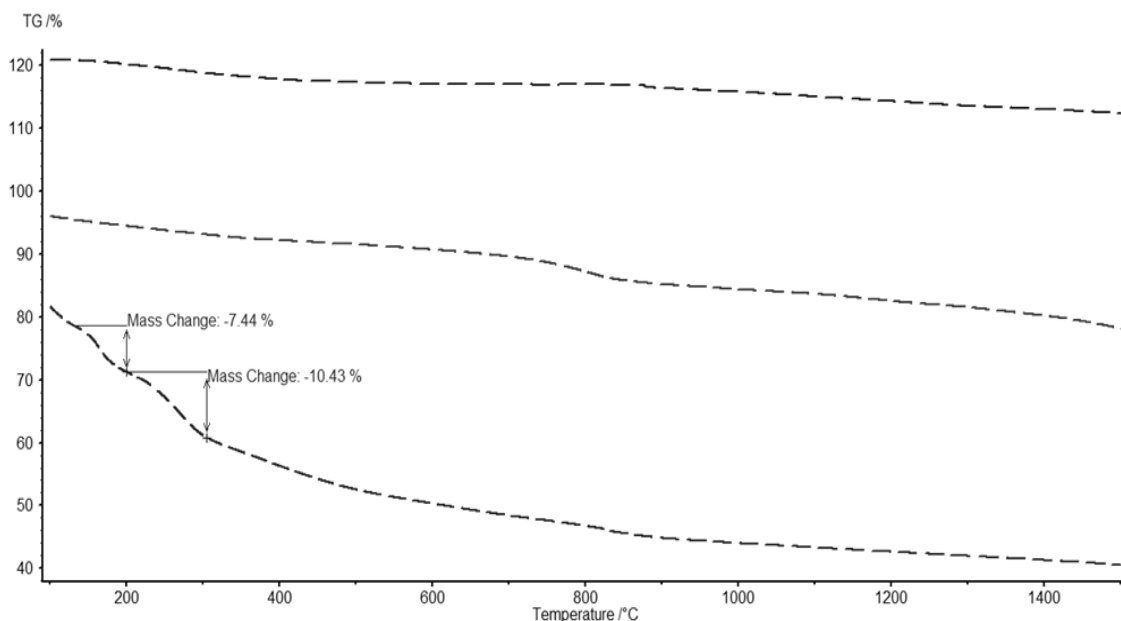


**Figure 5-6** TGA of as-bought CNT (top), granular charcoal (middle), and f-CNT (microwave refluxed in a 1:1 ratio of conc. nitric and sulphuric acid for 3 minutes) (bottom). Plots shifted from 100% on the Y axis for clarity.

These profiles indicate that the temperature induced mass-loss under inert conditions, for both amorphous carbon and single walled carbon nanotubes, are similar: whereby the majority of the carbon and SWCNTs remain after heating. However, the enhanced loss in the f-CNT sample indicates the removal of the side-wall and tube end functional moieties. The stepwise losses below 600°C provide some indication as to the presence of different functional groups.

The samples after heating to 1500°C under helium were further analysed by Raman spectroscopy (fig. 5-7). The SWCNT's unique Raman profile has been maintained in the un-functionalised, as-bought sample even after heating to 1500°C under an inert atmosphere, demonstrating the high temperature resilience of single

walled carbon nanotubes, and further indicating that they are the remaining bulk mass seen in the TGA experiments. After heating, the SWCNT Raman profile has been restored in the f-CNT sample, confirming the loss of the oxidative functionality and demonstrating that the earlier Raman spectra of the functionalized-SWCNTs, which showed a broad fluorescence, were indeed caused by the interaction with the functional groups (not because of the destruction of the tubes by the acid). The D/G ratio in the heat treated f-SWCNTs of about 8% has also been restored to that of the as-bought SWCNT material: indicating removal of defects to yield a pristine SWCNT structure.
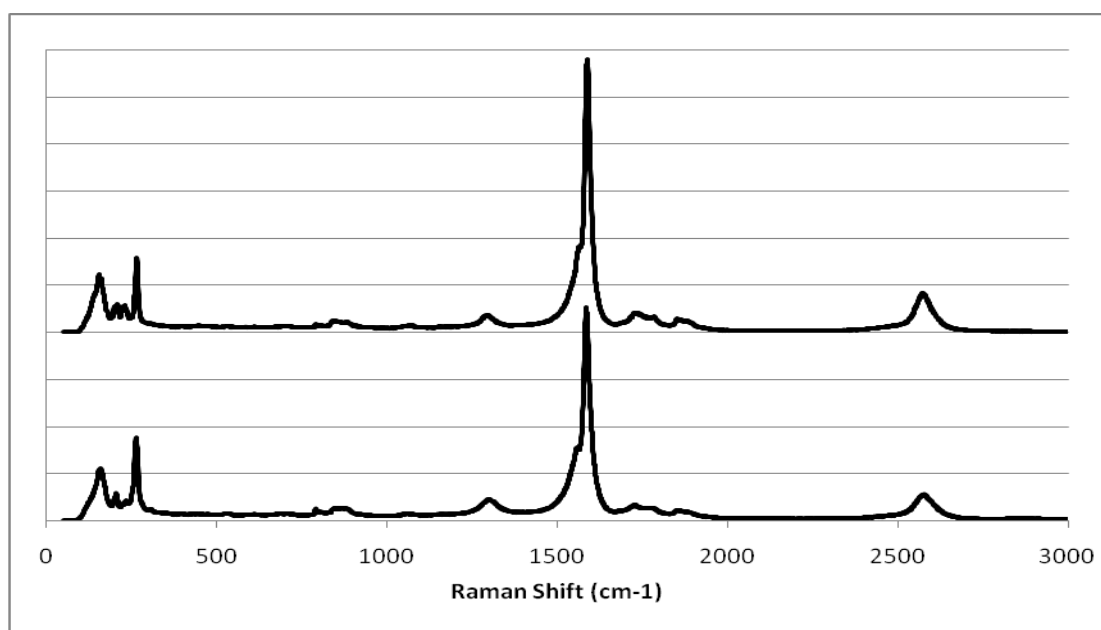


**Figure 5-7** Raman spectra of as-bought CNT (top); and f-CNT (microwave refluxed in a 1:1 ratio of conc. nitric and sulphuric acids for 3 min) after heating to 1500°C in an inert atmosphere (bottom).

In addition to the data shown by the Raman spectra and the thermogravometric analysis for the loss of functionality, testing was redone on the solubility of the sample after heating in an inert atmosphere. Suspensions were made under neutral, acidic, and basic, aqueous conditions and subjected to prolonged sonication (greater than 3 hours), no solubility was observed in any of the suspensions: providing further evidence for the complete removal of any acid induced functionality after heating.

Examination of the TGA data shows that heating up to 600°C in an inert atmosphere is sufficient to fully remove the nanotube functionality. Subsequently samples of the f-CNT were subjected to a heat treatment at 600°C for 2 hours under a 2 Lmin$^{-1}$ nitrogen flow. Analysis of the samples by Raman and solubility testing indicate the complete removal of surface and end-wall functionality.

## 5.4.4 Energy Dispersive X-ray Analysis

EDXA was performed on the 3 min microwave-irradiated sample of f-CNT taken from the scaled-up experiment. Signature emissions for carbon, oxygen, sulphur, and iron were observed, showing 61% carbon, 23% oxygen and 15% sulphur by weight was present (72%, 20.5%, 6.5% atomic % carbon, oxygen and sulphur respectively), accounted for by the presence of surface functional groups on the CNT structures. Less than 1 weight % iron was also detected, which can be attributed to the catalyst used in the CVD growth method that was used to generate the nanotubes. The weight percent of each element gives an overall 38% weight due to sulphur and oxygen, which correlates to the 40% mass loss seen by TGA. This analysis also indicates that the nanotubes have been functionalised by surface groups, yielding an atomic ratio of 3:1 oxygen to sulphur.

## 5.4.5 Infrared Analysis

FTIR spectroscopy was performed on the microwave functionalised carbon nanotubes, which were ground and pressed into a KBr disc (fig. 5-8). Major absorbance features are seen at 1300 cm$^{-1}$ and 1150 cm$^{-1}$ which can be attributed to the symmetric and anti-symmetric stretches of $SO_2$ containing groups such as, sulphones, and sulphonates. The absorbance at 1060 cm$^{-1}$ can be assigned to a sulfoxide single SO stretch[196]. The broad but weak absorbtion at 3400 cm$^{-1}$ could indicate a low level of OH groups present. No peaks indicated the presence of carboxyl groups (C=O carboxyl stretch 1760-1690 cm$^{-1}$), indicating sulphonation is the predominant functionalisation reaction occurring (C(sidewall)-(O)-$SO_x$(H)), this is unlike other functionalisation

methods which report carboxylation as the dominant mechanism for mixed nitric and sulphuric acid oxidation reactions[173, 177]. Experiments in the literature have been performed using thermal oxidation, under chemical conditions specifically designed to yield sulphonation of the carbon nanotubes, analysis in these instances suggests carboxylate functionalisation is however still occuring [197]. Analysis from our product suggests that selective sulphonation of nanotubes is possible using a microwave reflux process, this opens up a new route to the desired selective chemical manipulation of nanotubes.
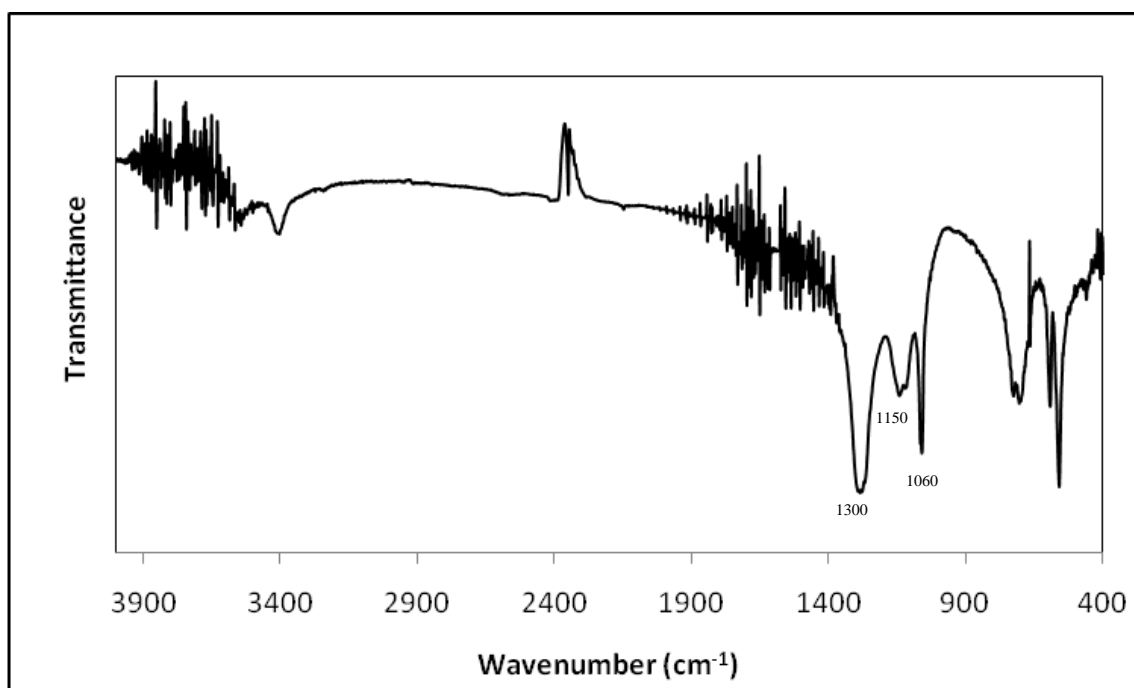


**Figure 5-8** Infrared spectra taken using powdered KBr to form a pellet with powdered f-SWCNT (3 minutes reflux in concentrated nitric and sulphuric acids (ratio of acids 1:1) under irradiation by a domestic microwave oven). Absorbances suggest the presence of sulphone and sulphonate functional species.

Microwave heating reactions are becoming evermore commonplace within the field of organic synthesis and other areas of chemistry. The ability of microwave radiation to enhance the rate of reaction, and yield of product, is attributed to its dielectric heating as a bulk effect[198]. Dielectric heating relies on the use of polar molecules in the reaction, which oscillate with the electric component of the microwave radiation, the molecules' vibrational lag time behind the radiation causes dielectric bulk

heating of the solution. The use of water in our functionalisation method provides the polar species for bulk heating of the solution. In addition to this heating effect, a second mechanism will take place in the conducting carbon nanotubes. Free electrons can oscillate with the microwave radiation resulting in resistive heating of the SWCNT themselves. For bulk conducting materials this effect is usually negligible, as the radiation will not penetrate far enough into the material before it is reflected. However, for SWCNT with only one atomic layer comprising the tube walls, and a nanoparticulate sizing, this effect will become more dominant. The resistive heating may also be concentrated around the tube defects, where ballistic conduction breaks down and scattering sites are present. This includes both along the tube walls and tube ends. This localised superheating could account for the fast reaction time of the microwave functionalisation, which seems more probable than any 'specific non-thermal' microwave effects[199, 200].

## 5.4.6 Morphology

The morphologies of the various samples were evaluated by field emission scanning electron microscopy and transmission electron microscopy (fig. 5-9). TEM and SEM images taken from the 3 minute irradiation samples, show evidence for the presence of tubular carbon (fig. 5-9 A&B), suggesting that the characteristic radial breathing modes, which are expected to be present in a Raman analysis of SWCNT samples, are indeed obscured or depleted by symmetry breaking effects caused by the functionalisation (see fig. 5-5 for Raman spectra, and section 5.4.2 for details of symmetry breaking). Substantial shortening of the tubes seems to have occurred after 6 minutes of irradiation. The presence of SWCNTs in the sample irradiated for 9 minutes could not be confirmed by SEM, and a high level of graphitization has been induced (fig. 5-9 D).
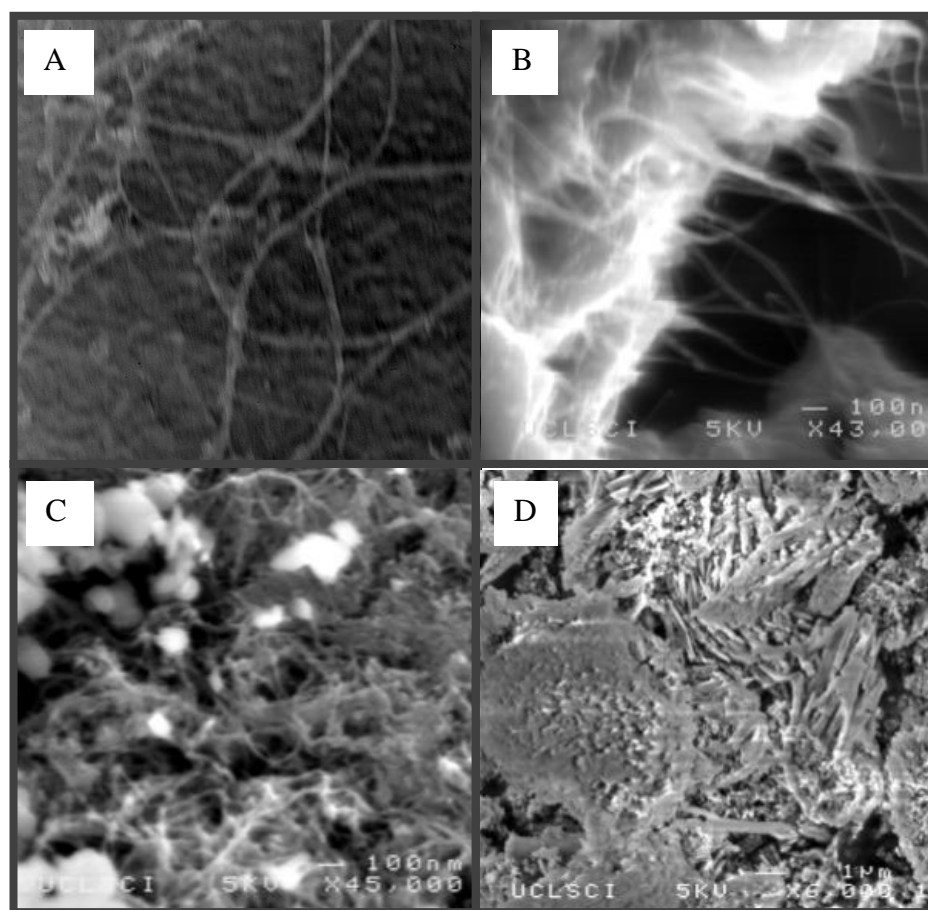
**Figure 5-9** TEM and SEM images of SWCNT samples after microwave irradiation reflux in a 1:1 ratio solution of conc. nitric and sulphuric acids *A)* 3 min irradiation (TEM). *B)* 3 min irradiation (SEM). *C)* 6 min irradiation (SEM). *D)* 9 min irradiation (SEM).

## 5.4.7 Electrical Conductivity testing

High electrical conductivity, due to high carrier mobility, is a feature of nanotubes which makes them an interesting candidate for a range of electronics applications. The as-bought SWCNTs (non-functionalised), f-SWCNT modified

sample, granular charcoal, and graphite all underwent testing to determine their electrical resistance. In addition, a sample was taken from the as-bought SWCNTs and subjected to acid reflux in 7 M nitric acid for 2 hours - this product showed no enhanced solubility but a change in resistivity was noted. The measurements were done by pressing 0.25 g of the raw material into a uniform disc-shaped pellet using 15 tons of pressure, the sheet resistance was then recorded using a four-point probe and the resistivity of the material calculated using the pellet thickness.

| Sample Type | Resistivity ($\Omega$.cm) |
|---|---|
| As-Bought SWCNT | $62 \times 10^{-3}$ |
| F-SWCNT (3 min micro irradiation) | $26 \times 10^{-3}$ |
| Graphitic Carbon | $7 \times 10^{-3}$ |
| Refluxed SWCNT (7M nitric/2 hours) | $23 \times 10^{-3}$ |

**Table 5-1** Table of resistivity values for various carbonatious samples, taken using electrical four point probe measurments. f-CNT were refluxed in conc acids under microwave radiation for 3 min. Refluxed CNT were thermally refluxed in 7M nitric acid for 2 hours.

The amorphous granular charcoal sample would not form a solid pellet and as such no resistivity value could be found. Graphitic carbon was the most conductive material as shown in table 5-1 (this value also correlates with the resistivity standard for graphite[156]). The microwave reflux functionalisation of the as-bought SWCNTs led to a decrease in the resistivity of the material. This decrease was also seen for the 7 M nitric acid refluxed sample, and can be attributed to removal of amorphous carbon from the as-bought material.

Amorphous carbon contains both $sp^2$ and $sp^3$ bonding, the ratio of these bond types controls the electrical properties of the material. However, the lack of long range ordering within amorphous carbon leads to localisation of $\pi$-bonds and as such it has an inferior conductivity to both graphite and carbon nanotubes[201]. Reflux in a strong acid will selectively oxidise the amorphous carbon in a sample due to the high number of

dangling bonds it contains. The oxidation of this amorphous carbon, to carbon dioxide gas, acts to purify the material leaving behind the highly electrically conductive nanotubes and increasing the conductivity of the sample material overall.

Quantization of the 2D graphitic band structure into 1D conducting SWCNT, yields both semiconducting and metallic tubes (as determined by theoretical and practical studies[40, 202]), this would intuitively be thought to cause a decrease in the overall conductivity of the material in the randomly assembled bulk as compared to metallic like graphite or metallic like MWCNTs. However, bundling of individual SWCNTs together leads to a mixing of electronic states and can allow for metallic like conductivity. Additional factors will also play a role in the determination of the conductivity, including: scattering at nanotube-nanotube junctions, and the extent of the connectivity between the tubes within the matrix (which has already shown to be affected by the presence of amorphous carbon in the material (table 5-1)). Therefore the purity of the nanotube sample, the pristine nature of the tubes, and the type of CNT all control the resulting conductivity of the material and limit the performance of any film deposited from this material.

## 5.5 Spray Coating of Thin Films

Randomly assembled thin films of carbon nanotubes were produced using both the as-bought SWCNT and the microwave functionalised SWCNT, using a spray coating technique. The method adopted is shown schematically in fig. 5-10. Both techniques displayed good coating properties under the experimental conditions, allowing production of high quality uniform films on the glass substrate fig. 5-11. The functionalised nanotubes showed significantly greater adherence to the glass substrate, passing the Scotch tape test and displaying resilience to rubbing action, however, they were still removable with a steel scalpel. The as-bought CNT were sprayed with a surfactant containing solution, which allows for solubility of the otherwise non-soluble as-bought product, these films passed the scotch tape test but were less adherent and displayed a greater haziness caused by the presence of surfactant molecules within the film.

**Surfactant Solution Based Spray Coating:**
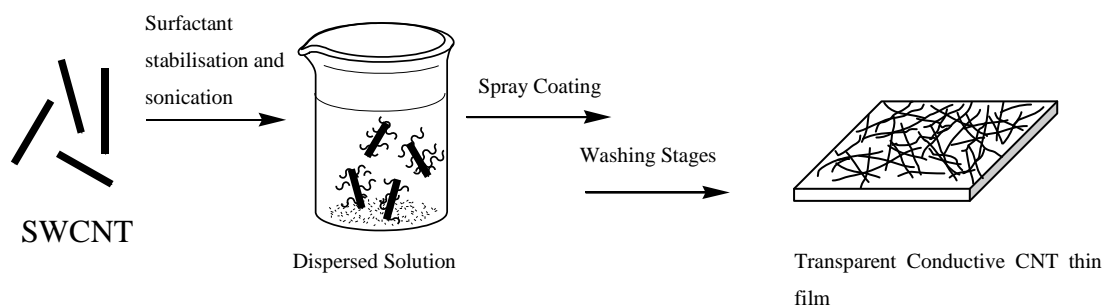


**Microwave Functionalised Solution Spray Coating:**
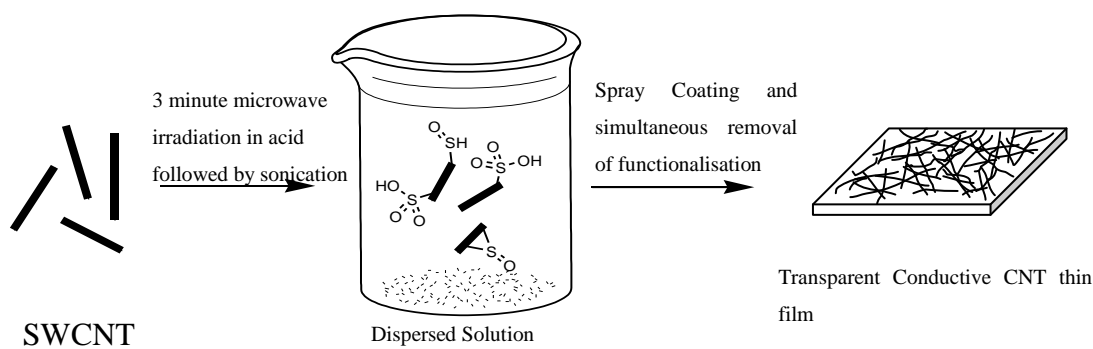


**Figure 5-10** Schematic diagram of the spray coating process for SWCNT thin films using the traditional surfactant based method and a microwave acid reflux funtionalised-SWCNT solution route.
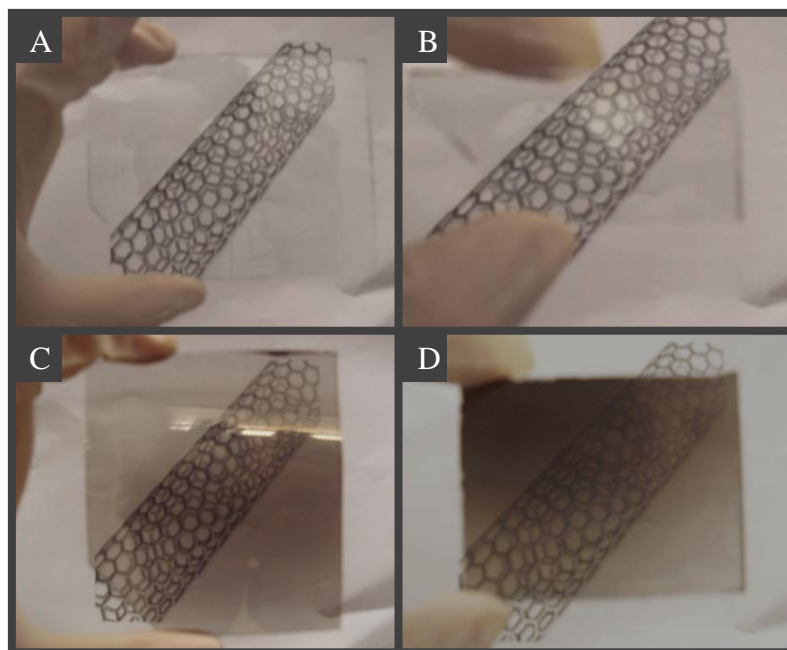
**Figure 5-11** Images of functionalised-SWCNT thin films on glass substrates *A)* plain glass substrate *B)* 40,000 Ω/□ film  *C)* 600 Ω/□ film  *D)* 300 Ω/□ film.
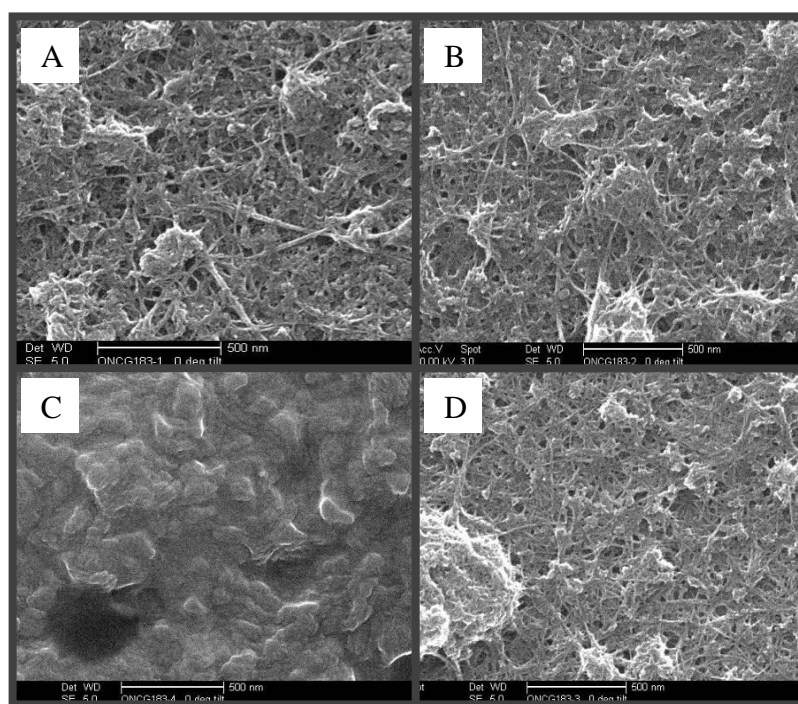


**Figure 5-12** SEM images of the spray coated SWCNT films *A)* As-deposited film from functionalised-SWCNT solution  *B)* Heat treated (600˚C inert atmosphere) film from functionalised-SWCNT solution *C)* As-deposited film from surfactant stabilised CNT solution  *D)* Washed film from surfactant stabilised solution.

178

Fig. 5-12 shows SEM images of the as-deposited film from the functionalized-SWCNT solution: showing good connectivity between the nanotubes and low impurity levels (fig. 5-12 A). The as-deposited film from the surfactant stabilised solution (fig. 5-12 C) shows no tubular structure due to high levels of amorphous surfactant coating the network. The amorphous coating is then shown to be removed upon washing the film (fig. 5-12 D). All images demonstrate a significant level of SWCNT bundling in the spray coated films.

## 5.5.1 X-ray Photo-electron Spectroscopy

X-ray photoelectron spectroscopy was performed on the surface of the SWCNT films (both the traditional surfactant stabilised method and the microwave functionalised spray coated films).
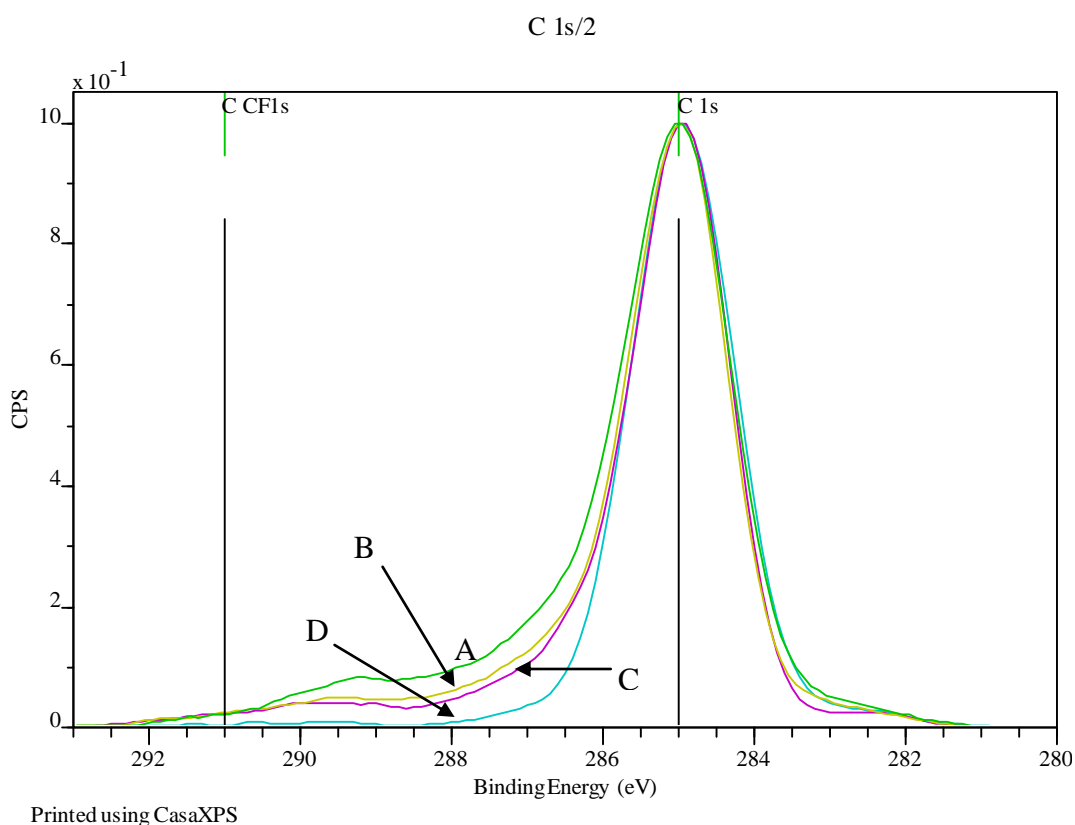


**Figure 5-13** XPS spectra showing the carbon 1s peak after background subtraction and peak normailsation. *A)* As-deposited film from functionalised-SWCNT solution  *B)* Heat treated (600˚C inert atmosphere) film from functionalised-SWCNT solution *C)* As-deposited film from surfactant stabilised CNT solution  *D)* Washed film from surfactant stabilised solution.

179

Figure 5-13 shows the XPS carbon 1s spectra from the nanotube thin films. Each spectrum shows a high signal at 285 eV, which corresponds to the photo-emission of the C 1s electron in a carbon-carbon or carbon-hydrogen environment. The small shoulder seen on the as-deposited f-SWCNT spectra, the heat treated f-SWCNT film, and the surfactant stabilized film at 289-289.5 eV (Figure 5-13 plots A, B, C), corresponds to the C 1s electron in an oxidized environment, which can be attributed to the carbon-sulphur bonding present in the film.
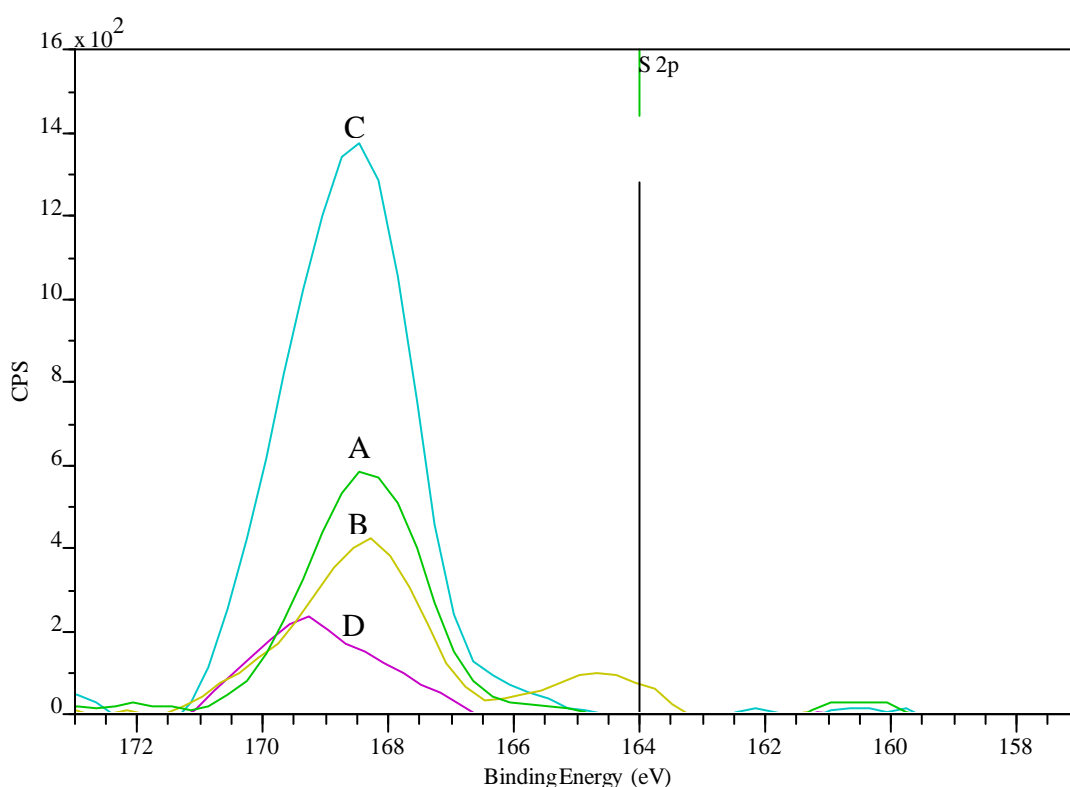


**Figure 5-14** XPS spectra showing the sulphur 2p peak after background subtraction and peak normailisation. *A)* As-deposited film from functionalised-SWCNT solution  *B)* Heat treated (600˚C inert atmosphere) film from functionalised-SWCNT solution *C)* As-deposited film from surfactant stabilised CNT solution  *D)* Washed film from surfactant stabilised solution.

Figure 5-14 shows the XPS sulphur 2p spectra from the nanotube thin films. Each spectrum shows a high signal at 168.5 eV which corresponds to the photo-emission of the sulphur 2p electron in a sulphonate ($SO_3$) environment. The intensity of this signal reflects the quantity of $SO_3$ groups present in the samples. The un-washed surfactant based film has the higheset levels of sulphonate present which after washing displays the lowest levels of sulphonation. The shoulder seen on the heat treated functionalised sample at 164.5 eV is characteristic of the S 2p electron orbital in an $SO_2$ environment (Figure 5-14 plot B). This indicates that the heat treatment (600˚C in an inert environment), has removed some of the oxygen from the sample and converted a proportion of the sulphonate ($SO_3$) functionalisation into sulphone ($SO_2$) functionalisation, which is not present in the as-deposited film (spray coated in air at 300˚C).

| Sample | Carbon (at.%) | Sodium (at.%) | Oxygen (at.%) | Sulphur (at.%) |
|---|---|---|---|---|
| As-deposited film from functionalised-SWCNT solution | 78 | 6.1 | 14 | 1.6 |
| Heat treated (600˚C inert atmosphere) film from functionalised-SWCNT solution | 86 | 3.3 | 8.16 | 1.3 |
| Washed film from surfactant stabilised solution. | 89 | - | 8.0 | - |
| As-deposited film from surfactant stabilised CNT solution | 68 | 11 | 16 | 4.8 |

**Figure 5-15** Atomic % ratios of carbon, sulphur, oxygen and sodium from the surface of the SWCNT thin films. Calculated from XPS surface spectroscopy measurements.

Figure 5-15 shows the atomic % ratios present in each of the SWCNT thin films. The results display the high levels of sulphur and sodium caused by the surfactant, which is shown to be completely removed by washing.

The as-deposited functionalised-SWCNT film displayed an atomic % ratio of sulphur at 1.6%, which is lower than the level of sulphur present in the functionalised powdered product detected by EDXA at 6.5% prior to deposition. This is further evidence indicating the removal of the functional groups during the deposition process.

## 5.5.2 Optical and Electrical Properties

Transmission spectra of both sets of CNT films were taken across the visible and near-infrared region of the spectrum. The insets on fig. 5-16 and fig. 5-17 show the typical spectra found for all CNT films on glass. These spectra demonstrate a steady increase in the transparency with increasing wavelength. The films did not display any semiconducting band-gap absorptions from the SWCNTs, presumably due to the tube/tube interactions quenching the electronic transitions in the van Hove density of states[145].
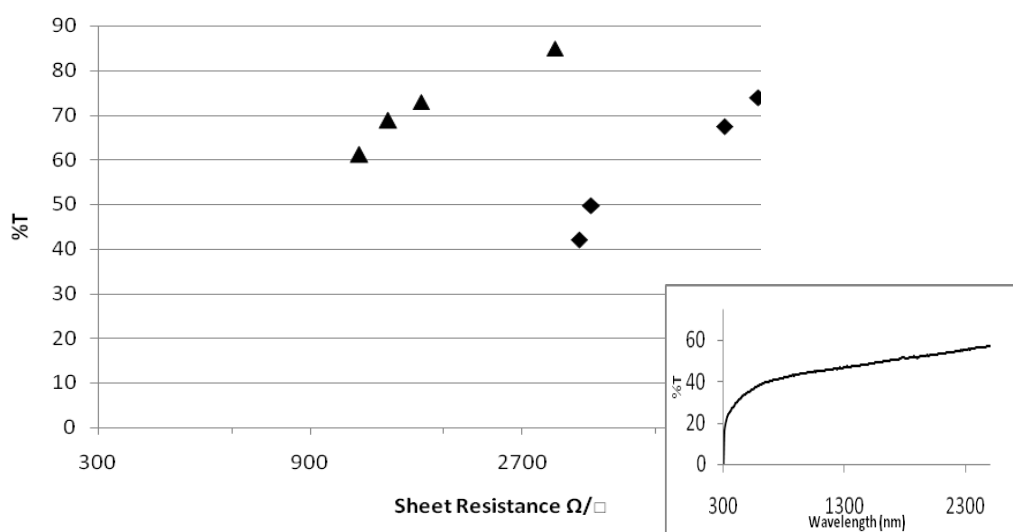


**Figure 5-16** Plot of Sheet Resistance versus Transmission (%T at 800 nm) for thin films of as-bought SWCNT with surfactant (square marker), and as-bought SWCNT films after washing (triangle marker). Inset shows example transmission spectra.
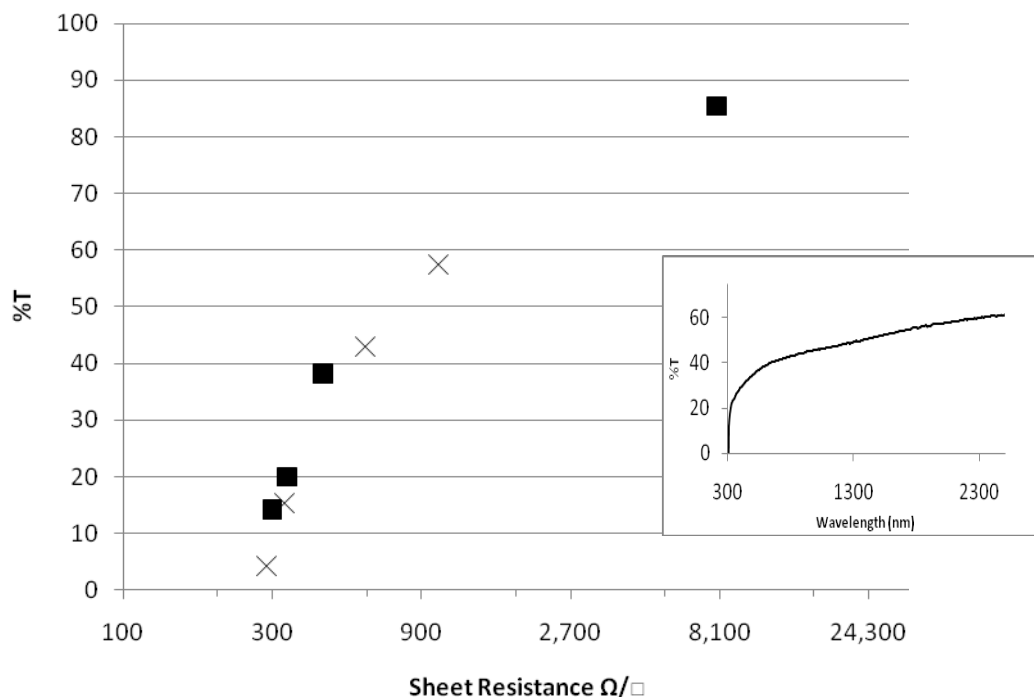
**Figure 5-17** Plot of Sheet Resistance versus Transmission (%T at 800 nm) for thin films of functionalised-SWCNT (cross marker), and functionalised films after heat treating (square marker). Inset shows an example transmission spectra for the functionalised CNT.

The sheet resistances of the films were taken using a four-point probe, and are shown in fig. 5-16 and fig. 5-17 plotted against the transparency of the film at 800 nm. Comparison of the data shows that the as-bought film deposited using surfactant gives a much lower transparency and lower conductivity. Washing of the surfactant is required for improved film properties. The functionalised films and the washed as-bought films display a similar performance giving 1000 $\Omega/\square$ for 60% transmission at 800 nm. The limiting sheet resistance seems to be in the region of 300 $\Omega/\square$, where optical transmission thereafter drops rapidly to zero. Heat-treating the f-CNT films at 600°C in an inert atmosphere resulted in an increase in resistance but also an increase in transparency as shown in fig. 5-17. The heated films still correlate with the transparency vs resistance trend of the untreated f-SWCNT thus indicating that this effect can be attributed to the loss of SWCNT from the film upon heating, presumably due to trace

oxygen present in the furnace environment. Further Raman analysis of the spray coated f-SWCNT films before heat treatment indicated that the substrate temperature during spray coating was sufficient to restore the pristine structure of the nanotubes. Indicating substantial, if not full, removal of the surface functional groups after spray coating.

The values of electrical resistance with relation to the optical transmission are highly dependent on the quality of the starting SWCNT material. The results shown in fig. 5-16 and fig. 5-17 demonstrate that when using the same source material both the traditional surfactant based method and the functionalised technique give comparable results. However, use of functionalised-SWCNT increases the affinity of the film towards the glass substrate, and does not require any cumbersome washing stages. This makes it a more desirable technique for large-scale production should the microwave reflux prove easily scaleable. To the best of our knowledge these are the first CNT thin films formed from a water based solution without the use of wrapping agents. Song et al. used dichloroethane as a solvent with no surfactant and achieved a 330 $\Omega/\square$ sheet resistance at 70% transmission from pristine nanotubes[48]. Other values quoted in the literature use the surfactant based method for spray coating, comparison of some of the best achieved results can be seen in the paper by Geng et al. where a 40 $\Omega/\square$ sheet resistance is achieved at a transparency of 70%[47]. However, these methods rely on purification of the nanotubes and post deposition treatment such as washing or doping in solutions for up to 1 hour which is impractical for large scale processing and often the doping effect diminishes over time.

### 5.5.2 Haze Measurments

Transmitted haze measurements were taken for the various CNT thin films and a plot of transmitted haze % versus average transmission is shown in fig. 5-18. Where:

$$\%H = \frac{\%T_{Diffuse}}{\%T_{Total}}$$

$\%T_{Diffuse}$ is defined as light scattered greater than 2.5° and $\%\ T_{Total}$ the total transmitted light through the sample.
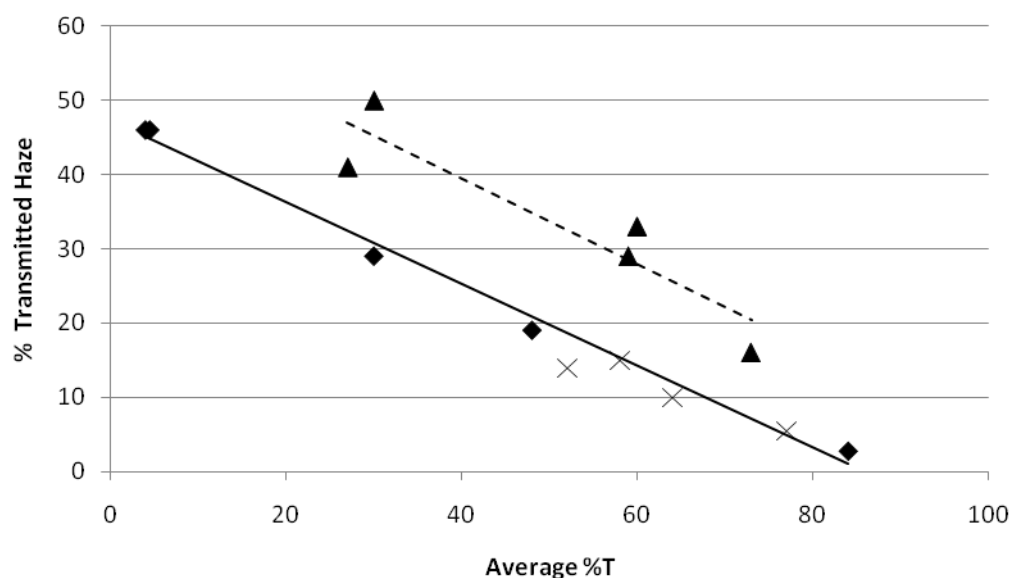


**Figure 5-18** Plot of Transmitted Haze versus the average transmission of visible light for a range of SWCNT thin films. As-bought SWCNT pre-washing (triangle marker), washed as-bought SWCNT films (cross marker) and functionalised-SWCNT films ( square marker ).

These plots show that with increasing thickness, as expected, there is also an increase in scattering of transmitted light. They also demonstrate the increased haze found in the unwashed samples containing surfactant molecules, which after washing return to the trend shown by the functionalised CNT films.

## 5.6 Conclusion

The results outlined in this chapter describe a rapid process for functionalisation of carbon nanotube surfaces with hydrophilic groups. The modified single-walled carbon nanotubes displayed a high solubility (0.74 mg/ml at pH 11) which is comparable to that of the surfactant stabilised solutions, it also displayed a maximum solubility dependency based on the pH of the solution. The presence of functional groups was determined through solubility experiments, EDXA, IR, and TGA data; the modification in the structural and electronic characteristics of the nanotubes was monitored by Raman spectroscopy and SEM imaging. Sulphones and sulphonate groups proved to be the dominant functionally bound species produced using this technique. No evidence of carboxylation was found, which is unusual for an acid reflux process and may prove to be a promising route to a more selective SWCNT surface chemistry. The functionalisation of the surface was shown to be a reversible process following heat treatment of the samples (determined by XPS), allowing for restoration of the SWCNT electronic structure. Atmospheric microwave acid reflux provides a fast and effective route to carbon nanotube solubility in aqueous media, avoiding the use of environmentally harmful solvents and additional surfactants in processing.

Subsequent spray-coating of glass substrates was achieved using both traditional surfactant based methods, and using the soluble microwave functionalized-SWCNT in water. This novel processing technique has shown to be an effective way of producing randomly assembled carbon nanotube thin films, and demonstrates the potential benefits of using a highly functionalised nanotube material suspended in water, which eliminates the need for cumbersome surfactant stabilisation.

# 6 Zinc Oxide

## 6.1 ZnO Thin Films Grown by AACVD

*Various metal-organic precursors were assessed for their viability in producing doped zinc oxide thin films by AACVD, for transparent conducting applications. Electrical conductivities in the resultant thin films were found to be inadequate for use in TCO applications; however, films produced from a zinc acetate $[Zn(C_2H_3O_2)_2]$ precursor displayed high photocatalytic activity, high transparency over the visible and infrared (80 -95 %), and a 001 (c-axis) preferred orientation. The films displayed a changing surface morphology, orientation, and crystallographic characteristics which were dependent on the substrate temperature during deposition. The photocatalytic activity of the films was determined using the destruction of stearic acid by UV irradiation: the rate was monitored via IR spectroscopy and showed appreciable activity in the films deposited at 650ºC. Water droplet contact angles on both ambient and UV irradiated ZnO surfaces were determined: the films formed at 650ºC displayed an increase in photo-induced hydrophillicity.*

## 6.2 Introduction

Chapters 2 and 3 presented research into various doped tin oxide systems, and the properties required for their application as transparent conducting oxide (TCO) materials [27]. A recent potential replacement for the FTO system is the Group III doping of zinc oxide, which is theoretically predicted to have superior transparency and conductivity properties[203], alongside a low cost of starting materials and the advantage of an ecologically friendly elemental composition[204] with an abundance of chemical precursors[205].

Un-doped zinc oxide adopts a hexagonal wurtzite structure, and is an intrinsic n-type semiconductor due to stoichiometric deviations arising from oxygen vacancies and interstitial zinc[27]. ZnO exhibits a direct wide band gap energy of ~3.37 eV and a large exiton binding energy of 60 meV at room temperature[206, 207]. These solid state properties make ZnO a candidate for not only TCO materials, but a variety of potential applications from optoelectronic devices such as solar cell and LED technologies[208, 209], to the use of its piezoelectric and piezo-optic effects for acoustoelectric and acousto-optic functionality[210]. It has been shown that the preferred crystal orientation along the *c*-axis, perpendicular to the substrate, affects the optical transparency of the zinc oxide, where a highly oriented (001) peak (*c*-axis) as shown in the X-ray diffraction pattern gives a low light propagation loss through the film[209].

There have been reported a variety of techniques for preparing thin films of doped-ZnO, ranging from photochemical methods[211] to sol-gel procedures[205]. There is a wealth of research which has gone into the chemical vapour deposition of ZnO thin films and their resulting properties, however the focus has been on evaporation techniques using Atmospheric Pressure or Low Pressure CVD[212]. These studies have yielded doped-zinc oxide thin films with promising properties: Park et al.[19] made gallium doped ZnO oxide with a resistivity value of 8 x $10^{-5}$ $\Omega$.cm; Fay et al.[22] produced boron doped ZnO films with a sheet resistance of 10 $\Omega/\square$ and a high haze value for light scattering; Sin et al.[213] deposited aluminum, gallium and indium doped zinc oxide with a 6 x $10^{23}$ cm$^{-3}$ charge carrier density and 3.61 x $10^{-4}$ $\Omega$.cm resistivity; Hongsingthong et al.[214] made 10 $\Omega/\square$ films of boron doped zinc oxide with high haze values and a pyramidal topology for light scattering. However, as of yet the consistency, repeatability, and scale-up of these processes has proved difficult on an industrial scale, thus hindering the commercial production of doped zinc oxide TCO products.

The following chapter outlines the attempted deposition of doped and un-doped zinc oxide using aerosol assisted chemical vapour deposition (AACVD) and a range of chemical precursors. This technique was investigated as a possible reliable and scaleable route for doped zinc oxide production. Additionally, the action of un-doped zinc oxide, produced by AACVD, as a photocatalytic super-hydrophillic material was

compared to titania (the leading commercial photocatayst used for self-cleaning surfaces, air and water purification and anti-microbial applications[68]).

## 6.3 Experimental

### 6.3.1 AACVD
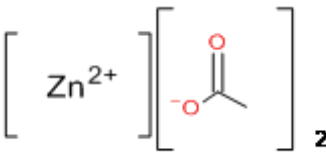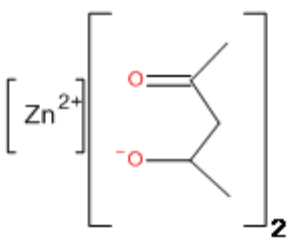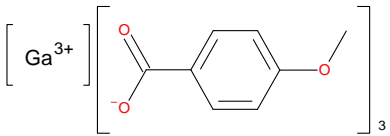
The Aerosol Assisted Chemical Vapour Deposition (AACVD) process was detailed in chapter 2: section 2.3.1, figure 2-1 and equation 2-1 so shall not be repeated here. The experiments in this chapter use the AACVD technique with an ultrasonic aerosol generation process - which has been reported to give a highly mono-disperse droplet size[215]. The droplet size is in turn dependent on the density and surface tension of the liquid medium and the operating frequency: as outlined in Lang's equation (Equation 2-1)[21]. Use of a methanol solvent and an operating frequency of 20 kHz gives the predicted aerosol droplet diameter of 45 µm.

Delivery of the aerosol solution to the reaction chamber is mediated using a manifold gas inlet to broaden the aerosol/carrier gas flow allowing a more even arrival rate onto the substrate surface.
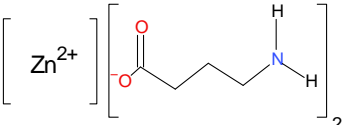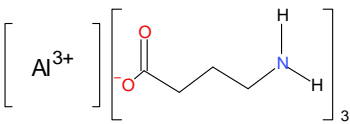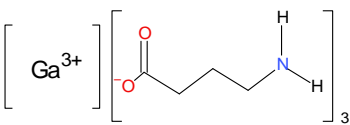
Pilkington barrier glass (30 nm layer of $SiO_2$ coated onto glass) was used as the substrate material, to prevent leaching of ionic impurities from the glass. The substrate temperature was taken to be that of the carbon heating block it was directly supported on (as measured by the thermocouples within the carbon block).
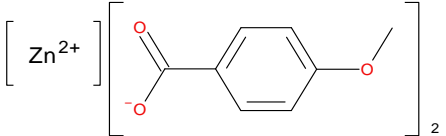
### 6.3.2 Doped Zinc Oxide

The series of structures shown in table 6-1 display the precursors used for the attempted deposition of doped zinc oxide thin films, for transparent conducting applications. Four different zinc precursors were investigated, each in combination with one of six different dopant precursors. Aluminium, gallium, and fluorine doping of the zinc oxide host matrix was investigated under a range of AACVD temperature conditions using methanol as a solvent. The aerosol was carried to the reactor using nitrogen as an inert carrier gas at a flow rate of 1.5 Lmin$^{-1}$.

| Zinc Precursor | Dopant Precursor | Doping ratio (at.% of zinc) | Deposition temperature (˚C) |
|---|---|---|---|
| Zinc (II) Acetate $Zn(O_2C_2H_3)_2$  OR Zinc (II) Acac  | Aluminium Nitrate $Al(NO_3)_3$ | 0.5 – 5% | 400-600 |
| | Aluminium isopropoxide $Al(O\text{-}i\text{-}Pr)_3$ | 1-5% | 500-600 |
| | Ga (III) 4-Methoxy Benzoate  | 1-10% | 500-600 |
| | Ammonium Fluoride $(NH_4)F$ | 1-50% | 500-600 |

**Table 6-1** The above tables show the zinc precursors and dopant precursors used in the attempted deposition of zinc oxide based transparent conducting thin films by AACVD. Experimental conditions giving atomic % ratios and substrate deposition temperatures are included.

| Zinc Precursor | Dopant Precursor | Doping ratio (at.% of zinc) | Deposition temperature (˚C) |
|---|---|---|---|
| Zinc(II)4-aminobutanoate  | Aluminium(III)4-aminobutanoate  | 1% | 450-600 |
|  | Gallium(III)4-aminobutanoate  | 1% | 550-600 |

| Zinc Precursor | Dopant Precursor | Doping ratio (at.% of zinc) | Deposition temperature (˚C) |
|---|---|---|---|
| Zinc(II)-4-methoxy-benzoate  | None | None | 450-600 |

**Table 6-1 cont.** The above tables show the zinc precursors and dopant precursors used in the attempted deposition of zinc oxide based transparent conducting thin films by AACVD. Experimental conditions giving atomic % ratios and deposition temperatures are included.

### 6.3.3 Un-Doped Zinc Oxide

A series of experiments were carried out in order to assess the effect of deposition temperature on the un-doped zinc oxide thin films, and the effect it had on their performance as a photo-induced superhydrophillic catalytic material. The degradation of stearic acid was used as a measure of the photocatalytic action (the technique is outlined in section 6.4.5); this action was then compared to the leading commercial standard, titania.

The precursor solution used for non-doped ZnO thin film deposition consisted of zinc acetate (0.4 g) in analytical grade methanol (50 ml) (0.044 mol/L), stirred vigorously for 20 min. The deposition temperature was varied from 400ºC to 650ºC at increments of 50ºC. A 1.5 Lmin$^{-1}$ flow of nitrogen carrier gas was used in all the experiments.

## 6.4 Results

The following results section is split into two distinct parts: the first, concerns the deposition of doped zinc oxide thin films using the precursors outlined in the experimental chapter; the second section, concerns the deposition of the un-doped ZnO material using zinc acetate, and the action of the coatings as photo-induced super-hydrophillic catalytic materials.

### 6.4.1 Doped Zinc Oxide for Transparent Conducting Applications

Depositions of doped-ZnO thin films were attempted using the series of reagents outlined in the experimental section of this chapter with the hope of producing transparent conducting oxide materials.

Zinc acetate and zinc acac precursors produced ZnO thin films with a high transparency (>85 %T in the visible including substrate absorption) and good adhesion to the glass substrate passing both the steel scalpel and scotch tape test.

The Zinc(II)-4-aminobutanoate precursor produced only partially decomposed coatings, evident from the viscous nature of the films, this was the case up to the high deposition temperature of 600˚C. A further annealing stage was required (600˚C for 3 hours) to fully decompose and crystallise the coatings in order to record optical and electrical properties.

The Zinc(II)-4-methoxy-benzoate was found to be insoluble in a range of solvents including; water, methanol, ethanol, isopropanol and toluene, as-such aerosol delivery was not possible and no films were formed with this compound.

The three zinc precursors which produced ZnO thin films (Zinc acetate, zinc acac and zinc(II)-4-aminobutanoate) were then mixed with the dopant precursors in the methanol solution prior to AACVD. The concentrations of zinc and dopant atoms were mixed in varying atomic ratios, as outlined in the experimental section. The resistance properties of the coatings were monitored using fixed distance (5mm), two point resistance measurements, across the surface of the films (repeated at multiple points and averaged). Table 6-1 shows the average minimum baseline resistance values for each of the three zinc precursor synthesised films without doping, alongside the minimum resistance values taken from the most promising doped coatings.

| Precursor System | Temperature of Deposition (˚C) | Minimum Average Two-Point Resistance (kΩ) |
|---|---|---|
| Zinc (II)Acetate | 500 | 1 |
| Zinc(II)Acetyl acetone (acac) | 450 | 50 |
| Zinc (II)4-aminobutanoate | 500 | Out of range |
| Zinc(II)Acetate/ Aluminum Nitrate (1 at. %) | 600 | 5 |
| Zinc(II)Acetyl acetone (acac) / Aluminium Nitrate (1 at. %) | 600 | 40,000 |
| Zinc(II)4-aminobutanoate / Gallium(II)4-aminobutanoate (1 at. %) | 550 | Out of range |

**Table 6-2** Minimum resistance values (averaged over multiple areas) for thin films of un-doped and doped Zinc Oxide coatings on barrier glass substrates; deposited by aerosol assisted chemical vapour deposition (AACVD).

Table 6-2 shows the minimum resistance values obtained for three un-doped zinc oxide coatings deposited using three different precursors; plus three doped-zinc oxide thin films deposited with the addition of aluminium and gallium containing dopant species. Not only did the doped films not display any enhanced conductivity properties, but the coatings actually gave higher resistance values than their un-doped counterparts. No combination of the conditions outlined in the experimental chapter gave doped films which showed any appreciable increase in conductivity.

The ability of zinc oxide to produce highly conductive films with aluminium, gallium, boron, and fluorine is widely acknowledged in the literature[205, 216-218], however, the use of AACVD seems incompatible with doping of the zinc oxide lattice. For an

explanation of this, the introductory chapter (section 1.5) should be referred to. Three explanations are given for the inability of a materials to dope, including; the formation of 'Killer defects', unsuitable donor energy levels and insoluble dopants. The energy levels formed by gallium, aluminium, boron, and fluorine doped into ZnO have all been shown to result in highly conductive coatings in the literature - therefore this cause can be eliminated. 'Killer defects' can be disregarded as these would form regardless of the deposition method. Therefore the inability of AACVD to produce conductive doped zinc oxide coatings, is most likely to be attributed to the formation of competing compound phase formation or impurity segregation. This can be attributed to the slow rate of deposition in the AACVD process, which allows for a high level of atomic mobility of the adsorbed constituent atoms before the build-up of subsequent layers. This high atomic mobility allows for thermodynamically favorable split phase coatings to form, where, instead of substituting aluminium or gallium atoms into the zinc oxide matrix, phase segregation of aluminium oxide and gallium oxide is occurring. This phase segregation has been reported elsewhere in the literature where $Ga_2O_3$ and $Al_2O_3$ formation, or metallic segregation occurs [216, 219]. This acts to increase resistance in the bulk films.

## 6.4.2 Un-doped zinc oxide for photocatalysis

Un-doped zinc oxide films were produced over a range of temperatures via the AACVD process, using zinc acetate precursor. The films showed high adhesion to the glass substrate, passing both the scotch tape test and steel scalpel scratch test. Solubility testing of the films was carried out in organic solvent (Ethanol and Toluene) and also under basic conditions (2M NaOH) and acidic conditions (2M HCl), where the film/substrate were left submerged for 24 hours. The presence of the film on the substrate surface was monitored using electrical resistance measurements. The films suspended in the organic solvents showed no change, those in the acid and base were completely removed after 24 hours.

Film thickness measurements by scanning electron microscopy, shown in figure 6-1, gave a depth range of 200 nm up to 600 nm depending on deposition temperature and sampling area. This large variation in thickness can be seen to change with increasing lateral distance from the manifold, indicating thermophoretic and mass limited transport effects taking place within the reactor. The use of a cold walled reactor results in a transverse temperature gradient causing thermal convection to impinge upon the main forced flow, this is then combined with mass limited transport of the zinc precursor, causing depletion of zinc feedstock as the carrier gas travels down the substrate. The mixing of these transport processes has resulted in a geometric variation of film thickness which is dependent on the temperature of the reaction chamber, the concentration of the aerosol solution, and the flow rate of the carrier gas. This temperature dependency is evident from the examination of interference fringe patterns caused by film thickness, where the coloured fringes change at a varying rate dependent on the temperature of the experiment. Testing performed at 650ºC resulted in a lateral deposition area of less than 10 mm, whereas those experiments performed at 400ºC gave a deposition length of more than 50 mm with an increased lateral coloured fringe width. These results show the incoming aerosol flow rate must be tailored for a specific reaction temperature in order to overcome the thermal barrier and achieve a uniform film deposition.



**Figure 6-1** Scanning electron micrographs of side on ZnO thin films deposited at: *Left)* 650ºC, and *Right)* 550ºC.

### 6.4.3 Surface Morphology

The presence of zinc oxide was further confirmed using energy dispersive x-ray analysis, showing the presence of zinc and oxygen with only minimal carbon contamination. The surface morphology of the ZnO thin films was evaluated by field emission scanning electron microscopy. The surface of the thin films deposited at 450ºC and above, showed a surface structure composed of disc like crystals. The average diameter of the disk structures increased with increasing temperature, as can be seen in figure 6-2. Those deposited at temperatures of 450ºC and 500ºC, showed an estimated diameter of 100 nm with stacking of multiple disks. Those deposited at 550ºC, 600ºC, and 650ºC show estimated diameters of 200 nm, 300 nm, and 500 nm respectively. The films deposited at substrate temperatures of 500ºC and 550ºC showed additional surface structures much smaller than the aforementioned disk like grains, these structures ranging in size between 10 and 50 nm appeared to be the spherical end of rod like projections emanating from the film. Mixing of the large disk structures and smaller crystallites has been reported previously in the literature[220], however, resolution of the smaller crystallites is difficult via SEM.

No surface structure was found for the film deposited at 400ºC, which can be attributed to a lack of orientated crystallinity in the film, as shown by the XRD data (table 6-3 *X-ray diffraction* section), or an inability to resolve the fine structure using SEM. Comparison of the surface morphlogy shown in figure 6-2 and the side-on SEM images shown in figure 6-1 suggests a Volmer-Weber type film growth[221]. This three dimensional island growth mode results from the nucleation of small clusters onto the substrate surface which grow into larger islands, and stack together to produce a continuous layer[26]. Volmer-Weber type growth implies greater affinity of the forming ZnO oxide layer to itself as opposed to the glass substrate.
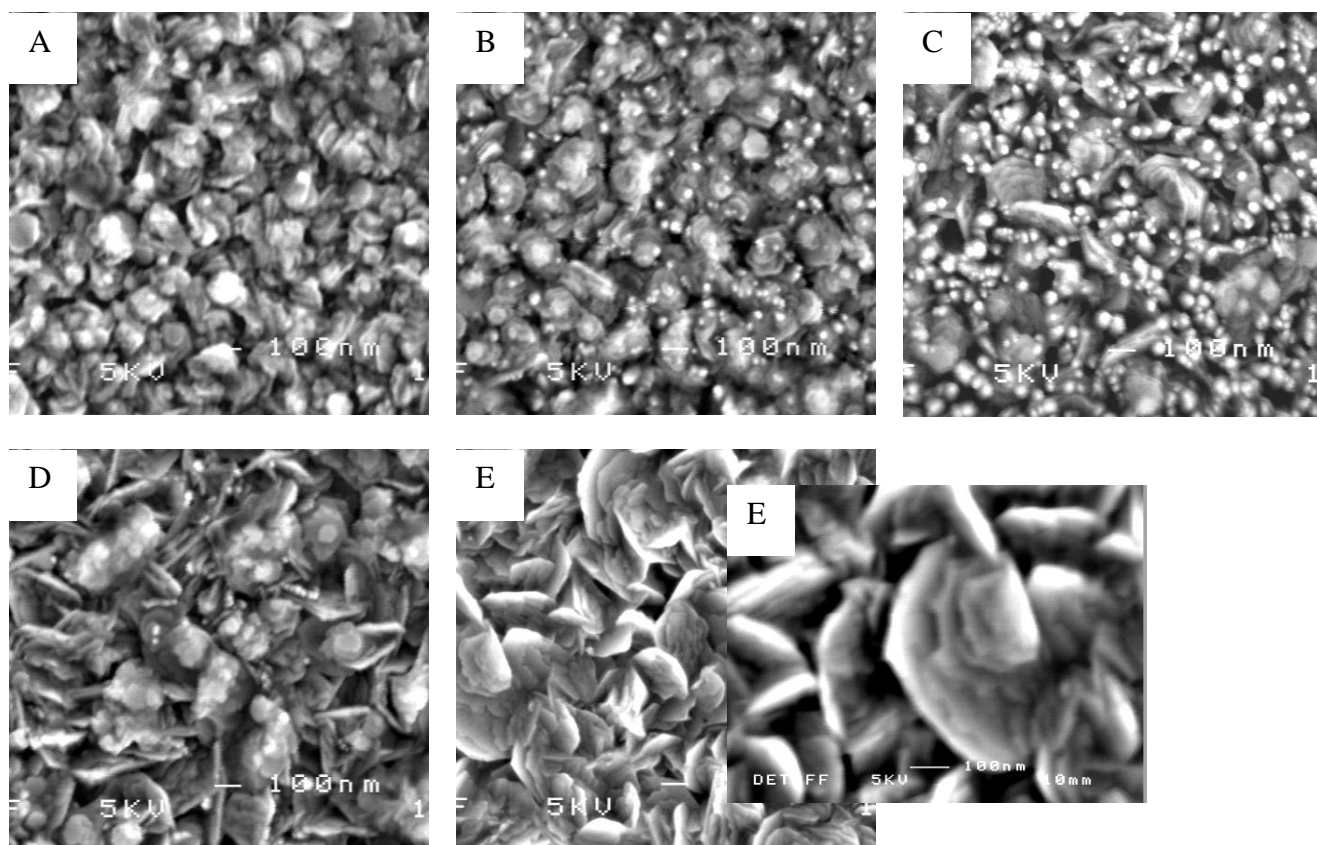
**Figure 6-2** Scanning electron micrographs of ZnO thin films deposited at *A)*450ºC,   *B)*500ºC, *C)*550ºC, *D)*600ºC, *E)*650ºC.

Figure 6-1 B shows the stacked, continuous film layer with a surface structure island projecting out of the film, thus providing evidence for Volmer-Weber type growth. Increasing the deposition temperature of the film allows for increased surface diffusion relative to the incoming flux of precursors, leading to the observed differences in the thin film properties. The high deposition temperature films showed the highest growth rates, with a maximum rate for the film grown at 650ºC showing 10 nm min$^{-1}$, whereas the film deposited at 400ºC showed a maximum rate of 2 nm min$^{-1}$.

198

### 6.4.4 X-Ray Diffraction Data

Crystallinity and preferred orientation of the films were investigated by XRD (shown in figure 6-3). The results display an overall increase in crystallinity with increasing temperature, and a greater peak intensity in the (002) Bragg lattice plane as the temperature of the substrate is increased. This indicates an increase in the *c*-axis crystal orientation perpendicular to the substrate surface with increased substrate temperature, this trend is concurrent with other results reported in the literature using different deposition techniques[222, 223].
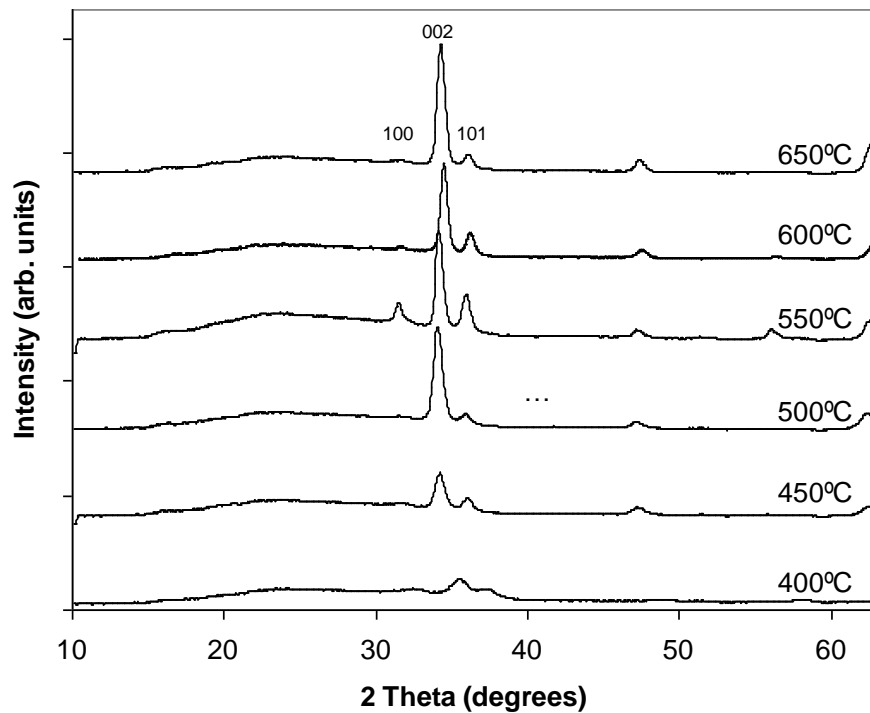


**Figure 6-3** The x-ray diffraction pattern of ZnO films prepared over six different substrate temperatures. Deposited by AACVD of zinc acetate in methanol over a barrier glass substrate.

The (002):(101) peak intensity ratio increases from 1.5 at 400°C, to 9 at 650°C, showing the temperature dependency of the *c*-axis orientation with respect to the other lattice planes. The relative peak intensities were further studied using a least squares Rietveld refinement[224] with application of the March-Dollase function[225, 226] to determine the March coefficient, *r*, this value characterises the relative strength of the preferred orientation and is related to the amount of sample deformation. Calculations were done using GSAS[227] and EXPGUI[228] software. The March-Dollase model gives an

*r* value which indicates the extent of preferred orientation (*r* = 1 shows random orientation), as the value of *r* moves further away from 1 the preferred orientation is increasing in the sample. Resulting *r* factors are presented in table 6-3, and clearly show that as the temperature of deposition increases the *r* value decreases from 1 for the (002) plane. This represents an increasing (002) preferred orientation with increasing temperature. For the film deposited at 550°C, the *r* value occurs at a higher value than the trend would suggest for the other films, this anomalous value could be linked to the high number of rod like protrusions present amongst the disc-like structures seen in the SEM images (fig. 6-2 C), these rod structures showing an alternate growth pattern and orientation will oppose the r value for the ZnO disk structures.

Table 6-4 shows the fitted lattice parameters for the experimentally obtained XRD patterns used to calculate the March coefficients, they show excellent correlation with the literature values for hexagonal ZnO (3.25 Å, 3.25 Å, 5.21 Å *a*, *b* , *c* respectively)[229], this shows a good data fit and confirmation of hexagonal ZnO.

| Film Deposition Temp.  (°C) | *r*  factor (001) plane |
|---|---|
| 400 | 0.71 (1) |
| 450 | 0.59 (1) |
| 500 | 0.50 (1) |
| 550 | 0.65 (1) |
| 600 | 0.49 (1) |
| 650 | 0.51 (1) |

**Table 6-3** March coefficient values-representing the preferred orientation of the (001) plane (relative to that of a randomly orientated polycrystalline structure) of ZnO thin films grown over a range of temperatures using AACVD from a methanol based solution of zinc acetate. Deviation from an r-factor of 1 indicates preferred orientation.

| Film Deposition Temperature (°C) | Fitted Lattice Parameters (Å) | |
|---|---|---|
| | *a* | *c* |
| 450 | 3.27 | 5.24 |
| 500 | 3.27 | 5.26 |
| 550 | 3.26 | 5.24 |
| 600 | 3.26 | 5.20 |
| 650 | 3.27 | 5.22 |

**Table 6-4** Fitted unit cell lattice parameters calculated using least squares crystal structure Rietveld refinement of the XRD data, obtained from ZnO thin films prepared using AACVD of a zinc acetate in methanol solution over a range of temperatures.

The 002 peak full width at half maximum (FWHM) was used to estimate the crystallite dimension in the *c*-axis direction. This was done using the Scherrer equation[230].

$$t = 0.9\lambda/B\cos\theta$$

**Equation 6-1** Scherrer Equation.

Where: t is crystallite thickness, $\lambda$ is the wavelength of the X-ray source, $\theta$ is the angle of reflection, and B is the full width of the reflection peak at half maximum intensity (FWHM).

The corrected FWHM (B) was found using the formula $B^2 = B_s^2 - B_o^2$, where $B_s$ is the measured width, and $B_o$ is the instrumental broadening value obtained by measuring the diffraction peak width of a lanthanum boride 110 peak, which occurs at a $2\theta$ angle of 30.5° close to the 32° 002 peak of ZnO. The results shown in figure 6-4 indicate a grain size ranging from 4nm to 20nm, and show that the crystallite *c*-axis dimension was dependent on the substrate temperature during deposition, leading to larger grain thickness as the temperature was increased. This small disc diameter along the *c*-axis could account for the disc stacking seen in SEM images, indicating each disc structure may be several layered distinct crystal regions.
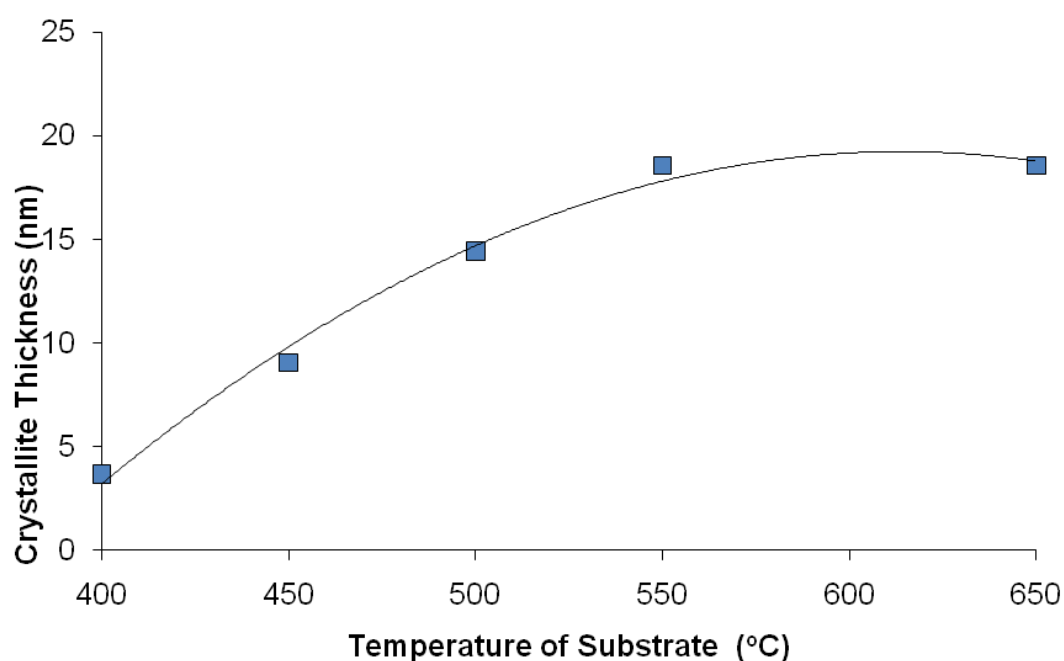


**Figure 6-4** Dependency of grain size in the c-axis direction with varying temperature of AACVD films of ZnO on glass formed from the AACVD of zinc acetate in methanol.

### 6.4.5 Optical Properties

The room temperature transmission and reflection characteristics of the un-doped zinc oxide thin films were investigated using visible/near IR spectrometry. The spectra shown in figure 6-5 indicate a high transparency across the visible and infrared. The transparency ranges from ~80% up to ~ 95% in the visible.

The films formed at low temperatures display prominent interference effects. These interference fringes are caused by the multiple reflections at the three interfaces of the thin film/transparent substrate bi-layer. The effect of interference becomes more pronounced at lower deposition temperatures because the film thickness becomes more uniform over the beam sampling area. The films grown at higher deposition temperatures have a greater variation in thickness over a set area, this causes the destruction of any interference pattern and an averaging of the transmission spectra. A method proposed by Swanepoel [231] can be used to estimate the thickness of the film from the interference pattern observed. The transmission spectra taken with an air background are used to calculate the refractive indices of the substrate and the thin film at its maxima and minima values, this then allows the film thickness to be determined. Performing this calculation on the film deposited at 450ºC, which displayed the clearest interference pattern, gives a thickness value of 530 nm which is consistent with the images seen in the SEM. This implies the oscillations seen in the transmission are a result of interference type patterns, and shows the difference in thickness variation between the films. The lower temperature films giving a greater interference pattern due to a more uniform layer depth across a sample area.
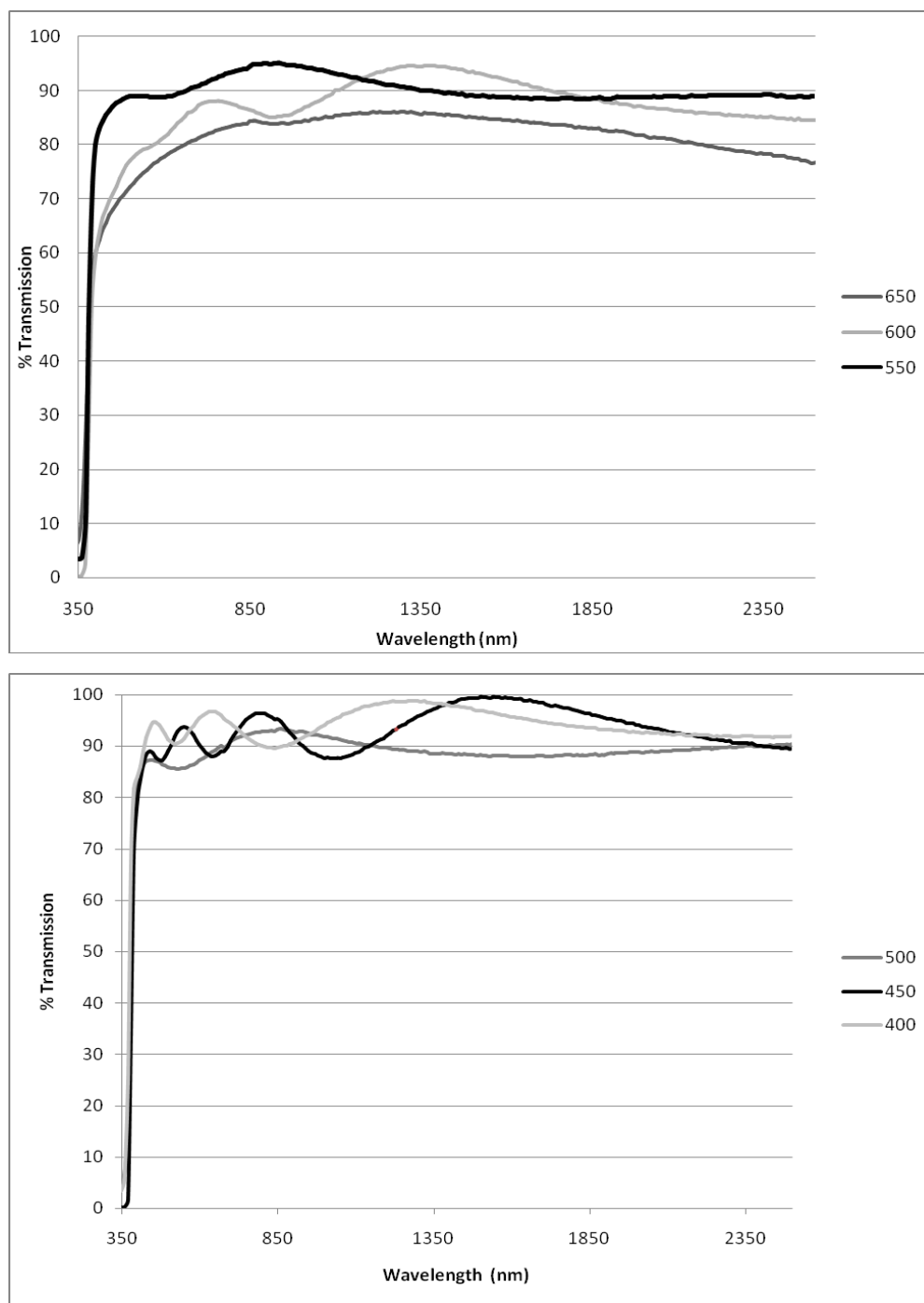
**Figure 6-5** Visible/Infrared transmission spectra of ZnO films prepared over different substrate temperatures. (Uncoated glass substrate used as background).

## 6.4.6 Photocatalytic Testing

The photocatalytic abilities of the un-doped ZnO films produced by AACVD at the high and low ends of the deposition temperature range were assessed using the stearic acid test.

A thin layer of stearic acid (0.5 ml of 0.02 M solution in MeOH) was spin coated onto the surface of the ZnO films, this was then allowed to dry at 120ºC for 15 min. The rate of stearic acid degradation (induced by 254 nm UV irradiation) was measured using IR spectrometry at 15 min intervals of irradiation. This was accomplished by integrating the characteristic peaks produced by the asymmetric and symmetric C-H stretching in the $CH_2$ groups, at 2923 $cm^{-1}$ and 2853 $cm^{-1}$ respectively[232]. The overall reaction is summarised as:

$$ZnO/UV254$$

$$CH_3(CH_2)_{16}CO_2H \; + \; 26O_2 \longrightarrow 18CO_2 \; + \; 18H_2O$$
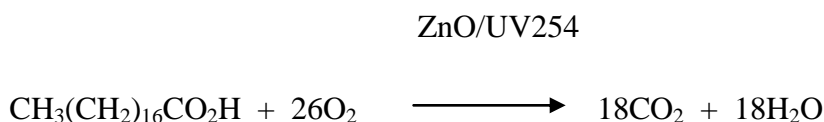
The area of the peaks is directly proportional to the amount of stearic acid present on the surface, and can be calculated using the following conversion factor as proposed by Mills et al[233]: where $9.7 \times 10^{15}$ molecules of stearic acid $cm^{-2}$ is proportional to an integrated area of 1 $cm^{-1}$.

The photocatalytic degradation of stearic acid is a zero order reaction, so linear lines of best fit can be plotted using the total integrated peak area versus irradiation time. The plots show that no stearic acid degradation occurred on the glass standard or the film deposited at 400ºC, whereas, the higher temperature film (650ºC) exhibited marked photocatalytic action.
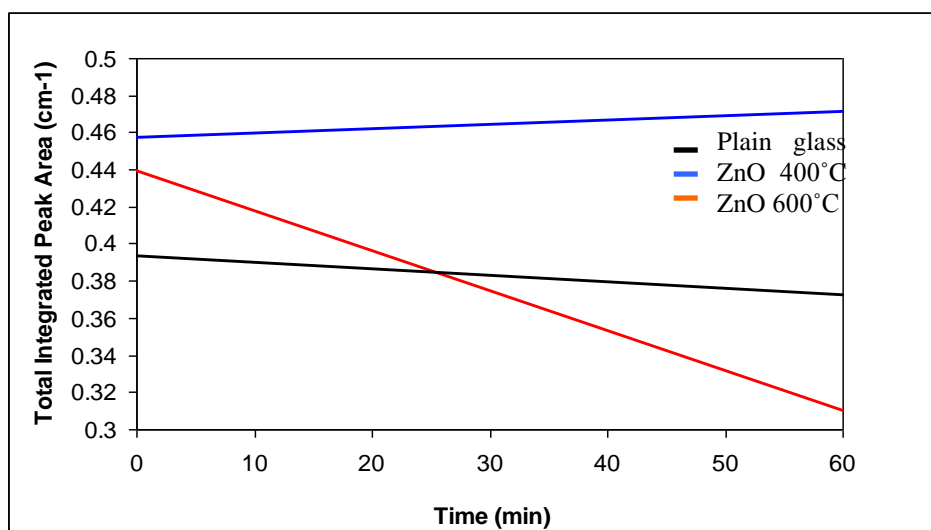
**Figure 6-6** Plot of total integrated peak area of the 2923cm^{-1} and 2853cm^{-1} stearic acid infrared absorbances vs. the time of UV irradiation of stearic acid coated substrates. Substrates include plain silica barrier glass and ZnO coated barrier glass formed by AACVD at 400˚C and 650˚C.

The photocatalytic ability can be attributed to the greater crystallinity present in the higher temperature deposition film, allowing for enhanced photon capture and electronic promotion; thus inducing formation of the catalytic radical species required for the stearic acid degradation. Using the conversion factor proposed by Mills et al.[232] and the gradient taken from the line of best fit, the high temperature ZnO layer gave a photocatalytic rate of $3.56 \times 10^{11}$ molecules of SA cm^{-1} s^{-1}. This rate can be represented as a formal quantum efficiency where:

$$FQE(SA) = \frac{\text{Rate of SA removal (molecules cm}^{-1}\text{ s}^{-1})}{\text{Rate of incident light (photons cm}^{-1}\text{ s}^{-1})}$$

**Equation 6-2** Formal quantum efficiency equation for stearic acid[234]

The photon flux calculated using actinometry gave a value of 2.48 x $10^{14}$ ± 1.93 x $10^{13}$ hv cm$^{-1}$ s$^{-1}$. This equates to a FQE(SA) for the ZnO film deposited at 650ºC of 1.44 x $10^{-3}$ molecules per photon. This rate is comparable to that of titania thin films as reported in the literature, where: Mills et al. quote a value of 2.5 x $10^{-3}$ molecules per photon [233] and Paz et al. give a value of 6.7 x $10^{-3}$ molecules per photon [235]. One study done by Miki-Yoshida et al. compared the photocatalytic ability of both ZnO and TiO$_2$ thin films inside Vycor tubing [236], the experiment was done monitoring butane conversion under UV irradiation. The results showed the titania system to have three times the catalytic rate constant (65.8 h$^{-1}$m$^{-2}$) when compared to zinc oxide (19.3 h$^{-1}$m$^{-2}$) this relative ratio of activity agrees with the observed result in our experiment. Another photocatalytic study done by Daneshvar et al. into the degradation of the insecticide diazinon using ZnO nanocrystals under 254 nm UV light showed a quantum yield of 0.013 molecules per photon, this again marks the catalytic ability of zinc oxide, but it also indicates the quantum efficiency varies vastly for different organic species.

### 6.4.7 Contact Angle Measurements

Water contact angles were calculated from diameter measurements of 5 μL water droplets deposited on the ZnO surface. The films were then UV irradiated for 24 hours under a 254 nm light source with a photon flux of 2.48 x $10^{14}$ ± 1.93 x $10^{13}$ hv cm$^{-2}$ s$^{-1}$, the measurements of the contact angles were then repeated. Figure 6-7 shows the change in contact angle related to the substrate deposition temperature.

The contact angle of the droplets taken on the surfaces exposed to the ambient light decreased with increasing deposition temperature of the films, this can be attributed to the change in the surface morphology. Cassie and Baxter [237] originally proposed the relation between surface roughness and the hydrophobicity of the material, regarding the top layer as an air solid composite surface. The wettability of the surface is determined by the composition ratio and structural spacing present. Clearly, the surface structure dependence on deposition temperature as seen in the SEM images is affecting the composition of the surface layer, increasing its hydrophilicity with increasing grain size.
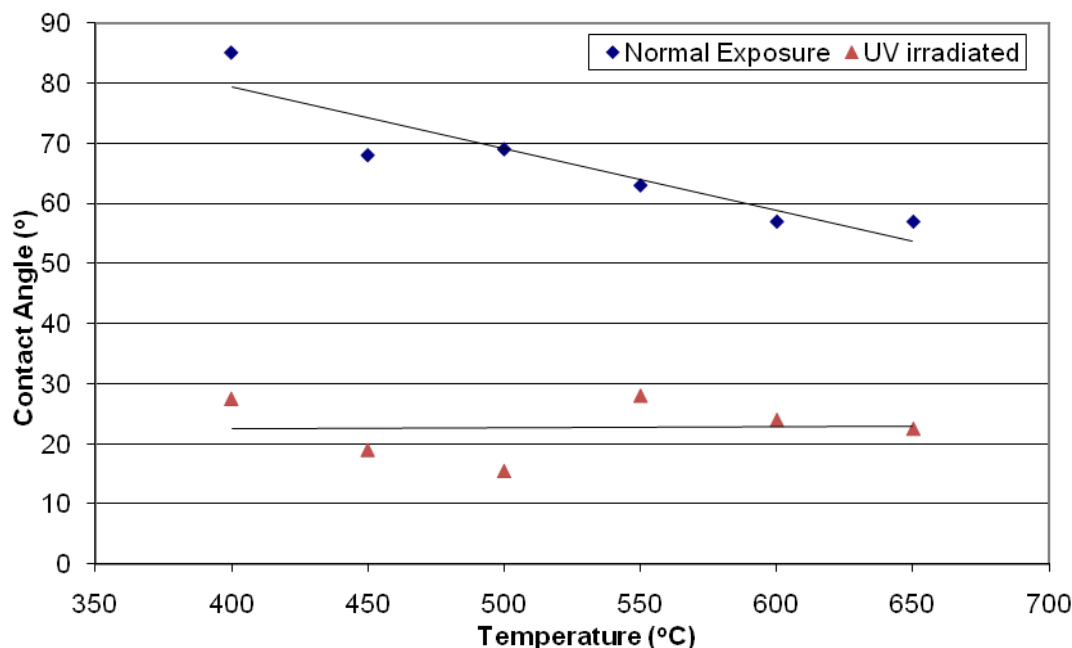
**Figure 6-7** Contact angles at the ZnO-Water boundary (5 µL water droplet on the thin film surface), for ZnO thin films deposited at varying temperatures (400ºC - 650 ºC).

The films also exhibited a photoinduced hydrophilicity (as shown in figures 6-7 & 6-8) where a large decrease in the contact angle occurs in the films which were UV irradiated for 24 hours, compared to the films under ambient light conditions. There are two mechanisms proposed to explain this phenomenon, the first, is the formation of reconstructed hydroxyl surface groups and, the second, is the removal of hydrophobic surface species via photocatalytic action[238]. It has been shown that the higher temperature films display photocatalytic properties, however, the film deposited at 400ºC showed no catalytic ability-yet displayed photoinduced hydrophilicity. This suggests that where degredation of hydrophobic species may play a role in the photoinduced hydrophilicity it is clearly not the only factor influencing this process.
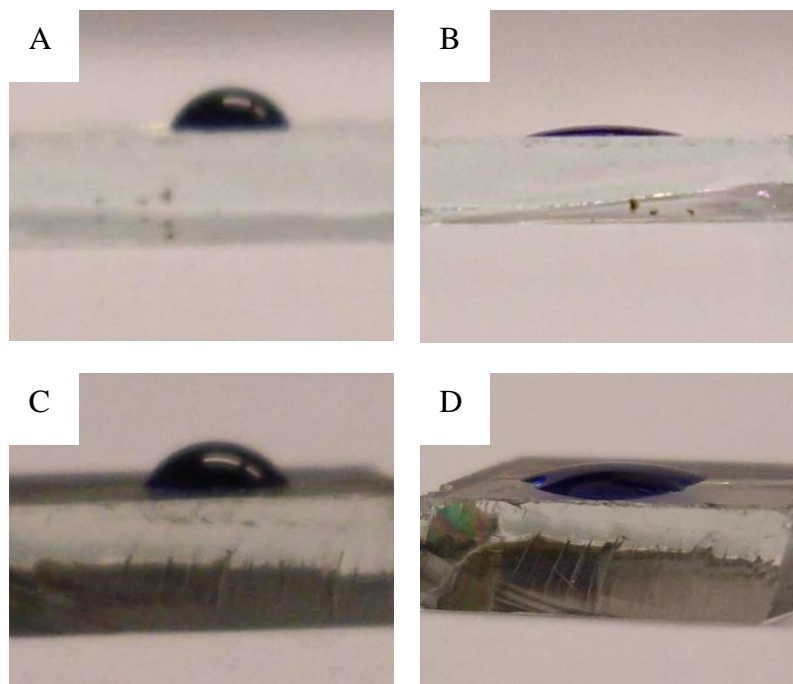
**Figure 6-8** Images of coloured water droplets (dyed with methylene blue) on the ZnO surfaces before and after 24 hour UV irradiation *A)* Ambient ZnO surface (400ºC deposition temperature). *B)* UV irradiated ZnO surface (400ºC deposition temperature). *C)* Ambient ZnO surface (650ºC deposition temperature). *D)* UV irradiated ZnO surface (650ºC deposition temperature).

Similar studies into the photoinduced hydrophillicity on zinc oxide have been done by various groups. The Fujishima group originally looked into the controllable wettability of zinc oxide and titania prepared by spray pyrolysis[239], their results showed a decrease in contact angle from 109º to less than 10º upon UV irradiation of the ZnO surface. Further work done by Wang et al.[240] looked at the relation between surface structure of the ZnO film and the photoinduced hydrophillicity, the films were prepared via a CVD technique to yield a hierarchical surface structure composed of micro and nano scale features. This group found that introducing these features amplified the effect, giving contact angles of 163º and 0º for the ambient and UV irradiated films respectively, the change is attributed to surface 2D and 3D capillary effects. These results show ZnO to be a highly photosensitive semiconductor and illustrate the effect of changing the surface structure of the metal oxide.

## 6.6 Conclusion

The attempted deposition of doped ZnO thin films by AACVD proved to be unsuccessful in the deposition of a TCO material. Various zinc precursors were tried in combination with various dopant precursors (including aluminium, gallium, and fluorine containing species), over a range of deposition conditions, yet no combination of experimental parameters yielded an appreciable conductivity in the ZnO thin films produced. The lack of improved conductivity using this technique has been attributed to the formation of mixed phase coatings containing zinc oxide and the oxide of the dopant species in separation (indicated by competing phase reflections in the XRD spectra of the highly doped films). As such, AACVD has proved to be a non-viable route towards the doping of zinc oxide, due to the slow rate of film formation and high mobility afforded to the adsorbed atomic species which allows for phase segregation.

The deposition of highly transparent (>80%) un-doped ZnO thin films from a zinc acetate precursor was achieved using the aerosol assisted chemical vapour deposition process. The properties of the films have been shown to be highly dependent on the temperature used during the deposition process; where influences, both microscopic and macroscopic were observed. The structural morphology and orientation of these poly-crystalline thin films have shown to be dependent upon the substrate temperature. Research has shown that when the film deposition temperature approaches that of the ZnO melting point, additional film relaxation channels are made energetically accessible, thus allowing increased crystallinity in the metastable structure[241]. The temperature range used in the experiments resulted in the crystallite boundaries of one preferred orientation (002) gaining increased mobility and allowing surface diffusion and recystallisation to take place. This manifests itself in the disk like grain morphology and the X-ray diffraction data which both show high peak intensity for the c-axis. Measurements taken to establish the contact angle and photocatalytic ability of these ZnO thin films show them to exhibit promising characteristics. The contact angle of water droplets is seemingly dependent upon the surface morphology, which itself is characteristic of the deposition temperature. The photocatalytic abilities of high temperature films have proven to exhibit a formal quantum efficiency of an

order comparable to that of commercially-utilised titania. Aerosol assisted chemical vapour deposition of ZnO has shown to be a promising method for deposition of undoped ZnO thin films with controllable structures, photocatalytic and hydrophillic properties.

# 7 Gas Sensing

## 7.1 Transparent Thin Film Gas Sensors

*The following chapter describes the high temperature gas sensing properties of thin film layers composed of functionalised-SWCNTs, functionalised-MWCNTs, hybrid ZnO-CNTs, ZnO, $SnO_2$, and Bi-doped $SnO_2$. The gas sensing performance of the transparent thin film materials was assessed using electrical resistivity based detection of gaseous ethanol, and of nitrogen dioxide, in air at elevated temperatures (300°C - 350°C) and under atmospheric pressure.*

## 7.2 Introduction

In the preceding chapters of this thesis a range of synthetic routes and deposition techniques have been developed and appraised for their use in the production of transparent conducting thin films. The primary purpose for the development of these materials is their use in 'Low-E' glazing, and as the transparent electrode in thin film photovoltaics. However, in chapter 6 the use of ZnO thin films in the photocatalytic degradation of organics was assessed with a view to its use in self-cleaning window coatings. The basis for this photocatalytic action stems from the semiconducting properties of the transparent conducting thin films, which, can also be utilised for the detection of gaseous chemical species (as outlined in the introductory chapter). Solid-state semiconducting films can monitor levels of gaseous species in the atmosphere through changes in the resistivity of the material. These resistivity changes are caused by electronic transfer upon adsorption of gas molecules to the thin film surface. This chapter outlines the response of the thin film materials, detailed thus far in this thesis

(plus additional hybrid CNT-ZnO materials), to both oxidizing ($NO_2$) and reducing ($C_2H_5OH$) gases.

Gas sensing has become progressively more widespread as the use of carbon based fuels and industrial chemicals plays an increasingly significant role in modern living. These developments necessitate the monitoring of various gaseous species including; oxygen levels (in controlled atmospheres and during combustion processes), flammable gases (preventing explosions and fires) and toxic gases (preventing harm to people and the environment)[242]. Solid state gas sensing has proved to be a highly robust and low cost way of monitoring gas levels, and as such it is an intensive area of research. Solid-state gas sensing, using the electrical resistance modulation of semiconductors, was first developed in the 1960s by Taguchi in Japan[73]. Since the initial development of this sensing technique, much research has gone into the development of new materials, operating conditions, and configurations for this type of gas sensor.

Metal oxides have proved to be the materials of choice for solid state gas sensing. $SnO_2$, $ZnO$, $WO_3$, $TiO_2$ and $SiO_2$ amongst many others, have proved excellent in the detection of many important types of gas [243, 244]. Metal oxides give a good sensitivity, selectivity, and a rapid, stable, on-off response to a wide range of gases. Continual improvements are being made to the materials in terms of mixed phase metal oxides[245], structural discrimination using porous over-layers[246, 247], and doping using catalytically active additives[248, 249], however, one progression which has proved elusive is the reduction of the operating temperature of the material. The high performance parameters attributed to gas sensing using metal oxides, are only notable at elevated temperatures ($\sim >200°C$), which means that additional circuitry and a heater ribbon are required in the sensor set-up, this leads to higher costs, added complexity, increased power consumption and less ease of integration[250].

Carbon nanotubes are a recent addition to the range of materials which produce resistivity based response to gaseous species. The unique electrical and physical properties of carbon nanotubes have been used to develop randomly assembled

networks of tubes which function as gas sensors that have the ability to operate at room temperature. Non-separated, SWCNT samples contain 2/3 semiconducting and 1/3 metallic tubes, therefore a randomly assembled network of the SWCNTs will give an overall semiconducting behavior, which can be used to register a response to oxidizing and reducing gases. This semiconducting behaviour, coupled with the high specific surface area (~1500 m$^2$/g)[251], hollow geometry, and a nano-size scale, renders SWCNT networks highly capable of gaseous adsorption and electrical response[252]. Small band-gap energies and high electrical mobility means that CNT films can be used for gas sensing at room temperature. However, room temperature operation leads to a low sensitivity compared with high temperature metal oxide gas sensors: requiring more sophisticated and expensive circuitry to monitor the response[253]. The rate of adsorption and desorption is also much slower than for high temperature metal oxide gas sensors, therefore the response is also much slower[254].

Owing to the advantages and disadvantages associated with each type of gas sensor, and the drive to produce a gas sensor which operates at room temperature, a move towards developing hybrid metal oxide-CNT sensors has begun. It is hoped that the metal oxide's high sensitivity and selectivity can be combined with the CNTs ability to function at low temperatures. Initial work using the SnO$_2$-CNT system has shown some promising results in combining these optimum properties into a gas sensor which functions at low temperatures [250, 253, 255, 256].

The purpose of the research outlined in this chapter is to investigate the high temperature gas sensing ability of the following: metal oxide thin films deposited by spray pyrolysis and AACVD, CNT thin films, and CNT-ZnO hybrid thin films. The research is intended to determine any benefits of using a metal oxide-CNT system at high temperature, and to investigate the possible mechanisms operating in this temperature regime, this is intended to compliment the room temperature mechanisms being studied elsewhere. Research into the ZnO-CNT hybrid system is much under-researched compared to the SnO$_2$-CNT system, and very few groups report the high temperature operation of hybrid systems. Better understanding of how the hybrid system operates at a high temperature, and comparison with the equivalent solo metal

oxide, could provide insight into how the addition of CNTs changes the mechanisms of conduction and charge transfer in the thin film gas sensors, allowing for a greater understanding of the chemical and electrical process in order to optimise the eventual move to room temperature operation of these materials.

## 7.3 Experimental

### 7.3.1 Gas Sensing Set-up

Gas sensing experiments were performed using commercially produced sensor chips which consisted of an alumina tile substrate with an inter-digitated gold electrode on the front (170 μm spacing), and a platinum heater track running across the reverse (Fig. 1). The front-face of the chips were coated using various techniques and gas sensing materials, which shall be outlined in the following section of the experimental. After the deposition of the gas sensing material, the uncoated sections of the gold and platinum contacts were connected to a larger chip housing unit by micro-welding 50 μm platinum wires between the contacts and the housing (Fig. 1).

The gas sensor chips were then connected into a pre-built rig. The rig consists of an eight channel free flow gas testing cell with Tylan General mass flow controllers (model FC-260) and Bürkert 3/2 and 2/2-way solenoid valves (model 0124) for gas delivery, this allows for precise mixing of the dry air and the pre-mixed nitrogen diode in air (800 ppb) or ethanol in air (100 ppm). The temperature of the gas sensor chips was controlled using resistive heating of the integrated platinum track as part of a Wheatstone bridge which maintains a constant resistance and therefore a constant temperature across the track.

The resistance measurements of the gas sensing material across the gold inter-digitated contacts were carried out using a triple potentiostat arrangement, which allows for calculation of the resistance based on measured voltage outputs. The voltage output values were recorded electronically at 1 second intervals over the experimental time period.
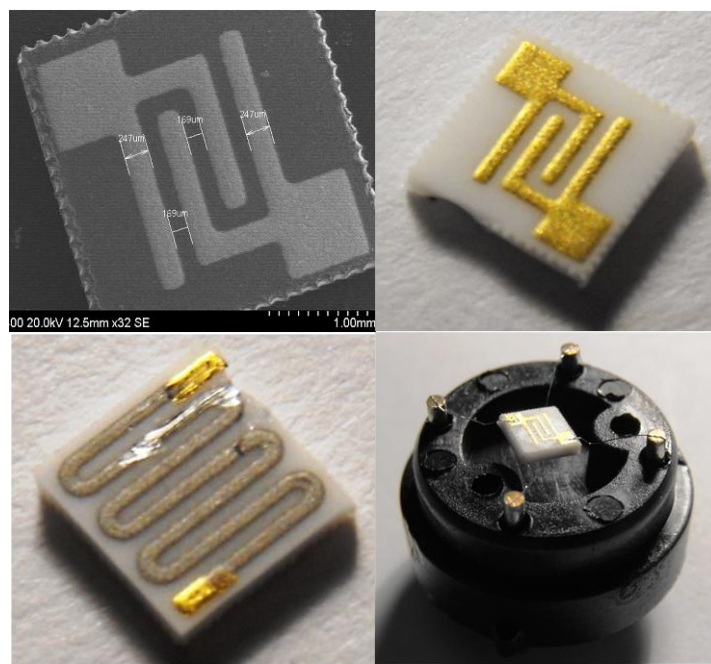
**Figure 7-1)** Images of the gas sensor chip design Top Left) SEM image of the gold electrode. Top Right) Photograph of the gold electrode. Bottom Left) Photograph of the platinum heater track. Bottom Right) Sensor chip connected into the housing unit.

Each gas sensor was tested over three temperature regimes: 300°C, 325°C and 350°C in separate experiments. Each experiment consisted of 10 test gas pulses over 5 different concentrations (each concentration was repeated once to check repeatability) each one separated by a 30 min dry air flow to allow measurement of speed of response. The $NO_2$ test gas was pulsed at 8, 32, 80, 400 and 800 ppb (parts per billion). The ethanol test gas was pulsed at 2, 10, 20, 50 and 80 ppm (parts per million).

## 7.3.2 Gas Sensing Material Deposition

The following section outlines the experimental details concerning the deposition of functionalised-CNT, ZnO and $SnO_2$ and variants of these materials. Each deposition technique was used to deposit thin films of the relevant materials onto the front face of the gas sensor chip, where it functions as the gas responsive material through changes in the conductivity of the film when exposed to the target gases.

### 7.3.3 AACVD of SnO$_2$ and Bi-doped SnO$_2$ films

AACVD was accomplished using the Collison method outlined in Chapter 2 (Section 2.3.1), the alumina chip substrate was placed face up in the reactor with the corner portions of the gold electrode masked by heat resistive tape. AACVD was used to deposit a tin oxide thin film (~ 200 nm thick SnO$_2$) onto the gas sensor chip using mono-butyl tin trichloide (10 g) in methanol (200 ml), at 500°C, with a deposition time of 10 min.

AACVD was also used to deposit bismuth-doped tin oxide thin films (~200nm thick) using a 30:100 Bi:Sn atomic ratio solution consisting of MBTC (10 g) and BiCl$_3$ (3.3 g) in methanol (200 ml).

### 7.3.4 Spray Coating of CNT, ZnO and ZnO-CNT hybrid films

Spray coating was accomplished using the set-up outlined in Chapter 5 (section 5.3.2), the alumina chip was placed face up on the carbon block heater, secured and masked using heat resistive tape prior to spray-coating.

*CNT Thin Films:*

SWCNT and graphitized-MWCNT (MWCNT heated in an inert atmosphere at 2000°C) were purchased from Cheaptubes Inc.. The purchased tubes were then functionalised following the methodology outlined and analysed in Chapter 5 (section 5.3.1). Films of f-SWCNTs were deposited onto the sensor chip by spray-coating 15 ml of a solution of f-SWCNTs (0.03 g) in water (50 ml pH11 (NaOH)), at 300°C, 1.5 ml.min$^{-1}$ syringing rate, 25 cm spray height and a pressure of 30 psi on a shuttling carbon block heater. This procedure was then repeated for the f-GMWCNTs.

*ZnO Thin Films:*

Zinc acetate (Zn(C$_2$H$_3$O$_2$)$_2$) (0.9 g) was dissolved in 20 ml of water. 15 ml of this solution was then spray coated at 400°C, at 2 ml.min$^{-1}$ syringing rate, 15 psi, and at a spray height of 25 cm, producing a thin film of ZnO on the face of the gas sensor chip.

***ZnO Coated f-SWCNT and f-GMWCNT films:***

f-SWCNTs (0.012 g) in water (20 ml) were tip sonicated for 2 min. then bath sonicated for 15 min. followed by the addition of zinc acetate (0.9 g) during the sonication process. These quantities give a zinc to CNT carbon atom ratio of 4:1 which was hoped to give approximately a 1.25-2.5 nm coating of ZnO on the SWCNTs. The SWCNT solution prior to the addition of the zinc complex was fully dispersed. Upon addition of the zinc acetate, the dispersion dropped out of solution. It was assumed from this solubility behavior that the $Zn^{2+}$ ions were interacting in solution with the negatively charged sulphonyl groups on the CNTs, thus causing a loss of solubility, but critically, forming a direct contact between the zinc atoms and the f-CNT to aid in the coating process. This mixture was then spray coated, using a magnetic stirrer in the syringe to aid continual mixing. The conditions were as follows: 15 ml solution, 400°C, 25 cm spray height, 2 ml.min$^{-1}$ and 30 psi.

The above process was then repeated with f-GMWCNTs to form ZnO coated f-GMWCNT films on the gas sensor chips.

## 7.3.5 Solution Coating and Screen Printing of ZnO coated CNTs

f-SWCNTs (0.03g) in water (250ml) were tip sonicated for 2 min. followed by bath sonication for 15 min.. This dispersion was then heated to 70°C, placed back in the bath sonicator, and zinc nitrate (1.5 g) was added. The solution was removed from the sonicator and stirred at a constant temperature of 70°C for 2.5 hours. Again, the dispersion was seen to crash out after addition of the zinc nitrate. After reaction the mixture was centrifuged to sediment the ZnO coated CNT, and the excess water was decanted off. The solid was left to dry in an oven at 100°C overnight, then annealed at 400°C for 2.5 hours. The solid was then ground into a solution with ethanol, and screen printed onto the top face of the gas sensor chip. The process was repeated for the f-GMWCNTs.

### 7.3.6 Heat Treatment

Annealing was performed on selected as-deposited gas sensor chips. Heating in atmospheric conditions and under the flow of a reducing $H_2/N_2$ mixture were performed. The gas sensor type and annealing conditions are detailed in table 7-1.

## 7.4 Results

Output voltage values were recorded from the gas sensing experiments over the relevant temperature, and gas conditions, as a function of time. Data points were recorded every second and the data was converted to a resistance value, using the resistivity value of the reference electrode of the triple potentiostat arrangenment. All plots shown in the following work display the response value R where $R = R_{gas}/R_{air}$, $R_{gas}$ is the average resistance during the gas pulse and $R_{air}$ is the baseline resistance directly before the gas pulse has entered. The response value allows for comparison of gas sensors with different starting resistance values (baseline resistances). Sensors which displayed a decrease in resistance upon target gas injection were plotted in terms of conductance, where: $R = C_{gas}/C_{air}$ , this allows comparison of the level of response between oxidizing and reducing gases.

### 7.4.1 Overview

The results presented in table 7-1 summarise the conditions and materials used for the production of each gas sensor. The final column in table 7-1 displays the response type (receptor function) which was registered for each of the gas-sensing materials.

The introductory chapter to this thesis outlined the widely accepted mechanism of conductance changes in semiconductors, which is based upon their operation in oxygen containing air. The mechanism is dominated by changes in adsorbed gas species and the interaction of target gases with adsorbed oxygen.

Nitrogen dioxide is a strongly oxidizing species which is assumed to adsorb to the semiconductor surface, and owing to its large value of electronegativity ($NO_2 = 2.28$ eV and oxygen = 0.43eV [250]) it will withdraw electrons from the material. This electronic transfer results in a decrease of the Fermi level (the highest occupied electronic energy level) and causes an electronic depletion layer, which begins at the surface and penetrates into the bulk. Adsorption of $NO_2$ onto an n-type conductor (where charge carrier electrons sit near the conduction band), leads to fewer charge carriers and an increase in resistance. Adsorption of $NO_2$ onto the surface of a p-type material (where 'holes' in the valence band are the dominant charge carriers) leads to an increased number of charge carrier holes, thus causing a decrease in resistance.

Ethanol is known as a reducing gas because it undergoes combustive reaction with adsorbed atmospheric oxygen (oxygen sits on the surface of the semiconductor as ionosorbed ions: $O_2^-$, $O^-$, or $O^{2-}$ which causes trapping of electrons and forms an electronic depletion layer at the surface of the semiconductor under ambient conditions), the reaction of ethanol and oxygen produces desorbed water and carbon dioxide, and in the process it acts to desorb the electronegative oxygen which injects the electronic charge back into the semiconductor as it leaves the surface. Electronic transfer back into the semiconductor leads to a resistance decrease in n-type materials and a resistance increase in p-type materials, as the Fermi level is increased.

| Gas Sensor Label | Material | Deposition Technique | Deposition Temperature (°C) | Annealing Temperature and Conditions | Sensor Response Type |
|---|---|---|---|---|---|
| **A-0** | f-SWCNT | Spray | 300 | - | p-type |
| **A-1** | f-SWCNT | Spray | 300 | $800/H_2$ | p-type |
| **B-0** | f-GMWCNT | Spray | 300 | - | None |
| **B-1** | f-GMWCNT | Spray | 300 | $800/H_2$ | None |
| **C-0** | ZnO/SWCNT | Spray | 400 | - | n-type |
| **C-1** | ZnO/SWCNT | Spray | 400 | 400/air | n-type |
| **C-2** | ZnO/SWCNT | Spray | 400 | $800/H_2$ | None |
| **D-0** | ZnO/GMWCNT | Spray | 400 | - | n-type |
| **D-1** | ZnO/GMWCNT | Spray | 400 | 400/air | None |
| **D-2** | ZnO/GMWCNT | Spray | 400 | $800/H_2$ | None |
| **E-0** | ZnO/SWCNT | Solution | 70 | 400/air | p-type |
| **E-1** | ZnO/SWCNT | Solution | 70 | $800/H_2$ | None |
| **F-0** | ZnO/GMWCNT | Solution | 70 | 400/air | None |
| **F-1** | ZnO/GMWCNT | Solution | 70 | $800/H_2$ | p-type |
| **G-0** | ZnO | Spray | 400 | - | n-type |
| **G-1** | ZnO | Spray | 400 | 500/air | n-type |
| **H-0** | $SnO_2$ | AACVD | 500 | | n-type |
| **H-1** | $SnO_2$ | AACVD | 500 | 500/air | n-type |
| **I-0** | $Bi:SnO_2$ | AACVD | 500 | - | n-type |
| **I-1** | $Bi:SnO_2$ | AACVD | 500 | 500/air | n-type |

**Table 7-1** Table summarising the material type and deposition technique used for each gas sensor, the pre-sensing annealing conditions to which the gas sensor chip was subject to, and the type of response registered by the gas sensor towards ethanol and nitrogen dioxide.

Table 7-1 illustrates that not all of the gas sensors, which were tested, displayed a change in resistivity towards either the oxidising $NO_2$ or the reducing ethanol. The GMWCNT films (B-0 and B-1) displayed no conductivity changes toward the target gases, however, this lack of response is unsurprising because the majority of MWCNTs are thought to be metallic-like conductors rather than semiconductors. The metallic nature of the MWCNT is attributed to the interaction between the concentric shells of the multi walled tubes[40].

Gas sensor G-1 did display a small p-type response which has been attributed to the GMWCNTs, this can be explained by the presence of semiconducting behavior from the randomly assembled thin film. A p-type response for MWCNT has been reported previously, however it has also proved to be a far weaker response than that given by SWCNTs [257-259].

Single walled carbon nanotube thin films (gas sensors A-0 and A-1) displayed a p-type behavior towards the target gases. The sensitivities (level of response at each target gas concentration) of the SWCNT randomly assembled films were lower than the equivalent sensitivity of the metal oxide, and metal oxide hybrid films, however the response values were within the same order of magnitude.

The zinc oxide and the tin oxide thin films displayed an n-type response to the target gases, as did the hybrid metal oxide-SWCNT films. This indicates that the n-type character of the metal oxide dominates the conductance properties of the hybrid films.

The following section shall detail the behavior of each gas sensor which showed a response to the target gases, with a view to allowing comparison between the mechanisms of operation of the metal oxide and the carbon nanotube films, and to assess whether the addition of CNTs to a metal oxide system at raised temperatures achieves improved performance.

### 7.4.2 Spray Coated ZnO Thin Films

This section details the response behavior of ZnO thin film gas sensors G-0 and G-1, which were formed using spray pyrolysis of a zinc acetate solution. The conditions used for the deposition gave very dense, uniform films of zinc oxide with little porosity and no pin-hole defects, as indicated by SEM imaging and pin-hole conductivity testing (films were deposited onto conductive layers and a damp sponge electrode was pressed onto the surface to check for defect holes through to the conductive under-layer). The presence of ZnO was determined by XRD analysis. The following results section is split into two parts; addressing the $NO_2$ target gas response and the ethanol target gas response separately.

### 7.4.3 $NO_2$ Response

Figure 7-2 shows a typical experimental response plot recorded for thin film zinc oxide gas sensors G-0 and G-1. As indicated earlier the response type was n-type. The plot shows 10 pulses of target gas, each lasting 10 minutes, and over 5 different concentrations (indicated on the plot). The response increases with increasing $NO_2$ concentration and shows a maximum response of 50 at 800 ppb and a 300°C operating temperature. The response shows rapid adsorption and desorption of the target gas as indicated by the square profile of each response pulse, which shows the maximum change is quickly reached. The higher concentration pulses show a large interference effect due to the large change in resistance values for the gas sensor which are approaching the limits of the triple potentiostat arrangement. The 8 ppb response cannot be seen on the scale of this plot however did register a resistance change.
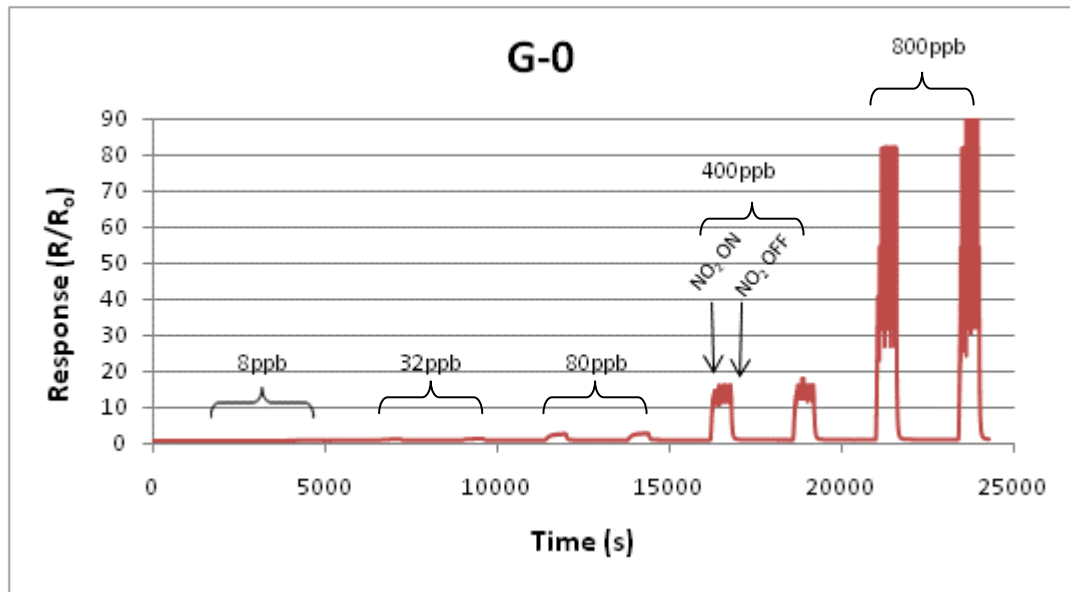
**Figure 7-2** Representative response profile of zinc oxide thin film gas sensor to $NO_2$. X-axis shows time from the start of the experiment. Y-axis shows response (R) (normalized resistance change of the semiconducting gas sensor material). This profile is taken from gas sensor G-0 at 300°C over five gas concentrations (8, 32, 80, 400 and 800 ppb). Each gas pulse lasts 10 mins. followed by a repeat of the same concentration.

The plots shown in figure 7-3 give the $NO_2$ concentration vs response for each gas sensor G-0 and G-1, and over each operating temperature. The plots indicate that at 325°C and 350°C both the annealed and non-annealed zinc oxide thin films show a linearly increasing response to the increasing $NO_2$ concentration, which allows for a facile calibration of the response with respect to gas concentration for the sensors operating over this temperature and concentrations of 8 ppb – 800 ppb.

However, the low temperature (300°C) plot shows a change in response mechanism between 400 ppb and 800 ppb indicated by the changing gradient of the plot. Temperature induced combustion can be ruled out as a cause of the changing mechanism because $NO_2$ is fully oxidized, and the plot above (figure 7-2) shows a very stable baseline resistance (when no target gas is present) and fast desorption of $NO_2$, so incremental quenching of the surface is not a cause of this non-linear response. A plausible explanation of this increased response at 800 ppb (300°C) could be a move from grain boundary controlled resistance, to a complete grain controlled resistance,

caused by an increased surface depletion layer, reaching a length longer than ½ the grain size of the thin film grains which are accessible by the gas. It was shown in the introductory chapter (Section 1.8.4) that this tipping point, when the Debye length is larger than ½ the grain length, causes a large increase in response. The reason this tipping point is not seen at the higher temperatures can be explained by a decreased adsorption of the $NO_2$ because of the higher temperature surface, evidence for this can be found in Figure 7-4 where the response is shown to be highest for the 300 °C sensors at not only 800 ppb but also 400 ppb before the concentration where the mechanism shift occurs.
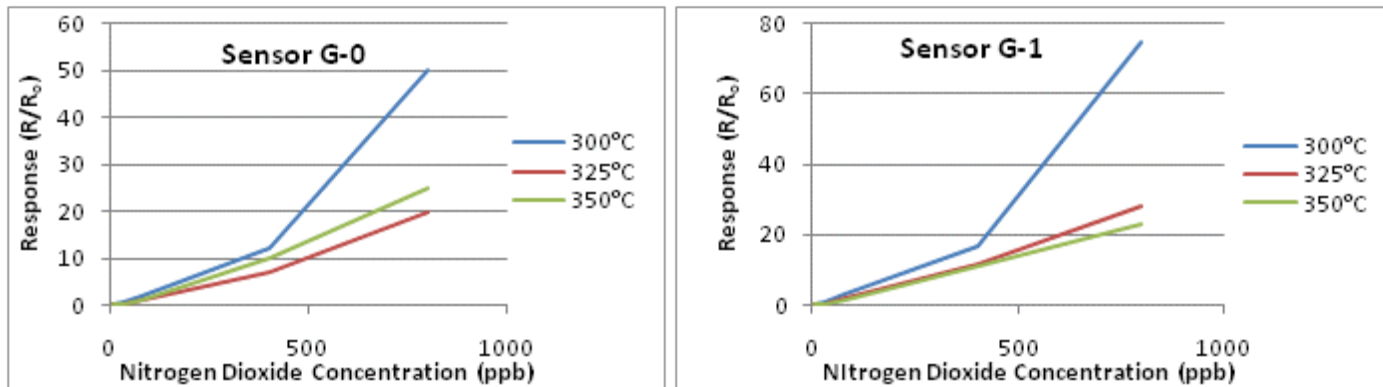


**Figure 7-3** Concentration of $NO_2$ pulse versus measured response to each concentration over each temperature of operation. *Left)* Gas Sensor G-0 (non-annealed ZnO thin film) *Right)* Gas sensor G-1 (ZnO thin film annealed at 500°C in air).
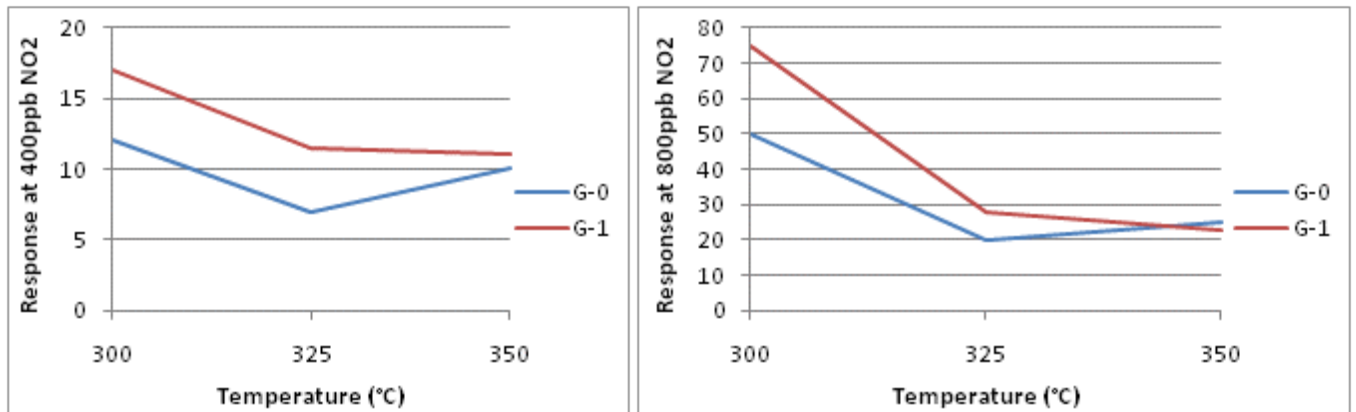


**Figure 7-4** Temperature of gas sensor operation versus the response at a designated concentration of $NO_2$, for gas sensors G-0 and G-1. Left) Temperature versus response at 400ppb $NO_2$. *Right)* Temperature versus response at 800 ppb $NO_2$.

### 7.4.4 Ethanol Response

The zinc oxide thin films displayed a very high response to the ethanol target gas. Figure 7-5 shows ethanol concentration versus response values for each of the operating temperatures, and each of the gas sensors G-0 and G-1. Both sensors display a linear relationship between ethanol concentration and response at 300°C, over the 2-80 ppm range. This linear relationship then breaks down at the higher temperatures because the response becomes saturated. This saturation can be attributed to an increased level of ethanol combustion at the higher temperatures, causing increased removal of oxygen from the surface of the sensor, which in turn leads to larger resistance decreases in the n-type material. The limit of oxygen removal is reached sooner because of the increased energy in the system promoting combustion; therefore the sensor becomes saturated in terms of the level of response. This would suggest the zinc oxide film has a relatively small surface area, providing a relatively small number of available sites for oxygen adsorption, which limits the sensors response at higher concentrations and temperatures.

Comparison between the non-annealed (G-0) and the annealed (G-1) shows a shift in the saturation limit towards operation at a higher temperature in the annealed film, this suggests annealing creates more surface sites for oxygen adsorption.



**Figure 7-5** Concentration of ethanol pulses (2, 10, 20, 50, 80 ppm) versus measured response to each concentration over each temperature of operation. *Left)* Gas Sensor G-0 (non-annealed ZnO thin film) *Right)* Gas sensor G-1 (ZnO thin film annealed at 500°C in air).
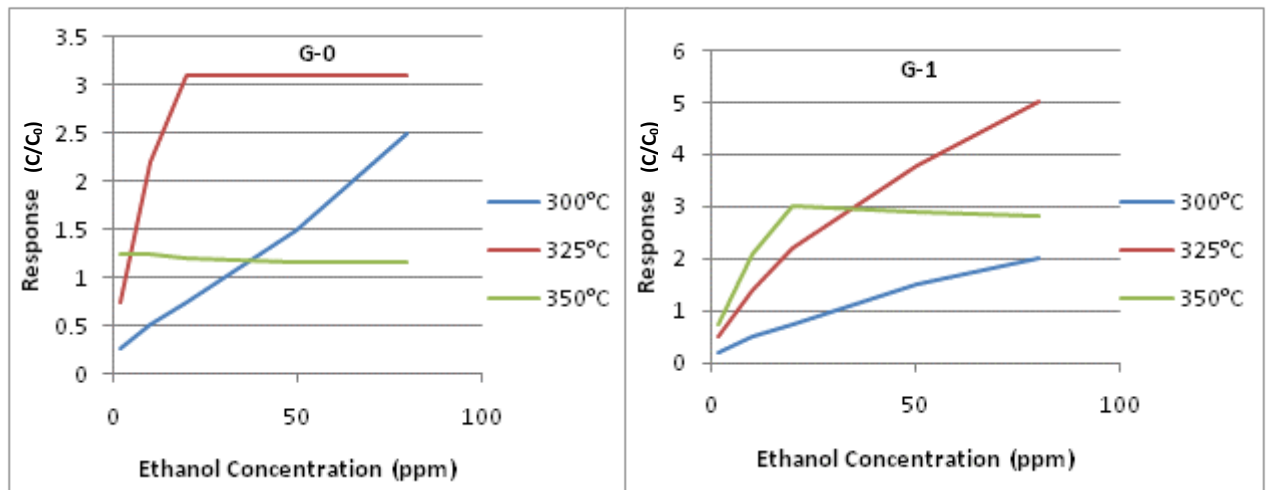
Figure 7-6 shows the temperature vs response at 50 ppm of the two sensors. The figure shows that in both cases the maximum response is seen at 325°C. This maximum response can be attributed to the competing processes of increased combustion at increased temperatures, and the diminishing baseline oxygen adsorption level at increasing temperatures. 325°C provides the best trade-off between these two processes.
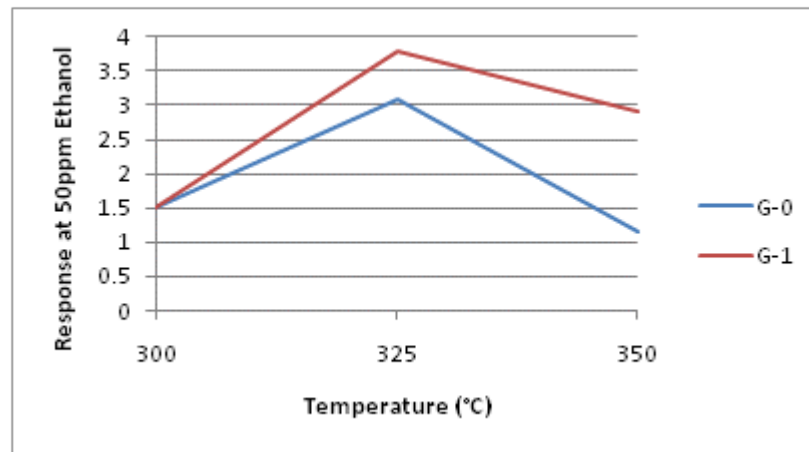


**Figure 7-6** Temperature of gas sensor operation versus the response at 50 ppm of ethanol. Gas sensors G-0 and G-1.

Figure 7-7 shows the response plots of the G-0 gas sensor at 300°C and 325°C operating temperatures. These plots clearly show the response saturation which takes place at 20 ppm. at the higher temperature. The profiles of the response pulses also indicate that the process of adsorption and desorption of the oxygen species is slower than that of $NO_2$ (Figure 7-2) due to the curvature of the top and bottom of the profiles.
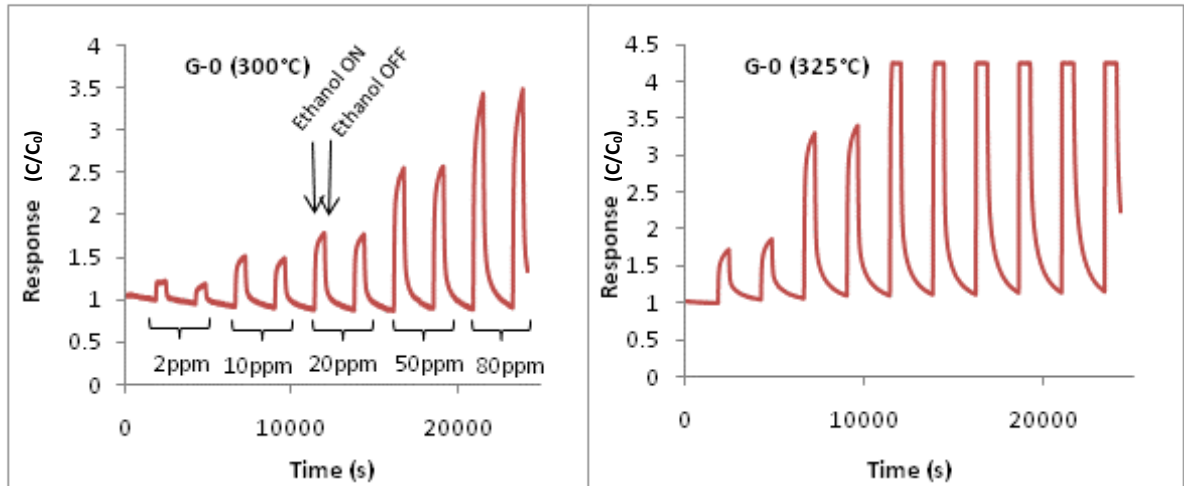
**Figure 7-7** Representative response profiles of zinc oxide thin film gas sensor to ethanol. X-axis shows time from the start of the experiment. Y-axis shows response R (normalized resistance change of the semiconducting gas sensor material). These profiles are taken from gas sensor G-0 over five gas concentrations (2, 10, 20, 50 and 80 ppm). Each gas pulse lasts 10 mins. followed by a repeat of the same concentration. *Left)* 300°C operational temp. *Right)* 325°C operational temperature.

### 7.4.5 Spray Coated SWCNT Thin Films

This section details the response of spray coated f-SWCNT thin film gas sensors to the same ethanol, and $NO_2$, experimental conditions as previously outlined. The structural and morphological analysis shall not be included in this section, as the film attributes were analysed in detail in chapter 5 (section 5.4). We can assume that the non-heat treated film (A-0) still has its sulphonic sidewall functionality present, however the heat treated film (A-1) will have returned to the pristine SWCNT structure (process outlined in chapter 5).

### 7.4.6 $NO_2$ Response

Sensor A-0 broke-down at an operating temperature of 350°C, so this data is excluded from discussion. Both sensors A-0 and A-1 displayed a p-type response to the target gases. However the $NO_2$ sensitivity was very low in comparison to results given by the metal oxide containing systems. SWCNT sensors A-0 and A-1 gave less than a 1 unit response, where-as the zinc oxide films in the preceding section gave responses measured in 10s of units.

Figure 7-8 shows the concentration vs response behavior of the SWCNT sensors, which indicates a roughly linear response. Figure 7-8 shows a rather large variance in measurements, which is caused by the low level of response compared to the baseline value. Gas sensor A-1 showed a temperature independent level of sensitivity over the 300-350°C operating range. Gas sensor A-0 seemed to show an increasing response with temperature, however the full data set is not available.
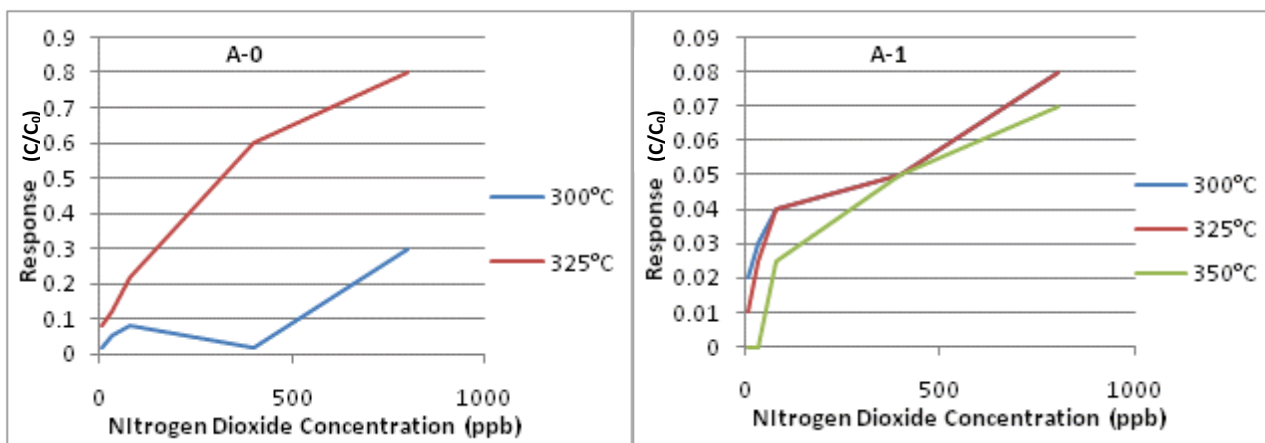


**Figure 7-8** Concentration of $NO_2$ pulse versus measured response to each concentration and over each temperature of operation. *Left)* Gas Sensor A-0 (non-annealed f-SWCNT thin film) *Right)* Gas sensor A-1 (f-SWCNT thin film annealed at 800°C in $H_2/N_2$).

Figure 7.9 shows the response profile taken from the f-SWCNT sensor A-0 at 325 °C. This plot displays a baseline which gives a relatively high level of variability when compared to the response levels. This variability would make reliable concentration calibration very difficult. The response times to the incoming $NO_2$ are very fast in terms of both adsorption and desorption, which are promising attributes. However, the top of the response pulses indicate after initial adsorption of the oxidizing $NO_2$, that this level of $NO_2$ cannot be maintained on the surface.

The loss of function at 350°C may be a result of carbon oxidation in the SWCNTs, or gradual removal of the functional side groups caused by the high temperature operation in air over a prolonged period of time. The sensor was running at 350°C for at least 2 days which could cause a slow but detrimental change in the baseline resistivity of the thin film. This is non-ideal for a functioning gas sensor which would need to operate at raised temperature for indefinite periods of time.
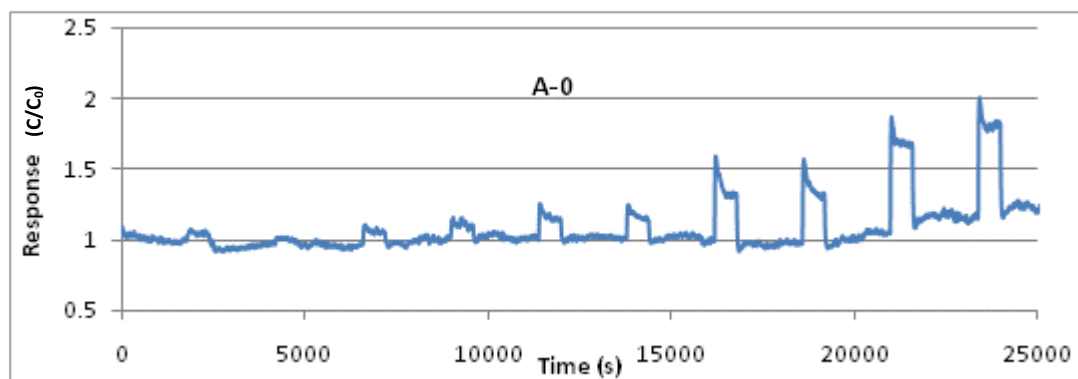
**Figure 7-9** Representative response profile of f-SWCNT thin film gas sensor to $NO_2$. X-axis shows time from the start of the experiment. Y- axis shows response R (normalized resistance change of the semiconducting gas sensor material). This profile is taken from gas sensor A-0 at 325°C over five gas concentrations (8, 32, 80, 400 and 800 ppb). Each gas pulse lasts 10mins. followed by a repeat of the same concentration.

## 7.4.7 Ethanol Response

During the ethanol experiments sensor A-1 broke-down at an operating temperature of 350°C, so this data is excluded from discussion. Both sensors A-0 and A-1 displayed a p-type response to ethanol target gas. Figure 7-10 shows the concentration vs response plot, highlighting the very low sensitivity and erratic data captured from gas sensor A-1 (annealed f-SWCNT film). The sensor A-0 shows a relatively high sensitivity, with nearly an order of magnitude greater response to ethanol than it displayed towards $NO_2$. This response is characterized by a linear concentration dependence (figure 7-10), and a sensitivity which increases with temperature (figure 7-11), presumably as the rate of ethanol combustion is increased. The A-0 sensor response showed no sign of response quenching, up to an R value of 2.5, unlike the ZnO thin films. However, the ZnO thin films only quenched at values of R above 3.5 for ethanol, not reached by the response of the SWCNT films.
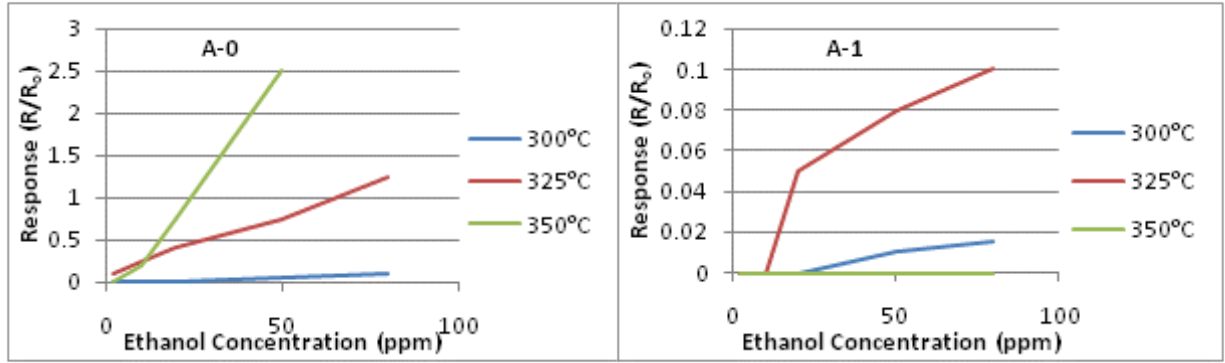
**Figure 7-10** Concentration of ethanol pulses (2, 10, 20, 50, 80 ppm) versus measured response to each concentration, over each temperature of operation. *Left)* Gas Sensor A-0(non-annealed f-SWCNT thin film). *Right)* Gas sensor A-1 (f-SWCNT thin film annealed at 800°C in $H_2/N_2$).

The representative response plot shown in figure 7-11 (right) demonstrates the rapid adsorption and desorption characteristics of the f-SWCNT films in response to ethanol target gas. Comparison of the fast kinetics occurring on the surface of the SWCNTs, with the slow desorption and adsorption seen for the zinc oxide thin films, indicates that the nanotubes may be playing a more catalytic role in the surface mediated combustion of ethanol than the zinc oxide films did.

Clearly the high temperature annealing of the f-SWCNT films was detrimental to the gas sensor sensitivity, which could be attributed the removal of the functional side groups from the tube walls.

The gradual drift of the response baseline shown in figure 7-11, indicates that at the operating temperatures used, there is a slow oxidation of the nanotubes taking place. This behavior was exaggerated at the highest operating temperature and can be attributed to oxidation of vulnerable carbon atoms in the nanotube structure, namely those atoms with dangling bonds such-as defects and tube ends. This oxidation causes structural deformation and shortening of the tubes, leading to an increase in resistance in the overall film and therefore an increase in the response baseline over the course of the seven hour experiment.

231
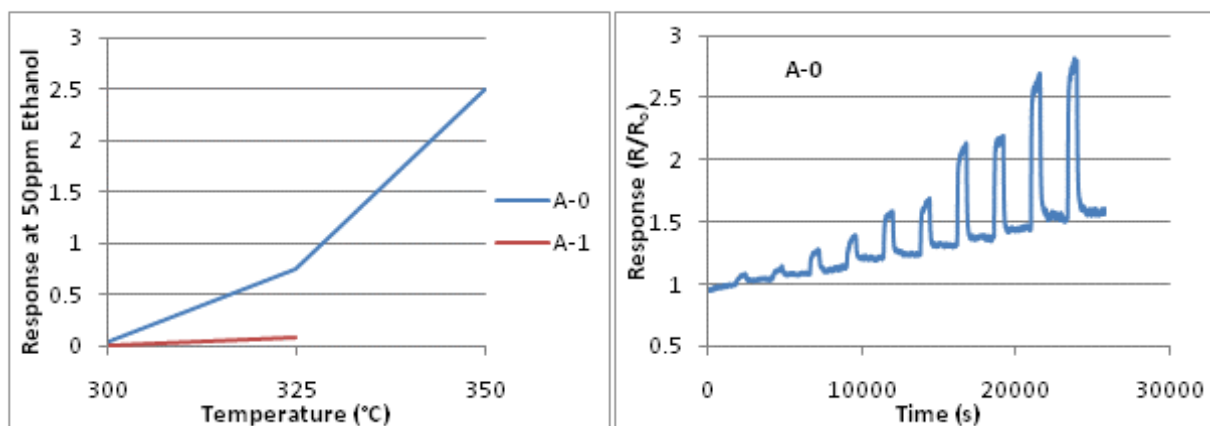
**Figure 7-11** *Left)* Temperature of gas sensor operation versus the response at 50 ppm of ethanol. Gas sensors A-0 and A-1. *Right)* Representative response profile of the f-SWCNT thin film gas sensor to ethanol. Taken from gas sensor A-0 over five gas concentrations (2, 10, 20, 50 and 80 ppm) at 325°C operating temperature.

## 7.4.8 Spray Coated ZnO-CNT Thin Films

This section details the behavior of ZnO-CNT hybrid thin films in response to ethanol and $NO_2$. Both f-SWCNT and f-GMWCNT were sonicated into solution with zinc acetate which was then subject to a spray pyrolysis deposition process to form the thin films.

## 7.4.9 $NO_2$ Response

The spray coating technique, outlined in the experimental section, resulted in adherent thin films of zinc oxide coated carbon nanotubes. Figure 7-12 shows SEM images of both the f-SWCNT and the f-GMWCNT based hybrid coatings. The images clearly show a highly porous layer consisting of zinc oxide particle coated tubes, and larger zinc oxide particle agglomerates have formed. The coated tubes range in thickness from 10 nm up to 100 nm in diameter, which is larger than either the diameter of the SWCNT(~2 nm) or the GMWCNT(~10 nm-20 nm).
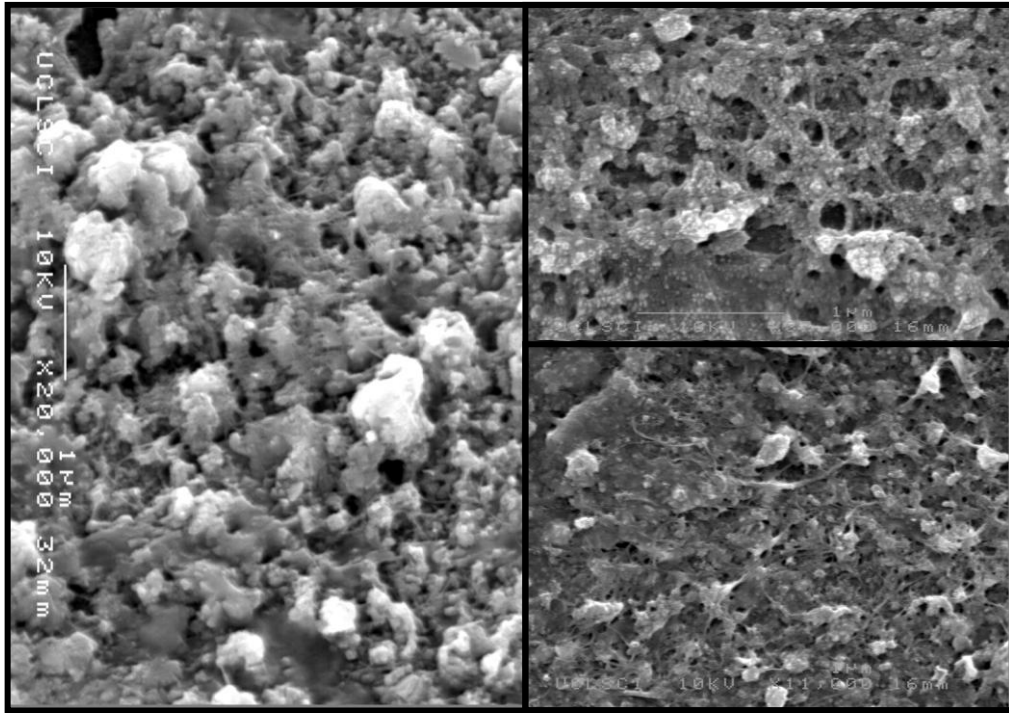
**Figure 7-12** SEM images of ZnO-CNT composite thin films synthesized by spray coating of a f-CNT and zinc acetate containing solution. *Left)* f-SWCNT/ZnO (30° angle) Top Right) f-SWCNT/ZnO (top down image) Bottom Right) f-MWCNT/ZnO (top down image).

Gas sensors C-0 (f-SWCNT-ZnO non-heated), C-1 (f-SWCNT heat treated at 400°C in air) and D-0 (f-GMWCNT-ZnO non-heated) all displayed an n-type response to the target gases. The n-type response indicates that the dominant material controlling the response mechanism is the n-type zinc oxide, not the p-type CNT films.

Figure 7-14 shows that sensors C-0 and D-0 display a linear concentration dependence at 300°C but above this temperature the mechanism of response seems to change between 400 ppb and 800 ppb, where the 800 ppb concentration of $NO_2$ gives a disproportionately high response. This non-linearity is seen over every temperature in the C-1 sensor. In section 7.4.3 the behavior of zinc oxide films indicated a changeover from boundary controlled resistance to grain controlled resistance at the higher concentration. This behavior, however, cannot explain the results seen for the CNT-hybrid films, because the temperature dependency (see figure 7-14) follows the opposite trend to the zinc oxide thin films. The ZnO thin films gave linear responses at higher temperatures due to the reduced adsorption of $NO_2$ because of the temperature, thus

233

preventing electronic depletion saturation of the grains. With the ZnO-CNT hybrid films, it is now the low temperature operation which gives linear concentration dependency. Cleary they are not showing a change between grain boundary control and grain control, as in the ZnO films.
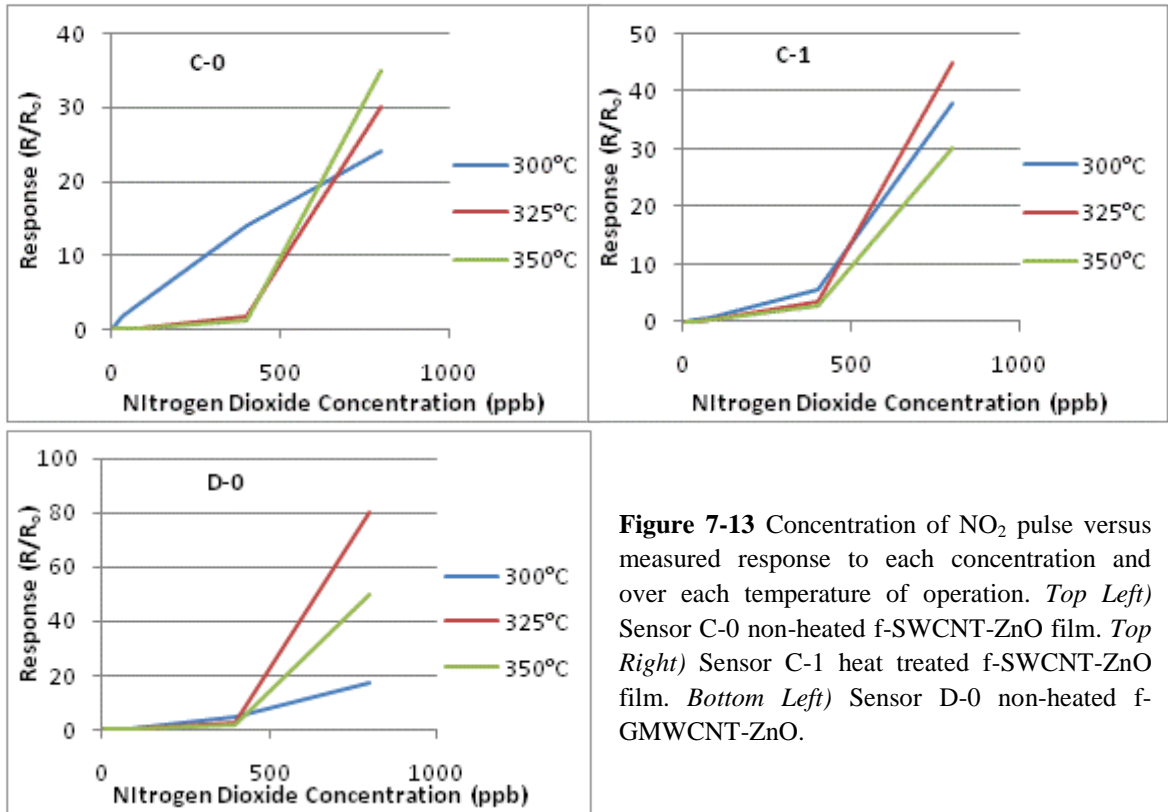


**Figure 7-13** Concentration of NO$_2$ pulse versus measured response to each concentration and over each temperature of operation. *Top Left)* Sensor C-0 non-heated f-SWCNT-ZnO film. *Top Right)* Sensor C-1 heat treated f-SWCNT-ZnO film. *Bottom Left)* Sensor D-0 non-heated f-GMWCNT-ZnO.

Figure 7-14 gives further insight into the change in mechanism between the two concentrations: at 400 ppb the temperature dependency of the response follows a downward trend with increasing temperature, whereas at 800 ppb the response follows an upward trend with increasing temperature. These two temperature dependencies could be explained by the temperature dependency of the zinc oxide conductivity with respect to the conductivity of the carbon nanotubes. At the higher temperatures thermal population of the zinc oxide conduction band begins to switch electronic propogation away from the CNT and through the zinc oxide coating, as the ZnO resistivity decreases. The zinc oxide coating then shows a rapid rise in response as again the concentration hits 800 ppb, because of the shift from grain boundary to grain control;

this would indicate the ZnO grain size is smaller in the hybrid material as depletion saturation occurs still at 350°C. So interplay of the ZnO and SWCNT conductivity with temperature, and the zinc oxide conductance limiting mechanisms with $NO_2$ adsorption levels is dominating the behavior of the hybrid sensors.
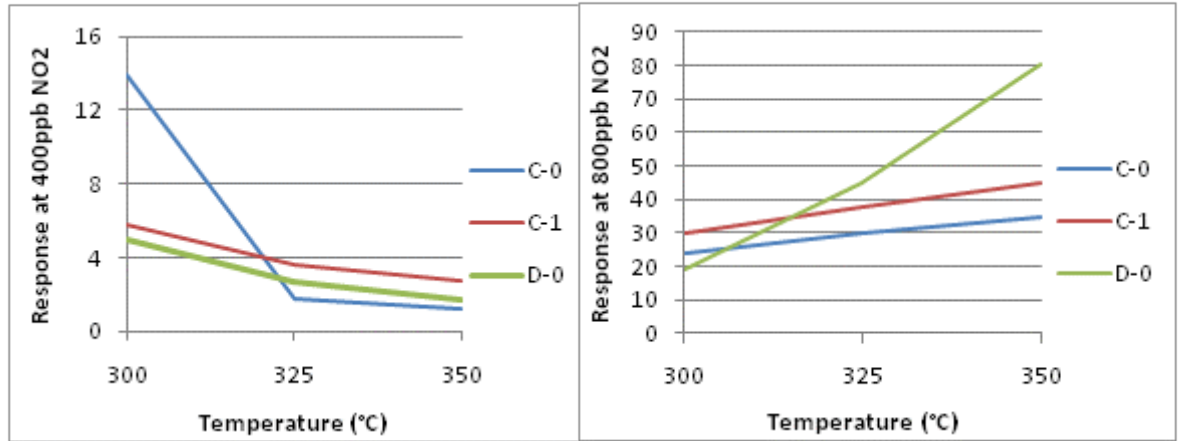


**Figure 7-14** Temperature of gas sensor operation versus the response at a designated concentration *Left)* 400ppb concentration of $NO_2$. *Right)* 800 ppb concentration of $NO_2$.

Figure 7-15 shows the response profiles of the hybrid materials to the $NO_2$ target gas. The profiles show rapid response characteristics, complete desorption of the $NO_2$ after the pulse and a very stable baseline in C-1.
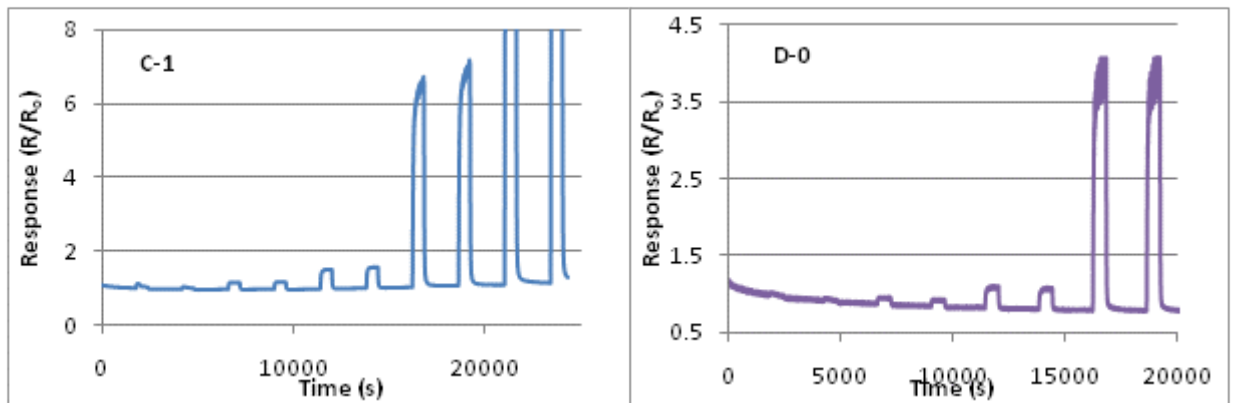


**Figure 7-15** Representative response profile of CNT-ZnO thin film gas sensor to $NO_2$. *Left)* Gas sensor C-1 (f-SWCNT-ZnO heat treated at 500°C) operating at 300°C over five gas concentrations (8, 32, 80, 400 and 800 ppb) 800ppb is out of axis range for clarity. *Right)* Gas sensor D-0 (f-GMWCNT-ZnO non-heated) operating at 325°C over 8, 32, 80, 400 ppb.

## 7.4.10 Ethanol Response

Gas sensors C-0, C-1, and D-0, all showed a strong response to the ethanol target gas. Sensors C-0 and D-0 (non-annealed) gave a linear response increase with concentration at an operating temperature of 350°C. The sensitivity of C-0 and D-0 at 300°C and 325°C is low, presumably due to lower levels of combustion taking place, whereas at the higher temperature of 350°C thermal activation of combustion allows for more surface oxygen removal and a higher response. Saturation is seen at the lower temperatures of 300 and 325°C.

The annealed sensor C-1 displayed response saturation at low concentrations over each operating temperature.



**Figure 7-16** Concentration of ethanol pulse versus measured response to each concentration, over each temperature of operation. *Top Left)* Sensor C-0 non-heated f-SWCNT-ZnO film. *Top Right)* Sensor C-1 heat-treated f-SWCNT-ZnO film. *Bottom Left)* Sensor D-0 non-heated f-GMWCNT-ZnO film.
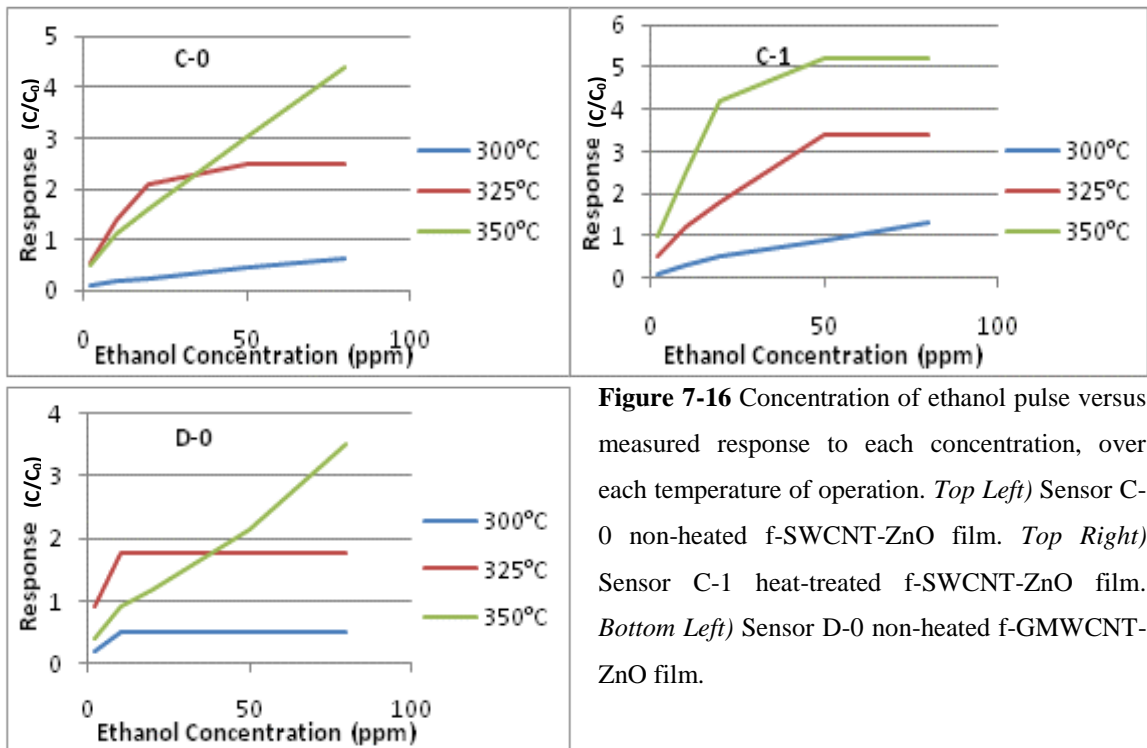
Figure 7-17 demonstrates that with increasing temperature of operation there is an increase in sensitivity of response. The limiting factor cannot be caused by a lack of surface oxygen (even at 80 ppm) because the increasing temperature and sensitivity trend is shown over every ethanol concentration, unlike the $NO_2$ target gas which changed behavior at higher concentrations. This indicates that it is the level of combustion with surface oxygen, rather than the ambient level of adsorbed surface oxygen which is the dominant process controlling response. This means that the temperature of operation controls the maximum response for each concentration, by controlling the rate of ethanol and oxygen combustion, thus changing the equilibrium at the surface with oxygen readsorbing.
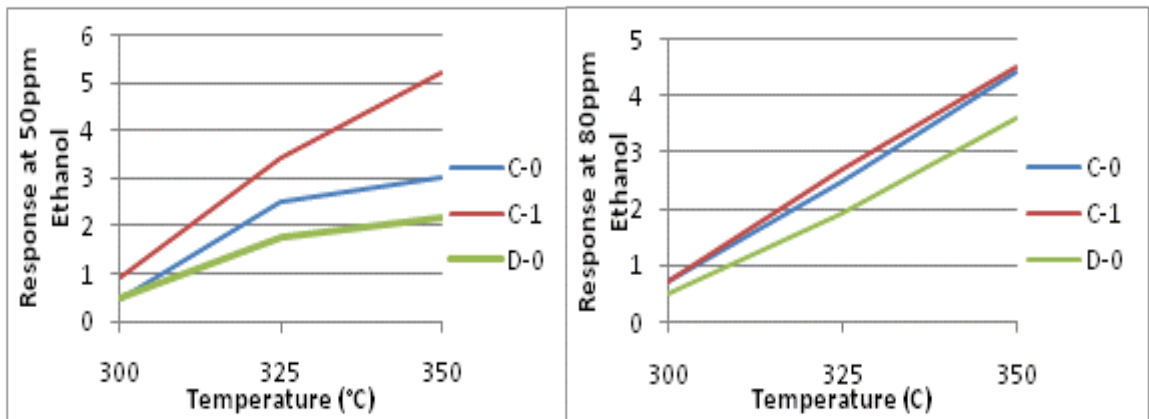


**Figure 7-17** Temperature of gas sensor operation versus the response at a designated concentration *Left)* 50 ppm concentration of ethanol. *Right)* 80 ppm concentration of ethanol.

Figure 7-18 shows the representative profiles of the sensors at the high temperature. C-1 clearly shows saturation at 50 ppm. However the sensor C-0, which was not heat treated prior to gas sensing, performs very well, giving a uniform profile, good repeatability at each concentration, a stable baseline, and a response which combines the fast desorption and adsorption of oxygen (by ethanol) shown by the SWCNT films, combined with the stability and high sensitivity shown by the zinc oxide thin films.
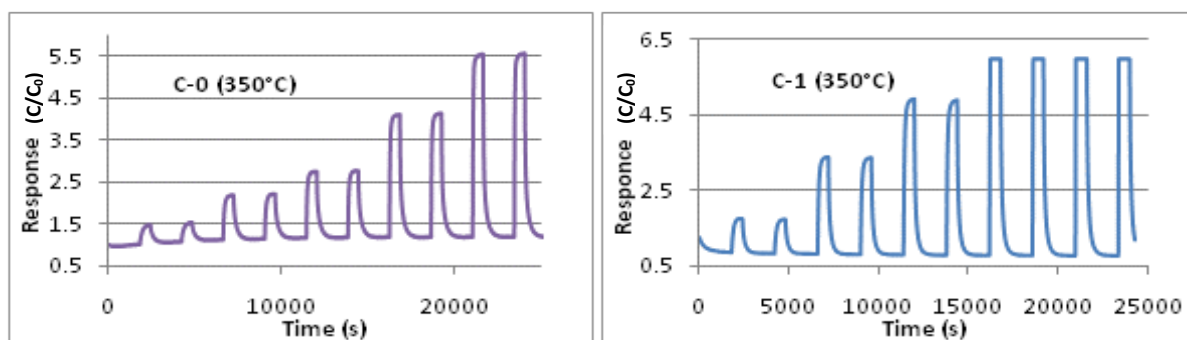


**Figure 7-18** Representative response profile of CNT-ZnO thin film gas sensors to ethanol. *Left)* Gas sensor C-0 (f-SWCNT-ZnO non-heated) operating at 350°C over five gas concentrations (2, 10, 20, 50, 80 ppm). *Right)* Gas sensor C-1 (f-SWCNT-ZnO heated at 500°C) operating at 350°C over 2, 10, 20, 50, 80 ppm.

Table 7-2 shows the response rise and fall times of each of the three sensors in response to ethanol at their optimum operating temperatures. The table shows that the f-SWCNT film provides the fastest switching behavior both in terms of oxygen desorption as the response rises, and oxygen adsorption as the response falls. This rapid response is retained in the hybrid f-SWCNT-ZnO material, which can be seen to be far faster than the plain ZnO film.

| Response Time | ZnO film (G-0) /s | f-SWCNT film (A-0) /s | f-SWCNT-ZnO Hybrid (C-0) / s |
|---|---|---|---|
| **Rise Time (to 90% max)** | 274 | 100 | 96 |
| **Fall Time(to -90% of max)** | 621 | 169 | 301 |

**Table7-2** Response times of each gas sensor to 400ppm ethanol injection. Rise time is the time the response takes to achieve 90% of its maximum value triggered by the start of an ethanol pulse. Fall time is the time taken for the maximum value to fall by 90% of its maximum value after the ethanol pulse has finished. The values were taken from each of the best performing operating temperatures 300, 325 and 350°C for G-0, A-0 and C-0 respectively.

### 7.4.11 Doped and Un-doped SnO$_2$ Thin Films by AACVD

The following section outlines the response of tin oxide based thin film gas sensors to NO$_2$ and ethanol target gases. The films were deposited by Collison-AACVD as outlined in chapter 2. The gas sensors which gave the best response are as follows: H-0 (non heat-treated SnO$_2$ thin film) and I-1 (bismuth doped tin oxide thin film from a 30:100 Bi:Sn atomic ratio solution, heat-treated at 500°C in air for 1 hour).

### 7.4.12 NO$_2$ Response

Both sensors displayed an n-type response to the target gases. Figure 7-19 shows the relatively linear response dependence on concentration for both of the gas sensors, over each operating condition (except for H-0 at 300°C). Figure 7-19 also shows that the sensitivity is relatively low when compared to the ZnO or hybrid thin films at each NO$_2$ concentration.

Figure 7-20 illustrates that the response sensitivity of the gas sensors are not responsive to changes in operating temperatures over the 300-350°C range.

Bismuth doping seems to have had little effect on the response of the tin oxide thin film to nitrogen dioxide.
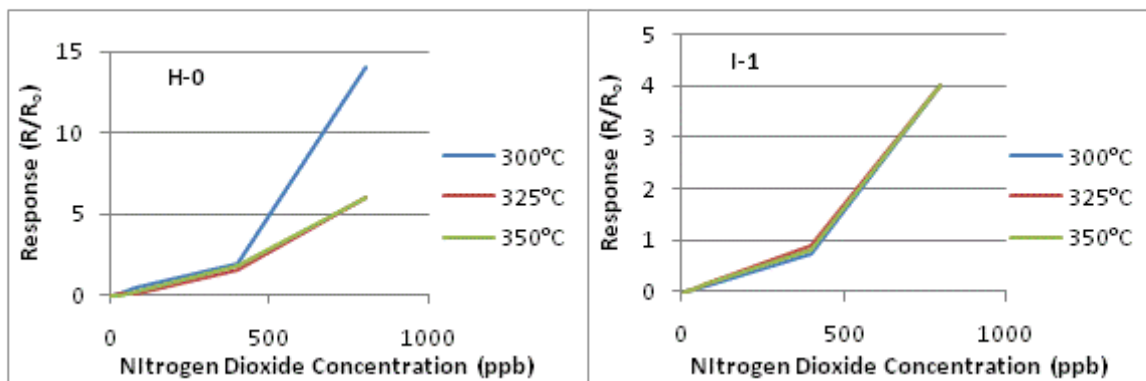


**Figure 7-19** Concentration of NO$_2$ pulse versus measured response to each concentration, over each temperature of operation. *Left)* Sensor H-0 non-heated SnO$_2$ film. *Right)* Sensor I-1 Heat treated Bi:SnO$_2$ film(500°C in air).
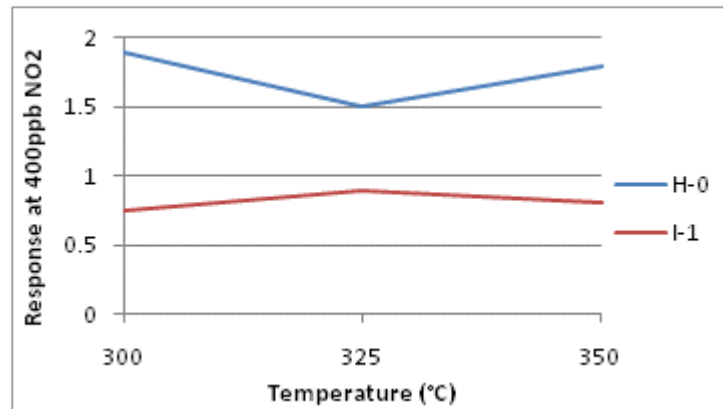
**Figure 7-20** Temperature of gas sensor operation versus the response at 400ppb concentration of $NO_2$.


Figure 7-21 shows the representative response profiles of the two gas sensors over the various concentration gas pulses of $NO_2$. The response shows a rapid adsorption and desorption characteristics and a stable baseline. Interestingly, the H-0 sensor displayed a low level of p-type response which can be seen during the first two low concentration (8 ppb $NO_2$) gas pulses, which then switches back to the n-type response at the higher $NO_2$ concentrations. No explanation of this anomaly can be given.
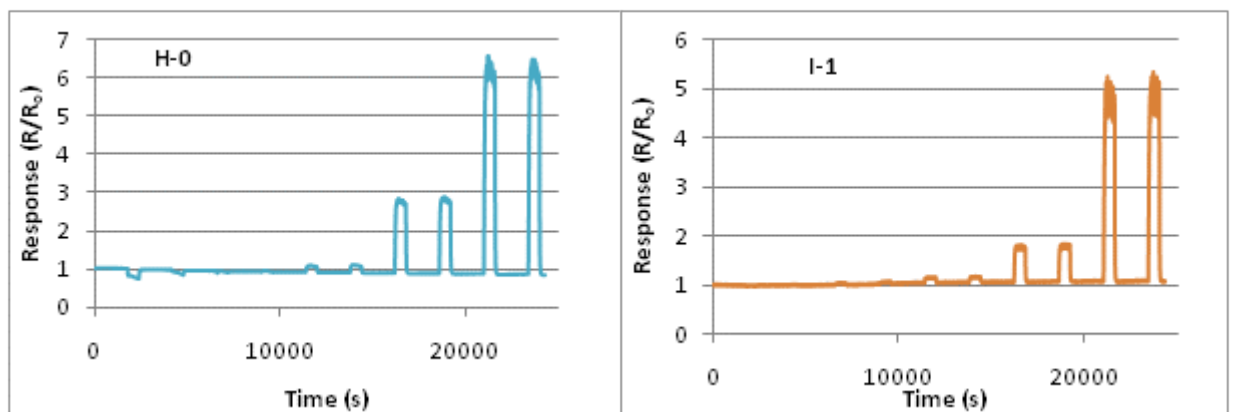


**Figure 7-21** Representative response profile of tin oxide based thin film gas sensors to $NO_2$. *Left)* Gas sensor H-0 ($SnO_2$ non heat treated) operating at 350°C over five gas concentrations (8, 32, 80, 400 and 800 ppb) *Right)* Gas sensor I-1 (Bismuth doped $SnO_2$ heat treated 500°C in air) operating at 350°C.

### 7.4.13 Ethanol Response

Figure 7-22 shows that the $SnO_2$ H-0 gas sensor gave a very high response, and a linearly increasing response to ethanol concentration at 300°C. This broke-down at higher temperatures as the gas sensors response becomes saturated. This can be attributed to a reduced level of adsorbed oxygen on the tin oxide surface at the higher temperatures. The gas sensor I-1, which is a bismuth doped tin oxide film, showed a more consistent concentration dependency over 300 and 325°C (data for 350°C is missing due to an electrical problem), although the sensitivity did not match the high value given by the un-doped tin oxide at 300°C.
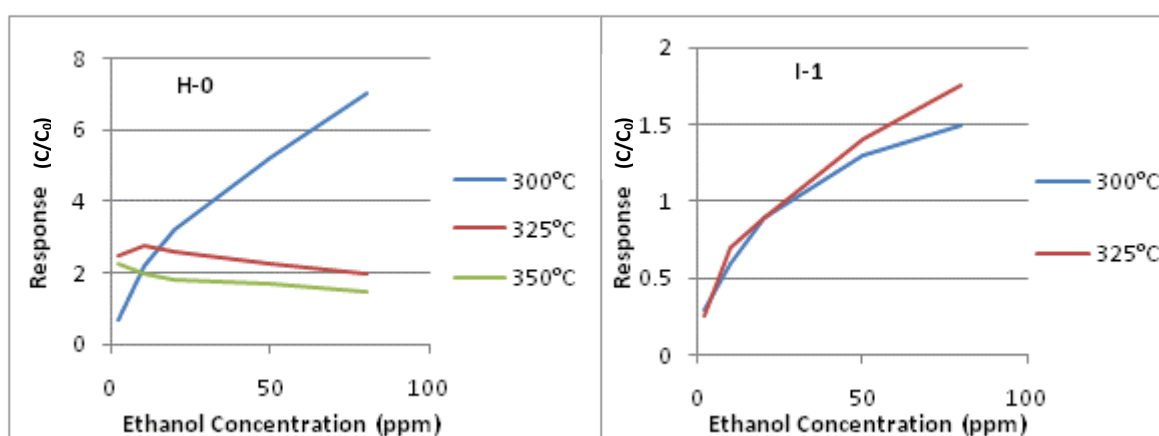


**Figure 7-22** Concentration of ethanol pulse versus measured response to each concentration, over each temperature of operation. *Left)* Sensor H-0 non-heated $SnO_2$ film. *Right)* Sensor I-1 Heat treated $Bi:SnO_2$ film (500°C in air).

Figure 7-23 shows representative response profiles of each of the sensors. The top left figure displaying H-0 operating at 300°C shows the concentration dependent profile with high sensitivity, which is lost at the higher temperature shown in the bottom left plot. The gas sensor I-1 displays a very fast rise and fall time in response and a very stable baseline over both 300°C and 325°C. The gas sensor I-1 also shows no sign of response saturation even at the higher temperature, unlike its un-doped counterpart. This rapid response rate and prevention of response saturation can be attributed to the effects of the bismuth atoms. Firstly bismuth has the same number of valence electrons as antimony so should facilitate an electronic donation into the tin oxide conduction band (seen in chapter 1), however, at the same time the very large ionic radii disrupts the tin

oxide crystal structure (seen in chapter 2) causing a reduction in the crystallinity. The partially filled conduction band has the effect of lowering the response caused by oxygen de-sorption because of the remaining high mobility delocalized conduction band electrons. More oxygen can bind because the electronic donation is facilitated by a higher Fermi energy, this prevents saturation of the response between the measured ethanol concentrations. The disrupted structure presumably creates additional oxygen binding sites such as steps, corners and dislocations, thus increasing the rate of oxygen re-adsorption.
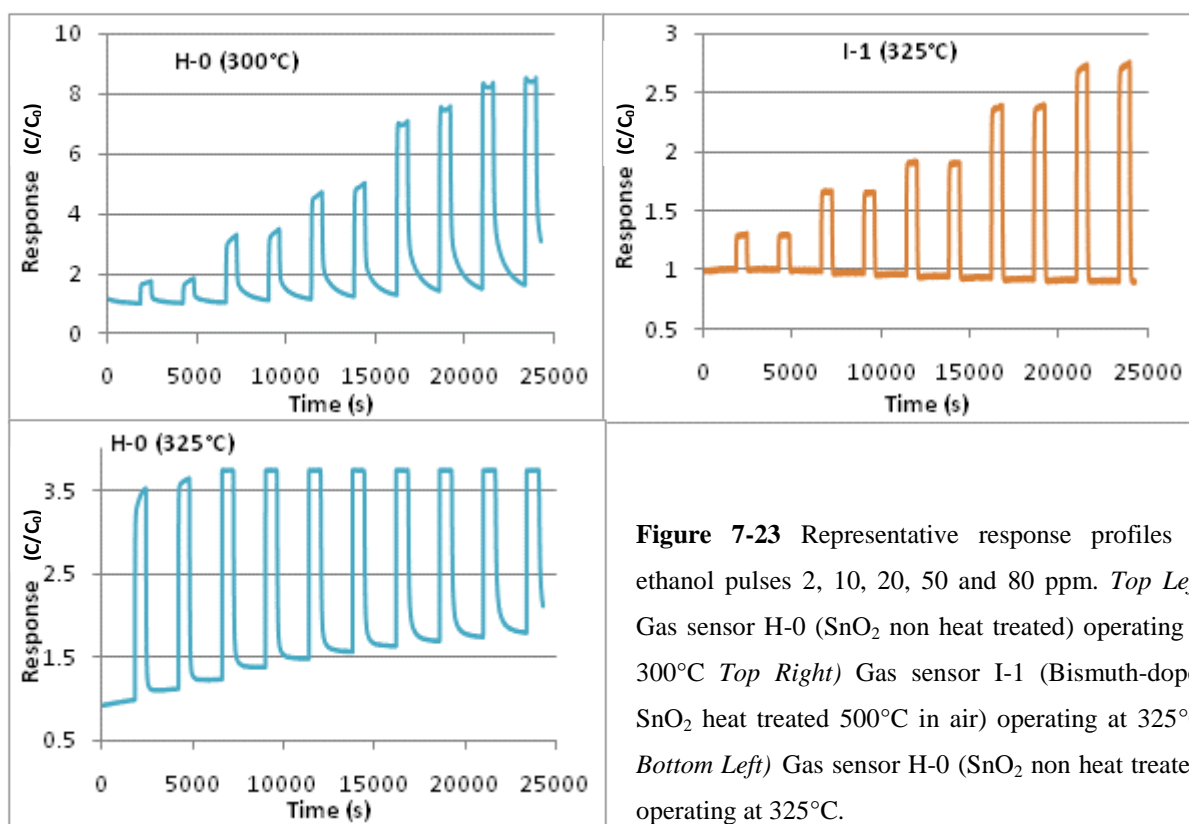


**Figure 7-23** Representative response profiles to ethanol pulses 2, 10, 20, 50 and 80 ppm. *Top Left)* Gas sensor H-0 ($SnO_2$ non heat treated) operating at 300°C *Top Right)* Gas sensor I-1 (Bismuth-doped $SnO_2$ heat treated 500°C in air) operating at 325°C. *Bottom Left)* Gas sensor H-0 ($SnO_2$ non heat treated) operating at 325°C.

242

## 7.5 Discussion Summary

### 7.5.1 $NO_2$ Sensing

Each of the four categories of film analysed in this chapter (ZnO, SWCNT, Hybrid CNT-ZnO and $SnO_2$) gave a signature electrical response to $NO_2$ gaseous molecules in dry air over 2-800 ppb and 300-350°C operating temperatures. The characteristic signature response of each film has been used to hypothesize possible mechanisms of resistivity changes upon gas injection, and to assess the pro's and con's of using each system as a functioning gas sensor. The spray coated thin films, and the hybrid ZnO-SWCNT films, showed the highest sensitivity to the $NO_2$ gas, giving response values of up to 80 units at 800 ppb $NO_2$ in dry air. The $SnO_2$ films showed a lower level of response, giving values of up to 8 units at 800 ppb, however the lowest response values were seen for the SWCNT films which gave normalized response values below 1 unit. Though the sensitivity is a critical factor in the performance of gas sensors, other factors must be taken into consideration to assess the full performance characteristics of the material, namely: response times, concentration range in which the sensor can function reliably, reversibility of the sensing response, and the stability of the material[260].

The SWCNT films showed rapid adsorption and desorption characteristics, however the stability of the baseline was very poor, this can been attributed to the oxidation of vulnerable carbon atoms in the CNTs or the loss of the functional surface groups over the experiment.

The ZnO thin films and the hybrid films both displayed high response sensitivity over the studied concentration range, they also displayed rapid adsorption and desorption rates upon injection and termination of the $NO_2$ gas pulses, and stable baseline conductivity over the course of the experiment.

Research has been done into the $SnO_2$-SWCNT and $TiO_2$-SWCNT hybrid systems at room temperature by Wei et al.[253] and Van Duy et al.[256] who suggested that using p-type carbon nanotubes creates an n-p junction with the metal oxide coating which amplifies the response. They reasoned that the increased response they saw at

243

room temperature can be attributed to the n-p characteristics because the morphology, film thickness, and surface area were relatively constant between plain metal oxide and metal oxide-CNT films which they tested. The theory is based on the work done by Zhang et al.[261] who made a highly sensitive gas sensing device for $NO_2$ which was based on a metal oxide-silicon n-p junction. Wei et al. assumed that: *sensitivity = Δi/Δc* where *i* is current across the film and *c* is concentration of $NO_2$. This current can then be split into 2 components: $i_A$ (through the metal oxide), and $i_B$ (through the SWCNT and metal oxide) as shown in figure 7-24.
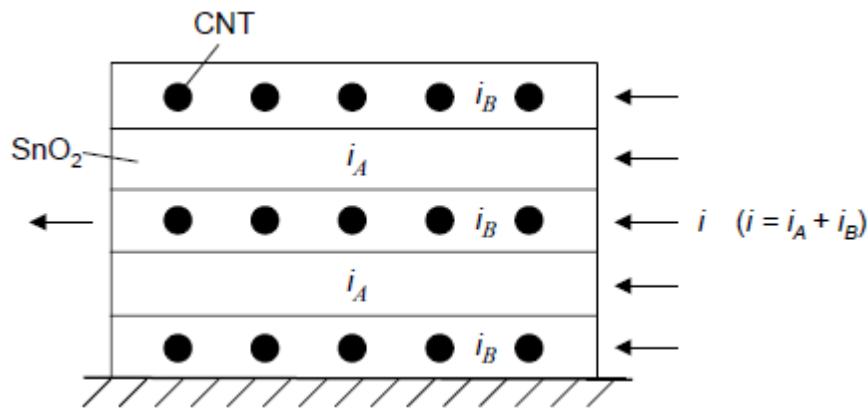


**Figure 7-24** Diagram reproduced from Wei et al.[253] showing the conduction pathays through the metal oxide- CNT composite. i represents current flow, $i_A$ is through solely the zinc oxide and $i_B$ is through the CNT-ZnO composite layer.

The sensitivity in pure metal oxide films at room temperature was found to be very low, therefore they assumed *Δi$_A$/Δc* is negligible and can be ignored. This means the dominant responsive pathways are occurring through the metal oxide and SWCNT layer as shown in figure 7-25. Wei et al. assert that the composite forms an n-p junction between the n-type metal oxide, and the p-type SWCNT, this causes not only depletion zones on the surface of the metal oxide but also at the SWCNT-metal oxide junction, resulting in a depletion layer which is affected by $NO_2$ adsorption not only on the surface but also at the SWCNT-metal oxide junction, this then amplifies any electronic

changes. Figure 7-25 shows the depletion region changing from $d_1$-$d_3$ to $d_2$-$d_4$ upon $NO_2$ adsorption, the authors credit the increase in sensitivity to this process.
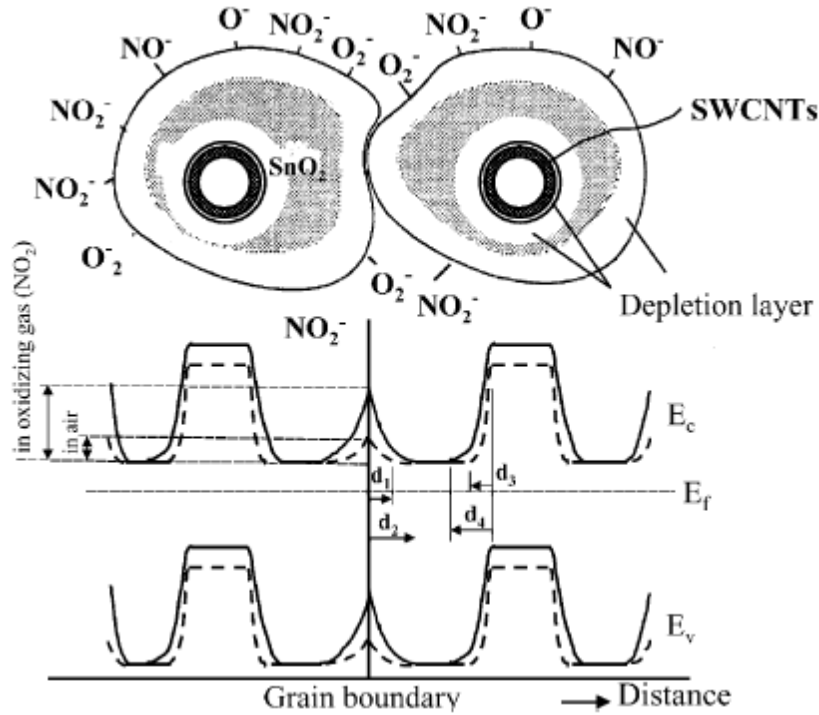


**Figure 7-25** Diagram reproduced from work by Wei et al.[253] showing the band structure modifications caused by SWCNT in a metal oxide. The SWCNT produce a secondary depletion zone which is affected by $NO_2$ adsorption and amplifies the resistivity changes caused by the target gas.

However, this mechanism was rejected by Nguyen et al.[250], who measured Ohmic I-V characteristics across the hybrid material, and thus dismissed any diode behavior. Nguyen et al. hypothesized that there exists two channels of conduction through metal oxide coated SWCNT (see figure 7-26): 1) along the SWCNT which are highly conductive and 2) through the metal oxide which is a poor conductor. They state that the metal oxide is mostly exposed to the gas so must be the dominant contributor to the resistivity changes upon $NO_2$ adsorption. They state that the three mechanisms of conductivity response are; surface depletion layers, grain boundary depletion layers, and

inter-nanotube grain boundary layers. They cite the first two mechanisms as the likely dominant controlling factors.
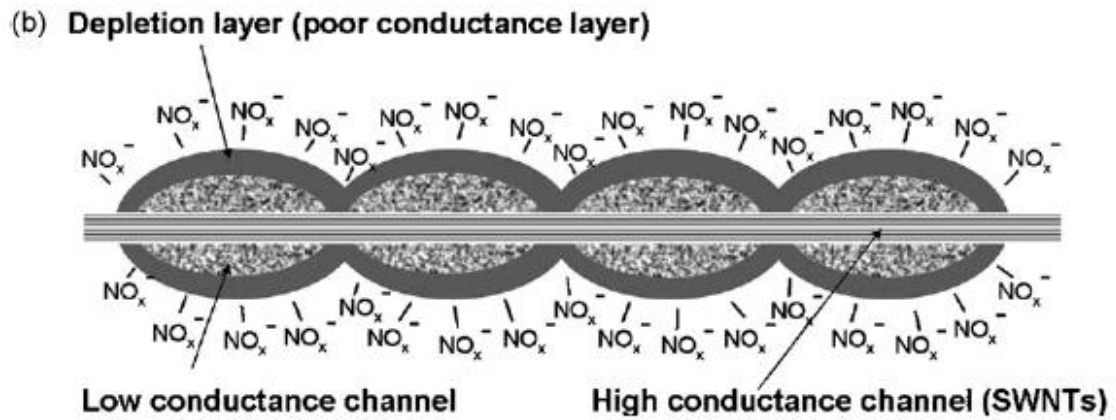


**Figure 7-26** Diagram reproduced from Nguyen et al.[250] showing their hypothesized conductance channels in tin oxide coated SWCNT gas sensors thin films.

The results from the plain ZnO films, detailed in this chapter, gave a linear response vs concentration dependency at 325°C and 350°C, however, displayed a changeover in the sensing mechanism at 300°C and 800 ppb which was attributed to depletion layer saturation of the grains, causing a shift from grain boundary control to grain controlled response. As such, these films are functioning through the two likely mechanisms outlined by Nguyen (through grain boundary limited resistance and a changeover to total surface limited resistance). This changeover in mechanism implies limitations in the sensing temperatures, and gas concentrations which can be monitored using this system without detailed calibration and testing.

The hybrid SWCNT-ZnO films also displayed a changeover in response mechanism, however the behavior was different to that of the plain ZnO films, in that the tipping point, where a drastic response increase was observed, only occured at the higher temperatures. It was suggested that the SWCNT were playing a role in this change of mechanism owing to their high conductivity over all temperatures, meaning it is not until a high level of thermal population in the zinc oxide conduction band takes place that the zinc oxide is exploited for electronic propogation and the sensitivity of the

hybrid material becomes much greater. This conclusion would seem to fit with the analysis presented by Nguyen et al. where by the conduction routes are either through the CNT, or the metal oxide. Whereas Nguyen performed the experiments at room temperature, the experiments detailed in this thesis have been performed at raised temperatures where activation of the metal oxide conductive channels is greater, thus transferring an increasing amount of current through the zinc oxide, which then in turn increases the response drastically as the concentration of $NO_2$ causes depletion layer saturation of the entire grains.

The data presented in this chapter suggests that at higher temperatures an interplay between the two conductive channels is taking place in the hybrid material which supports the ideas presented by Nguyen et al. However, this hypothesis relies on ZnO as the dominant response material and, as such, we have seen very little benefit from adding SWCNT into the system at raised temperatures. Nguyen et al. however did show a raised sensitivity at room temperature operation, which their response mechanism cannot account for. Wei et al. proposed that the n-p junction created by the SWCNT-metal oxide interface should amplify the response, our results did not show a significant change in response between the hybrid systems and the pure ZnO films. However, this lack of amplification could be a result of the increased temperature causing thermal excitation of electrons which mitigates and junction effect, therefore it is difficult to draw any solid conclusion from this theory using our data.

### 7.5.2 Ethanol Sensing

The four categories of gas sensor outlined in this chapter displayed an electrical response to ethanol over 2-80 ppm in dry air, over 300-350°C operating temperatures. The un-doped $SnO_2$ displayed the highest level of sensitivity giving a $R/R_0$ response of 8 units at 80 ppm, the $Bi:SnO_2$ gave a $R/R_0$ response of 3 units at 80 ppm, the hybrid films showed a maximum $R/R_0$ response of 4.5 units at 80 ppm, the SWCNT films displayed a maximum $R/R_0$ response of 1.5 units at 80 ppm and the plain ZnO films gave a maximum $R/R_0$ response of 5 units at 80 ppm. The levels of sensitivity are relatively consistent across all materials, however the rate of response, saturation levels, and stability, varied widely across each material.

The worst performers were the ZnO films and the SWCNT films. The ZnO displayed a sensitivity at the higher end of the values achieved, however the saturation of the response occurred at 20 ppm (well below the range of 20 – 800 ppm required for driving breathalyser tests[262]), showing that these films could only operate at low ethanol concentrations. Additionally the response rate was also very slow in terms of both removal of the surface oxygen and re-adsorption of oxygen, making rapid, accurate detection impossible.

The non-annealed SWCNT film sensor showed a relatively high level of sensitivity compared to the low response values it had given in the detection of $NO_2$, though it was still the worst performing material in terms of sensitivity. The annealed SWCNT sensor gave a very low response indicating that the surface functionality, which was only present on the non-annealed film, could be playing a catalytic role in the combustion process. Work by Sayago et al.[259] suggested this increased sensitivity with functionalisation occurs for $NO_2$ detection. Though the sensitivity was low, the response rates of the desorption and adsoption of oxygen were extremely fast, and the response showed a linear dependency with concentration and no sign of saturation. The stability of the baseline for the SWCNT film was again very poor, presumably due to the gradual oxidation of vulnerable carbon atoms in the nanotubes.

The hybrid SWCNT-ZnO films displayed a comparably high sensitivity which is attributed to the zinc oxide coating, and displayed very fast rate of responses to both desorption and adsorption of oxygen, which is attributed to the influence of the SWCNTs. This process can be explained by firstly the exposed CNT surfaces which are in close proximity to the zinc oxide acting as a catalytic sites for the combustion of adsorbed oxygen on the nanotube surface, which in turn transfers the electronic changes to the zinc oxide, and secondly, as a spillover zone, whereby rapid adsorption of oxygen occurs on the active carbon nanotube and spills over onto the surface of the zinc oxide. This spill-over effect has been noted at the proximity between metal oxides and catalytically active contact electrodes such as a noble metals[263]. The hybrid materials displayed saturation at higher ethanol concentrations because the combustion of the extra ethanol was self limiting, it was shown however, that this saturation could be

prevented by operation at higher temperatures thus encouraging full reaction of the ethanol present. The combination of SWCNT and ZnO into a hybrid material for ethanol gas sensing at high temperatures does show promise. The SWCNTs have shown the ability to increase the rate of reaction and adsorption on the metal oxide surface which could help increase the speed of gaseous detection.

The final material tested was the $SnO_2$ and bismuth doped $SnO_2$. The un-doped material displayed the highest response to ethanol of all the systems tested, however it also showed saturation of the response at higher temperatures. The addition of bismuth to the tin oxide had the effect of lowering the sensitivity, however it prevented the saturation limit being reached up to 80 ppm and the rate of response was vastly increased. The bismuth doped material gave a highly stable baseline, excellent response profile peaks, and a temperature independent linear response dependency on concentration.

## 7.6 Conclusion

The gas sensing properties of thin film layers composed of functionalised-SWCNTs, functionalised-MWCNTs, hybrid ZnO-CNTs, ZnO, $SnO_2$, and Bi-doped $SnO_2$ have been studied. The spray coated ZnO thin films and hybrid SWCNT-ZnO films proved most effective for the detection of $NO_2$, though the addition of SWCNT had no significant impact upon the device performance. The bismuth doped tin oxide proved the most effective sensor for the detection of ethanol over the experimental conditions used. The addition of SWCNT to the ZnO system was shown to be beneficial to the rate of response, both on and off, in the detection of ethanol, and could prove to be a valuable technique for increasing the speed of combustible gas detection in general.

The results and analysis presented in this chapter go some way to inferring response mechanisms and the benefits of each of the variants, in each sensing materials used. However, further experimentation is required to further verify the behaviors which have been hypothesized.

# 8 Conclusion

## 8.1 Summary of Results

The results presented in this thesis demonstrate novel findings into the synthesis, characterization, and application of both established, and new, transparent conducting thin film technology. Both metal oxide and carbon nanotube based materials have been used to fabricate visibly transparent, and electrically conductive thin films which were assessed in their performance for a multitude of applications, including: 'low-E' heat mirror glazing, transparent electrode materials for thin film photovoltaics, photocatalytic degredation of organic materials, and gas sensing.

Chapter two developed the use of Aerosol Assisted Chemical Vapour Deposition (AACVD), as a viable method for the laboratory scale production of doped tin oxide, Transparent Conducting Oxide (TCO) thin films. The best performing fluorine doped tin oxide coatings, produced by collision-type AACVD, had a thickness of ~700 nm, a sheet resistance of 7 $\Omega/\square$, a resistivity of 5 x $10^{-4}$ $\Omega$cm, a charge carrier density of 6.4 x $10^{20}$ cm$^{-3}$, a mobility of 25 cm$^2$/Vs and a visible transparency of > 90%. Variation in deposition conditions allowed for a tailoring of the morphology of the coatings for either Low-E, or Photovoltaic application, giving haze values producing either optical clarity, or light scattering, respectively. Careful selection of deposition conditions yielded coatings which could outperform the current leading commercial products.

Chapter three outlined a dual coating methodology, using AACVD and APCVD, for the high throughput growth of doped tin oxide TCO coatings with a modified surface structure. The results have shown that using an aerosol precursor solution it is

250

possible to influence the $R_a$ roughness, the Root Mean Square height irregularities, the kurtosis, the surface area and the waviness of the final films. Modification of the final coatings was shown to reduce the percentage of diffuse transmission through the samples resulting in a high clarity coating.

Chapter four detailed the findings of experiments into the synthesis of carbon nanotubes (CNT) and other related materials: where novel catalysts for CNT growth were demonstrated, and novel carbon nanofibres (CNF) were synthesised. The growth methodology was analysed in order to highlight the specific nuances taking place during the synthesis of tubular carbon structures, in order to further aid the selection of appropriate catalytic materials for targeted carbon nano-structured growth.

The review of results over a large number of conditions illustrated the importance of controlling temperature, flow rates, and catalyst type in the growth of CNTs. The temperature and flow rates of methane and hydrogen proved to be critical in the formation of structured carbon, but the most important factor controlling the carbon species type seemed to be the metal catalyst itself.

To the author's knowledge this is the first time chromium has been used as a solo-catalyst in the growth of MWCNTs, which were produced in very high yield. In addition to the growth of carbon nanotubes, novel CNF type structures were formed in high yield using a gold catalyst and the decomposition of methane under a reducing atmosphere. To the author's knowledge this is the first time the growth of these CNF structures has been recorded, the structures differ to traditional CNFs in their segmented nature rather than the solid fibres usually grown under decomposition conditions.

Chapter five demonstrated the scalability and efficacy of the acid-microwave reflux functionalisation of carbon nanotubes, and proved that the dominant sulphonic functionalisation of the surface renders the treated material water soluble. Results showed that the functionalised material was suitable for the deposition of carbon nanotube-nanonet thin films. The functionalisation was a fully reversible process, sensitive to thermal treatment. The films displayed promising transparency and

electrical conductivity, although, there is more research required before the nanonet films can compete with their metal oxide counterparts.

The modified single-walled carbon nanotubes displayed a high solubility (0.74 mg/ml at pH 11). Sulphones and sulphonate groups proved to be the dominant functionally bound species produced using this technique. No evidence of carboxylation was found, which is unusual for an acid reflux process and may prove to be a promising route to a more selective single-wall carbon nanotube (SWCNT) surface chemistry. The functionalisation of the surface was shown to be a reversible process following heat treatment of the samples, allowing for restoration of the SWCNT electronic structure. Atmospheric microwave acid reflux was shown to provide a fast and effective route to carbon nanotube solubility in aqueous media, avoiding the use of environmentally harmful solvents and additional surfactants in processing.

Chapter six detailed the AACVD of zinc oxide thin films, and the inability of the process to yield a doped material. However, the deposition of highly transparent (>90%) un-doped ZnO thin films from a zinc acetate precursor was achieved using the aerosol assisted chemical vapour deposition process. The properties of the films have been shown to be highly dependent on the temperature used during the deposition process, which changed the structural morphology and orientation of the poly-crystalline thin films. The contact angle and photocatalytic ability of the films were measured, and it was shown that the contact angle of water droplets was dependent upon the surface morphology, and the irradiation of the surface with UV light, resulting in photo-induced super hydrophillic coatings. The photocatalytic abilities of high temperature films exhibited a formal quantum efficiency of an order comparable to that of commercially-utilised titania.

Chapter seven demonstrated the combination of the metal oxide and carbon nanotube development to yield CNT-metal oxide hybrid coatings for use as gas sensing materials. The hybrid materials displayed enhanced response times to combustible target gases, which was attributed to the catalytic effects of exposed carbon nanotube

surfaces and the spillover of adsorbed oxygen from the active nanotubes to the metal oxide surface.

The results and discussion presented in this thesis illustrate the technical demands being placed on transparent conducting materials, as the technologies they are integrated into become more wide ranging and seek ever higher performance standards. In the short term, metal oxide materials will doubtlessly remain the first choice for high performance/high specification transparent conducting applications, with an increasing emphasis being placed on exact control over charge carrier mobility, charge carrier density, work-function, morphology, and surface structure properties, to improve device performance. In the longer term, the development of alternate transparent conducting materials to replace metal oxides is highly likely. Where, materials like carbon nanotubes or graphene will be able to offer not only improved electrical and optical performance at a reduced cost, but also a flexible material for integration of this technology into every aspect of everyday life.

## 8.2 Developmental Implications

The findings outlined in this thesis could prove beneficial to not only the glass manufacturing industry, but have ramifications for the photovoltaics and gas sensing communities.

The various doped tin oxide materials and production processes show promise for enhanced performance in glazed building products; where higher infrared reflection, colour modification, and control over the diffuse transmittance could help create enhanced functionality.

The findings detailed into the high throughput dual process for modification of the tin oxide surfaces, is a promising development which could help towards the development of increased efficiency photovoltaic modules, through the reduction of electrical shorting between layers and tailored light scatter.

The new methodologies and materials concerning the production of hybrid CNT-Metal oxide coatings are promising candidates for a new generation of transparent, high performance, high response gas sensors.

## 8.3 Future Perspectives

Further investigations into the results outlined in this thesis could yield valuable additional information, and see the processes and materials move closer to commercial application.

Further controlled testing and analysis of the dual AACVD/APCVD process is required to build up a larger data set of conditions and repeats. This should allow in-depth statistical analysis, thus establishing, and quantifying, the changes taking place and the root cause of the decreased light scatter. Analysis of the integration of AACVD and the online coating process is required to establish the possibility of modifying the commercial line.

The CNT nanonet thin film coatings require further study in order to boost the transparency and electrical conductivity of the films if they are to be brought in line with commercial metal oxide coatings. This is most likely to be achieved by limiting the resistive losses at inter-nanotube junctions, by either: increasing the average nanotube length-thus reducing the number of junctions; or using a conductive tube coating (such as a sulphur doped conductive polymer) to decrease the resistance at the junctions.

The addition of SWCNTs to metal oxide gas sensing materials is a promising line of investigation, which could yield increased rate of response towards combustible target gases. Further testing is required over a range of metal oxides, and a range of combustible gases to establish a firm link, and to establish an enhanced system for a target gas where speed of detection is critical.

# References

1. M. Birkholz, *Thin Film Analysis by X-Ray Scattering*. Wiley-VCH: Weinheim 2006, pp.108-109.
2. S. J. S. Qazi; A. R. Rennie; J. K. Cockcroft; M. Vickers, *Journal of Colloid and Interface Science* **2009,** 338, (1), 105-110.
3. L. J. v. d. Pauw, *Philips Technical Review* **1958,** 20, 20-224.
4. P. P. Edwards; A. Porch; M. O. Jones; D. V. Morgan; R. M. Perks, *Dalton Transactions* **2004**, (19), 2995-3002.
5. K. Gelin; A. Roos; F. Geotti-Bianchini; P. v. Nijnatten, *Optical Materials* **2005,** 27, (4), 705-712.
6. B. C. Ginley DS, guest editors, *MRS Bulletin* **2000** 25, (8), 15.
7. K.Badeker, *Annals of Physics* **1907,** (22), 749.
8. G.Rupprecht, *Z.Phys* **1954,** (139), 504.
9. G. Gruner, *Journal of Materials Chemistry* **2006,** 16, (35), 3533-3539.
10. L. D. Smith, *Thin-Film Deposition Principles & Practice*. McGraw-Hill: New York, 1995, pp.1-7.
11. M.L.Hitchman; K.F.Jenson, *Chemical Vapor Deposition Principles and Applications*. Academic Press Limited: Salt Lake City, 1993, pp.35-39.
12. R.A.Stradling, *Growth and Characterisation of Semiconductors*. IOP Publishing Ltd: New York, 1990, 17-35.
13. K.-N.Tu; W.J.Mayer; C.L.Feldman, *Electronic Thin Film Science*. Macmillan: New York, 1992, pp.157-181.
14. M. A. Aegerter; J. Puetz; G. Gasparro; N. Al-Dahoudi, *Optical Materials* **2004,** 26, (2), 155-162.
15. G. Srinivasan; N. Gopalakrishnan; Y. S. Yu; R. Kesavamoorthy; J. Kumar, *Superlattices and Microstructures* **2008,** 43, (2), 112-119.
16. L. I. Maissel; M. H. Francombe, *An introduction to Thin films*. Gordon and Breach: New York, 1973, pp.14-36.
17. H. K. Pulker, *Surface and Coatings Technology* **1999,** 112, (1-3), 250-256.
18. R. G. Sharafutdinov; S. Y. Khmel; V. G. Shchukin; M. V. Ponomarev; E. A. Baranov; A. V. Volkov; O. I. Semenova; L. I. Fedina; P. P. Dobrovolsky; B. A. Kolesov, *Solar Energy Materials and Solar Cells* **2005,** 89, (2-3), 99-111.
19. S.M.Park; T.Ikegami; K.Ebihara; P.K.Shin, *Applied Surface Science* **2006,** 253, (3), 1522-1527.
20. S. W. Rees, *CVD of Nonmetals*. VCH: Weinheim, 1996, pp.12-18.
21. K. L. Choy, *Progress in Materials Science* **2003,** 48, (2), 57-170.
22. S. Faÿ; J. Steinhauser; N. Oliveira; E. Vallat-Sauvain; C. Ballif, *Thin Solid Films* **2007,** 515, (24), 8558-8561.
23. H. Y. Lee; J. N. Kim; H. Kim; D. S. Jang; J. J. Lee, *Thin Solid Films* **2008,** 516, (11), 3538-3543.
24. M. Hamid; A. A. Tahir; M. Mazhar; F. Ahmad; K. C. Molloy; G. Kociok-Kohn, *Inorganica Chimica Acta* **2008,** 361, (1), 188-194.
25. X. Hou; K.-L. Choy, *Chemical Vapor Deposition* **2006,** 12, (10), 583-596.

26. M.L.Hitchman, *Chemical Vapor Deposition Principles and Applications*. Academic Press Limited: Salt lake City, 1993, pp.6-40.

27. H. Hartnagel, *Semiconducting Transparent Thin Films*. IOP Publishing Ltd: 1995, pp.1-358.

28. L. Solymar; D. Walsh, *Electrical Properties of Materials*. 8$^{th}$ Edn.; Oxford Univresity Press: New York, 2010, pp.98-111.

29. P. A. Cox, *The Electronic Structure and Chemistry of Solids*. Oxford University Press: New York, 1995, pp.1-43.

30. J. Singleton, *Band Theory and Electronic Propeties of Solids*. Oxford University Press: New York, 2001, pp.16-20.

31. A.R.West, *Basic Solid State Chemistry*. 2$^{nd}$ Edn.; John Wiley & Sons Inc: New York, 1999, pp.110-121.

32. P. Atkins, *The Elements of Physical Chemistry*. Oxford University Press: Oxford, 2001, pp.356-263.

33. H. Hosono, *Thin Solid Films* **2007,** 515, (15), 6000-6014.

34. S. B. Zhang; S. H. Wei; A. Zunger, *Physica B: Condensed Matter* **1999,** 273-274, 976-980.

35. A.Zunger, *National Renewable Energy Laboratory,* **2001,** Report Number CP-590-31034.

36. M. Gross; A. Winnacker; P. J. Wellmann, *Thin Solid Films* **2007,** 515, (24), 8567-8572.

37. H. W. Kroto; J. R. Heath; S. C. O'Brien; R. F. Curl; R. E. Smalley, *Nature* **1985,** 318, (6042), 162-163.

38. S.Iijima, *Nature* **1991**, 354, 56-58.

39. S.V.Rotkin; S.Subramoney, *Applied Physics of Carbon Nanotubes*. Heidelberg:Springer-Verlag: Berlin, 2005, pp.41-82.

40. M.S.Dresselhaus; G.Dresselhaus; Ph.Avouris, *Carbon Nanotubes Synthesis, Structure, Properties, and applications*. Heidelberg:Springer-Verlag: Berlin, 2001, pp.1-9.

41. G. Kunal, *Electronic Band Structure of Carbon Nanotubes*. [Leaflet] Stanford University, Nov 2005, 4-15.

42. R. Saito; G. Dresselhaus; M. S. Dresselhaus, *Physical Properties of Carbon Nanotubes*. Imperial College Press: London, 1998, p.25.

43. C. Kittel, *Introduction to Solid-State Physics*. Wiley: London, 2005, pp.161-252.

44. O.S.Koswatta; S.Hassan; M.S.Lundstrom; M.P.Anantram; D.E. Nikonov, *Applied Physics Leters.* **2006,** 89, 023125.

45. Boris I.; Yakobson; P. Avouris, *Mechanical Properties of Carbon Nanotubes*. Springer-Verlag: Berlin, 2001; Vol. 80, pp.23-35.

46. Z. Wu; Z. Chen; X. Du; J. M. Logan; J. Sippel; M. Nikolou; K. Kamaras; J. R. Reynolds; D. B. Tanner; A. F. Hebard; A. G. Rinzler, *Science* **2004,** 305, (5688), 1273-1276.

47. Y. I. Song; C.-M. Yang; D. Y. Kim; H. Kanoh; K. Kaneko, *Journal of Colloid and Interface Science* **2008,** 318, (2), 365-371.

48. Y. S. Shi; C.-C. Zhu; W. Qikun; L. Xin, *Diamond and Related Materials* **2003,** 12, (9), 1449-1452.

49. A. Schindler; J. Brill; N. Fruehauf; J. P. Novak; Z. Yaniv, *Physica E: Low-dimensional Systems and Nanostructures* **2007,** 37, (1-2), 119-123.

50. Solymar and D.Walsh, Lectures on the Electrical Properties of Materials, Oxford Science Publications: Oxford, 1998, pp.101-130.

51. P. Drude, *Annalen der Physik* **1900,** 306, (3), 566-613.

52. P. Drude, *Annalen der Physik* **1900,** 308, (11), 369-402.

53. G. J. Exarhos; X.-D. Zhou, *Thin Solid Films* **2007,** 515, (18), 7025-7052.

54. C. G. Granqvist, *Solar Energy Materials and Solar Cells* **2007,** 91, (17), 1529-1598.

55. P. Robinson; J. Littler, *Solar Energy* **1993,** 50, (2), 129-134.

56. J. C. C. Fan; F. J. Bachner, *Applied Optics* **1976,** 15, (4), 1012-1017.

57. U. Eicker, *Solar Technologies for Buildings*. John Wiley & Sons: Chichester, 2001, pp.1-12.

58. H. J. Berginski M, Schulte M, Schope G, Stiebug H, Rech B., *Journal of Applied Physics* **2007,** 101, 074903.

59. W. Beyer; J. Hüpkes; H. Stiebig, *Thin Solid Films* **2007,** 516, (2-4), 147-154.

60. http://www.pilkington.com/resources/lowebrochure.pdf, Pilkington NSG, 2007, (accessed Jun. 2008).

61. K. Hara; H. Arakawa, in: *Handbook of Photovoltaic Science and Engineering*, A. Luque; S. Hegedus, (Eds.) John Wiley and Sons: New York, 2003; pp.663-700.

62. B. O'Regan; M. Gratzel, *Nature* **1991,** 353, (6346), 737-740.

63. K.Takahashi; M.Konagai, *Amorphous Silicon Solar Cells*. North Oxford Academic Publishers: London, 1983,102-110.

64. C. Beneking; B. Rech; S. Wieder; O. Kluth; H. Wagner; W. Frammelsberger; R. Geyer; P. Lechner; H. Rübel; H. Schade, *Thin Solid Films* **1999,** 351, (1-2), 241-246.

65. F. Ruske; C. Jacobs; V. Sittinger; B. Szyszka; W. Werner, *Thin Solid Films* **2007,** 515, (24), 8695-8698.

66. J. Müller; B. Rech; J. Springer; M. Vanecek, *Solar Energy* **2004,** 77, (6), 917-930.

67. Ü. Dagkaldiran; A. Gordijn; F. Finger; H. M. Yates; P. Evans; D. W. Sheel; Z. Remes; M. Vanecek, *Materials Science and Engineering: B* **2009,** 159-160, 6-9.

68. A. Mills; S. Le Hunte, *Journal of Photochemistry and Photobiology A: Chemistry* **1997,** 108, (1), 1-35.

69. H. Zhang; G. Chen; D. W. Bahnemann, *Journal of Materials Chemistry* **2009,** 19, (29), 5089-5121.

70. A. Mills; S.-K. Lee, *Journal of Photochemistry and Photobiology A: Chemistry* **2002,** 152, (1-3), 233-247.

71. A. Fujishima; X. Zhang; D. A. Tryk, *Surface Science Reports* **2008,** 63, (12), 515-582.

72. S. Rehman; R. Ullah; A. M. Butt; N. D. Gohar, *Journal of Hazardous Materials* **2009,** 170, (2-3), 560-569.

73. E. Comini; G. Fagalia; G. Sberveglieri, *Solid State Gas Sensing*. Springer Science + Business Media: New York, 2009, pp.1-99.

74. S.M.Sze, *Semiconductor Sensors*. John Wiley & Sons: New York, 1994, pp.1-27.

75. S. C. Naisbitt; K. F. E. Pratt; D. E. Williams; I. P. Parkin, *Sensors and Actuators B: Chemical* **2006,** 114, (2), 969-977.

76. N. Yamazoe, *Sensors and Actuators B: Chemical* **1991,** 5, (1-4), 7-19.

77. D. E. Williams, *Sensors and Actuators B: Chemical* **1999,** 57, (1-3), 1-16.

78. P. Ãgoston; K. Albe; R. M. Nieminen; M. J. Puska, *Physical Review Letters* **2009,** 103, (24).

79. H. L. Hartnagel; A. L. Dawar; A. K. Jain; C. Jagadish, *Semiconducting Transparent Thin Films*. IOP Publishing Ltd: Bristol 1995; p 1-10, 40-74, pp.130-160.

80. I. P. Parkin; T. D. Manning, *Journal of Chemical Education* **2006,** 83, (3), 393.

81. P. Gerhardinger; D. Strickler, *Key Engineering Materials* **2007,** 380, 169-178.

82. *Tin Markets for Photovoltaics, [Online report] NanoMarkets, Glen Allen, VA*, July 15, 2009 (accessed Jul 2010).

83. T. Fukano; T. Motohiro, *Solar Energy Materials and Solar Cells* **2004,** 82, (4), 567-575.

84. Z. Remes; M. Vanecek; H. M. Yates; P. Evans; D. W. Sheel, *Thin Solid Films* **2009,** 517, (23), 6287-6289.

85. D. W. Sheel; H. M. Yates; P. Evans; U. Dagkaldiran; A. Gordijn; F. Finger; Z. Remes; M. Vanecek, *Thin Solid Films* **2009,** 517, (10), 3061-3065.

86. R. G. Palgrave; I. P. Parkin, *Chemistry of Materials* **2007,** 19, (19), 4639-4647.

87. T. Saeed; P. O'Brien, *Thin Solid Films* **1995,** 271, (1-2), 35-38.

88. G. Walters; I. P. Parkin, *Applied Surface Science* **2009,** 255, (13-14), 6555-6560.

89. M. Saeli; C. Piccirillo; I. P. Parkin; I. Ridley; R. Binions, *Solar Energy Materials and Solar Cells* 94, (2), 141-151.

90. C. Piccirillo; R. Binions; I. P. Parkin, *Thin Solid Films* **2008,** 516, (8), 1992-1997.

91. C. S. Blackman; X. Correig; V. Katko; A. Mozalev; I. P. Parkin; R. Alcubilla; T. Trifonov, *Materials Letters* **2008,** 62, (30), 4582-4584.

92. A. J. Hickey, *Pharmaceutical inhalation aerosol technology*. M. Dekker: New York, 2004, p.240.

93. T. T. Kodas; T. T. Kodas; M. J. Hampden-Smith, *Aerosol Processing of Materials*. Wiley-VCH: New York, 1999, pp.126-136.

94. M. R. Waugh; G. Hyett; I. P. Parkin, *Chemical Vapor Deposition* **2008,** 14, (11-12), 366-372.

95. A. Le Bail, The practice of structure determination from powder data: how to succeed, Powder Diffraction, satellite meeting of the XVth IUCr congress, Toulouse, France, 1990, 99-100.

96. A. V. Moholkar; S. M. Pawar; K. Y. Rajpure; C. H. Bhosale; J. H. Kim, *Applied Surface Science* **2009,** 255, (23), 9358-9364.

97. M. Klementova; M. Rieder; Z. Weiss, *International Journal of Inorganic Materials* **2000,** 45, 155-157.

98. F. M. Amanullah; K. J. Pratap; V. Hari Babu, *Materials Science and Engineering B* **1998,** 52, (2-3), 93-98.

99.    H. H. Afify; F. S. Terra; R. S. Momtaz, *Journal of Materials Science: Materials in Electronics* **1996,** 7, (2), 149-153.

100.   C. Agashe; J. Hüpkes; G. Schöpe; M. Berginski, *Solar Energy Materials and Solar Cells* **2009,** 93, (8), 1256-1262.

101.   D. Belanger; J. P. Dodelet; B. A. Lombos; J. I. Dickson, *Journal of The Electrochemical Society* **1985,** 132, (6), 1398-1405.

102.   A. I. Martinez; L. Huerta; J. M. O. R. d. Leon; D. Acosta; O. Malik; M. Aguilar, *Journal of Physics D: Applied Physics* **2006,** 39, (23), 5091-5096.

103.   R. J. Betsch, *Journal of Crystal Growth* **1986,** 77, (1-3), 210-218.

104.   M. Batzill; U. Diebold, *Progress in Surface Science* **2005,** 79, (2-4), 47-154.

105.   K. Subba Ramaiah; V. Sundara Raja, *Applied Surface Science* **2006,** 253, (3), 1451-1458.

106.   H. Haitjema; J. Elich, *Solar Energy Materials* **1987,** 16, (1-3), 79-90.

107.   H. Cachet, *Fluorinated Materials for Energy Conversion*, T. Nakajima; H. Groult, (Eds.) Elsevier Ltd.: The Netherlands 2005, 513-548.

108.   B. Thangaraju, *Thin Solid Films* **2002,** 402, (1-2), 71-78.

109.   S. Noguchi; H. Sakata, *Journal of Physics D: Applied Physics* **1980,** 13, (6), 1129.

110.   B. H; Herring, *Physical Review Letters* **1951,** 83 879.

111.   E. M. Conwell; V. F. Weisskopf, *Physical Review letters* **1950,** (388), 77.

112.   E. Shanthi; A. Banerjee; K. L. Chopra, *Thin Solid Films* **1982,** 88, (2), 93-100.

113.   I. S. Athwal; R. K. Bedi, *Solid-State Electronics* **1985,** 28, (11), 1165-1165.

114.   S. R. Vishwakarma; J. P. Upadhyay; H. C. Prasad, *Thin Solid Films* **1989,** 176, (1), 99-110.

115.   V. Casey; M. I. Stephenson, *Journal of Physics D: Applied Physics* **1990,** 23, (9), 1212.

116.   A. H. Hamdi; R. C. O. Laugal; A. B. Catalan; A. L. Micheli; N. W. Schubring, *Thin Solid Films* **1991,** 198, (1-2), 9-15.

117.   J. C. Manifacier, *Thin Solid Films* **1982,** 90, (3), 297-308.

118.   J. Bruneaux; H. Cachet; M. Froment; A. Messad, *Thin Solid Films* **1991,** 197, (1-2), 129-142.

119.   S. Shanthi; C. Subramanian; P. Ramasamy, *Journal of Crystal Growth* **1999,** 197, (4), 858-864.

120.   K. C. Mishra; K. H. Johnson; P. C. Schmidt, *Physical Review B* **1995,** 51, (20), 13972.

121.   R. G. Egdell; W. R. Flavell; P. Tavener, *Journal of Solid State Chemistry* **1984,** 51, (3), 345-354.

122.   A. L. Dawar; J. C. Joshi, *Journal of Materials Science* **1984,** 19, (1), 1-23.

123.   M. D. Allendorf, *Thin Solid Films* **2001,** 392, (2), 155-163.

124.   J. A. Anna Selvan; A. E. Delahoy; S. Guo; Y.-M. Li, *Solar Energy Materials and Solar Cells* **2006,** 90, (18-19), 3371-3376.

125.   R. G. Gordon; J. Proscia; F. B. Ellis; A. E. Delahoy, *Solar Energy Materials* **1989,** 18, (5), 263-281.

126.   J. G. O'Dowd, *Solar Energy Materials* **1987,** 16, (5), 383-391.

127.   G. Gouesbet, *Journal of Quantitative Spectroscopy and Radiative Transfer* 110, (14-16), 1223-1238.

128.    T. L. Chu; S. S. Chu; S. T. Ang; M. K. Mantravadi, *Solar Cells* 21, (1-4), 73-80.
129.    R. W. Miles, *Vacuum* **2006,** 80, (10), 1090-1097.
130.    D. Nečas; P. Klapetek *Gwyddion*, http://gwyddion.net/, 2009, (accessed Nov. 2010)
131.    K. Pearson, *Philosophical Transactions, Royal Society London* **1896, 187**, 253-318.
132.    Ç.Öncel; Y.Yürüm, *Fullerenes, Nanotubes and Carbon Nanostructures* **2006,** 14, (1), 17 - 37.
133.    E. Lamouroux; P. Serp; P. Kalck, *Catalysis Reviews: Science and Engineering* **2007,** 49, (3), 341 - 405.
134.    J. Shinar; Z. V. Vardeny; Z. H. Kafafi, *Optical and electronic properties of fullerenes and fullerene based materials.* Marcel Dekker: New York, 2000, 1-380.
135.    J.-P. Tessonnier; D. Rosenthal; T. W. Hansen; C. Hess; M. E. Schuster; R. Blume; F. Girgsdies; N. Pfänder; O. Timpe; D. S. Su; R. Schlögl, *Carbon* **2009,** 47, (7), 1779-1798.
136.    R. Brukh; S. Mitra, *Chemical Physics Letters* **2006,** 424, (1-3), 126-132.
137.    Z. Y. Juang; J. F. Lai; C. H. Weng; J. H. Lee; H. J. Lai; T. S. Lai; C. H. Tsai, *Diamond and Related Materials* 13, (11-12), 2140-2146.
138.    W. Wasel; K. Kuwana; P. T. A. Reilly; K. Saito, *Carbon* **2007,** 45, (4), 833-838.
139.    F.-B. Rao; T. Li; Y.-L. Wang, *Physica E: Low-dimensional Systems and Nanostructures* **2008,** 40, (4), 779-784.
140.    H. Chunnian; Z. Naiqin; H. Yajing; L. Jiajun; S. Chunsheng; D. Xiwen, *Materials Science and Engineering: A* **2006,** 441, (1-2), 266-270.
141.    S. Tang; Z. Zhong; Z. Xiong; L. Sun; L. Liu; J. Lin; Z. X. Shen; K. L. Tan, *Chemical Physics Letters* **2001,** 350, (1-2), 19-26.
142.    H. Li; C. Shi; X. Du; C. He; J. Li; N. Zhao, *Materials Letters* **2008,** 62, (10-11), 1472-1475.
143.    G. Ortega-Cervantez; G. Rueda-Morales; J. Ortiz-López, *Microelectronics Journal* 36, (3-6), 495-498.
144.    W. Z. Li; J. G. Wen; M. Sennett; Z. F. Ren, *Chemical Physics Letters* **2003,** 368, (3-4), 299-306.
145.    M. J. O'Connell; S. M. Bachilo; C. B. Huffman; V. C. Moore; M. S. Strano; E. H. Haroz; K. L. Rialon; P. J. Boul; W. H. Noon; C. Kittrell; J. Ma; R. H. Hauge; R. B. Weisman; R. E. Smalley, *Science* **2002,** 297, (5581), 593-596.
146.    C. K. Gupta, *Chemical Metallurgy: Principles and Practice*. Wiley-VHC: Weinheim 2003, 363.
147.    H.-Y. Lin; Y.-W. Chen; C. Li, *Thermochimica Acta* **2003,** 400, (1-2), 61-67.
148.    G. Bond; K. C. Molloy; F. S. Stone, *Solid State Ionics* **1997,** 101-103, (Part 2), 697-705.
149.    T. Inoue; I. Gunjishima; A. Okamoto, *Carbon* **2007,** 45, (11), 2164-2170.
150.    B. Liu; W. Ren; L. Gao; S. Li; Q. Liu; C. Jiang; H.-M. Cheng, *The Journal of Physical Chemistry C* **2008,** 112, (49), 19231-19235.
151.    M. S. Dresselhaus; G. Dresselhaus; R. Saito; A. Jorio, *Physics Reports* **205,** 409, 47-99.

152. S.Maruyama; Y.Miyauchi; Y;Murakami; S.Chiashi, *New Journal of Physics* **2003,** 5, (1), 149.

153. H. Kataura; Y. Kumazawa; Y. Maniwa; I. Umezu; S. Suzuki; Y. Ohtsuka; Y. Achiba, *Synthetic Metals* **1999,** 103, (1-3), 2555-2558.

154. H. Kuzmany; W. Plank; M. Hulman; C. Kramberger; A. Grüneis; T. Pichler; H. Peterlik; H. Kataura; Y. Achiba, *The European Physical Journal B - Condensed Matter and Complex Systems* **2001,** 22, (3), 307-320.

155. B. Chase; N. Herron; E. Holler, *The Journal of Physical Chemistry* **1992,** 96, (11), 4262-4266.

156. D. R. Lide, *Handbook of Chemistry and Physics*. CRC Press LLC: 2004, (75) p.295.

157. V. G. Tsirel'son; A. S. Avilov; Y. A. Abramov; E. L. Belokoneva; R. Kitaneh; D. Feil, *Acta Crystallographica B* **1998,** 54, 8-17.

158. P. Trucano; R. Chen, *Nature* **1975,** 258, 136-137.

159. H. E. Swanson; E. N. B. o. S. Tatge, 539, 1-95., *National Bureau of Standards* **1953,** 539, 1-95.

160. R. T. K. Baker; P. S. Harris, *The formation of filamentous carbon*. Marcel Dekker Inc: New York., 1978; pp.83-165.

161. S. B. Sinnott; R. Andrews; D. Qian; A. M. Rao; Z. Mao; E. C. Dickey; F. Derbyshire, *Chemical Physics Letters* **1999,** 315, (1-2), 25-30.

162. C. P. Deck; K. Vecchio, *Carbon* **2006,** 44, (2), 267-275.

163. K. P. De Jong; J. W. Geus, *Catalysis Reviews: Science and Engineering* **2000,** 42, (4), 481 - 510.

164. I. Vesselényi; K. Niesz; A. Siska; Z. Kónya; K. Hernadi; J. B. Nagy; I. Kiricsi, *Reaction Kinetics and Catalysis Letters* **2001,** 74, (2), 329-336.

165. Rodriguez, *Journal of Materials Research* **1993,** 8, 12.

166. H. Okamoto; T. Massalski, *Journal of Phase Equilibria* **1984,** 5, (4), 378-379.

167. B. O. Boskovic; V. Stolojan; R. U. A. Khan; S. Haq; S. R. P. Silva, *Nature Materials* **2002,** 1, (3), 165-168.

168. N. Latorre; J. Villacampa; T. Ubieto; E. Romeo; C. Royo; A. Borgna; A. Monzón, *Topics in Catalysis* **2008,** 51, (1), 158-168.

169. K. Wang; P. Birjukovs; D. Erts; R. Phelan; M. Morris; H. Zhou; J. D. Holmes, J*ournal of Materials Chememistry* **2009,** 19, 1331-1338.

170. T. Minami, *Thin Solid Films* **2008,** 516, (7), 1314-1321.

171. M. W. Rowell; M. A. Topink; M. D. McGeheea; H. Prall; G. Dennler; N. S. Sariciftci; L. Hu; G. G., *Applied Physical Letters* **2006,** 88, 233506.

172. Q. Cao; J. A. Rogers, *Advanced Materials* **2009,** 21, 9-53.

173. G.-W. Lee; J. Kim; J. Yoon; J.-S. Bae; B. C. Shin; I. S. Kim; W. Oh; M. Ree, *Thin Solid Films* **2008,** 516, (17), 5781-5784.

174. P. Liu, *European Polymer Journal* **2005,** 41, (11), 2693-2703.

175. C. Hu; Z. Chen; A. Shen; X. Shen; J. Li; S. Hu, *Carbon* **2006,** 44, (3), 428-434.

176. H. Geng, *Journal Materials Chemistry* **2008,** 18, 1261-1266.

177. S. Goyanes; G. R. Rubiolo; A. Salazar; A. Jimeno; M. A. Corcuera; I. Mondragon, *Diamond and Related Materials* **2007,** 16, (2), 412-417.

178. Z. Wang; Q. Liu; H. Zhu; H. Liu; Y. Chen; M. Yang, *Carbon* **2007,** 45, (2), 285-292.

179. E. C. Vermisoglou; V. Georgakilas; E. Kouvelos; G. Pilatos; K. Viras; G. Romanos; N. K. Kanellopoulos, *Microporous and Mesoporous Materials* **2007,** 99, (1-2), 98-105.

180. Y. Wang; Z. Iqbal; S. Mitra, *Journal of the American Chemical Society* **2005,** 128, (1), 95-99.

181. B. A. Kakade; V. K. Pillai, *Applied Surface Science* **2008,** 254, (16), 4936-4943.

182. Y. Tsukahara; T. Yamauchi; T. Kawamoto; Y. Wada, *Bulletin of the Chemical Society of Japan* **2008,** 81, (3), 387-392.

183. B. B. Parekh; G. Fanchini; G. Eda; M. Chhowalla, *Applied Physics Letters* **2007,** 90, (12), 3.

184. M. A. Meitl; Y. Zhou; A. Gaur; S. Jeon; M. L. Usrey; M. S. Strano; J. A. Rogers, *Nano Letters* **2004,** 4, (9), 1643-1647.

185. X. Yu; R. Rajamani; K. A. Stelson; T. Cui, *Surface and Coatings Technology* **2008,** 202, (10), 2002-2007.

186. Y. Guo; J. Wu; Y. Zhang, *Chemical Physics Letters* **2002,** 362, (3-4), 314-318.

187. Z. Li; H. R. Kandel; E. Dervishi; V. Saini; Y. Xu; A. R. Biris; D. Lupu; G. J. Salamo; A. S. Biris, *Langmuir* **2008,** 24, (6), 2655-2662.

188. S. Frank; P. Poncharal; Z. L. Wang; W. A. Heer, *Science* **1998,** 280, (5370), 1744-1746.

189. S. Datta, *Quantum Transport: Atom to Transistor.* Cambridge University Press: Cambridge, 2005, 141-150.

190. M. A. Grado-Caffaro; M. Grado-Caffaro, *The Journal of Chemical Physics* **2009,** 130, (12), 126101.

191. M. A. Grado-Caffaro; M. Grado-Caffaro, *Physics Letters A* **2008,** 372, (45), 6770-6772.

192. Z. R. Li; H. R. Kandel; E. Dervishi; V. Saini; A. S. Biris; A. R. Biris; D. Lupu, *Applied Physics Letters* **2007,** 91, (5), 3.

193. M. F. Islam; E. Rojas; D. M. Bergey; A. T. Johnson; A. G. Yodh, *Nano Letters* **2003,** 3, (2), 269-273.

194. R. Graupner, *Journal of Raman Spectroscopy* **2007,** 38, (6), 673-683.

195. B. Scheibe; E. Borowiak-Palen; R. J. Kalenczuk, *Materials Characterization* 61, (2), 185-191.

196. B. Smith, *Infrared Spectral Interpretation.* CRC Press LLC: 1999, 67-75 and 153-158.

197. H. Yu; Y. Jin; Z. Li; F. Peng; H. Wang, *Journal of Solid State Chemistry* **2008,** 181, (3), 432-438.

198. S. Caddick; R. Fitzmaurice, *Tetrahedron* **2009,** 65, (17), 3325-3355.

199. P. Lidström; J. Tierney; B. Wathey; J. Westman, *Tetrahedron* **2001,** 57, (45), 9225-9283.

200. M. A. Herrero; J. M. Kremsner; C. O. Kappe, *The Journal of Organic Chemistry* **2007,** 73, (1), 36-47.

201. S. R. P. Silva, *Properties of Amorphous Carbon.* INSPEC publishing: London, 2003, p.62.

202. K.Tanaka; T.Yamabe; K.Fukui, *The Science and Technology of Carbon Nanotubes*. Elsevier Science: Oxford 1999, pp.107-128.
203. C. G. V. d. Walle, *Journal of Physics: Condensed Matter* **2008,** 20, (6), 064230.
204. A. W. Y.Imai, *Journal of Materials Science:Materials in electronics* **2004,** 15, 743-749.
205. V. Fathollahi; M. M. Amini, *Materials Letters* **2001,** 50, (4), 235-239.
206. Y.-F. Lu; Z.-Z. Ye; Y.-J. Zeng; H.-P. He; L.-P. Zhu; B.-H. Zhao, *Chemical Vapor Deposition* **2007,** 13, (6-7), 295-297.
207. Y. Gu; X. Li; W. Yu; X. Gao; J. Zhao; C. Yang, *Journal of Crystal Growth* **2007,** 305, (1), 36-39.
208. M. H. Huang; S. Mao; H. Feick; H. Yan; Y. Wu; H. Kind; E. Weber; R. Russo; P. Yang, *Science* **2001,** 292, (5523), 1897-1899.
209. S. J. Pearton; D. P. Norton; K. Ip; Y. W. Heo; T. Steiner, *Progress in Materials Science* **2005,** 50, (3), 293-340.
210. S.Takada, *Journal of Applied Physics* **1993,** (10),73.
211. G. E. Buono-Core; G. Cabello; A. H. Klahn; R. Del Río; R. H. Hill, *Journal of Non-Crystalline Solids* **2006,** 352, (38-39), 4088-4092.
212. H. Sato; T. Minami; T. Miyata; S. Takata; M. Ishii, *Thin Solid Films* **1994,** 246, (1-2), 65-70.
213. K. U. Sim; S. W. Shin; A. V. Moholkar; J. H. Yun; J. H. Moon; J. H. Kim, *Current Applied Physics* 10, (3, Supplement 1), S463-S467.
214. A. Hongsingthong; I. Afdi Yunaz; S. Miyajima; M. Konagai, *Solar Energy Materials and Solar Cells* 95, (1), 171-174.
215. O. Renault; M. Labeau, *Journal of The Electrochemical Society* **1999,** 146, (10), 3731-3735.
216. S. B. Majumder; M. Jain; P. S. Dobal; R. S. Katiyar, *Materials Science and Engineering B* **2003,** 103, (1), 16-25.
217. H. Agura; A. Suzuki; T. Matsushita; T. Aoki; M. Okuda, *Thin Solid Films* **2003,** 445, (2), 263-267.
218. K. Haga; P. S. Wijesena; H. Watanabe, *Applied Surface Science* **2001,** 169-170, 504-507.
219. C. W. Gorrie; M. Reese; J. D. Perkins; M. F. A. M. van Hest; J. L. Alleman; M. S. Dabney; B. To; D. S. Ginley; J. J. Berry in: *Transparent conducting contacts based on zinc oxide substitutionally doped with gallium*, Photovoltaic Specialists Conference, 2008. PVSC '08. 33rd IEEE, 2008; 1-3.
220. J.Hu; R.G.Gordon, *J.Appl.Phys.* **1992,** (2), 71.
221. J. W. P.; Schmelzer, *Nucleation Theory and Applications*. Wiley-VHC: 2006; pp. 219-222.
222. T.Maruyama; J.Shinoya, *Journal of Materials Science Letters* **1992,** 11, 170-172.
223. G. L. Mar; P. Y. Timbrell; R. N. Lamb, *Chemistry of Materials* **1995,** 7, (10), 1890-1896.
224. H.M.Rietveld, *Journal of Applied Crystallography* **1969**, 65-71.
225. A.March; Zeitschrift für Kristallographie, **1932,** 81, 285-297.
226. W.A.Dollase, *Journal of Applied Crystallography* **1986,** 19, 267-272.

227. A. C. Larson; R. B. V. Dreele, GSAS Manual, Los Alamos National Laboratory Report, 1988, 86-784.
228. B. H. Toby, *Journal of Applied Crystallography* **2001,** 34, 210-213.
229. S.C.Abrahams; J.L.Bernstein, *Acta. Crystallographica B* **1969,** 25, 1233-1236.
230. M.Birkholz, *Thin Film Analysis by X-Ray Scattering*. Wiley-VCH: 2006, pp.108-109.
231. R.Swanepoel; Journal of Physics E: *Scientific Instruments,* **1983,** (16), 1214
232. A. Mills; M. McFarlane, *Catalysis Today* **2007,** 129, (1-2), 22-28.
233. A. Mills; J. Wang, *J. Photochem. Photobiol. A: Chem.* **2006,** 182, 181.
234. A.Mills; S.Le Hunt, *Journal of Photochemistry & Photobiology A* **1997,** 108, (1), 1-35.
235. Y.Paz; Z.Luo; L.Rabenberg; A.Heller, *Journal of Material Research* **1995,** 10, 2842-2848.
236. M. Miki-Yoshida; V. Collins-Martínez; P. Amézaga-Madrid; A. Aguilar-Elguézabal, *Thin Solid Films* **2002,** 419, (1-2), 60-64.
237. B. D. Cassie; S. Baxter, *Transactions of the Faraday Society* **1944,** 40, 546-551.
238. S. Tatsuo; S. Nobuyuki; F. Katsutoshi; E. Yasuo; S. Takayoshi, *The Journal of Physical Chemistry*, **2007,** 9, (19), 2413-2420.
239. R.-D. Sun; A. Nakajima; A. Fujishima; T. Watanabe; K. Hashimoto, *The Journal of Physical Chemistry B* **2001,** 105, (10), 1984-1990.
240. S. Wang, *Journal of Photochemistry and Photobiology C: Photochemistry Reviews* **2007,** 8, 18-29.
241. C. R. M. Grovenor; H. T. G. Hentzell; D. A. Smith, *Acta Metallica* **1984,** 32, (773).
242. P. T. Moseley, *Measurement Science and Technology* **1997,** 8, (3), 223.
243. I. Lundström, *Sensors and Actuators B: Chemical* **1996,** 35, (1-3), 11-19.
244. G. Korotcenkov, *Materials Science and Engineering: B* **2007,** 139, (1), 1-23.
245. K. Zakrzewska, *Thin Solid Films* **2001,** 391, (2), 229-238.
246. K. Sahner; G. Hagen; D. Schönauer; S. Reiß; R. Moos, *Solid State Ionics* **2008,** 179, (40), 2416-2423.
247. M. Vilaseca; J. Coronas; A. Cirera; A. Cornet; J. R. Morante; J. Santamaria, *Sensors and Actuators B: Chemical* **2007,** 124, (1), 99-110.
248. S. J. Gentry; T. A. Jones, *Sensors and Actuators* **1986,** 10, (1-2), 141-163.
249. M. Ivanovskaya; P. Bogdanov; G. Faglia; P. Nelli; G. Sberveglieri; A. Taroni, *Sensors and Actuators B: Chemical* **2001,** 77, (1-2), 268-274.
250. H.-Q. Nguyen; J.-S. Huh, *Sensors and Actuators B: Chemical* **2006,** 117, (2), 426-430.
251. M. Lucci; A. Reale; A. Di Carlo; S. Orlanducci; E. Tamburri; M. L. Terranova; I. Davoli; C. Di Natale; A. D'Amico; R. Paolesse, *Sensors and Actuators B: Chemical* **2006,** 118, (1-2), 226-231.
252. M. Penza; R. Rossi; M. Alvisi; M. A. Signore; E. Serra; R. Paolesse; A. D'Amico; C. Di Natale, *Sensors and Actuators B: Chemical* 144, (2), 387-394.
253. B.-Y. Wei; M.-C. Hsu; P.-G. Su; H.-M. Lin; R.-J. Wu; H.-J. Lai, *Sensors and Actuators B: Chemical* **2004,** 101, (1-2), 81-89.
254. J. Suehiro; H. Imakiire; S.-i. Hidaka; W. Ding; G. Zhou; K. Imasaka; M. Hara, *Sensors and Actuators B: Chemical* **2006,** 114, (2), 943-949.

255. N. Van Hieu; L. T. B. Thuy; N. D. Chien, *Sensors and Actuators B: Chemical* **2008,** 129, (2), 888-895.
256. N. Van Duy; N. Van Hieu; P. T. Huy; N. D. Chien; M. Thamilselvan; J. Yi, *Physica E: Low-dimensional Systems and Nanostructures* **2008,** 41, (2), 258-263.
257. T. Ueda; S. Katsuki; K. Takahashi; H. A. Narges; T. Ikegami; F. Mitsugi, *Diamond and Related Materials* 17, (7-10), 1586-1589.
258. T. Ueda; M. M. H. Bhuiyan; H. Norimatsu; S. Katsuki; T. Ikegami; F. Mitsugi, *Physica E: Low-dimensional Systems and Nanostructures* **2008,** 40, (7), 2272-2277.
259. I. Sayago; H. Santos; M. C. Horrillo; M. Aleixandre; M. J. Fernández; E. Terrado; I. Tacchini; R. Aroz; W. K. Maser; A. M. Benito; M. T. Martínez; J. Gutiérrez; E. Muñoz, *Talanta* **2008,** 77, (2), 758-764.
260. M. J. Madou; S. R. Morrison, *Chemical Sensing with Solid State Devices*. Academic Press, INC.: London, 1989, pp.1-56.
261. W. Zhang; H. Uchida; T. Katsube; T. Nakatsubo; Y. Nishioka, *Sensors and Actuators B: Chemical* **1998,** 49, (1-2), 58-62.
262. J.-K. Park; H.-J. Yee; K. S. Lee; W.-Y. Lee; M.-C. Shin; T.-H. Kim; S.-R. Kim, *Analytica Chimica Acta* **1999,** 390, (1-3), 83-91.
263. G. Korotcenkov, *Materials Science and Engineering: R: Reports* **2008,** 61, (1-6), 1-39.